4-24-2015

Investigation of Diesel Engine Emissions Oxidation and Sulfation Mechanisms

Hom Sharma
University of Connecticut - Storrs, sharma.hom@gmail.com

Investigation of Diesel Engine Emissions Oxidation and Sulfation Mechanisms

Hom Nath Sharma, PhD

University of Connecticut, 2015

Noble metal (Pt/Pd) based diesel oxidation catalysts (DOCs) represent the most widely used aftertreatment catalysts to treat emissions from diesel engine exhaust. Due to increasingly stringent regulations to control emissions, the DOCs need to be robust and efficient, which in turn requires a complete understanding of the catalytic reactions taking place inside those units. Despite the excellent activity of currently used DOCs towards engine emissions, they are susceptible to deactivation due to sulfur oxides (SO_x) in the diesel engine exhaust. Interactions of SO_x with the catalyst metal and support can result in sulfate formation which leads to the release of untreated toxic emissions to the air. In this thesis, aforementioned two issues are investigated. Specifically, our study is targeted to (a) fundamental understanding of the emissions oxidation chemistry on DOC, and (b) Identification of mechanism of sulfation of DOC. In the first strand, a comprehensive microkinetic model for primary emissions oxidation (e.g., CO, NO, NH_3, HCN, and CH_2O) is developed on Pt DOC. The developed microkinetic model was validated against multiple monolith and fixed bed experiments conducted in practically more relevant operating conditions such as dilute emissions concentrations, atmospheric pressure, and short residence times. This approach is extended to explore the reaction kinetics of SO_x on the Pt surface. The second part of the work undertaken in this thesis focuses on understanding the sulfation mechanism of DOC utilizing state-of-the-art first principles computations. A systematic study is conducted for SO_x interactions on Pt(111) and Pd(111) surfaces using density functional theory (DFT). To understand the surface reaction mechanism involving

various SO_x species, we investigate the minimum energy pathways and estimated the oxidation barriers for SO_x oxidation on both surfaces. As a stepping stone towards understanding sulfation, we successfully implement our first principles computed parameters as inputs into the SO_2 oxidation microkinetic model to predict DOC relevant experimental results. Going forward, we explored the SO_x interactions with Pt and Pd surfaces in realistic temperature and pressure conditions, and under oxidizing and sulfating environments using first principles thermodynamics approach. For the first time we are able to explain why Pd behaves so differently towards sulfation compared to Pt. Few critical descriptors are identified which can be useful for the future quest of sulfur resistant catalysts materials.

Investigation of Diesel Engine Emissions Oxidation and Sulfation Mechanisms

Hom Nath Sharma

B.Sc., Tribhuvan University, 2004

B.S., University of New Hampshire, 2010

A Dissertation

Submitted in Partial Fulfillment of the

Requirements for the Degree of Doctor of Philosophy

at the

University of Connecticut

2015

2015

APPROVAL PAGE

Doctor of Philosophy Dissertation

Investigation of Diesel Engine Emissions Oxidation and Sulfation Mechanisms

Presented by

Hom Nath Sharma, B.Sc., B.S.

Major Advisor_____

Rampi Ramprasad

Associate Advisor_____

Ashish B. Mhadeshwar

Associate Advisor_____

Steven L. Suib

Associate Advisor_____

William E. Mustain

Associate Advisor_____

Kristina M. Wagstrom

University of Connecticut

2015

I would like to dedicate this thesis to my loving parents Agni Prasad Gyawali and Til Kumari Gyawali. . .

Acknowledgements

First and foremost I offer my sincerest gratitude to my major advisor, Dr. Rampi Ramprasad, who has supported me the last three years of my thesis with his patience and depth of knowledge whilst allowing me the room to work in my own way. I learned a lot from him after joining his group as a beginner in the field of quantum mechanics and density functional theory. I simply can not thank him enough for his moral support and encouragement.

I would like to express by deepest respect to my previous advisor Dr. Ashish Mhadeshwar, who helped me to become a graduate level engineer from an amateur undergraduate student and tolerated me in the most difficult phase of the graduate school. I learned from him lot by working together since I had a privilege to be his first graduate student. I would like to thank him for being available 24/7 for the help.

My sincere respect goes to Dr. Steve Suib for his help and support. I really enjoyed the exposure to the wet-lab experiments and equipments during the project with him. His perspective provided me a another dimension to my thesis work. I really enjoyed working with his team in the Department of Chemistry at UCONN.

I would like to thank my committee members Dr. William Mustain and Dr. Kristina Wagstrom for kind help and valuable advice, which are important to me in the whole process of my graduate studies.

Special thanks goes to Dr. Ameya Joshi and Lakshitha Pahalagedara for their help, support and work during the project with Corning Inc. This opportunity was truly an amazing experience. I learned a lot.

My present and past group members owe a big thanks from me. They are always there with me whenever I need some help. Thanks to Dr. Huan Tran, Dr. Vinit Sharma , Dr. Ghanshyam Pilania, Dr. Chiho Kim, Dr. Sridevi Krishnan, Dr. Satyesh Yadav, Dr. Clive Bealing, Dr. Chenchen Wang, Dr. Yenny Cardona Quintero, Dr. Angie Moreno, Molly Koehle, Ameya Akkalkotkar, Venkatesh Botu, Lihua Chen, Arun Kumar Mannodi-Kanakkithodi, and Rohit Batra for all the help.

Huge thanks to my Nepali friends for making me feel Storrs like my home. You guys are always helpful and amazing. Thanks Pujan Joshi, Dr. Sujan Shrestha, Pragati Shrestha, Bibek Shretha, Sushil Dahal, Uday Dahal, Niraj Ghimire, Rajeev Ghimire, Sudikshya Ghimire, Geeta Dahal, Binu Shrestha, Sadikshya Bhandari, Surendra Baniya, Suvash Dhakal, Chaman Ranjit, and Yerina Ranjit.

My parents deserve my utmost respect. Many thanks goes to my parents Agni Prasad Gyawali and Til Kumari Gyawali for their continuous support and love. I would like to extend my thanks to by brother and sister and their family for all the love they have given. I would like to thank my father-in-law, mother-in-law, and brother-in-laws for their love, support and encouragements.

I would like to extend my thanks to my wife Sarita Neupane for all the love, support, and help. This journey would not have been possible without her. You are my morale booster whenever I felt low. Thank you !

Finally, the funding support from the Department of Education GAANN fellowship, Corning Inc., and the Environmental Protection Agency STAR fellowship (fellowship number FP917501) is greatly acknowledged.

Table of contents

List of figures

List of tables

Chapter 1

Introduction and Background

1.1 Diesel Engine Emissions

Diesel engines are an essential part of the modern society and backbone of the global economy. Diesel is the predominant source of power used in trucks, railroads, shipping, agriculture, public transportation, airport operations, mining as well as homeland security and defense. [1] Diesel provides better fuel economy, greater power density, better performance, unmatched durability, and longer engine life than many other energy sources. Diesel engines offer significantly higher efficiency than current gasoline spark-ignition engines; in some vehicles, fuel efficiency can be improved by 20% to 50% compared to gasoline. This provides the potential for reduced greenhouse gas emissions and reduced petroleum demand in the U.S., improving energy security. [2, 3] More than 13 million diesel vehicles are responsible for transportation of 94% of the goods in the U.S. and use $\sim$ 4 million barrels of diesel per day [4–6]. In the European market, 53% of the passenger cars run on diesel and the global market share of diesel passenger vehicles is expected to double in the next 10 years [2, 7], However, diesel engines are responsible for producing toxic compounds such as carbon monoxide (CO), carbon dioxide (CO_2), nitrogen

oxides (NO_x), hydrocarbons (HC), sulfur oxides (SO_x), volatile organic compounds (VOCs), [8–10] poly aromatic hydrocarbons (PAHs), [11, 12] soluble organic fractions (SOF), and particulate matter (PM). [3, 13, 14] Furthermore, solid emissions such as metals, inorganic compounds, sulfates and solid hydrocarbons, [14, 15] nitrogen containing emissions such as hydrogen cyanide (HCN) and ammonia (NH_3) as well as aldehydes such as formaldehyde (CH_2O) and acetaldehyde (CH_3CHO) have also been observed in the diesel engine exhaust. [16–20] These emissions are known to cause cancer, premature death, acute and chronic respiratory injury, asthma attacks, ground level ozone formation, acid deposition, particulate haze, visibility impairment; and they can damage plants, animals, crops, and water resources. [3, 20–24] According to a US-based study by the Clean Air Task Force, toxic emissions from diesel engine exhaust claim 21,000 lives per year due to respiratory and cardiovascular diseases ($\sim$3,000 from lung cancer); result in 27,000 heart attacks and 400,000 asthma attacks per year; lead to $\sim$139 billion in monetized damages or losses per year; and cause an enormous threat to the environment. [4, 6] Major emission components and their ranges from a typical diesel engine exhaust are shown in Table 1.

1.2 Emissions Standards and Regulations

The year 1970 brought major changes to air pollution regulation.The Clean Air Act amendments of 1970 established the basic approach to mobil sources that continues today.The statute mandated reductions in mobile-source emissions by 90 percent for hydrocarbon, carbon monoxide, and nitrogen oxides, with an initial target date of 1975. The diesel engine emission standards were set by the EPA and California Air Resources Board (CARB) from the mid-1980s. Diesel oxidation catalysts (DOC) and Exhaust gas recirculation (EGR) were introduced to meet the emissions standard set by the EPA. Since 1990, engine manufacturers have reduced the diesel

Table 1.1 Typical diesel engine exhaust composition at an equivalence ratio (λ) of 1.1–6 [3, 7, 25–31]. λ is 1, when the air to fuel ratio (A/F) is 14.7.

Species	Concentration range	Unit
CO	100-10000	ppm
NO_x	30-1000	ppm
HC	50-500	ppm C_1
SO_x	Proportional to fuel sulfur [3], 10-100[a] [25], ~1.0[b]	ppm
CO_2	2-12	%
PM	20-200	mg/m^3
O_2	5-15	%
H_2O	1.4-7	%
NH_3	2	mg/mile
Cyanides	1	mg/mile
Benzene	6	mg/mile
Toluene	2	mg/mile
PAH	0.3	mg/mile
Aldehydes	0.0131-0.1244	mg/km

[a] Based on the information that fuel with 500 ppm of sulfur produces ~20 ppm SO_x.
[b] Based on current EPA regulations for fuel sulfur level (15 ppm maximum).

particulates (soot) significantly. With new regulation set in 2007 requires all US heavy-duty diesel vehicles must have a diesel particulate filter (DPF) in the exhaust system to reduce the particulate matter (PM) level to below 0.01 g/bhp-hr. Similarly, catalytic devices were introduced in 1990s to meet the more stricter NO_x reduction standards. In Europe, the standards set by the EU were first established as Euro 1 standards in 1993. Euro 6 standard, comparable in stringency to the US 2010 standards, became effective in 2013, for diesel engine emissions in Europe. Since 2010, the PM, NO_x, and the non-methyl hydrocarbon (NMHC) standards are 0.01 g/bhp-hr, 0.2 g/bhp-hr, and 0.14 g/bhp-hr, respectively. Figure 1.1 shows the PM and NO_x standards over the years for heady-duty diesel engines in the USA.

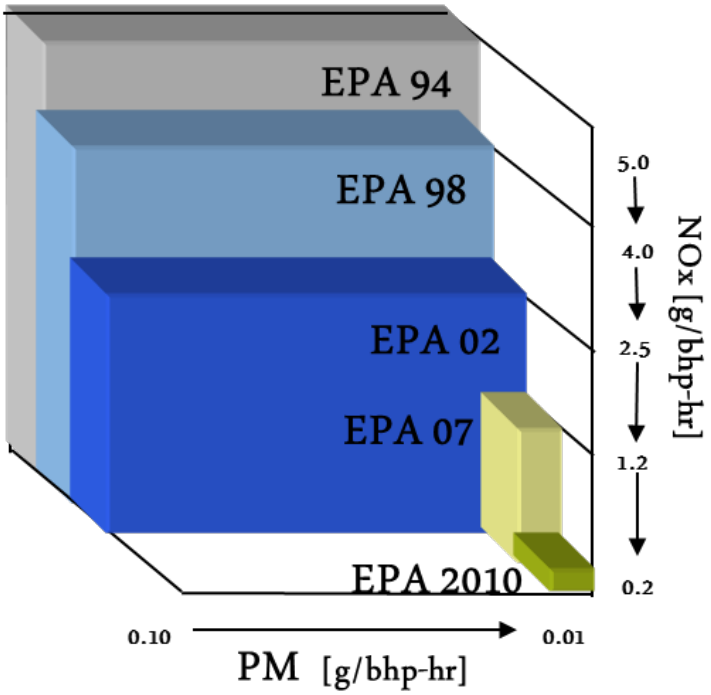

Fig. 1.1 Emission regulations over the years from EPA for heavy-duty trucks in the US.

1.3 Exhaust Aftertreatment Components

Many changes have been made to engine design and fuel composition to reduce emission production, whilst aftertreatment units have been developed to capture emissions or convert them into less harmful components. Due to a higher air to fuel (A/F) ratio compared to traditional gasoline engines (A/F = 14.7), the traditional Three Way Catalyst (TWC) for gasoline exhaust (Three way converter works under stoichiometric condition to oxidize CO and HC and reduce NO_x simultaneously) is unable to effectively control emissions from diesel engine exhaust; and therefore, the diesel engine exhaust aftertreatment system is quite complex. [22, 32] Multiple aftertreatment units are needed to control various components of diesel engine emissions, as shown in Figure 1.2.

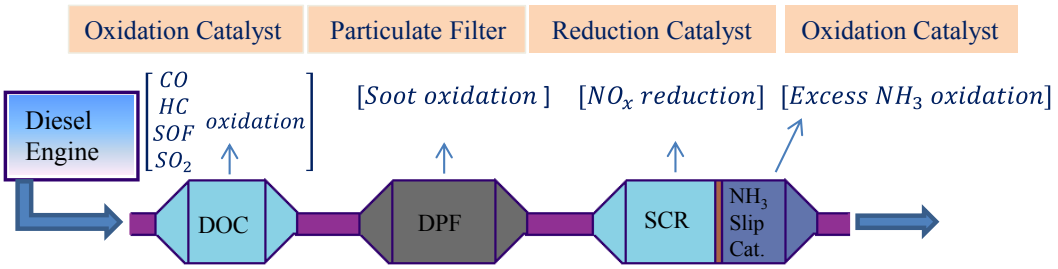

Fig. 1.2 Schematic of DOC, DPF, DeNO$_x$, and Ammonia Slip Catalyst (ASC) components in a typical diesel engine exhaust aftertreatment system. Position of the aftertreatment component units can vary according to the manufacturer, type of DeNO$_x$ unit used, and the regulations.

1.3.1 Diesel Particulate filters (DPFs)

Diesel Particulate Filters (DPF) are the most popular aftertreatment technology to control particulates/soot and to meet the stringent PM emissions standards. [8, 33] DPFs are made of porous materials and consist of channels which are alternately plugged, [2] so the exhaust gas is forced through the channel walls, but the PM is trapped on the filter wall. [34] Even though DPFs are efficient in removing particulates from the engine exhaust, periodic regeneration of DPF is necessary to avoid any plugging/back-pressure. Oxygen (10-15% of exhaust stream) is the main oxidant to burn off the soot particles typically at high temperature ($\sim$600 °C); however, presence of NO_2 in the exhaust stream (from NO oxidation on DOC) can enhance the DPF efficiency significantly by reducing the required temperature ($\sim$300 °C) along with catalytic coating (in catalytic DPF (cDPF)). [30, 35–38] The schematic DPF with channels is shown in Figure 1.3.

The oxidation of diesel soot, represented here as carbon, by oxygen can be described by one of the following reactions:

$$\mathrm{C} + \mathrm{O_2} \rightarrow \mathrm{CO_2} \tag{1.1}$$

$$\mathrm{C} + \frac{1}{2}\mathrm{O_2} \rightarrow \mathrm{CO} \tag{1.2}$$

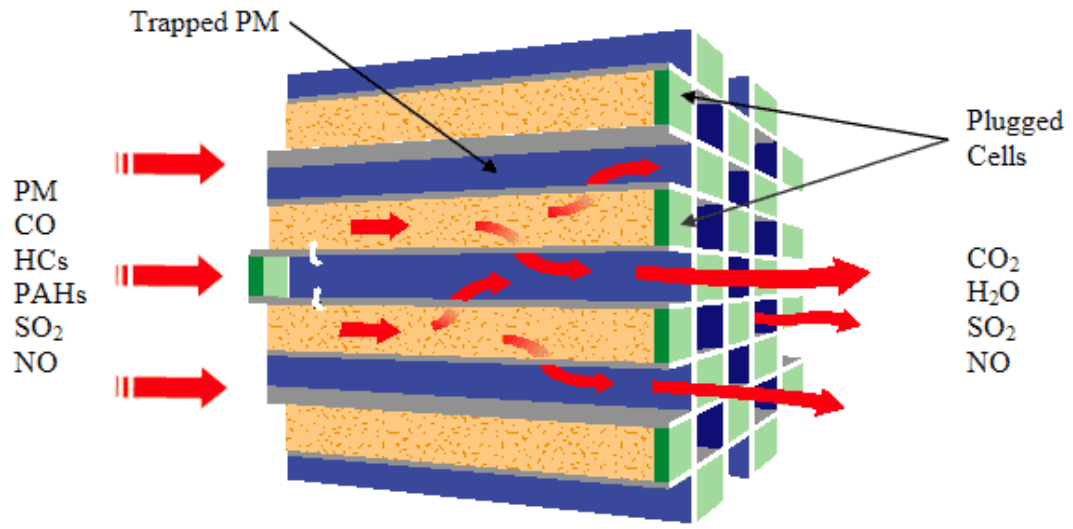

Fig. 1.3 Schematic of DPF channels with alternate plugging and DPF process. [39]

In the case of soot oxidation by NO_2, the reaction is:

$$C + NO_2 \rightarrow CO_2 + NO \tag{1.3}$$

1.3.2 DeNO$_x$ Technologies

It is extremely difficult to reduce NO_x from the diesel engine exhaust under excess oxygen conditions. [40] To reduce/remove NO_x from the diesel engine exhaust, two common strategies are considered, viz., Selective Catalytic Reduction (SCR) and NO_x Storage and Reduction (NSR). SCR selectively reduces the nitrogen oxides (NO and NO_2) to N_2 using either NH_3/Urea (typically V_2O_5-WO_3/TiO_2 catalyst) or hydrocarbons (Ag/Al_2O_3 based catalyst). [22, 41–46] On the other hand, NSR catalysts (also known as Lean NO_x Traps (LNT)) first remove NO_x from a lean gas stream by reversible chemical adsorption onto a catalyst (typically Pt/BaO/Al_2O_3) in the form of nitrates/nitrites, followed by reduction under stoichiometric or rich conditions. [47–49]

Urea/NH_3-SCR is a popular technology for NO_x reduction. However, it is also associated with excess/unreacted NH_3 in the downstream, typically $\sim$10 ppm. [50] A Pt/Al_2O_3 coated oxidation catalyst–Ammonia Slip Catalyst (ASC)–is often installed after the NH_3/Urea-SCR to control the excess NH_3. [51–54] ASC oxidizes NH_3 to N_2 with high selectivity, allows high NH_3/urea dosing without increasing NH_3 emissions, and avoids undesirable products such as NO_x and N_2O. [54, 55]

The selective catalytic reduction involves the following set of reactions which are divided into three categories.

Standard SCR Reaction: This reaction involves reduction of NO by NH_3 in the presence of O_2 and is given as:

$$4NH_3 + 4NO + O_2 \rightarrow 4N_2 + 6H_2O \tag{1.4}$$

Fast SCR Reaction: When both NO and NO_2 in the feed react simultaneously to produce N_2 and H_2O; it is called as a fast SCR reaction, which is faster than the standard SCR reaction and given as:

$$2NH_3 + NO + NO_2 \rightarrow 2N_2 + 3H_2O \tag{1.5}$$

NO_2 SCR Reaction: When NO_2 reacts with NH_3, it is called as the NO_2 SCR reaction and it can be written as:

$$4NH_3 + 3NO_2 \rightarrow 3.5N_2 + 6H_2O \tag{1.6}$$

1.3.3 Diesel Oxidation Catalysts

Diesel Oxidation Catalysts (DOCs) represent the most predominant technology to oxidize the toxic emissions/byproducts from diesel engine exhaust. [32, 56–62] Typical DOCs are Platinum (Pt)/Palladium (Pd)/Pt-Pd alloy coated honeycomb like structures, as shown in Figure 1.4. Pd is essential to prevent the sintering of Pt particles at high temperature, which improves the

overall DOC lifetime and thermal stability. [63] Pd also reduces the DOC cost, which is a very expensive component of diesel exhaust aftertreatment. In the next section, we elaborate on the role of DOC in diesel engine exhaust aftertreatment.

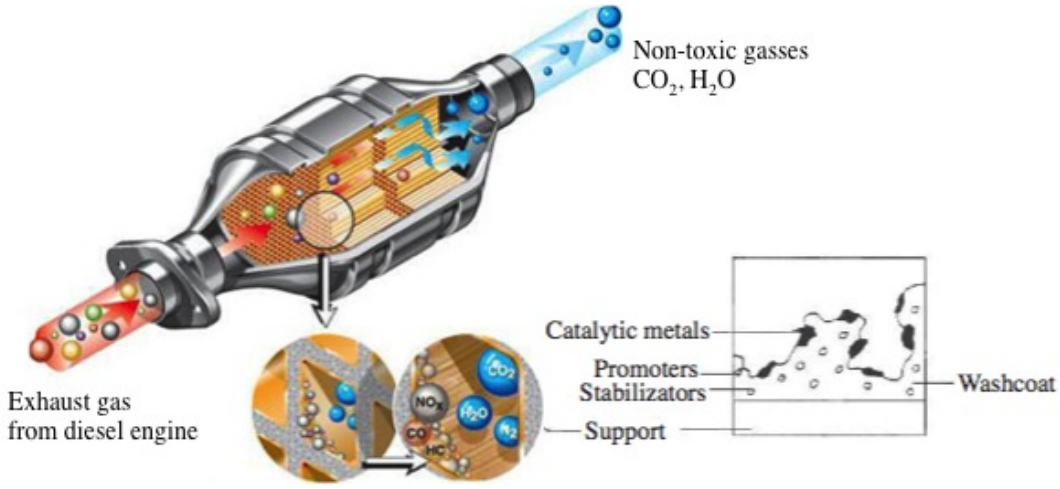

Fig. 1.4 Typical honeycomb like monolithic structure of diesel oxidation catalyst (DOC). [64] Monolithic channels and metal on support structures are shown in insets.

1.4 Role of DOC in Exhaust Aftertreatment

The primary function of the DOC is to oxidize HC, NO, CO, and byproducts from upstream components to less/non toxic compounds. Furthermore, DOC also provides NO_2 for a downstream urea-SCR, which operates efficiently at an equimolar ratio of NO and NO_2. [32] NO_2 produced from DOC can also be used to oxidize soot in the DPF at lower temperature than with O_2 alone.[32, 65, 66] Finally, DOC may be needed downstream of a hydrocarbon (HC)-SCR to oxidize the SCR byproducts (or unreacted species), such as CO, HC, NO, NH_3, HCN, CH_2O, N_2O, acetonitrile (CH_3CN), and CH_3CHO. [16, 17, 67, 68] Figure 1.5 shows couple of representative configurations of aftertreatment components where DOC plays an important role.

Major catalytic reactions on the DOC can be summarized as follows. [60, 61, 69, 70]

$$CO + \frac{1}{2}O_2 \rightarrow CO_2 \tag{1.7}$$

$$[HC] + O_2 \rightarrow CO_2 + H_2O \tag{1.8}$$

$$NO + \frac{1}{2}O_2 \rightarrow NO_2 \tag{1.9}$$

$$NH_3 + O_2 \rightarrow N_2 + NO_x + H_2O \tag{1.10}$$

$$HCN + O_2 \rightarrow NO_x + CO_2 + H_2O \tag{1.11}$$

$$[\text{Aldehydes}] + O_2 \rightarrow CO_2 + H_2O \tag{1.12}$$

$$[SOF] + O_2 \rightarrow CO_2 + H_2O \tag{1.13}$$

$$SO_2 + \frac{1}{2}O_2 \rightarrow SO_3 \tag{1.14}$$

Despite the versatile nature and utility of DOC, its deactivation due to sulfur is a major challenge in diesel engine exhaust aftertreatment, which is the primary focus of the sections to follow.

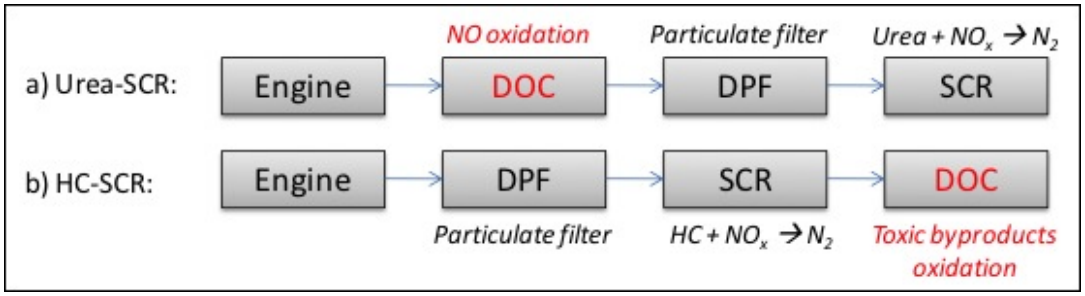

Fig. 1.5 Role of DOC in toxic emissions oxidation from diesel engine exhaust. The representative configurations focused around (a) Urea–SCR and (b) HC–SCR illustrate the importance of DOC in both cases.

1.5 Impact of Sulfur on DOC

Most catalysts deactivate over time, as reflected by decreased conversion/selectivity, thereby requiring catalyst regeneration/replacement and/or process shutdown. Typical catalyst deactivation mechanisms include (i) poisoning, (ii) fouling, (iii) thermal degradation, (iv) vapor formation, (v) vapor-solid and/or solid-solid reactions, and (vi) attrition/crushing. [71, 72] Here, we focus on the deactivation of DOC due to sulfur (poisoning).

Sulfur is present in the diesel fuel and it also comes from the lubricants used. [15, 49, 60] Due to the United States Environmental Protection Agency (EPA) regulations, the currently used ultra low sulfur diesel (USLD) contains up to 15 ppm sulfur. [49, 73–75] Despite the sulfur regulations, typical diesel engine exhaust contains $\sim$1 ppm of sulfur in oxide form [9] which can deactivate the DOC after long term exposure as well as increase the PM emissions. [9, 15, 76, 77] An example of DOC deactivation due to sulfur in the fuel is shown in Figure 1.6, where the NO oxidation performance decreases significantly in a few hours in the presence of sulfur. [9] Lubricant oil can also adversely impact the sulfur level in exhaust leading to catalyst deactivation. [78]

Sulfur in the diesel fuel and lubricants is oxidized to sulfur dioxide (SO_2) in the engine. [60] Due to the excess oxygen in the exhaust, SO_2 can be further oxidized to sulfur trioxide

(SO_3) on the DOC or cDPF above 300 C. [15, 60, 79–81] SO_3 has been reported to be stable up to 700 C. [32, 82] Both sulfur oxides interact with the DOC, resulting in its deactivation. In general, catalyst deactivation due to sulfur is a complex phenomena, associated with changes in structural, morphological, and electronic properties. [83] For simplicity, DOC deactivation due to sulfur can be divided into three major categories, viz., metal oxide sulfation, support sulfation, and species sulfate formation (through interactions with species in the exhaust), as described next.

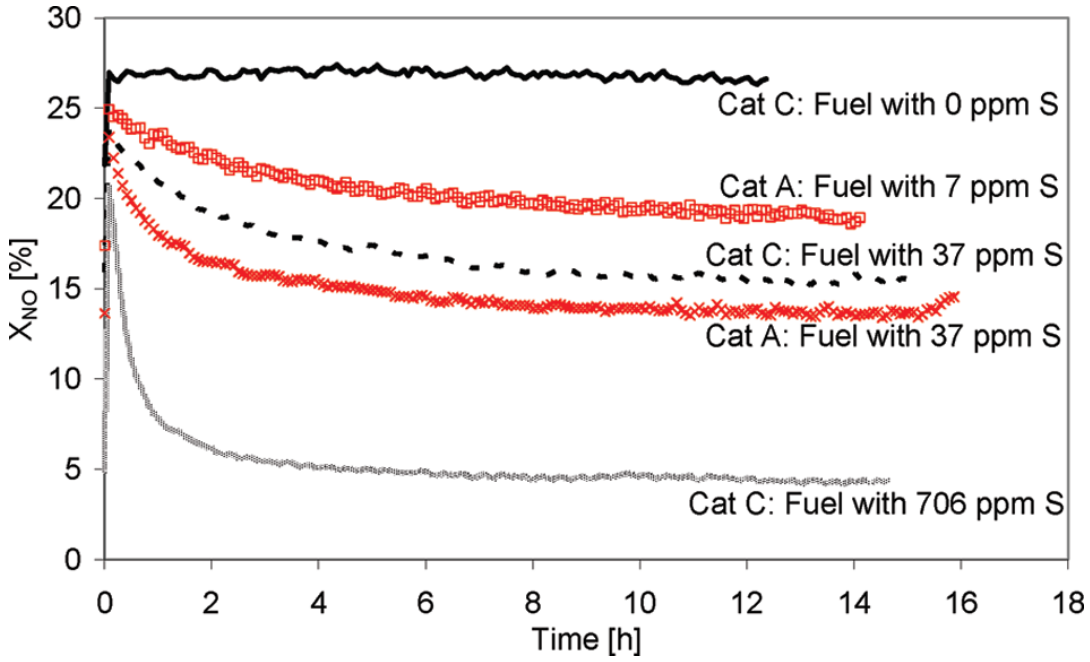

Fig. 1.6 Effect of fuel sulfur level on NO conversion on commercial DOCs. [9] Reprinted from Kröcher, O. et al., Adsorption and Desorption of SO_x on Diesel Oxidation Catalysts. Ind. Eng. Chem. Res. 48(22), 2009, 9847-9857, with permission from American Chemical Society (ACS).

1.5.1 Metal Oxide Sulfation

The sensitivity order of sulfation of oxidation catalysts used in diesel engine exhaust aftertreatment is Pd > Pt > Rh, [84] i.e., Pd is more likely to be sulfated compared to Pt DOCs. Pd is

typically converted to PdO due to the high oxygen content in the diesel engine exhaust, whereas Pt remains in the metallic form. [63] Pt is highly active for SO_2 oxidation [79, 85, 86] but Platinum sulfate ($PtSO_4$) formation is not favored. [15, 31] On the other hand, palladium sulfate ($PdSO_4$) formation is widely reported in the literature. [78, 87] Under lean-burn Natural Gas Vehicles (NGV) operating conditions (in the presence of SO_2), deactivation of Pd catalysts due to formation of inactive $PdSO_4$ has also been observed. [81, 87] Overall reaction for the metal oxide sulfation can be written as follows. [60, 88]

$$PdO + SO_3 \rightarrow PdSO_4 \tag{1.15}$$

1.5.2 Support Sulfation

In Pt-Pd based DOCs, the precious metal catalysts are dispersed on a support (wash-coat) to increase the catalyst surface area which in turn provides higher catalytic activity. Supports can also provide thermal/mechanical stability. [25, 60] Typically, γ-Al_2O_3, SiO_2, or ZrO_2 are used as support materials as they are highly porous inorganic oxides and ideal for gas diffusion; among these, γ -Al_2O_3 is most common support for DOCs. [25, 32, 60, 69] However, presence of sulfur oxides in the diesel engine exhaust can be detrimental to the Al_2O_3 support, which ultimately deteriorates the DOC activity. [60, 78, 79, 89, 90] Studies show that SO_3 strongly interacts with the Al_2O_3 support in DOC. [91] Once SO_3 is formed on the catalyst, there is a reaction with Al_2O_3 to form aluminum sulfate ($Al_2(SO_4)_3$) [91–93], which blocks the alumina pores or covers its surface, resulting in decreased surface area [32, 56, 94] and decreased catalytic activity. [92] Even though the support sulfation reaction is reversible, i.e., $Al_2(SO_4)_3$ forms Al_2O_3 and SO_3 upon heating [84], this decomposition reaction requires a very high temperature ($\sim$727 °C). [95] The overall reaction of Al_2O_3 support sulfation can be

written as follows. [69]

$$Al_2O_3 + 3SO_3 \rightarrow Al_2(SO_4)_3 \tag{1.16}$$

1.5.3 Species Sulfate Formation

Diesel engine exhaust contains significant water vapor (1.4 -7%, see Table I); therefore, SO_3 can also react with the water vapor to form sulfuric acid (H_2SO_4), thus creating tremendous challenges for emissions aftertreatment. [9, 60] H_2SO_4 contributes to the increase in particulates formation; ultra-fine particles in diesel exhaust are considered especially hazardous because of their ability to penetrate deeply into the lungs. [15, 96, 97] H_2SO_4 can desorb at 350- 400 °C or decompose back to SO_3 and H_2O at > 250 °C. [9] The overall reaction of sulfuric acid formation from SO_3 and water vapor can be written as follows.

$$H_2O + SO_3 \leftrightarrow H_2SO_4 \tag{1.17}$$

Presence of NH_3, e.g., through urea injection in SCR of NO_x or through NH_3 formation in HC-based SCR of NO_x, could also result in ammonium (bi)sulfate ($(NH_4)_2SO_4$) formation, which increases the catalyst deactivation rate. [95, 98, 99] The overall reaction of $(NH_4)_2SO_4$ formation can be written as follows.

$$2NH_3 + SO_3 + H_2O \leftrightarrow (NH_4)_2SO_4 \tag{1.18}$$

1.6 Research Objectives and Outline

The primary objective of this thesis to investigate the diesel engine emissions oxidation and sulfation mechanism. To achieve these goals, we investigate the soot oxidation kinetics on

the diesel particulate filter, primary emissions and sulfur oxides oxidations, and sulfation mechanism in the diesel oxidation catalysts. The soot oxidation kinetics study is mostly an experimental work using thermogravimetric analysis (TGA) method. The comprehensive study is performed with multiple samples including carbon black and diesel engine soot samples. This study provides many insights on the kinetics parameters of soot oxidation. Details of this work and results are provided in the Appendix A. The core of this thesis encompasses the work on DOC, which involves the development of fundamental understandings of emissions oxidation (i.e. CO, NO, CH_2O, NH_3 and HCN) and SO_x oxidation mechanism study and sulfation study to identify descriptors for sulfur deactivation of DOCs. Hydrocarbon emissions oxidation (i.e. C_2H_4 oxidation) is provided the appendix K. In essence, the soot oxidation kinetics information along with the structure-activity correlations will provide design guidelines for DPF and optimal temperature of operations to make it more economical and produce less emissions. The study of emissions oxidation chemistry will give information about the primary DOC chemistry, important reaction pathways and catalysts sizing. Such information will be crucial for efficient and economical design of DOC. On the other hand, study of the underlying molecular level sulfation mechanism will help to understand the fundamentals of DOC deactivation in the presence of sulfur oxides, identify key features of sulfation and provide some guidelines to identify new sulfur resistant catalyst materials. Next, the thesis organization is briefly discussed.

Chapter 2 provides a brief introduction to the methodologies utilized in this work. First, experimental setup is discussed for the BenchCAT reactor experiments using powder and monolith catalysts. Then, a brief description is provided for the microkinetic modeling with plug flow reactor model. At last, density functional theory and other first principles computations based methods (e.g. the first principles thermodynamics, structure prediction method called USPEX) are discussed.

Chapter 3 focus on developing a detailed mechanistic understanding of the catalytic reaction kinetics for the oxidation of five major emissions species (C_1 and N_1 components) on Pt-based DOCs. Those emissions species include CO, NO, CH_2O, NH_3, and HCN. The chapter addresses development of elementary step reaction mechanism, kinetics and thermodynamic parameter estimation using various techniques, and the model validation using plug flow reactor modeling coupled with detailed reaction mechanism.

Chapter 4 surveys the challenging problem of SO_x interactions with DOC. It provides a brief background on the past work and focuses on the development of detailed microkinetic modeling of SO_2 oxidation of Pt based DOC.

Chapter 5 discuses the development of microkinetic model for H_2SO_4 formation on DOC due to SO_x and H_2 interactions. Two possible pathways for the H_2SO_4 formation is analyzed and the most favorable pathway is proposed.

Chapter 6 covers the first principles based investigation of SO_x interactions with Pt(111) and Pd(111) surfaces. Thermodynamics, kinetics of SO_x oxidation are compared to understand the interactions of Pt and Pd with SO_x. This chapter also discusses how DFT can be coupled with microkinetic modeling to study the SO_x oxidation process.

Chapter 7 focuses on a comprehensive analysis of sulfation behaviors of Pt and Pd DOC. The first principles thermodynamics is employed to study the phases under oxidizing and sulfating environments. From this study, few important descriptors are identified which could help us to design future sulfur resistant catalysts for DOC.

In the last Chapter, I provide a summary of this work, few key achievements, and a broad outlook for the future directions to further this research.

Chapter 2

Methods

2.1 Introduction

In this work, microkinetic modeling, density functional theory, and experimental approaches have been implemented to understand the oxidation and sulfation mechanism of diesel oxidation catalysts (DOCs). In this chapter, a brief review of the methodologies is provided. Primary emissions oxidation chemistry (e.g, CO, NO, CH_2O, NH_3, HCN) and SO_x oxidation chemistry are studied using microkinetic modeling technique coupled with steady state plug flow reactor model. More complex SO_x interactions on the Pt or Pd surfaces are studied using the first principles DFT. The first principles thermodynamics was implemented to understand temperature and pressure dependent behavior under oxidizing and sulfating environments. Fixed bed and monolith scale experiments in the BenchCAT reactor were used to study the selected emissions species oxidation on Pt based DOCs. Figure 2.1 shows a overall approach using multiple techniques to understand fundamentals of emissions oxidations and sulfation mechanism of DOCs.

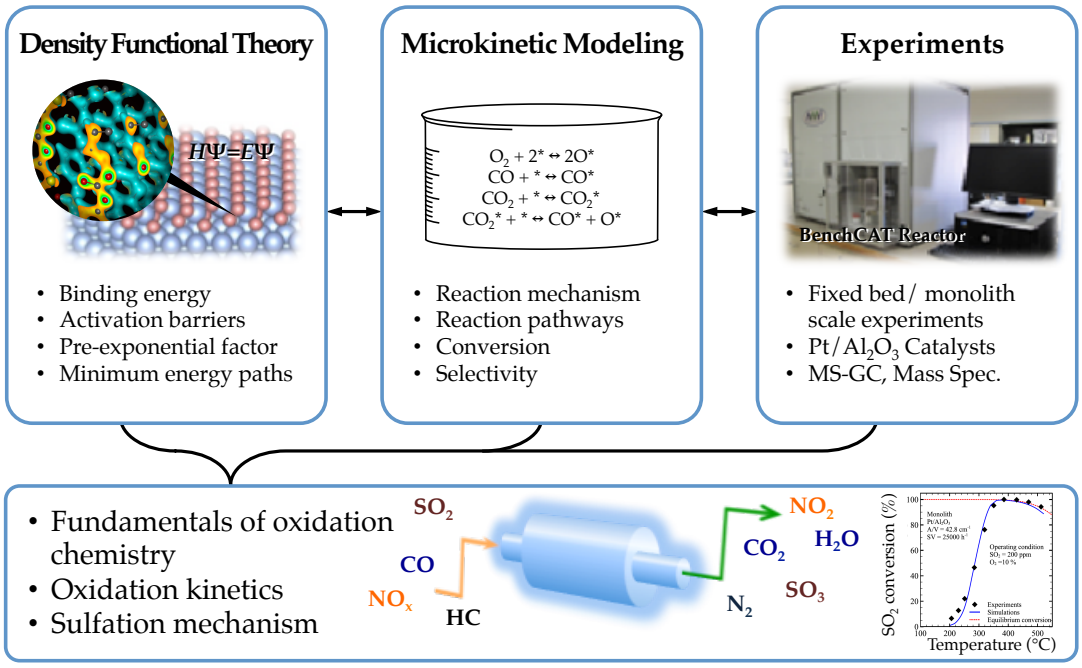

Fig. 2.1 Overall schematics showing various methodologies utilized to study emissions oxidation and sulfation mechanism.

2.2 Experiments

Altamira BenchCAT reactor is used to conduct the oxidation experiments of CO and C_2H_4. Both monolith and fixed bed type experiments were conducted. The fixed bed reaction was carried out on 1-5 mg of catalyst loaded in a 0.34 cm i.d. quartz tube reactor inside a temperature controlled furnace. Dycor Dymaxion mass spectrometer and Agilent Micro GC were used for the gas species analysis in the product stream. Oxidation study was carried out in a temperature range relevant to the DOC operating conditions. 1% CO oxidation experiments were carried out with 10% oxygen and balance Ar. For C_2H_4 experiments, effects of O_2 partial pressure (6 -14 %), C_2H_4 concentration (500 - 3000 ppm), and space velocity (20000 - 60000 h^{-1}) on catalytic performance were tested for the temperature range of 50-300 °C. Ar was used as a balance gas in the experiments. All experiments were performed at near atmospheric pressure condition.

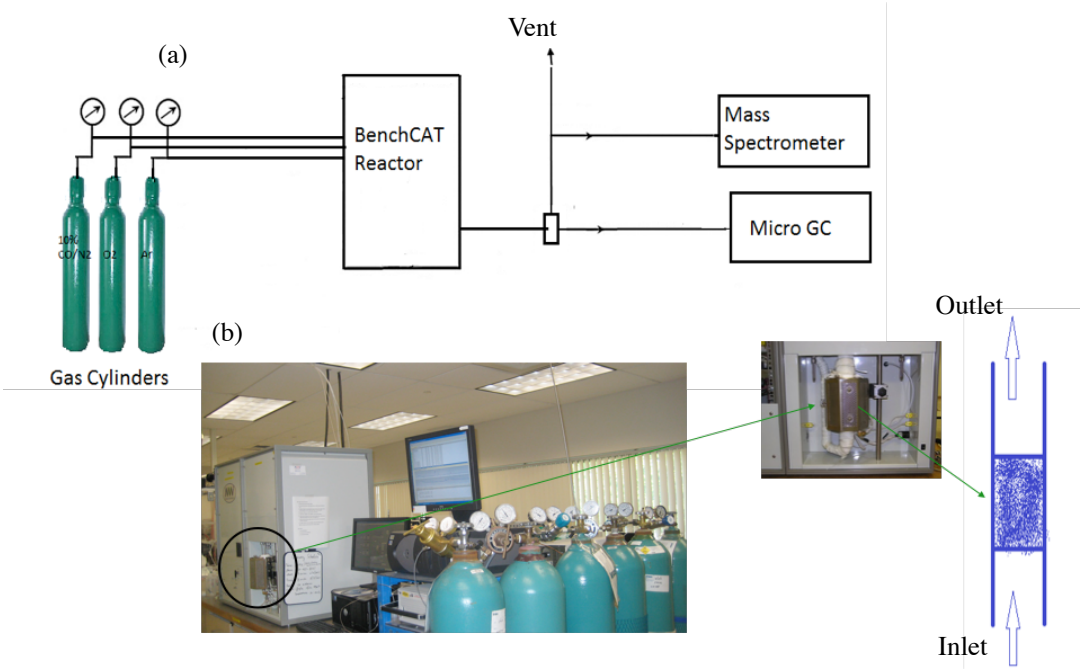

Fig. 2.2 Experimental Setup. (a) Schematic of the experimental setup used for CO and C_2H_4 oxidation experiments. (b) Picture of the BenchCAT reactor and catalyst holder.

2.3 Microkinetic Modeling

Microkinetic modeling approach was introduced by Dumesic *et al.* in 90s. [100] Ever since it has been successfully implemented to study variety of reactions in different environments. [101–106] Microkinetic modeling typically involves setting up a network of elementary-step reactions for a given reaction based on the information on reactants, products and the possible intermediates. Microkinetic modeling can be used to predict surface coverages, most abundant reaction intermediate(s) (MARI), conversion, and rate-determining steps without any a priori assumptions about the reactions RDS, PE, QSS, or MARI. In this thesis, microkinetic modeling is performed to study the oxidation mechanism of various emissions species. Next, a brief description of the steps is provided.

2.3.1 Mechanism Development

A set of elementary step surface reactions mechanism is developed for a particular reaction. The reaction steps are considered based on the experimental or theoretical information on the possible intermediates and products for a given initial reactants. For example, CO oxidation can be expressed into a set of elementary reaction as:

$$CO_{(g)} + * \leftrightarrow CO^* \tag{2.1}$$

$$O_{2(g)} + * \leftrightarrow 2O^* \tag{2.2}$$

$$CO^* + O^* \leftrightarrow CO_2^* \tag{2.3}$$

$$CO_2^* \leftrightarrow CO_{2(g)} \tag{2.4}$$

2.3.2 Kinetic Parameters Estimation

Kinetic parameters for the proposed mechanism were estimated/extracted using various methods, i.e. simulations of UHV temperature programmed surface science experiments in literature, semi-empirical UBI-QEP method [107, 108], and first principles DFT calculations. For each stable species in the reaction mechanism, we have considered multiple TPD experimental data on Pt facets to extract the species binding energies (Q) and adsorbate-adsorbate interactions (α). Various TPR experimental data sets in the literature are used to extract the activation energies (Ea and bond indices (BI) for the reactions. DFT calculations are carried out to estimate binding energies (Q) and adsorbate-adsorbate interactions (α) parameters of various intermediates and

radicals along with stable species. Such calculations will reduce the inherent error introduced to the model due to parameters, as all parameters are computation with same level of theory and accuracy. The semi-empirical UBI-QEP method is used to estimate the coverage and temperature dependent activation energies on-the-fly in these simulations. Functional forms to compute the activation energies using UBI-QEP formalism are discussed in the Appendix B. In UBI-QEP formalism, temperature and coverage dependence to compute activation barriers are introduced through binding energy as shown in equation.

$$\mathrm{Q(T)} = \mathrm{Q_o} - \alpha\theta - \gamma \mathrm{R(T - T_o)} \tag{2.5}$$

where, α is the coverage dependence coefficient (kcal/mol/ML), θ is the coverage of species (ML), γ is the temperature dependence coefficient for binding energies (unit-less), R is the universal gas constant (kcal/mol/K), and T is the temperature (K). ML stands for monolayer. T_o is taken as 300 K. The temperature dependence (γ) is derived from the statistical mechanics based calculations for degrees of freedom lost/gained upon adsorption.[26] Bond index represents the position of the transition state along the reaction coordinate, which is also used to compute the activation energies in the UBI-QEP formalism. [107, 108] It is defined for a reaction pair in the forward direction only. It ranges between 0 and 1, with a typical initial estimate of 0.5 is used here. Pre-exponential factors are taken either from literature (if available) or taken as initial estimates based on transition state theory (TST), e.g., $10^{13}\mathrm{s}^{-1}$ for desorption and $10^{11}\mathrm{s}^{-1}$ for Langmuir-Hinshelwood type surface reactions. Sticking coefficients for the adsorption reactions are taken from values reported in literature, otherwise taken as unity. Site density σ of $1\times10^{15}\mathrm{s}^{-1}$ sites/cm^2 (2.5×10^{9}mol/cm^2) is used in the simulations based on the typical estimate for the most stable Pt(111) facet.

2.3.3 Reactor Modeling

Steady state isothermal plug flow reactor (PFR) modeling was used to simulate the monolith scale experiments conducted in various operating conditions. Isothermal assumption is based on the very small amount of heat generated during the oxidation of very dilute concentration levels of the emissions in the exhaust. The governing equations for steady state PFR are given as:

$$\frac{dY_z}{dZ} = \frac{G_k M_k}{\rho \mu} + (\frac{A_c}{V_R})\frac{S_k M_k}{\rho \mu} \qquad \text{fork} = 1, ..., g_{gas} \tag{2.6}$$

$$S_k = 0 \qquad \text{fork} = n_{gas} + 1, ..., n_{gas} + n_{surf} \tag{2.7}$$

$$\sum \theta_k = 1 \qquad \text{fork} = n_{gas} + 1, ..., n_{gas} + n_{surf} \tag{2.8}$$

where, k indicates the species index, n_{gas} is the number of gas phase species, n_{surf} is the number of surface species, z is the reactor length variable, Y_k is the mass fraction of gas phase species, G_k is rate of gas phase species, M_k is the molecular weight of species, S_k is the catalytic rate of gas phase species (through adsorption and desorption), ρ is the mass density, μ is the velocity, and A_c/V_R is the catalyst area per unit reactor volume.

The surface coverages at the reactor inlet are estimated using transient simulations until it reaches steady state coverage. The GRI Mech 3.0 gas phase reaction mechanism [109] was used to account for the gas phase chemistry. The resulting set of differential and algebraic (DAE) equations was solved using the DDASPK solver. [110]

2.4 Density Functional Theory (DFT)

A parameter free, in principles, method which takes the electronic and ionic charges and masses as inputs to perform the quantum mechanical calculations is referred to as "first-principles" or "ab-initio" method. Among the currently practiced electronic structure methods, density functional theory (DFT) provides the best tradeoff between computational cost and accuracy. There are many flavors of *ab-initio* methods, which are being used to compute the properties of the material. In this thesis, the main focus will be on one particular flavor, or more correctly, combination of methodologies and approximations. That is the plane-wave pseudopotential method, within density functional theory, employing a gradient corrected functional to describe the exchange-correlation energy.

Kohn and Sham [111] extended the work of Hohenberg and Kohn [112] and showed how the intractable many-body problem of interacting electrons in a static external potential is reduced to a tractable problem of non-interacting electrons moving in an effective potential. The effective potential includes the external potential and the effects of the Coulomb interactions between the electrons, e.g., the exchange and correlation interactions. This resembles aspects of the Hartree-Fock approximation of one-electron wavefunctions. As in Hartree-Fock theory, the n-electron system is reduced to a set of n non-interacting one-electron systems. In Hartree-Fock theory this is the basic approximation upon which the solution is built, but in DFT it is simply a tool to calculate the exact component of an unknown term. The Kohn-Sham equation is defined by a local effective external potential in which the non-interacting particles move, typically denoted as $V_{eff}(\vec{r})$, called the Kohn-Sham potential.

$$\Big[-\frac{1}{2}\nabla^2 + V_{\text{eff}}(\overrightarrow{r})\Big]\phi_i = \varepsilon_i\phi_i \qquad\qquad i = 1,2,.....,n \tag{2.9}$$

Here, ε_i is the orbital energy of the corresponding Kohn-Sham orbital, ϕ_i, and the density for an n-particle system is:

$$\rho = \sum_{\mathrm{i}}^{\mathrm{n}} < \phi_{\mathrm{i}} | \phi_{\mathrm{i}} > \tag{2.10}$$

The DFT is a SCF theory as Kohn-Sham equations are solved iteratively where $\mathrm{V}_{eff}(\vec{r})$ depends on the electron density, therefore on the orbitals. Everything except the functional form of E_{XC} is known exactly. The fact that the exact functional for exchange and correlation is not known results in an intrinsic limitation of, otherwise exact, current DFT and practical implementations need to rely on approximate functionals. The two approximate functional used in the present work axe the local density approximation (LDA) and the generalized gradient approximation (GGA). While in LDA the functional depends only on the density at the local coordinate where the functional is evaluated, GGA also takes into account the gradient of the density at the local coordinate. A brief history about the DFT has been provided in the Appendix J. More details and background can be found elsewhere.

DFT is capable of predicting electronic structure and geometrical details of periodic and non-periodic systems, vibrational frequencies of molecules, phonon frequencies of solids, elastic constants of solids, and relative energies of different phases and surface/interface energies of solids, static and optical dielectric constants, etc. Here brief description of the computations performed using DFT.

2.4.1 Computational Details

For all DFT calculations described in this work (otherwise stated), we used the Vienna ab-initio simulation package (VASP) code [113] with the PBE implementation of the generalized gradient approximation (GGA) exchange-correlation functional.[114]

2.4.2 Pt or Pd

The structure of bulk FCC Pt/Pd (see Figure 2.3) is calculated within a primitive face-centered cubic (FCC) cell using a Monkhorst-Pack K-point mesh. The calculated bulk lattice constant of Pt and Pd were 3.97 Å and 3.95 Å respectively, which are in good agreement with previous theoretical calculations (Pt, a_o= 3.96 Å–4.0 Å[115–117] and Pd, a_o= 3.94 Å– 3.97 Å[117–119] as well as experimental (Pt, a_o= 3.92 Å [118, 120] and Pd, a_o= 3.89 Å [117, 121]) results. The calculated cohesive energies were 5.6 eV/atom (experimental $E_{cohesive}$ = 5.8 eV/atom [122]) and 3.7 eV/atom (experimental $E_{cohesive}$ = 3.89 eV/atom [121]) for Pt and Pd respectively.

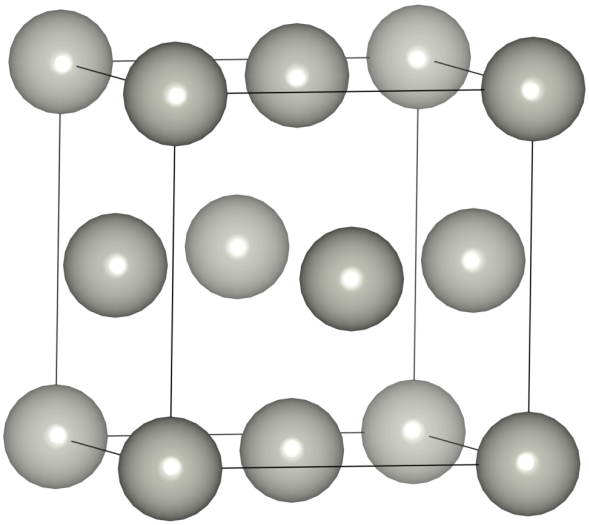

Fig. 2.3 Schematics of the FCC bulk model of Pt/Pd used in this study.

2.4.2.1 Surface Slab Models

In this work, the (111) surface of Pt and Pd metals is used. Most of the calculations were performed using a 5-layer slab model (see Figure 2.4)with the bottom two layers frozen. Typically, an intervening vacuum layer of 10-15 A was applied. For the k-point sampling, a Monkhorst-Pack scheme was used. Surface work function (φ) calculated for Pt and Pd

slabs were 5.78 eV and 5.05 eV, respectively, which are consistent with the corresponding experimental values of 5.8 eV [122] and 5.0 eV [123], respectively. Furthermore, the calculated surface energies were 97.9 meV/Å^2 and 82.4 meV/Å^2 for Pt(111) and Pd(111), which are in agreement with previous DFT studies. [124]

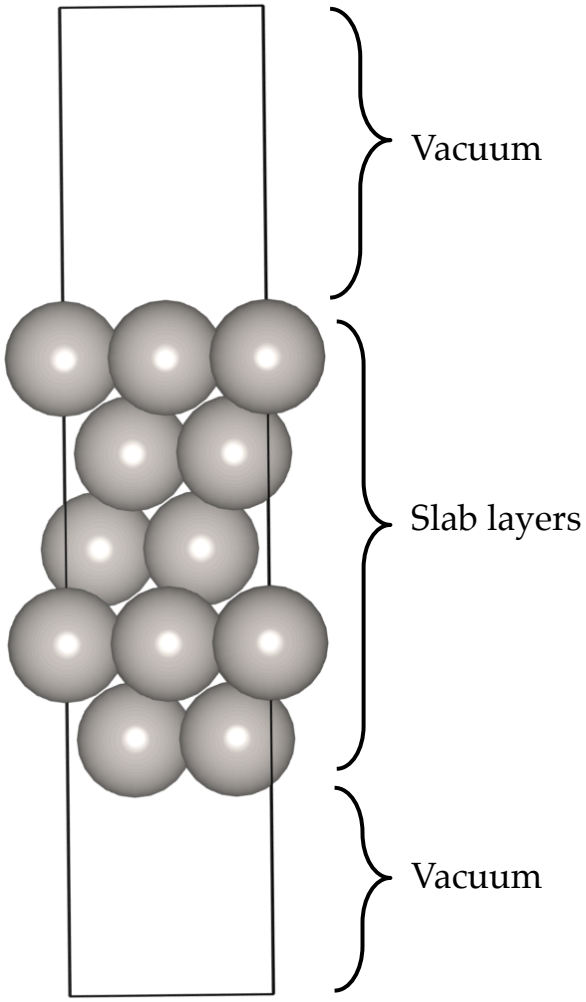

Fig. 2.4 Schematics of the 5-layer slab model of Pt/Pd(111) used in this study.

2.4.2.2 Surface Energy

Surface energy can be defined as the energy required to create one unit of surface area. The surface energy can be calculated for a symmetric slab as;

$$\gamma = \frac{1}{2}\left[\frac{\mathrm{E_{slab}} - \mathrm{N_{atom}E_{bulk}}}{\mathrm{A}}\right] \tag{2.11}$$

where E_{slab} is the total energy of the slab with N atoms, E_{bulk} is the energy per atom of the bulk metal, A is the cross-section area of the surface of the slab. The factor of 1/2 is to account for the two surfaces of the slab.

2.5 First Principles Thermodynamics

DFT computations can be utilized to compute many properties and compare the stability of various systems. However, the 0 K DFT can not provide accurate information of the systems at the elevated temperature and pressure conditions. The stability and physical properties of surfaces and interfaces can depend strongly on their detailed chemical composition and change with the surrounding environment. Identification of relevant compositions of these systems requires a thermodynamic treatment at the DFT computations are only enthalpies in nature. Thus, at finite temperatures, however, both configurational and vibrational entropy can be significant and must be accounted for. The temperature and pressure dependence are incorporated to the first principles DFT computations, also referred to as a first principles thermodynamics.

This recently developed approach of the first principles thermodynamics and have been successfully applied to a variety of systems, aimed at addressing problems from diverse fields; spanning from catalysis design to alloy optimization, and from study of corrosion phenomena

to investigation of materials in the earth's mantle. [125–128]The FPT approach is primarily employed to use information pertaining to the potential energy surface calculated at the level of electronic structure theory, for a system in equilibrium (or in a meta stable state), to calculate an appropriate thermodynamic potential function such as the Gibbs free energy G. The Gibbs free energy of any system decomposed in terms of various contributing factors can be given as follows:

$$\mathrm{G(T,P) = E^{total} + F^{vib} - TS^{conf} + pV} \tag{2.12}$$

where E^{total}, S^{conf}, p and V represent the total energy of the system, configurational entropy, pressure, and volume terms respectively. The contribution to Gibbs free energy from pV term and configurational entropy are negligible for the adsorption process, hence discarded in this study. Thus, we incorporate this contribution through harmonic normal mode analysis of the adsorbates and the substrate layers involved in the case of surface models using Bose-Einstein model approximations. The approximation is computed as, [129]

$$\mathrm{F^{vib} = \frac{1}{2}\sum_{i} 3N\varepsilon_i + K_B T \sum_{i} 3N \ln(1 - e^{-\beta\varepsilon_i})} \tag{2.13}$$

where $\varepsilon_i = \mathrm{h}\nu$ represents the phonon energy at different vibrational modes, ν_i represents the vibrational frequency and $\beta = (\mathrm{K}_B\mathrm{T})^{-1}$.

When a surface is exposed to a reservoir, it tries to establish the equilibrium state as guided by the partial pressure of the surrounding. Figure 2.5 shows such scenario of a surface in oxygen environment. The surface energy of the slab with adsorbates will be stable compared to the clean slab if the surface energy of the former is lower (i.e. $\gamma_{slab+adsorbates} < \gamma_{slab}$) and change in Gibbs free energy, $\Delta\mathrm{G}^{ads} \geq 0$. In general, surface energy of a surface model system

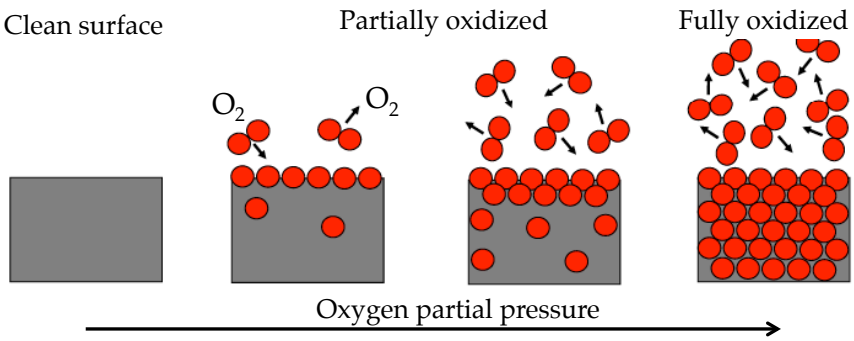

Fig. 2.5 Schematics showing various equilibrium surface phases under oxygen environment with the increase/decrease of oxygen partial pressure.

in equilibrium with the surrounding gas phase reservoir can be expressed as follows.

$$\gamma(T, p\{i\}) = \frac{1}{A}\left[G^{surf} - \sum_{i=1}^{n} N_i \mu_i(T, p_i)\right] \tag{2.14}$$

where, G^{surf}, A, μ_i, n, and N_i represent the Gibbs free energy, surface area of the slab, individual gas species in the system, number of gas species, number of atoms/molecules of gas species, respectively. More details are provided in the Appendix.

2.6 Universal Structure Predictor: Evolutionary Xtallography (USPEX)

USPEX is a method developed by the Oganov laboratory since 2004, which is mostly famous for crystal structure prediction. [130, 131] The code/method, predicts the crystal packing from only a knowledge of chemical species, compositions, or the molecular geometries, has met tremendous success in correctly identifying and predicting the crystal structures of various classes of systems (bulk crystals, [132, 133] nanoclusters, [134] 2D crystals, [135] surfaces, [136] and new polymers [137, 138]). In this work, we explored the structural space of experi-

mentally unknown $PtSO_4$ and known $PdSO_4$, with a fixed stoichiometric composition, allowing up to four formula units per unit cell. Details of the USPEX methodology and background can be found elsewhere. [130, 131]

Chapter 3

Oxidation of C_1 and N_1 Species on Diesel Oxidation Catalysts (DOCs)

3.1 Introduction

In this chapter, we focus on developing a detailed mechanistic understanding of the catalytic reaction kinetics for the oxidation of five major emissions species (C_1 and N_1 components) on Pt-based DOCs. The five chemistries include oxidation of CO, NO, CH_2O, NH_3, and HCN (see Table 3.1). Even though CO and NO oxidation chemistries are well studied, [7, 103, 139–148] this work presents the first comprehensive reaction mechanism for a Pt-based DOC that can be used to predict the oxidation behavior of five key primary or secondary emissions. The chapter is organized as follows. First, we discuss the methodology for the development of emissions oxidation chemistry in Section 3.2. In Section 3.3, we discuss the estimation of kinetic parameters from ultra-high vacuum (UHV) temperature programmed desorption/reaction (TPD/TPR) experiments in literature. Performance of the reaction mechanism is demonstrated in Section 3.4 at practically more relevant operating conditions. Preliminary mechanism reduction

is discussed in Section 3.5. Finally, we discuss the overall limitations of this work in Section 3.6, followed by conclusions.

3.2 Emissions Oxidation Chemistry Development

The overall approach for the development of a comprehensive microkinetic model for the oxidation of five emissions consists of three major steps. First, an elementary step reaction mechanism is proposed for the oxidation of each of the five emissions. Second, the kinetic parameters associated with various species and reactions are extracted from literature surface science experiments or estimated from theory. Finally, the surface reaction mechanism, combined with reactor modeling, is validated against multiple monolith and fixed bed experiments conducted in practically more relevant operating conditions such as dilute emissions concentrations, atmospheric pressure, and short residence times.

Table 3.1 Overall chemistry for the oxidation of engine exhaust emissions.

Emission component	Chemistry
CO	$CO + \frac{1}{2}O_2 \rightarrow CO_2$
NO	$NO + \frac{1}{2}O_2 \rightarrow NO_2$
CH_2O	$CH_2O + O_2 \rightarrow$ CO, CO_2, H_2, and H_2O
NH_3	$NH_3 + O_2 \rightarrow$ NO, NO_2, N_2O, N_2, H_2, and H_2O
HCN	$HCN + O_2 \rightarrow$ CO, CO_2, NO, NO_2, N_2O, C_2N_2, H_2, and H_2O

3.2.1 Development of the Surface Reaction Mechanism

Elementary surface reactions for the oxidation of CO, NO, NH_3, HCN, and CH_2O on Pt are shown in Table 3.3. The complete oxidation products include CO_2, NO_2, and H_2O, whereas the incomplete oxidation products include CO, NO, and N_2O. Additional stable species, such as O_2, N_2, H_2, and C_2N_2 (cyanogen), as well as intermediates such as, C, H, OH, COOH, N,

Table 3.2 List of species binding energies (or activation energies for associative desorption) and adsorbate interactions extracted from various TPD simulations (see Section 3.3.1 for details of the TPD simulations). If the extracted adsorbate interactions are insignificant based on the experiments at multiple initial coverages, they are explicitly indicated with zeros (for NO_2, HCN, and C_2N_2).

Species	**Q or E [kcal/mol]**	**Catalyst and reference**	**Q or E range from literature [kcal/mol]**
O_2 (asso. des.)	49.5-34θ_O	Pt(111) [149]	40-60 [145, 149, 151–153]
	55 - 29θ_O	Pt(111)[150]	
	52.6 - 34θ_O	Pt(111) [151]	
CO	36 - 6.1θ_{CO}	Pt(100)[154]	29-54 [145, 147, 157–162]
	34.9 - 7.5θ_{CO}	Pt(111) [155]	
	37 - 7.7θ_{CO}	Pt(111)[139]	
	35.8 - 12θ_{CO}	Pt(111) [156]	
H_2 (asso. des.)	21 - 5θ_H	Pt(111) [163]	13-34 [105, 165–171]
	19.8 - 2.5θ_H	Pt(111) [164]	
H_2O	11.4 - 2.8θ_{H_2O}	Pt(111) [154]	6-15 [154, 173–178]
	10.9 - 1.9θ_{H_2O}	Pt(111) [172]	
NH_3	20.7 - 9.9θ_{NH_3}	Pt(111)[179]	14-23 [182–189]
	21.2 - 10θ_{NH_3}	Pt(111) [180]	
	20.1 - 8.8θ_{NH_3}	Pt(111)[181]	
NO	29.5 - 9.7θ_{NO}	Pt(111),[148]	18-43 [49, 146–148, 184, 191, 192]
	29.8 - 7.6θ_{NO}	Pt(111) [190]	
	28.4 - 6.8θ_{NO}	Pt(111)[152]	
NO_2	19 - 0θ_{NO_2}	Pt(111)[193]	17-38 [191–197]
HCN	26.1 - 0θ_{HCN}	Pt(112) [198]	14-30 [184, 200]
	16.6	Pt(111) [199]	
CH_2O	14.7	Pt(111) [201]	11-16 [165, 168]
	21	Pt(111)[202]	
C_2N_2	22.3 - 0$\theta_{C_2N_2}$	Pt(111) [203]	12-42 [204, 205]
	19.7	Pt(111)[202]	

NH, NH_2, CN, and HCO, are also considered. Inclusion of various cross-interactive reaction pathways, such as (i) CO and H_2 oxidation, (ii) NO and H_2 oxidation, (iii) CO oxidation and carbon formation/oxidation, and (iv) HCN oxidation and C_2N_2 formation, is a unique and

novel feature of this comprehensive mechanism. The overall reaction mechanism consists of 21 surface species and 124 irreversible surface reactions (62 reversible pairs).

3.3 Parameter Estimation From UHV Experiments

As mentioned previously, UHV-TPD simulations of various species are carried out to extract the species binding energies and adsorbate-adsorbate interactions (see Table 3.2). Similarly, UHV-TPR simulations are carried out for various systems to extract the bond indices (related to activation energies). First, we discuss representative TPD simulations, and follow up with the TPR simulations, along with reaction path analysis (RPA) to provide mechanistic insights.

3.3.1 UHV-TPD Simulations

In this work, we have studied desorption of multiple species included in the reaction mechanism. For each species, multiple TPD data sets (>25 experimental data sets in total) on Pt surface are used to extract species binding energies and adsorbate-adsorbate interactions (see Figure 3.1 for a few representative TPD simulations and comparison to experimental data). All desorption rates are shown in mol/cm^2/s, but turn-over frequencies (s^{-1}) can be obtained by dividing with the site density (mol/cm^2). Extracted kinetic parameters from the TPD simulations are given in Table 3.2. Even though this analysis is fairly straightforward, next we briefly discuss a few important parameters and features.

From multiple CO TPD experiments (see Figure 3.1a for an example), we have extracted QCO (35-37 kcal/mol) and CO*-CO* adsorbate interactions (6-12 kcal/mol/ML). Our estimates are within the reported heat of CO chemisorption range of 29-54 kcal/mol. [103, 157–162] We note that the binding energies and adsorbate interactions for the CO oxidation chemistry are similar to the ones reported by Mhadeshwar and Vlachos. [103] The extracted QNO

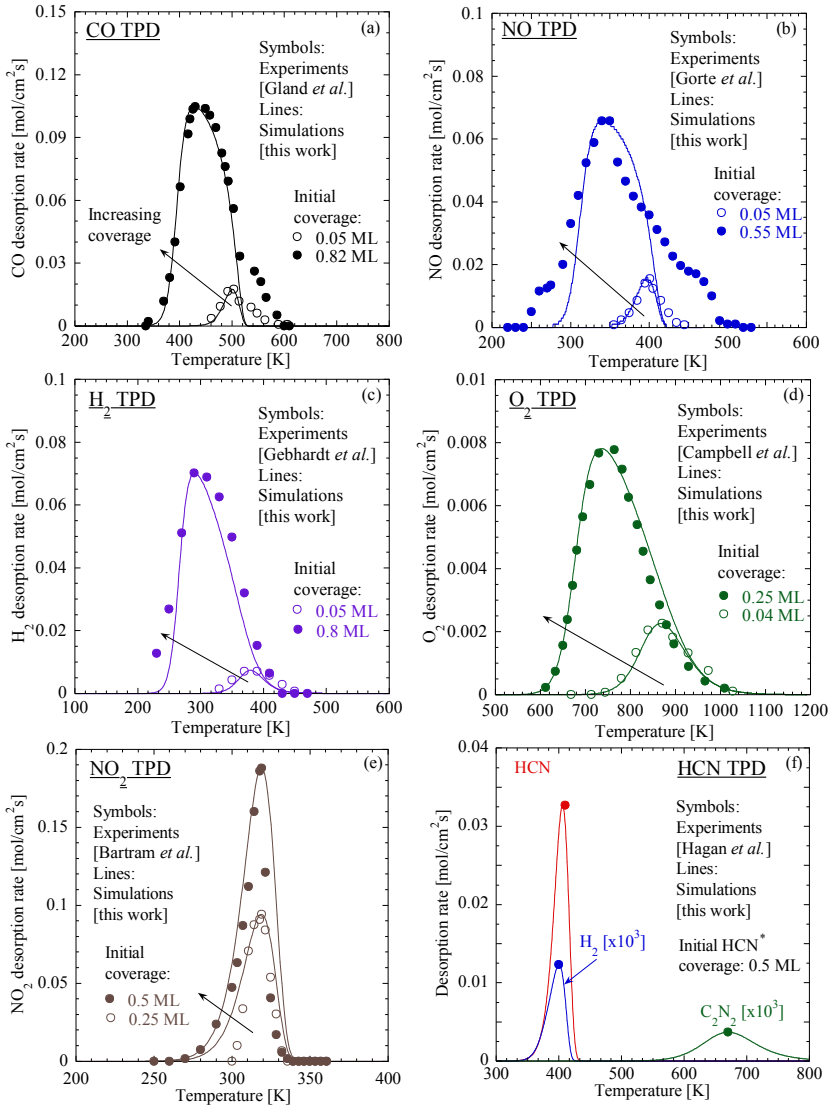

Fig. 3.1 UHV-TPD analysis of (a) CO, (b) NO, (c) H_2, (d) O_2, (e) NO_2, and (f) HCN on Pt. Symbols represent the experimental data, whereas lines represent our simulations. Panel a: CO TPD; [139] initial high and low CO* coverages are 0.82 ML and 0.05 ML, respectively; ramp rate=13 K/s. Panel b: NO TPD; [148] initial high and low NO* coverages are 0.55 ML and 0.05 ML, respectively; ramp rate=10 K/s. Panel c: H_2 TPD; [169] initial high and low H* coverages are 0.8 ML and 0.05 ML, respectively; ramp rate=7.9 K/s. Panel d: O_2 TPD, [151] initial high and low O* coverages are 0.25 ML and 0.04 ML, respectively; ramp rate=8 K/s. Panel e: NO_2 TPD; [195] initial high and low NO_2* coverages are 0.5 ML and 0.25 ML, respectively; ramp rate=10 K/s. Panel f: HCN TPD; [198] initial HCN* coverage is 0.5ML; ramp rate=2 K/s. See Table 3.2 for the extracted kinetic parameters from these simulations.

based on multiple NO TPD experiments (see Figure 3.1b for an example) is in the range of 28-30 kcal/mol with NO*-NO* adsorbate interactions of 6-10 kcal/mol/ML. These estimates are well aligned with the reported Q_{NO} (18-43 kcal/mol [49, 146, 148, 206]). Based on the work of Hauptmann et al., Q_{NO} depends on the O* coverage as well; and these repulsive interactions are taken as 16 kcal/mol/ML. [147] The H*-H* adsorbate interactions are small (1.9 kcal/mol/ML), as seen from the relatively smaller shift in peak temperatures (see Figure 3.1c). O*-O* adsorbate interactions of 13.3 kcal/mol/ML are taken from the literature [147] and are also consistent with our TPD simulations shown in Figure 3.1d. Based on our TPD simulations (not shown), the estimated Q(NH_3) of 20-22 kcal/mol is also within the reported range of 14-23 kcal/mol. [182–185, 207] Based on the peak shift with initial coverage, the NH_3*NH_3* adsorbate interactions are estimated to be 9.5 kcal/mol/ML. Q(NO_2) is estimated to be 19 kcal/mole, which is consistent with literature estimates of 17-38 kcal/mol; [191–197] but no significant adsorbate interactions are observed in the experimental data [193] and the TPD simulations (see Figure 3.1e). Q(CH_2O) is estimated as 14.7 kcal/mol (not shown), which is consistent with the reported range of 11-16 kcal/mol. [165, 166, 208]

Compared to other species, the TPD behavior of HCN is different (see Figure 3.1f), as it shows decomposition and formation of H_2 and C_2N_2 as products along with typical HCN desorption. From TPD experiments [209], Q_{HCN} is estimated to be 26.1 kcal/mol. This is consistent with the literature reported range of 14-30 kcal/mol. [184, 200] Experimental data suggest that desorption of HCN from Pt is independent of the surface coverage, i.e., the adsorbate interactions are insignificant [210]. Q(C_2 N_2)$_{avg}$ is estimated to be 21 kcal/mol from the TPD simulations of C_2N_2 on Pt(111) surface. [202, 203, 211] To correctly capture the peak location of C_2N_2 formation from the HCN TPD (670 K), bond index of the reaction pair R_{123}-R_{124}: C_2N_2 + * $\leftrightarrow$ 2CN* is modified to 0.73 (starting from 0.5). With this modification,

our model shows good agreement with the peak locations for all three products (HCN, H_2, and C_2N_2), as shown in Figure 3.1.

These and many other kinetic parameters estimated from the UHV-TPD simulations (see Table 3.2) form the basis of the UHV-TPR simulations described next, and also of the fixed bed and monolith simulations described in Section 3.4.

3.3.2 UHV-TPR Simulations

3.3.2.1 CO Oxidation

Figure 3.2a shows the peaks for CO_2 formation rate and excess CO desorption rate from the CO oxidation UHV-TPR experiments on Pt(111) by Gerrard et al. [140] Initial coverages include 0.29 ML of CO* and 0.25 ML of O*. As CO* oxidation to CO_2* (R_{10}) is the most important reaction, bond index of that reaction pair R_9-R10: CO_2*+* $\leftrightarrow$ CO*+O* is adjusted to 0.73 (starting from 0.5) to correctly capture the location of the CO_2 desorption peak. The bond index modification implemented here is similar to the earlier work (bond index = 0.8) by Mhadeshwar and Vlachos [103] for this reaction based on DFT-derived Polanyi-type relations in literature. The small difference originates from our use of TPR experimental data to extract the bond index. Figure 3.2b shows the simulated coverage profiles. CO* and O* react on the surface at $\sim$340 K to produce CO_2*, which desorbs. The excess CO* desorbs at $\sim$500 K. A small modification of CO binding energy to 40 kcal/mol ($Q_{CO}{}^{avg}$ $\sim$36 kcal/mol from TPD in Table 3.2), within the reported range in literature (29-54 kcal/mol), is carried out to correctly capture the experimental data. To validate the bond index modification, another set of TPR experimental data for CO oxidation on Pt (initial coverages: 0.82 ML of CO* and 0.17 ML of O*) by Gland and Kollin [139] is also simulated without any parameter adjustment (Figures 3.2c and 3.2d).

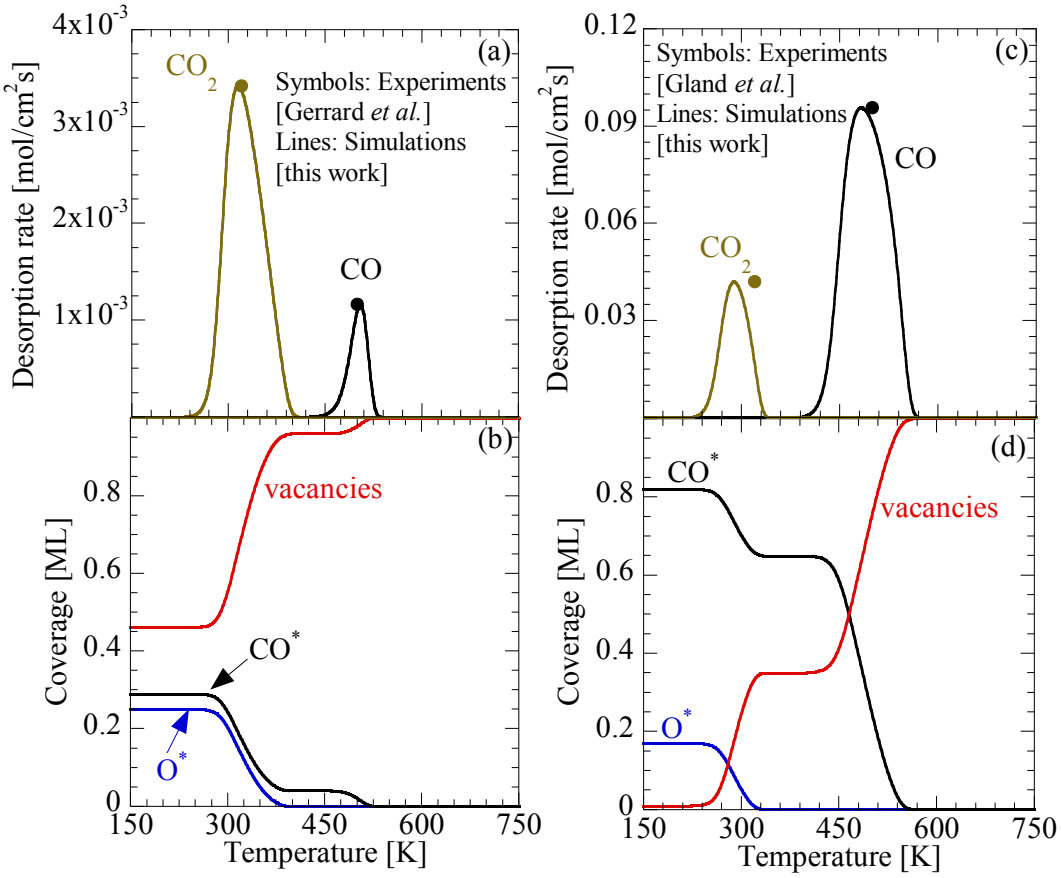

Fig. 3.2 Rate (panels a and c) and coverage (panels b and d) for UHV-TPR analysis of CO oxidation on Pt(111). Symbols represent the experimental data, [139, 140] whereas lines represent our simulations. Operating conditions for panels a and c: initial surface coverages O* and CO* are 0.25 ML and 0.29 ML, respectively; ramp rate=1 K/s. [140] Operating conditions for panels b and d: initial surface coverages of O* and CO* are 0.17 ML and 0.82 ML, respectively; ramp rate=13 K/s. [139] Simulations are in close agreement with the experimental data.

The mechanism predictions are in excellent agreement with the experimental data. Overall, the reaction mechanism captures the CO oxidation chemistry well at UHV conditions.

3.3.2.2 NO Oxidation

To extract some of the kinetic parameters for the NO oxidation chemistry, we have used the UHV-TPR experiments conducted on Pt(111) by Mudiyanselage et al. [212] Initial coverages include 0.15 ML of NO* and 0.75 ML of O*. Bartram et al. [213] reported that NO oxidation to NO_2 is not favored on Pt(111) at low O* coverage ($\sim$0.25 ML) due to the larger activation barrier for NO oxidation compared to NO desorption; however, they suggested the possibility of NO_2 formation at higher oxygen coverage ($\sim$0.75 ML). A DFT study of NO oxidation on Pt(111) by Ovesson et al. suggested that the oxidation is oxygen coverage (θ_O) dependent; and θ_O needs to be more than 0.25 ML for the reaction to be favorable. [192] Along the similar lines, Mudiyanselage et al. reported NO oxidation to NO_2 with high θ_O ($\sim$0.75 ML) on Pt(111). [212] Without any adjustment of the kinetic parameters, we observe N_2 formation due to NO* decomposition; however, N_2 formation was not reported in the TPR experiments. To slow down the NO* decomposition chemistry, we have adjusted the bond index of the NO* decomposition reaction pair R_{71}-R_{72}: NO*+*$\leftrightarrow$N*+O* to 0.89 (starting from 0.5). This adjustment is consistent with the bond index modification reported earlier in Section 3.1.1 for decomposition reactions, where the increase in bond index typically results in increased activation energy. A minor adjustment of NO binding energy to 30.5 kcal/mol ($Q_{NO}{}^{avg}$ $\sim$29.2 kcal/mol from TPD in Table 3.2) is made to correctly capture the experimental data. As shown in Figure 3.3a, the NO oxidation mechanism captures the experimental peaks for all three species (NO*, NO_2*, and O*) very well.

Simulated coverage profiles, shown in Figure 3.3b, indicate that NO* oxidation starts immediately at low temperatures (>100 K) under the UHV conditions. This feature is also

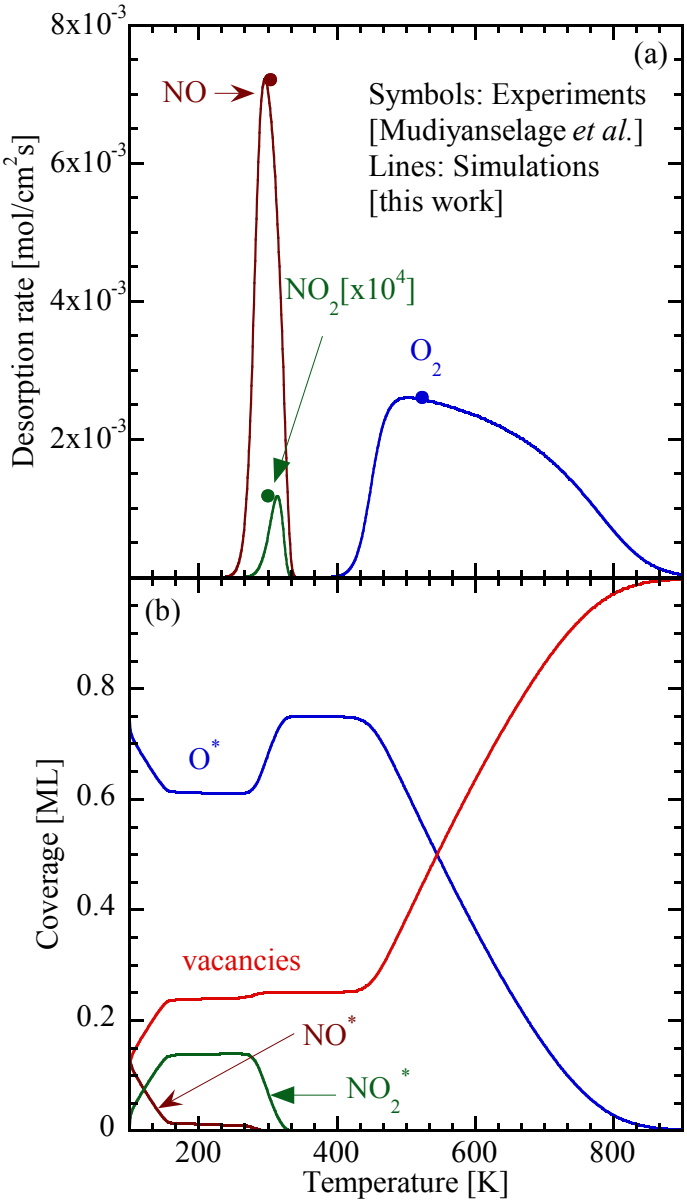

Fig. 3.3 Rate (panel a) and coverage (panel b) profiles for UHV-TPR analysis of NO oxidation on Pt(111). Symbols represent the experimental data, [212] whereas lines represent our simulations. Operating conditions: initial surface coverages of O* and NO* are 0.75 ML and 0.15 ML, respectively; ramp rate=2 K/s. Simulations are in close agreement with the experimental data.

reported by Mieher et al. [181] in their NO oxidation experiments, where they observed exchange of oxygen between labeled NO and O2. Above 200 K, we observe that NO2* decomposition to NO* and O* also becomes significant, therefore all of the NO* is not oxidized to NO_2*. At ∼300 K, NO* desorption results in the NO peak. At this temperature, most of the NO* is re-generated from NO_2* decomposition, which is also consistent with the increase in O* coverage. Furthermore, NO_2 desorption also competes with NO_2* decomposition, resulting in a smaller NO_2 desorption peak, consistent with the experimental observation by Mudiyanselage et al. [212] Finally, the excess O* desorbs at higher temperature (400-800 K), consistent with the experiments. Overall, the surface reaction mechanism captures the NO oxidation chemistry very well as UHV conditions.

3.3.2.3 CH_2O Oxidation

UHV-TPR experimental data of Attard et al. [214] for CH_2O oxidation on Pt(111) is used to simulate the CH_2O oxidation chemistry. Here, the initial coverages include 0.5 ML of CH_2O* and 0.3 ML of O*. As shown in Figure 3.4a, the simulated peak temperatures of the gaseous products are in close agreement with the reported experimental data, without any modification of the initial kinetic parameters. We note that the model predicted peak for CH_2O desorption (198 K) is higher than the experimentally reported value (134 K); however the model predicted peak and the corresponding binding energy of CH_2O (see Table 3.2) are consistent with other CH_2O TPD experiments [201, 208] (see Section 3.1) as well as literature DFT estimates. [165, 166]

Simulated coverage profiles, shown in Figure 3.4b, indicate that at ∼150 K, CH_2O* and O* coverages start to decrease, resulting in the formation of CO*, H*, and OH*. RPA shows that reaction R_{99}: CH_2O* +* ↔ HCO* + H* is dominant in this region. Once formyl (HCO*) is produced, it rapidly oxidizes to CO* and OH* through reaction R_{108}: HCO* + O* ↔ CO* + OH*. With further increase in the temperature, formyl oxidizes to H_2O* through reaction R_{110}:

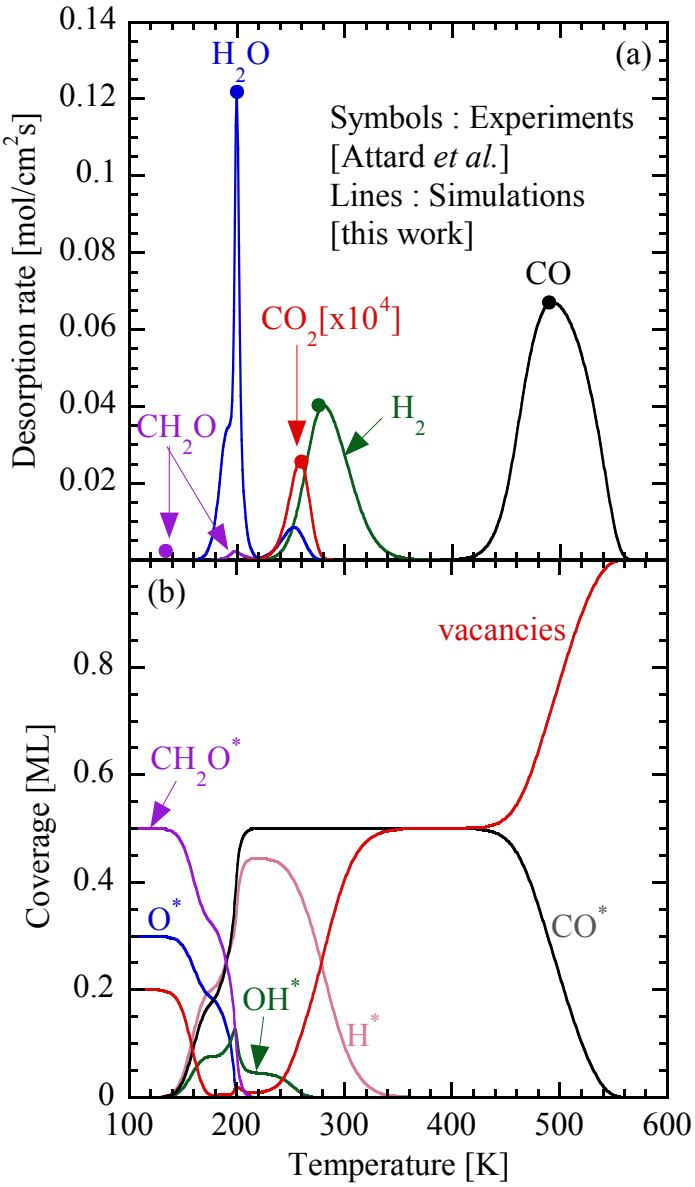

Fig. 3.4 Rate (panel a) and coverage (panel b) profiles for UHV-TPR analysis of CH_2O oxidation on Pt(110). Symbols represent the experimental data, [214] whereas lines represent our simulations. Operating conditions: initial surface coverages of O* and CH_2O* are 0.3 ML and 0.5 ML, respectively; ramp rate=10 K/s. Simulations are in good agreement with the experimental data.

HCO* + OH* $\leftrightarrow$ H_2O* + CO*, which subsequently results in H_2O desorption at $\sim$200 K. This is also consistent with the decrease in OH* coverage at this temperature. The second water peak at $\sim$250 K (much smaller and not observed experimentally) is due to the reaction between OH* and H*. The model predictions also show a very small CO_2 desorption peak at $\sim$260 K (magnified by a factor of 10,000), consistent with the experiments. This peak is due to reaction R_{28}: CO*+OH* $\rightarrow$ CO_2* + H*. With further increase in the temperature, H* (primarily formed from CH_2O* decomposition) associatively desorbs (R_{14}: 2H* $\rightarrow$ H_2 + 2*) at $\sim$280 K, similar to the experimentally observed peak. Finally, the only species left on the surface is CO*, which desorbs at $\sim$495 K, consistent with the experiments. Overall, the CH_2O oxidation mechanism shows excellent agreement with the experimentally observed peaks for multiple products under the UHV conditions, without any adjustment of the kinetic parameters.

3.3.2.4 NH_3 Oxidation

Some of the kinetic parameters for NH_3 oxidation are extracted from the UHV-TPR experimental data on Pt(111) reported by Mieher and Ho. [181] Initial coverages include 0.12 ML of NH_3* and 0.25 ML of O*. The mechanism predictions for rates and coverages are shown in Figures 3.5a and 3.5b, respectively. Even though there is some discrepancy in the H_2O desorption peak (238 K vs. 350 K), we have verified the H_2O binding energy from additional TPD experiments [154, 172] (see Section 3.1) and literature DFT calculations. [167, 215] The mechanism predictions for other gaseous products (NO and N_2) are in excellent agreement with the experimental data. Increasing the NH_3 binding energy from 20.7 kcal/mol to $\sim$33.5 kcal/mol helps in capturing the H_2O desorption peak at 350 K (as it delays reaction R_{62}: NH_3* + OH* $\leftrightarrow$ NH_2* + H_2O*), but such modification is beyond the accepted literature range reported in Table 3.2; hence, it is not carried out. Decreasing the binding energy of NH_2 to 39-47 kcal/mol [184, 187, 188, 216], which has been reported in literature using UBI-QEP and DFT

calculations for less stable configurations (top sites), has a similar effect of shifting the water peak to higher temperature. However, such modification is also inconsistent with the literature binding energy values for stable configurations (bridge sites) using DFT calculations (54-58 kcal/mol [184, 187, 187, 216]) (see Table 3.2); hence, it is not carried out.

Simulated coverage profiles in Figure 3.5b provide some insights about the surface chemistry, but RPA is required to understand the dominant reactions in the NH_3 oxidation chemistry. RPA at 150 K shows that NH_3* undergoes oxidative dehydrogenation through reaction R_{55}: NH_3* + O* $\leftrightarrow$ NH_2* + OH*. As soon as OH* is formed, both OH* and O* participate in the oxidative dehydrogenation reactions R_{62}: NH_3* + OH* $\leftrightarrow$ NH_2* + H_2O* and R_{58}: NH_2* + O* $\leftrightarrow$ NH* + OH*, resulting in the formation of NH*. Water formed in reaction R_{62} desorbs, which is also observed in the experiments. RPA at 400 K and 450 K shows that there are four competing pathways for NH* consumption, viz., reaction R_{76}: NH* + O* $\leftrightarrow$ NO* + H* that subsequently results in the NO desorption peak, as well as reactions R_{60}: NH*+O* $\leftrightarrow$ N* + OH*, R_{53}: NH* + * $\leftrightarrow$ N* + H*, and R_{66}: NH* + OH* $\leftrightarrow$ N* + H_2O* that eventually lead to the N_2 desorption peak. The second water peak (much smaller and not observed experimentally) at higher temperature ($\sim$450 K) is due to reactions R_{22} : OH* + H* $\leftrightarrow$ H_2O* + * and R_{24}: 2OH* $\rightarrow$ H_2O* + O*. We have adjusted the bond indices of reaction pairs R_{75}-R_{76}, R_{53}-R_{54}, R_{59}-R_{60}, and R_{65}-R_{66} to 0.23, 0.57, 0.65, and 0.71 (starting from 0.5), respectively, to improve the agreement with experimental data. The bond index modification, although brute-force, is necessary to ensure that both NO and N_2 peaks are observed in the simulations and to capture the correct kinetics for the formation of multiple products. Finally, excess oxygen, albeit negligible ($\sim$0.02 ML), desorbs at higher temperatures ($\sim$820 K). The O_2 peak was not reported by Mieher and Ho, [181] as the experiments were carried out only up to 700 K.

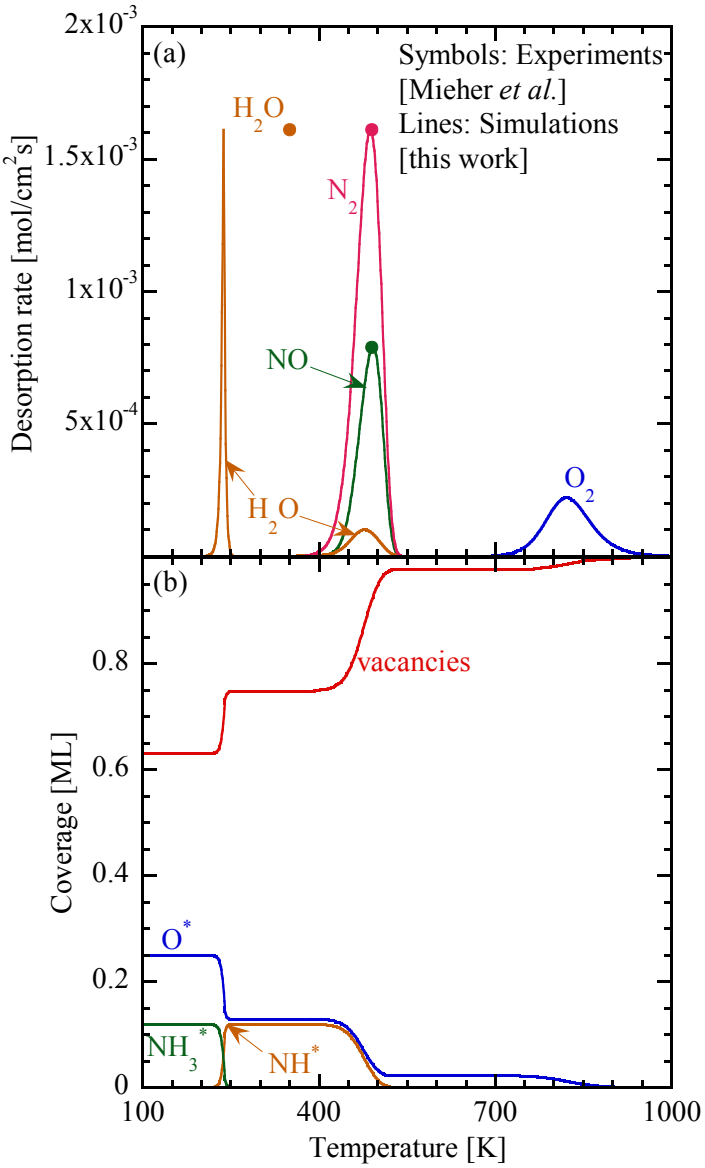

Fig. 3.5 Rate (panel a) and coverage (panel b) profiles for UHV-TPR analysis of NH_3 oxidation on Pt(111). Symbols represent the experimental data, [181] whereas lines represent our simulations. Operating conditions: initial surface coverages of O* and NH_3* are 0.25 ML and 0.12 ML, respectively; ramp rate=2 K/s. Simulations are in good agreement with the experimental data. Discrepancy in the peak locations for H_2O and O_2 is discussed in the text.

3.3.2.5 HCN oxidation

UHV-TPR simulations for HCN oxidation are compared against the experimental data on Pt(112) reported by Guo et al. [209] Here, the initial coverages include 0.67 ML of HCN* and 0.25 ML of O*. Simulated rate and coverage profiles are shown in Figures 3.6a and 3.6b, respectively. A number of products are observed in the TPR experiment, viz., unreacted HCN, CO, CO_2, H_2O, H_2, N_2, and C_2N_2. We have modified the bond index of the reaction pair R_{87}-R_{88}: HCN* + O* $\leftrightarrow$ CN* + OH* to 0.44 (starting from 0.5) to correctly capture most of the product peak temperatures.

RPA at low temperature shows that HCN* oxidizes to CN* via reaction R_{87}: HCN* + O* $\rightarrow$ CN* + OH*. As soon as OH* is formed, it oxidizes HCN* to CN* and H_2O* via reaction R_{89}: HCN* + OH* $\rightarrow$ CN* + H_2O*. Water desorbs immediately after the formation at $\sim$ 260 K, consistent with the experiments. At the same temperature, CN* is oxidized to produce CO* and N* via reaction R_{94}: CN* + O* $\rightarrow$ CO* + N*. CO* reacts with O* to form CO_2* via reaction R_{10}: CO* + O* $\rightarrow$ CO_2* + *, which desorbs at $\sim$260 K, whereas N_2 desorbs at $\sim$280 K. We note that our model predictions show CO_2 and N_2 formation at significantly lower temperatures than those reported in the experiments. In case of CO_2, we have rigorously validated the CO oxidation activation energy (and temperature) from other TPR experiments reported in Sections 3.2.1 and 3.2.3. The discrepancy in N_2 formation peak could be due to potentially missing reaction pathways in our reaction network. However, under the practical operating conditions of emissions oxidation to partially and fully oxidized products, the formation of N_2 (a reduction product) is less important for a DOC. Nonetheless, it is certainly a limitation of the proposed surface reaction mechanism. The model correctly captures the H_2 desorption peak at $\sim$415 K, which originates from the decomposition reaction R_{85}: HCN* + * $\rightarrow$ H* + CN*. The unreacted HCN desorbs at $\sim$425 K and the remaining CO* desorbs at $\sim$500 K, consistent with the experiments. Finally, a small quantity of cyanogen (C_2N_2*), formed from reaction R_{124}: 2CN* $\rightarrow$ C_2N_2* + * desorbs at a much higher temperature ($\sim$675 K), consistent with the experiments. As seen from this analysis, HCN oxidation is a very complicated chemistry, and it is quite challenging to capture the formation of all the products. Our surface reaction

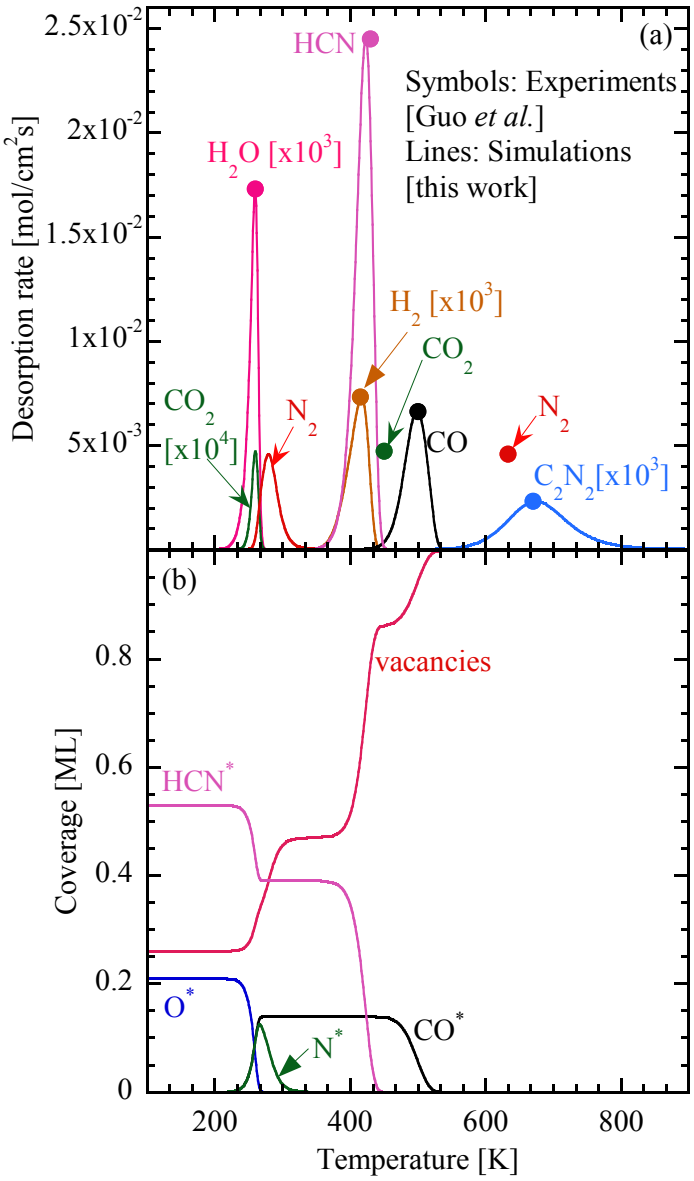

Fig. 3.6 Rate (panel a) and coverage (panel b) profiles for UHV-TPR analysis of HCN oxidation on Pt(112). Symbols represent the experimental data [209], whereas lines represent our simulations. Operating conditions: initial surface coverages of O* and HCN* are 0.25 ML and 0.67 ML, respectively; ramp rate=2 K/s. Simulations are in reasonable agreement with the experimental data. Discrepancy in the peak locations for CO_2 and N_2 is discussed in the text.

mechanism shows the formation of all important products observed in the UHV conditions, and captures most of the product desorption peak locations.

Table 3.3 Surface reaction mechanism for oxidation of CO, NO, CH_2O, NH_3, and HCN on Pt. Activation energies in the last column are temperature and coverage dependent, but only representative values are shown at 300 K. Coverage dependence originates from the use of UBI-QEP [107] for the estimation of activation energies, whereas the temperature dependence is derived from the statistical mechanics based calculations for degrees of freedom lost/gained upon adsorption. [101] Further details on the functional form f are given in Appendix B. Shaded reactions in the second column are the least important ones for typical DOC conditions, and can be ignored during the simulations

No.	**Reactions**	**Bond index (BI) [unitless]**	**Sticking coefficient [unitless] or Pre exponential factor [s^{-1}]**	**Activation energy at 300 K [kcal/mol]**
	Oxygen adsorption/desorption			
R_1	$O + * \rightarrow O^*$	0.5	1	0.0
R_2	$O^* \rightarrow O + *$	0.5	1×10^{13}	86 - 13.3θ_O - 1.5RΔT[173]
R_3	$O_2 + 2* \rightarrow 2O^*$	0.5	0.05[151, 217]	0.0
R_4	$2O^* \rightarrow O_2 + 2*$	0.5	1×10^{13}	52.9 - 26.6θ_O + f(T)
	CO oxidation			
R_5	$CO + * \rightarrow CO^*$	0.5	0.5[218]	0.0
R_6	$CO^* \rightarrow CO + *$	0.5	5.7×10^{16}[a]	40 - 8.3θ_{CO} - 2RΔT[147, 219]
R_7	$CO_2 + * \rightarrow CO_2^*$	0.5	1	0.0
R_8	$CO_2^* \rightarrow CO_2 + *$	0.5	1×10^{13}	3.6 - 2RΔT
R_9	$CO_2^* + * \rightarrow CO^* + O^*$	0.73 [b]	1×10^{11}	23.4 + f(θ_O,θ_{CO},T)

[a]Based on CO oxidation atmospheric pressure simulations (Section 3.4.1).
[b]Based on CO oxidation UHV-TPR simulations (Section 3.3.2.1).

R_{10}	$CO^* + O^* \rightarrow CO_2{}^* + *$	0.73^b	1×10^{10a}	18.6 + f(θ_O,θ_{CO},T)
	H_2 oxidation			
R_{11}	$H + * \rightarrow H^*$	0.5	1	0.0
R_{12}	$H^* \rightarrow H + *$	0.5	1×10^{13}	60.9 - 1.9θ_H - 1.5RΔT [165, 220]
R_{13}	$H_2 + 2* \rightarrow 2H^*$	0.5	1	0.0
R_{14}	$2H^* \rightarrow H_2 + 2*$	0.5	1×10^{13}	17.6 - 3.8θ_H + f(T)
R_{15}	$H_2O + * \rightarrow H_2O^*$	0.5	1	0.0
R_{16}	$H_2O^* \rightarrow H_2O + *$	0.5	1×10^{13}	10.3 - 2.5RΔT
R_{17}	$OH + * \rightarrow OH^*$	0.5	1	0.0
R_{18}	$OH^* \rightarrow OH + *$	0.5	1×10^{13}	63 - 33θ_O - 2RΔT[221]
R_{19}	$OH^* + * \rightarrow H^* + O^*$	0.5	1×10^{11}	27 + f(θ_O,θ_H,T)
R_{20}	$H^* + O^* \rightarrow OH^* + *$	0.5	1×10^{11}	8.6 + f(θ_O,θ_H,T)
R_{21}	$H_2O^* + * \rightarrow OH^* + H^*$	0.5	1×10^{11}	18.3 + f(θ_O,θ_H,T)
R_{22}	$OH^* + H^* \rightarrow H_2O^* + *$	0.5	1×10^{11}	12.6 + f(θ_O,θ_H,T)
R_{23}	$H_2O^* + O^* \rightarrow 2OH^*$	0.5	1×10^{11}	9.4 + f(θ_O,T)
R_{24}	$2OH^* \rightarrow H_2O^* + O^*$	0.5	1×10^{11}	22.1 + f(θ_O,T)
	Water promoted CO oxidation			
R_{25}	$COOH + * \rightarrow COOH^*$	0.5	1	0.0
R_{26}	$COOH^* \rightarrow COOH + *$	0.5	1×10^{13}	56.3 - 2.5RΔT
R_{27}	$CO_2{}^* + H^* \rightarrow CO^* + OH^*$	0.5	1×10^{11}	5.4 + f(θ_O,θ_{CO},θ_H,T)
R_{28}	$CO^* + OH^* \rightarrow CO_2{}^* + H^*$	0.5	1×10^{11}	19 + f(θ_O,θ_{CO},θ_H,T)
R_{29}	$COOH^* + * \rightarrow CO^* + OH^*$	0.5	1×10^{11}	5.8 + f(θ_O,θ_{CO},T)
R_{30}	$CO^* + OH^* \rightarrow COOH^* + *$	0.5	1×10^{11}	18.7 + f(θ_O,θ_{CO},T)
R_{31}	$COOH^* + * \rightarrow CO_2{}^* + H^*$	0.5	1×10^{11}	2.1 + f(θ_H,T)
R_{32}	$CO_2{}^* + H^* \rightarrow COOH^* + *$	0.5	1×10^{11}	1.3 + f(θ_H,T)
R_{33}	$CO^* + H_2O^* \rightarrow COOH^* + H^*$	0.5	1×10^{11}	23.9 + f(θ_{CO},θ_H,T)
R_{34}	$COOH^* + H^* \rightarrow CO^* + H_2O^*$	0.5	1×10^{11}	5.4 + f(θ_{CO},θ_H,T)
R_{35}	$CO_2{}^* + OH^* \rightarrow COOH^* + O^*$	0.5	1×10^{11}	25.8 + f(θ_O,T)
R_{36}	$COOH^* + O^* \rightarrow CO_2{}^* + OH^*$	0.5	1×10^{11}	8.2 + f(θ_O,T)
R_{37}	$CO_2{}^* + H_2O^* \rightarrow COOH^* + OH^*$	0.5	1×10^{11}	17.3 + f(θ_O,T)

R_{38}	$COOH^* + OH^* \rightarrow CO_2{}^* + H_2O^*$	0.5	1×10^{11}	12.4 + f(θ_O,T)
	NH_3 oxidation			
R_{39}	$N + * \rightarrow N^*$	0.5	1	0.0
R_{40}	$N^* \rightarrow N + *$	0.5	1×10^{13}	107.4 - 1.5RΔT[105]
R_{41}	$N_2 + 2* \rightarrow 2N^*$	0.5	1	27.9 + f(T)
R_{42}	$2N^* \rightarrow N_2 + 2*$	0.5	1×10^{13}	16.7 + f(T)
R_{43}	$NH_3 + * \rightarrow NH_3{}^*$	0.5	1	0.0
R_{44}	$NH_3{}^* \rightarrow NH_3 + *$	0.5	1×10^{13}	20.7 - 9.5θ_{NH_3} - 2.5RΔT
R_{45}	$NH_2 + * \rightarrow NH_2{}^*$	0.5	1	0.0
R_{46}	$NH_2{}^* \rightarrow NH_2 + *$	0.5	1×10^{13}	54.6 - 2.5RΔT[187]
R_{47}	$NH + * \rightarrow NH^*$	0.5	1	0.0
R_{48}	$NH^* \rightarrow NH + *$	0.5	1×10^{13}	83 - 2RΔT[184]
R_{49}	$NH_3{}^* + * \rightarrow NH_2{}^* + H^*$	0.5	1×10^{11}	21.5 + f(θ_H,θ_{NH_3},T)
R_{50}	$NH_2{}^* + H^* \rightarrow NH_3{}^* + *$	0.5	1×10^{11}	7.3 + f(θ_H,θ_{NH_3},T)
R_{51}	$NH_2{}^* + * \rightarrow NH^* + H^*$	0.5	1×10^{11}	18.7 + f(θ_H,T)
R_{52}	$NH^* + H^* \rightarrow NH_2{}^* + *$	0.5	1×10^{11}	16.5 + f(θ_H,T)
R_{53}	$NH^* + * \rightarrow N^* + H^*$	0.57[c]	1×10^{11}	19 + f(θ_H,T)
R_{54}	$N^* + H^* \rightarrow NH^* + *$	0.57[c]	1×10^{11}	24.5 + f(θ_H,T)
R_{55}	$NH_3{}^* + O^* \rightarrow NH_2{}^* + OH^*$	0.5	1×10^{11}	12.5 + f(θ_O,θ_{NH_3},T)
R_{56}	$NH_2{}^* + OH^* \rightarrow NH_3{}^* + O^*$	0.5	1×10^{11}	16.7 + f(θ_O,θ_{NH_3},T)
R_{57}	$NH^* + OH^* \rightarrow NH_2{}^* + O^*$	0.5	1×10^{11}	24.8 + f(θ_O,T)
R_{58}	$NH_2{}^* + O^* \rightarrow NH^* + OH^*$	0.5	1×10^{11}	8.6 + f(θ_O,T)
R_{59}	$N^* + OH^* \rightarrow NH^* + O^*$	0.65[c], 0.6[d]	1×10^{11}	39.6 + f(θ_O,T)
R_{60}	$NH^* + O^* \rightarrow N^* + OH^*$	0.65[c], 0.6[d]	1×10^{11}	15.8 + f(θ_O,T)
R_{61}	$NH_2{}^* + H_2O^* \rightarrow NH_3{}^* + OH^*$	0.5	1×10^{11}	3.5 + f(θ_O,θ_{NH_3},T)
R_{62}	$NH_3{}^* + OH^* \rightarrow NH_2{}^* + H_2O^*$	0.5	1×10^{11}	12 + f(θ_O,θ_{NH_3},T)
R_{63}	$NH^* + H_2O^* \rightarrow NH_2{}^* + OH^*$	0.5	1×10^{11}	16.4 + f(θ_O,T)
R_{64}	$NH_2{}^* + OH^* \rightarrow NH^* + H_2O^*$	0.5	1×10^{11}	12.9 + f(θ_O,T)

[c]Based on NH_3 oxidation UHV-TPR simulations (Section 3.2.4).
[d]Based on NH_3 oxidation atmospheric pressure simulations (Section 3.4.4).

R_{65}	$N^* + H_2O^* \rightarrow NH^* + OH^*$	0.71[c]	1×10^{11}	33.4 + f(θ_O,T)
R_{66}	$NH^* + OH^* \rightarrow N^* + H_2O^*$	0.71[c]	1×10^{11}	22.2 + f(θ_O,T)
	NO oxidation			
R_{67}	$NO + * \rightarrow NO^*$	0.5	0.88	0.0
R_{68}	$NO^* \rightarrow NO + *$	0.5	1×10^{16}	30.5[e] - 8θ_{NO} - 16θ_O-2RΔT[106]
R_{69}	$NO_2 + * \rightarrow NO_2^*$	0.5	1	0.0
R_{70}	$NO_2^* \rightarrow NO_2 + *$	0.5	1×10^{13}	23.5[e] - 2.5RΔT[194]
R_{71}	$NO^* + * \rightarrow N^* + O^*$	0.89[f]	1×10^{11}	31.7 + f(θ_O, θ_{NO}, T)
R_{72}	$N^* + O^* \rightarrow NO^* + *$	0.89[f]	1×10^{11}	43.8 + f(θ_O, θ_{NO}, T)
R_{73}	$NO^* + H^* \rightarrow N^* + OH^*$	0.5	1×10^{11}	4.6 + f(θ_O, θ_H,θ_{NO}, T)
R_{74}	$N^* + OH^* \rightarrow NO^* + H^*$	0.5	1×10^{11}	35.1 + f(θ_O, θ_H,θ_{NO}, T)
R_{75}	$NO^* + H^* \rightarrow NH^* + O^*$	0.23[c]	1×10^{11}	8.2 + f(θ_O, θ_H,θ_{NO}, T)
R_{76}	$NH^* + O^* \rightarrow NO^* + H^*$	0.23[c]	1×10^{11}	14.9 + f(θ_O, θ_H,θ_{NO}, T)
R_{77}	$NO^* + OH^* \rightarrow NO_2^* + H^*$	0.5	1×10^{11}	38.2 + f(θ_O, θ_H,θ_{NO}, T)
R_{78}	$NO_2^* + H^* \rightarrow NO^* + OH^*$	0.5	1×10^{11}	0.0 + f(θ_O, θ_H,θ_{NO}, T)
R_{79}	$NO_2^* + * \rightarrow NO^* + O^*$	0.5	1×10^{11}	1.4 + f(θ_O,θ_{NO}, T)
R_{80}	$NO^* + O^* \rightarrow NO_2^* + *$	0.5	3×10^{12}[e]	21.2 + f(θ_O,θ_{NO}, T)
	HCN oxidation			
R_{81}	$HCN + * \rightarrow HCN^*$	0.5	1	0.0
R_{82}	$HCN^* \rightarrow HCN + *$	0.5	1×10^{13}	21.3g - 2.5RΔT
R_{83}	$CN + * \rightarrow CN^*$	0.5	1	0.0
R_{84}	$CN^* \rightarrow CN + *$	0.5	1×10^{13}	78.2 - 2RΔT [184]
R_{85}	$HCN^* + * \rightarrow H^* + CN^*$	0.5	1×10^{11}	21.1 + f(θ_H,T)
R_{86}	$H^* + CN^* \rightarrow HCN^* + *$	0.5	1×10^{11}	13.2 + f(θ_H,T)
R_{87}	$HCN^* + O^* \rightarrow OH^* + CN^*$	0.44h, 0.7g	1×10^{11}	17.1 + f(θ_O,T)
R_{88}	$OH^* + CN^* \rightarrow HCN^* + O^*$	0.44h, 0.7g	1×10^{11}	27.6 + f(θ_O,T)
R_{89}	$HCN^* + OH^* \rightarrow CN^* + H_2O^*$	0.5	1×10^{11}	5.7 + f(θ_O,T)
R_{90}	$CN^* + H_2O^* \rightarrow HCN^* + OH^*$	0.5	1×10^{11}	3.4 + f(θ_O,T)

[e]Based on NO oxidation atmospheric pressure simulations (Section 3.4.2).
[f]Based on NO oxidation UHV-TPR simulations (Section 3.3.2.2).

R_{91}	$CN^* + O^* \rightarrow C^* + NO^*$	0.3g	1×10^{11}	8.9 + f(θ_O,T)
R_{92}	$C^* + NO^* \rightarrow CN^* + O^*$	0.3g	1×10^{11}	4.7 + f(θ_O,T)
R_{93}	$CO^* + N^* \rightarrow CN^* + O^*$	0.7g	1×10^{11}	76.5 + f(θ_O,θ_{CO},T)
R_{94}	$CN^* + O^* \rightarrow CO^* + N^*$	0.7g	1×10^{11}	15.4 + f(θ_O,θ_{CO},T)
	CH_2O oxidation			
R_{95}	$CH_2O + * \rightarrow CH_2O^*$	0.5	1	0.0
R_{96}	$CH_2O^* \rightarrow CH_2O + *$	0.5	1×10^{13}	14.7 - 2.5RΔT
R_{97}	$HCO + * \rightarrow HCO^*$	0.5	1	0.0
R_{98}	$CHO^* \rightarrow HCO + *$	0.5	1×10^{13}	54.4 - 2.5RΔT[168]
R_{99}	$CH_2O^* + * \rightarrow HCO^* + H^*$	0.5	1×10^{11}	8.1 + f(θ_H,T)
R_{100}	$HCO^* + H^* \rightarrow CH_2O^* + *$	0.5	1×10^{11}	20.7 + f(θ_H,T)
R_{101}	$HCO^* + OH^* \rightarrow CH_2O^* + O^*$	0.5	1×10^{11}	30.9 + f(θ_O,T)
R_{102}	$CH_2O^* + O^* \rightarrow HCO^* + OH^*$	0.5	1×10^{11}	0.0 + f(θ_O,T)
R_{103}	$HCO^* + H_2O^* \rightarrow CH_2O^* + OH^*$	0.5	1×10^{11}	18.3 + f(θ_O,T)
R_{104}	$CH_2O^* + OH^* \rightarrow HCO^* + H_2O^*$	0.5	1×10^{11}	0.0 + f(θ_O,T)
R_{105}	$HCO^* + * \rightarrow H^* + CO^*$	0.5	1×10^{11}	0.0 + f(θ_{CO},θ_H,T)
R_{106}	$H^* + CO^* \rightarrow HCO^* + *$	0.5	1×10^{11}	30.8 + f(θ_{CO},θ_H,T)
R_{107}	$CO^* + OH^* \rightarrow HCO^* + O^*$	0.5	1×10^{11}	49.2 + f(θ_O,θ_{CO},T)
R_{108}	$HCO^* + O^* \rightarrow CO^* + OH^*$	0.5	1.5×10^{12}[g]	0.0 + f(θ_O,θ_{CO},T)
R_{109}	$CO^* + H_2O^* \rightarrow HCO^* + OH^*$	0.5	1×10^{11}	36.5 + f(θ_O,θ_{CO},T)
R_{110}	$HCO^* + OH^* \rightarrow CO^* + H_2O^*$	0.5	1×10^{11}	0.0 + f(θ_O,θ_{CO},T)
	C formation and oxidation			
R_{111}	$C + * \rightarrow C^*$	0.5	1	0.0
R_{112}	$C^* \rightarrow C + *$	0.5	1×10^{13}	158.2 - 1.5RΔT [222, 223]
R_{113}	$CO^* + * \rightarrow C^* + O^*$	0.5	1×10^{11}	54.4 + f(θ_O,θ_{CO},T)
R_{114}	$C^* + O^* \rightarrow CO^* + *$	0.5	1×10^{11}	1.3 + f(θ_O,θ_{CO},T)
R_{115}	$2CO^* \rightarrow C^* + CO_2{}^*$	0.5	1×10^{11}	48.3 + f(θ_{CO},T)
R_{116}	$C^* + CO_2{}^* \rightarrow 2CO^*$	0.5	1×10^{11}	0.0 + f(θ_{CO},T)

[g]Based on CH_2O oxidation atmospheric pressure simulations (Section 3.4.3).

	N_2O and C_2N_2 formation/decomposition			
R_{117}	$N_2O + * \rightarrow N_2O^*$	0.5	1	0.0
R_{118}	$N_2O^* \rightarrow N_2O + *$	0.5	1×10^{13}	6.7 - 2.5RΔT[194]
R_{119}	$N_2O^* + * \rightarrow NO^* + N^*$	0.5	1×10^{11}	3.9 + f(θ_{NO},T)
R_{120}	$NO^* + N^* \rightarrow N_2O^* + *$	0.5	1×10^{11}	19.8 + f(θ_{NO},T)
R_{121}	$C_2N_2 + * \rightarrow C_2N_2^*$	0.5	1	0.0
R_{122}	$C_2N_2^* \rightarrow C_2N_2 + *$	0.5	1×10^{13}	21 - 2.5RΔT
R_{123}	$C_2N_2^* + * \rightarrow 2CN^*$	0.73[h]	1×10^{11}	29.6 + f(T)
R_{124}	$2CN^* \rightarrow C_2N_2^* + *$	0.73[h]	1×10^{11}	28.1 + f(T)

3.4 Mechanism Performance and Validation

Most of the kinetic parameters in our emissions oxidation surface reaction mechanism are extracted from UHV-TPD/TPR experiments on single crystal surfaces, but it is also important to assess the mechanism performance at practically relevant operating conditions. Such conditions include monolith and fixed bed experiments conducted at atmospheric pressure with dilute levels of emissions in the feed at short residence times. As the typical concentration levels of emissions considered in this paper are very low (few tens to hundreds of ppm), we have selected relevant literature experiments consistent with such levels. To simulate the steady state experimental data, here we use an isothermal plug flow reactor (PFR) model. The assumption about isothermality is based on the very small amount of heat generated during the oxidation of dilute concentration levels for the emissions components (except for 1% CO, but here the experimental data is reported at controlled steady state temperatures). Finally, it is important to note that the kinetic parameters extracted from UHV conditions on single crystal surfaces

[h]Based on HCN oxidation UHV-TPR simulations (Section 3.3.2.5).

provide an excellent estimate for the simulations discussed in this section. However, some minor parameter tuning is expected given the pressure (UHV vs. atmospheric) and materials (single crystals vs. polycrystalline and supported catalysts) gap.

3.4.1 CO oxidation

Simulations using our CO oxidation reaction mechanism from Table 3.3 are compared against three sets of experiments conducted with monolith catalysts. The first comparison, shown in Figure 3.7a, is against the experiments conducted with a Pt/γ-Al_2O_3 monolith. [224] The support and catalyst details are as follows [224]: monolith length = 2.3 cm, monolith diameter = 1.3 cm, monolith cell density = 400 cells per square inch (CPSI), washcoat loading = 0.15 g, Pt content = 0.3 mg, and BET surface area = 151 m^2/g of washcoat.

Only two kinetic parameters (pre-exponential factor for reactions R_{16}: CO* desorption and R_{10}: CO* oxidation) were slightly modified to 5.7 $\times 10^{16}$ s^{-1} (starting from 1×10^{16} s^{-1} [219]) and 1×10^{10} s^{-1} (starting from 1×10^{11} s^{-1}), respectively, to capture the experimental data. Surface coverages in Figure 3.7b show that the surface is poisoned by CO* at low temperatures, consistent with the previous literature studies [141, 226, 227]. With increase in temperature, CO* starts to desorb, freeing up the vacancies for O_2 dissociative adsorption and subsequent CO* oxidation. At higher temperatures, as CO* is completely consumed, O* is the most abundant reaction intermediate (MARI) on the catalyst surface. We note that the pre-exponential factors proposed here for CO oxidation are different (approximately by an order of magnitude) from the ones reported by Mhadeshwar and Vlachos [103], but such discrepancy is expected given the different types of experimental data selected (ignition and molecular beam data in the earlier paper vs. monolith and fixed bed data in this work).

We also validated the CO oxidation mechanism against experimental data on a Pt/Al_2O_3 monolith reported by Carlsson and Skoglundh [225] as well as against our BenchCAT [228]

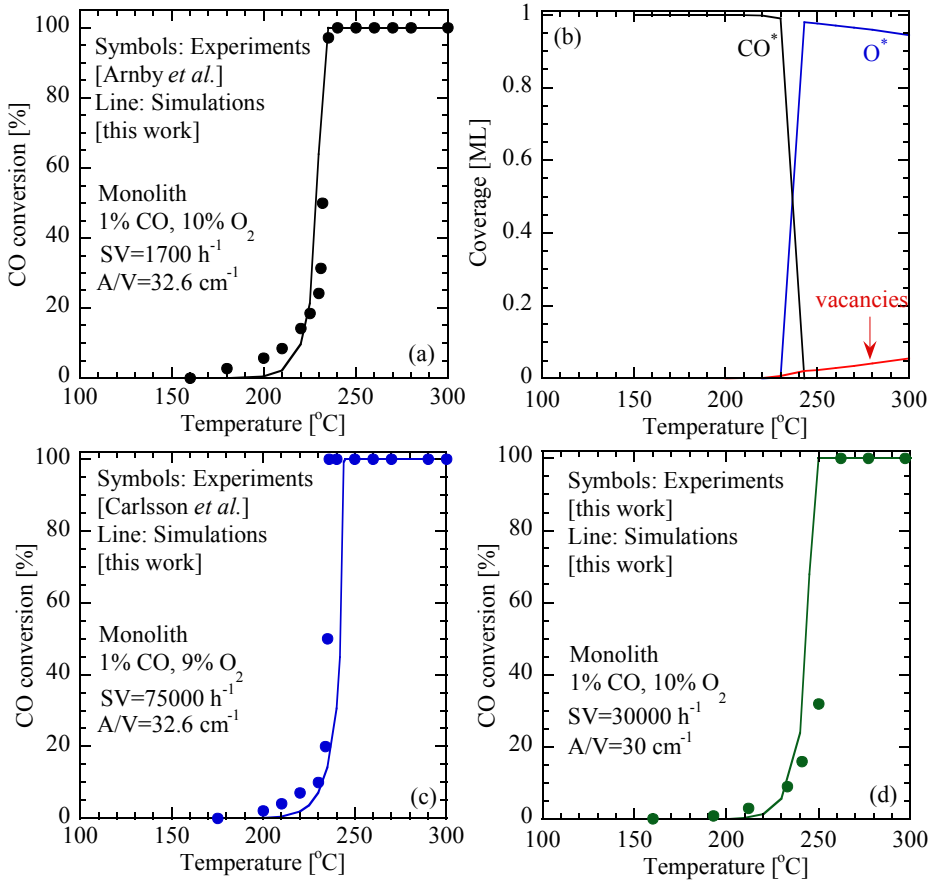

Fig. 3.7 Performance (panel a), analysis (panel b), and validation (panels c and d) of the microkinetic model for CO oxidation on Pt monoliths. Symbols represent the experimental data, whereas lines represent our simulations. Operating conditions for panels a and b: Pt/Al_2O_3 monolith; [224] feed of 1% CO, 10% O_2, and 89% Ar; space velocity of 17,000 hr^{-1}; and catalyst area per unit reactor volume of 32.6 cm^{-1}. Operating conditions for panel c: Pt/Al_2O_3 monolith; [225] feed of 1% CO, 9% O_2, and 90% N_2; space velocity of 75,000 hr^{-1}; and catalyst area per unit reactor volume of 32.6 cm^{-1}. Operating conditions for panel d: Pt/ZnO monolith (this work); feed of 1% CO, 10% O_2, 9% N_2, and 80% Ar; space velocity of 30,000 hr^{-1}, and catalyst area per unit reactor volume of 30 cm^{-1}. A Dycor Dymaxion mass spectrometer and Agilent Micro GC 3000A were used for identification and quantification of the gaseous species in the product stream. Simulations are in close agreement with the experimental data.

experiments on a Pt/ZnO monolith. In the experiments conducted by Carlsson and Skoglundh, [225] support and catalyst details are as follows: monolith length = 1.5 cm, monolith diameter = 1.2 cm, monolith cell density = 400 CPSI, washcoat loading = 0.2 g, and catalyst coating = 0.12 g/cm^3. On the other hand, support and catalyst details for the experiments carried out in our lab are as follows: monolith length = 1 cm, channel size = 1 mm $\times$ 1 mm, total channels = 6, BET surface area = 6.4 m^2/g, Pt particle diameter = 2.6 nm, Pt loading = 2%, and monolith cell density = 400 CPSI. The mechanism predictions, without any parameter modification, are shown in Figures 3.7c and 3.7d, for the respective experiments. Overall, the proposed reaction mechanism captures the CO oxidation chemistry well against multiple experimental data sets at practically relevant operating conditions.

3.4.2 NO oxidation

Figure 3.8 shows the comparison of our model predictions with monolith and fixed bed reactor experiments for NO oxidation on Pt. [145, 229] The literature experiments reported by Bhatia et al. [229] were carried out using practically relevant NO and O_2 concentration levels (482 ppm and 5%, respectively) on a Pt/Al_2O_3 coated monolith (Figures 3.8a and 3.8b). Similarly, fixed bed reactor experiments were carried out by Crocoll et al. [145] using 500 ppm of NO and 3% O_2 (Figure 3.8e). Support and catalyst details for the experiments by Bhatia et al. [93] are as follows: monolith length = 1.5 cm, monolith diameter = 1.7 cm, monolith cell density = 400 CPSI, Pt loading = 70 g/ft3, Pt loading = 2.63 wt.%, Pt dispersion = 20.3%, Pt area = 2.21 m^2/g of washcoat, and Pt particle size = 5.59 nm. Similarly, the support and catalyst details for the NO oxidation experiment by Crocoll et al. [145] are as follows: Pt/γ-Al_2O_3 powder catalyst, Pt loading = 2%, BET surface area = 175 m^2/g, total pore volume = 0.70 cm^3/g, pore diameter = 8.6 nm, active Pt surface area = 5.3 m^2/g(Pt), and catalyst weight = 1 g.

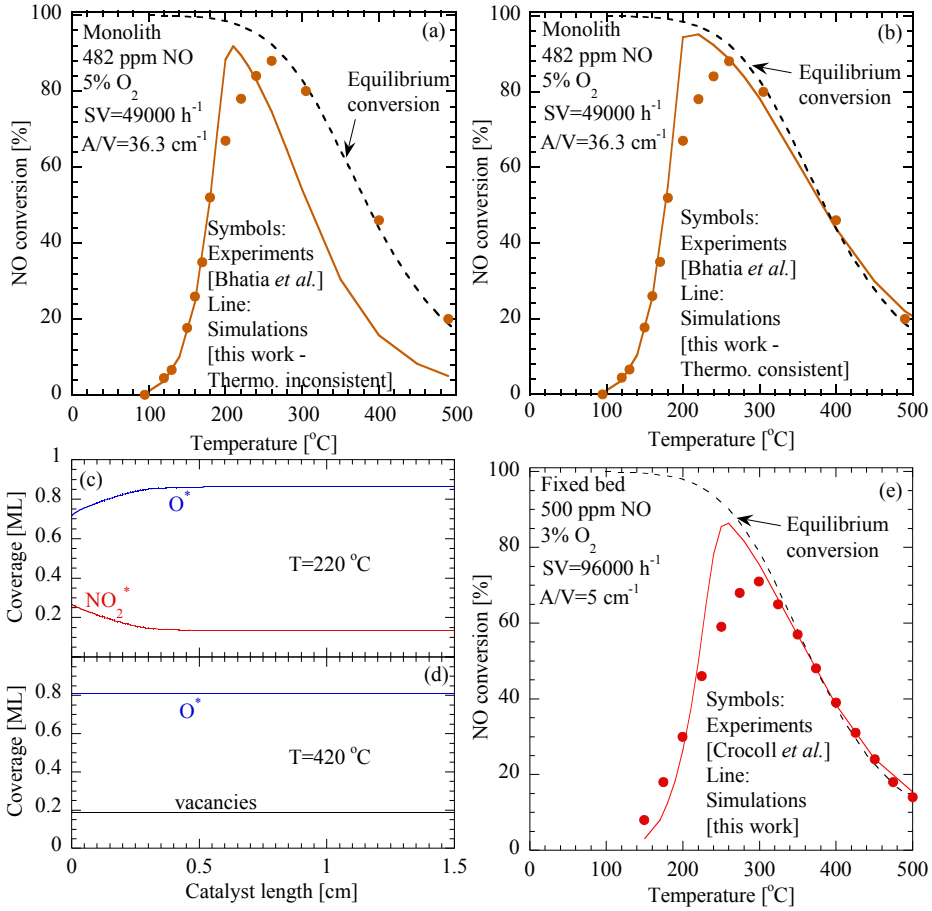

Fig. 3.8 Performance (panel a and b), analysis (panels c and d), and validation (panel e) of the microkinetic model for NO oxidation on Pt monolith and fixed bed. Symbols represent the experimental data; solid lines represent our simulations; and dashed lines represent the equilibrium calculations using GASEQ software. [230] Panel b shows the improvement in mechanism predictions after ensuring thermodynamic consistency (see text for details). Operating conditions for panels a-d: Pt/Al_2O_3 monolith; [229] feed of 482 ppm NO, 5% O_2, and ~95% N_2; space velocity of 49,000 hr^{-1}; and catalyst area per unit reactor volume of 36.3 cm^{-1}. Operating conditions for panel e: Pt/Al_2O_3 fixed bed [145]; feed of 500 ppm NO, 3% O_2, and ~97% N_2, space velocity 96,000 h^{-1}, and catalyst area per unit reactor volume of 5 cm^{-1}. Simulations are in close agreement with the experimental data.

Unlike CO oxidation, the experimental data show that NO conversion decreases after ∼250 °C. Equilibrium calculations conducted using GASEQ software [230] at the high temperature conditions indicate that the experimental data for NO oxidation are equilibrium limited. RPA indicates that the oxidation of NO* via R_{80}: NO* + O* → NO_2* + * is the most important step in the kinetically controlled low temperature region; and its pre-exponential factor was slightly tuned from 1×10^{11} s^{-1} to 3×12^{11} s^{-1} to improve the agreement with the experimental data. Minor adjustment of NO_2 binding energy to 23.5 kcal/mol (${Q_{NO_2}}^{TPD}$ =19 kcal/mol, literature range 17-38 kcal/mol [191, 192, 194, 196, 197, 206, 213]) is also carried out to improve the low temperature (kinetically controlled region) NO conversion predictions. Despite such modifications, the model predictions severely under predict the higher temperature equilibrium limited data in Figure 3.8a.

The origin of this discrepancy at high temperature is associated with the lack of thermodynamic (primarily entropic) consistency of kinetic parameters, as discussed by several previous papers [101, 143, 229, 231, 232]. Maintaining thermodynamic consistency is critical, especially for correctly capturing the equilibrium limited data. In our reaction mechanism, this is accomplished by a modified Arrhenius equation with temperature exponent β of -0.93 (forward) and +0.93 (backward) for reaction pair R_{79}-R_{80}: NO_2* + * ↔ NO* + O*, (where

$$k = A(\frac{T}{T_o})^{\beta} e^{\frac{-E_a}{RT}} \tag{3.1}$$

and T_o is 300 K). This allows one to match the entropy values for gas phase NO oxidation to NO_2 (NO + O → NO_2) with the overall catalytic pathway for NO oxidation to NO_2 (NO adsorption, oxygen adsorption, NO* + O* → NO_2* + *, and NO_2 desorption). Including temperature exponents through a modified Arrhenius equation is a standard practice in gas phase reaction mechanism development community; [109] and it is also consistent with the

approach for catalytic reaction mechanisms to fulfill the thermodynamic constraints determined by Hess?s law, as described by Mhadeshwar et al. [101] Performance of the thermodynamically consistent NO oxidation reaction mechanism is shown in Figure 3.8b. The agreement with experimental data is significantly improved under the equilibrium limited high temperature conditions

Simulated coverage profiles along the catalyst length at two different temperatures (240 °C and 420 °C corresponding to kinetically controlled and equilibrium limited regions, respectively) are shown in Figures 3.8c and 3.8d. Under both conditions, the catalyst surface is pre-dominantly covered by O*, which is consistent with the high O_2 concentration in the feed compared to that of NO. NO_2* coverage is non-negligible in the kinetically controlled region due to NO* oxidation, but it is negligible in the equilibrium limited region due to NO_2* desorption. The thermodynamically consistent NO oxidation mechanism is further validated against fixed bed experimental data of Crocoll *et al.* [145] without any further modification of the kinetic parameters. As shown in Figure 3.8e, the NO oxidation mechanism predicts the conversion profile well in both kinetically controlled and equilibrium limited regions.

3.4.3 CH_2O Oxidation

The CH_2O oxidation reaction mechanism is compared against two sets of experimental data, [233, 234] as shown in Figures 3.9a and 3.9d. Some of the operating conditions in the first set of experiments (CH_2O concentration of 100 ppm, space velocity of 50000 hr^{-1}) on Pt/TiO_2 fixed bed are reasonably close to the typical conditions in diesel engine exhaust aftertreatment; however, the O_2 level is much higher (20%). In the second set of experiments, the space velocity is so high (1,250,000 hr^{-1}) that it does not represent practically relevant operating conditions (extremely short catalyst length). Under such conditions, we believe that mass transfer limitations will dominate over the surface kinetics, but we have still included this data

set as a validation of our mechanism under extreme conditions. Support and catalyst details for the experiments by Zhang et al. [233] are as follows: Pt/TiO_2 powder catalyst, Pt loading = 1 wt.%, Pt particle size = $\sim$1 nm, and BET surface area = 47.4 m^2/g. Similarly, the support and catalyst details for the experiments by Peng and Wang [234] are as follows: Pt/TiO_2 powder catalyst, BET surface area = 61.5 m^2/g, pore volume = 0.24 cm^3/g, average pore diameter = 11.5 nm, support particle size = 15.4 nm, Pt dispersion = 68.5%, Pt metal size = 1.5 nm, and catalyst weight = 0.25 g.

In the first set of experiments (Figure 3.9a), it is observed that CH_2O oxidation is close to 100% even at room temperature. The surface coverage profiles along the catalyst length at 40 °C (Figure 3.9b) show that O* is the MARI, whereas CO* (produced from CH_2O*) is rapidly consumed at the catalyst entrance. Decrease in CO* coverage is consistent with increase in H* coverage due to reaction R_{28}: CO* + OH* $\rightarrow$ CO_2* + H*. RPA in Figure 3.9c shows that CH_2O* oxidation leads to the formation of formyl, which is further oxidized to CO* and OH* via reaction R_{108}: HCO* + O* $\rightarrow$ CO* + OH*. The intermediates CO* and OH* react via reaction R_{28} to produce CO_2* and H*. Finally, H* is completely oxidized to H_2O* via reaction R_{22}: H* + OH* $\rightarrow$ H_2O* + *. This is consistent with the CH_2O oxidation experiments of McCabe and McCready, [235] who suggested that CO and H are reaction intermediates that subsequently oxidize to form CO_2 and H_2O. Based on the RPA, we have modified only one pre-exponential factor for the most important reaction R_{108} from 1×10^{11} s^{-1} to 1.5×10^{12} s^{-1} to improve the agreement with the experiments. For the second set of experiments, despite the severe mass transfer limitations, our CH_2O oxidation mechanism reasonably predicts the experimental data at temperatures higher than 60 °C without any further parameter modification. The evaluation of mass transfer limitations in this specific experiment is beyond the scope of the current work.

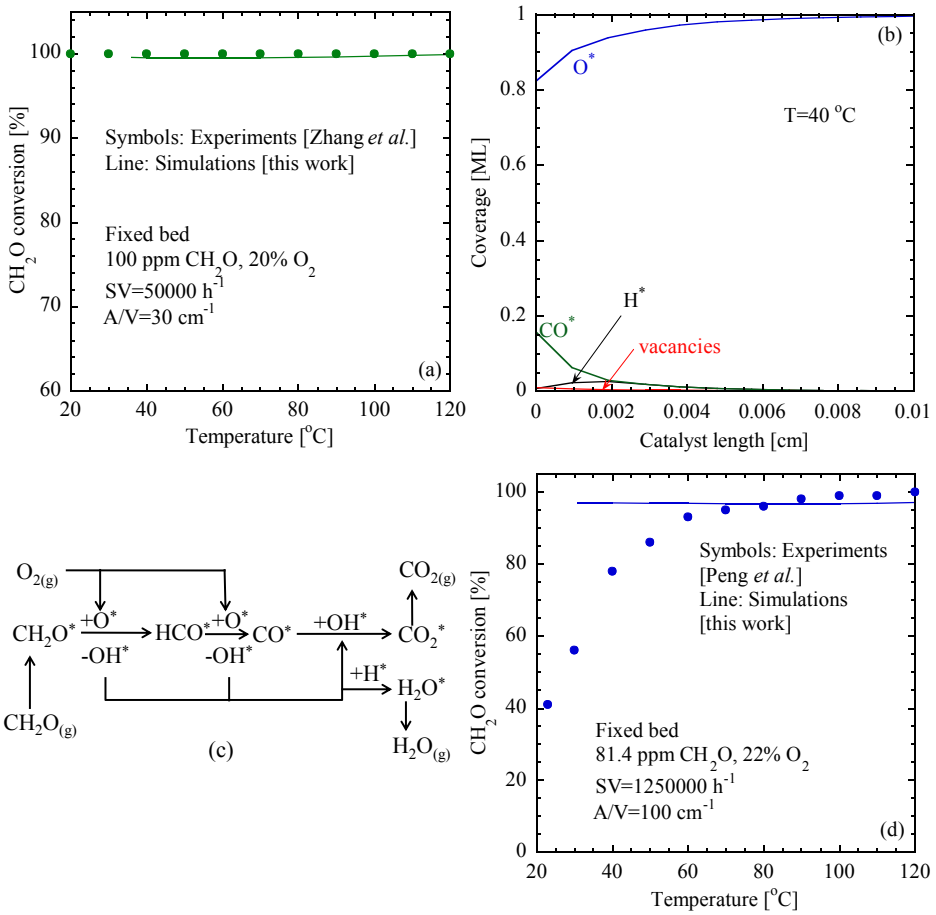

Fig. 3.9 Performance (panel a), analysis (panels b and c), and validation (panel d) of the microkinetic model for CH_2O oxidation on Pt fixed beds. Symbols represent the experimental data, whereas lines represent our simulations. Panel b shows the coverage profiles of dominant surface species along the catalyst length (actual length=0.47 cm) at 40 °C. Panel c shows the dominant reaction pathways in the CH_2O oxidation chemistry at 40 °C (at the entrance of the catalyst). Operating conditions for panels a-c: Pt/TiO_2 fixed bed; [233] feed of 100 ppm CH_2O, 20% O_2, and ∼80% He; space velocity of 50,000 hr^{-1}; and catalyst area per unit reactor volume of 30 cm^{-1}. Operating conditions for panel d: Pt/TiO2 fixed bed; [234] feed of 81.4 ppm CH_2O, 22% O_2, and ∼78% N_2; space velocity of 1,250,000 hr^{-1}; and catalyst area per unit reactor volume of 100 cm^{-1}. Simulations are in reasonable agreement with the experimental data. Discrepancy in panel d due to high space velocity is discussed in the text.

3.4.4 NH_3 Oxidation

Figure 3.10a compares the performance of our NH_3 oxidation reaction mechanism against the fixed bed reactor experiments on Pt/Al_2O_3 [236]. The support and catalyst details are as follows [236]: Pt/Al_2O_3 powder catalyst, BET surface area = 120 m^2/g, catalyst pore volume = 0.81 cm^3/g, Pt loading = 2%, and catalyst weight = 0.3 g. Here, 700 ppm of NH_3 was oxidized using 8% O_2 in N_2 at atmospheric pressure. The surface coverage profiles along the catalyst length (Figure 3.10b) at 300 °C show that NH_x* species are depleted close to the entrance, while NO_2* is produced. Most of the surface ($\sim$90%) is covered with O* (not shown). RPA in Figure 3.10c shows that NH_3* is sequentially oxidized to N* via reactions R_{55}: NH_3*+ O* $\rightarrow$ NH_2* + OH*, R_{58}: NH_2* + O* $\rightarrow$ NH* + OH*, R_{53}: NH* + * $\rightarrow$ N* + H*, and R_{60}: NH* + O* $\rightarrow$ N* + OH*. The alternate path for NH* oxidation is via R_{76}: NH* + O* $\rightarrow$ NO* + H* to form NO*. This is consistent with the work of Bradley et al. [237], who suggested that the oxidation of NH intermediate could lead to the formation of NO and N_2. N* formed in reactions R_{60} and R_{53} desorbs as N_2, whereas NO* formed in reaction R_{76} further oxidizes through reaction R_{80}: NO* + O* $\rightarrow$ NO_2* + *. Most of the NO_2* desorbs, but some of it is converted back to NO* through reaction R_{78}: NO_2* + H* $\rightarrow$ NO* + OH*. RPA at 275 °C shows that the H_2O originates from reactions R_{62}: NH_3*+OH* $\rightarrow$ NH_2* + H_2O*, R_{64}: NH_2* + OH* $\rightarrow$ NH* + H_2O*, R_{24}: 2OH* $\rightarrow$ H_2O* + O*, and R_{22}: H* + OH* $\rightarrow$ H_2O* + *.

With a minor adjustment of only one bond index for reaction pair R_{59}-R_{60}: N* + OH* $\rightarrow$ NH* + O* from 0.5 to 0.6, the model is able to capture the experimental data over the entire temperature range. We note that this bond index was earlier set to 0.65 in the TPR analysis presented in Section 3.2.4. Even though the UHV-TPR experiments conducted on single crystal surfaces typically provide decent initial estimates of kinetic parameters, some further refinement is typically necessary to capture the practically more relevant atmospheric pressure data on polycrystalline or supported catalysts (this again points to the pressure and materials gap).

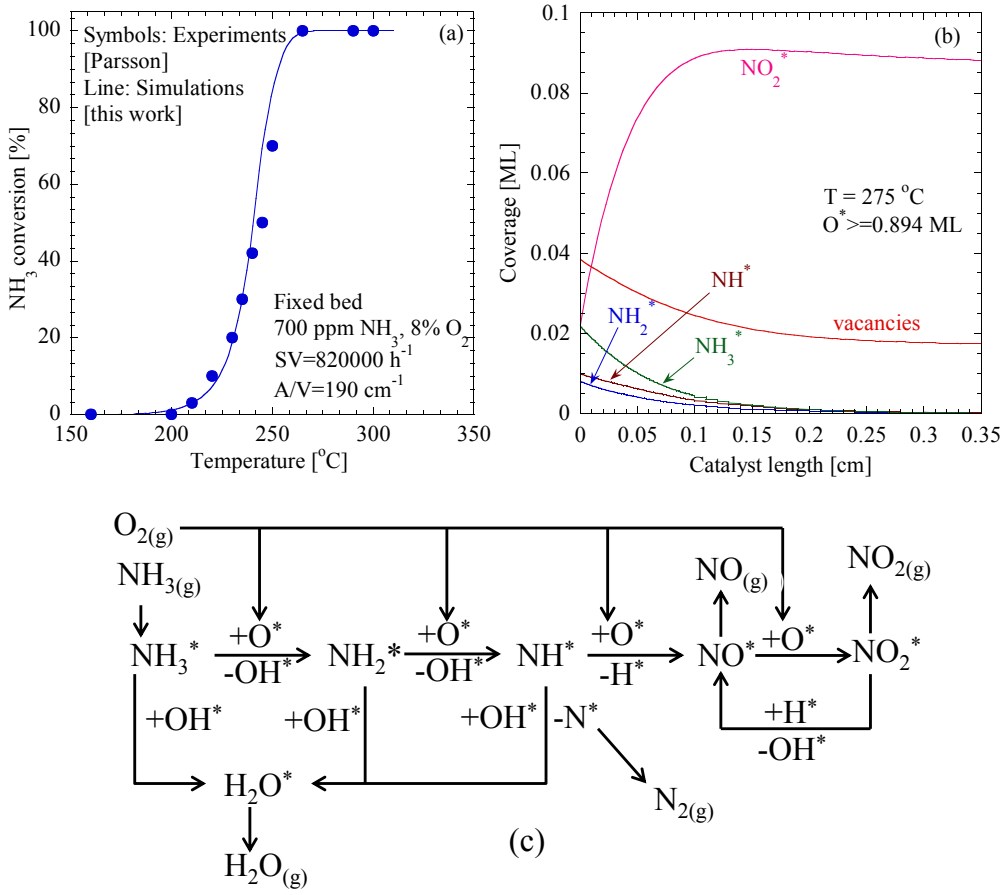

Fig. 3.10 Performance (panel a) and analysis (panels b and c) of the microkinetic model for NH_3 oxidation on Pt/Al_2O_3 fixed bed. Symbols represent the experimental data, whereas lines represent our simulations. Panel b shows the coverage profiles of dominant surface species (O* ∼90%, not shown) along the catalyst length at 275 °C. Panel c shows the dominant reaction pathways in the NH_3 oxidation chemistry at 275 °C (at the entrance of the catalyst). Operating conditions: Pt/Al_2O_3 fixed bed reactor; [236] feed of 300 ppm NH_3, 6% O_2, and ∼94% N_2; space velocity of 820,000 hr^{-1}; and catalyst area per unit reactor volume of 190 cm^{-1}. Simulations are in close agreement with the experimental data.

3.4.5 HCN oxidation

The final comparison for model predictions vs. experimental data is for HCN oxidation on Pt, as shown in Figure 3.11a. The experimental data is taken from fixed bed reactor experiments conducted with 30 ppm of HCN and 6% O_2 on a Pt/Al_2O_3 catalyst. [16] The support and catalyst details are as follows [16]: Pt/Al_2O_3 pellete catalyst (cylindrical extrudates), catalyst volume = 2 cm^3, pellets length = 0.13 inch, pellets diameter = 0.13 inch, Pt loading = 0.5%, and catalyst weight = 2.1 g. Axial surface coverage profiles at 225 °C (Figure 3.11b) show that HCN* decreases along the catalyst length, while NO_2* increases. Similar to NH_3 oxidation, most of the surface ($\sim$97%) is covered with O* (not shown). RPA, shown in Figure 3.11c, indicates that under these operating conditions, HCN oxidation path via reaction R_{87}: HCN* + O* $\rightarrow$ CN* + OH* dominates the alternative path of HCN decomposition via reaction R_{85}: HCN* + * $\rightarrow$ H* + CN*.

We have adjusted the bond index of reaction pair R_{87}-R_{88} from 0.5 to 0.7 to capture the low temperature HCN conversion data. We note that this bond index was earlier set to 0.44 in the TPR analysis presented in 3.2.5. As mentioned earlier, some parameter refinement is generally required for the transition from UHV simulations to practically more relevant atmospheric pressure simulations on polycrystalline or supported catalysts. Once CN* is formed, it is oxidized via two major pathways, viz., reactions R_{91}: CN* + O* $\rightarrow$ C* + NO* and R_{94}: CN* + O* $\leftrightarrow$ CO* + N*, producing NO* and N*, respectively. Bond indices of these two reaction pairs (R_{91}-R_{92} and R_{93}-R_{94} are modified from 0.5 to 0.3 and 0.7, respectively, to facilitate NO* formation and subsequent oxidation to NO_2 and N_2O, which were reported as oxidation products by Zhao et al. in their experiments. [16] Binding energy of HCN was slightly adjusted to 21.3 kcal/mol ($Q_{HCN}{}^{TPD}$ = 26.1 kcal/mol, $Q_{HCN}{}^{avg}$ = 21.4 kcal/mol from Table 3.2, literature range 14-30 kcal/mol [184, 200]) to capture the experimental data. Our HCN oxidation reaction mechanism shows good agreement with the experimental data, albeit with some parameter

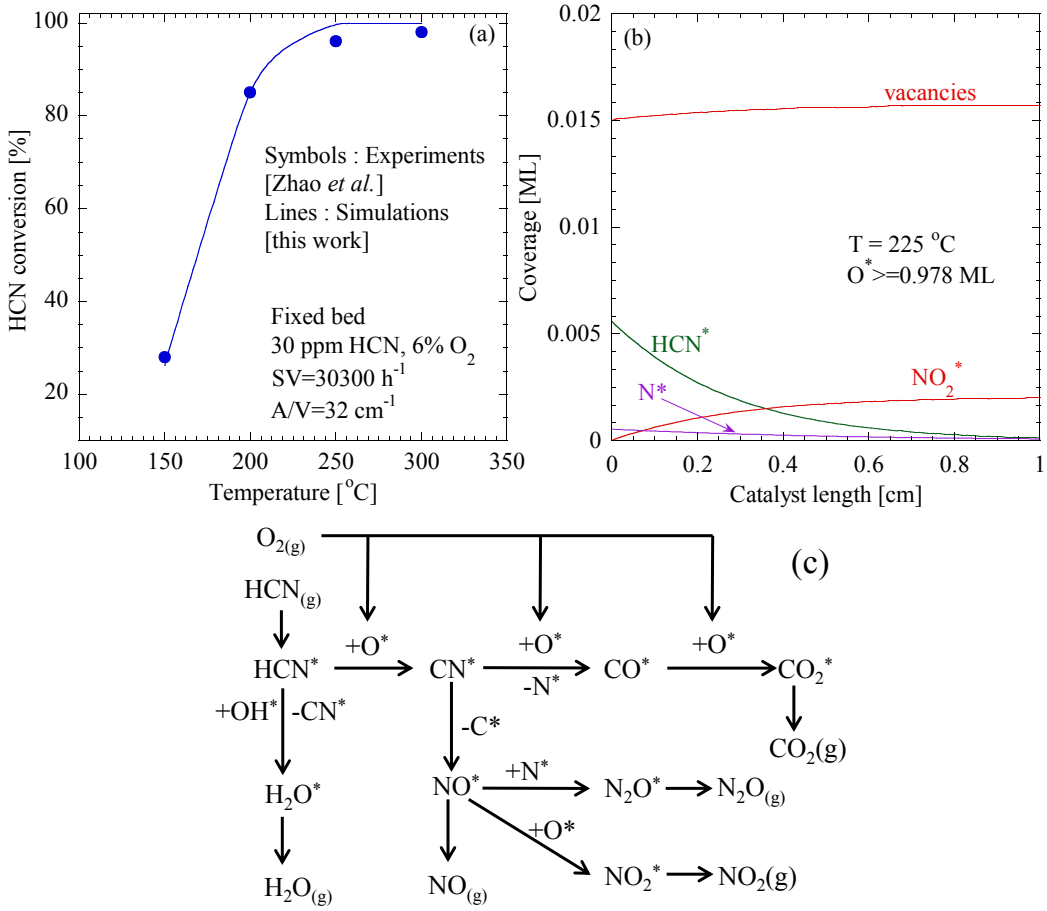

Fig. 3.11 Performance (panel a) and analysis (panels b and c) of the microkinetic model for HCN oxidation on Pt fixed bed. Symbols represent the experimental data, whereas lines represent our simulations. Panel b shows the coverage profiles of dominant surface species (O* ∼97%, not shown) along the catalyst length at 225 °C. Panel c shows the dominant reaction pathways in the HCN oxidation chemistry at 225 °C (at the entrance of the catalyst). Operating conditions: Pt/Al_2O_3 fixed bed reactor [16]; feed of 30 ppm HCN, 6% O_2, and ∼94% N_2; space velocity of 30,300 hr^{-1}; and catalyst area per unit reactor volume of 32 cm^{-1}. Simulations are in close agreement with the experimental data.

modification. In general, the HCN oxidation experiments are rare in literature, due to its high toxicity and lethal nature. Additional validation of this reaction mechanism will be carried out in the future, as more data becomes available for HCN oxidation under practically relevant operating conditions.

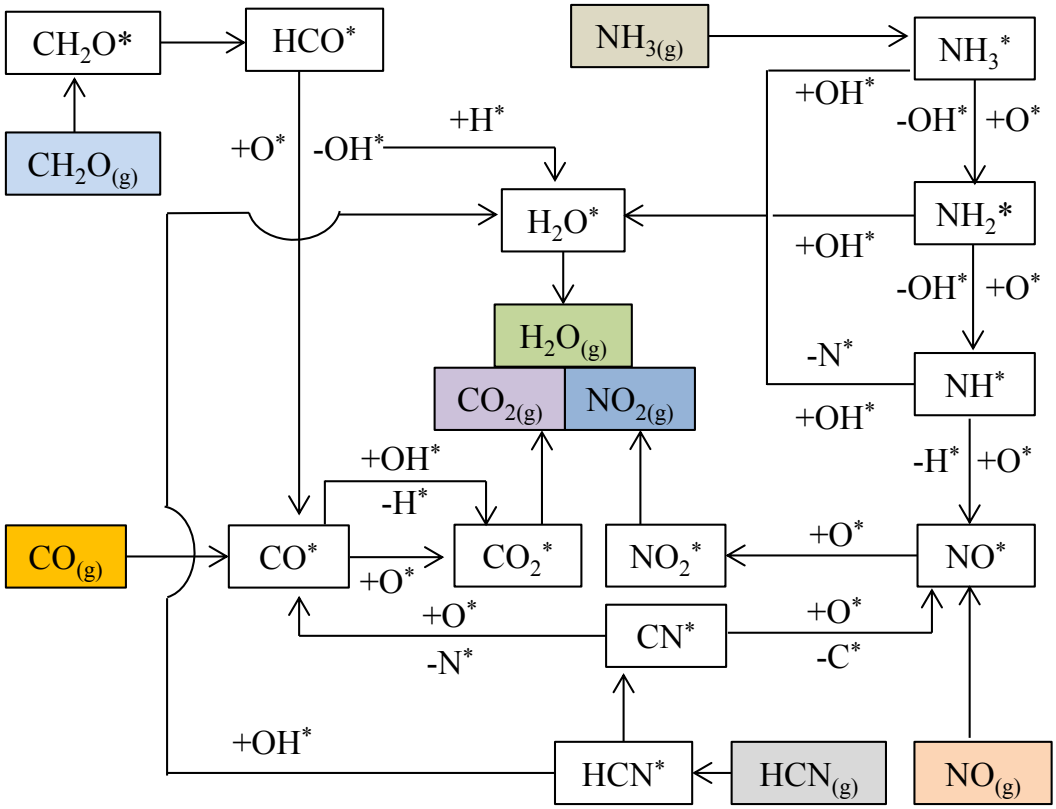

Fig. 3.12 Schematic of the important reaction pathways, intermediates, reactants, and products from the microkinetic model for oxidation of emissions on Pt. The reactants and products in gas phase are shown in shaded boxes.

3.5 Preliminary Mechanism Reduction

Based on RPA, some reactions in the detailed surface reaction mechanism are identified as the least important ones. These include the adsorption/desorption steps for radicals, viz., H, O, OH,

COOH, HCO, N, NH, NH_2, C, and CN, as these species are more dominant on the catalyst surface than in the gas phase. Based on the HCN-TPD (Section 3.1) and HCN-TPR (Section 3.2.5) simulations, the C_2N_2 adsorption/desorption and formation/decomposition chemistry is important only at high temperatures ($\sim$700 K); therefore, it can be ignored from the simulations at typical DOC conditions. Finally, some of the reactions in the COOH* chemistry (e.g., reactions of COOH* with H*, O*, and OH* are found to be less important than its formation from CO* + OH* and its decomposition to CO_2* + H*. This preliminary model reduction results in a shorter surface reaction mechanism with 94 steps (47 reversible) and 20 surface species. The unimportant reactions are listed in Table 3.3 (shaded reactions in the second column). Finally, the schematics of the major oxidation reaction pathways for all five emissions species are shown in Figure 3.12.

3.6 Limitations of the Overall Approach

To our knowledge, the reaction mechanism presented in this work is the first comprehensive microkinetic model on Pt that simultaneously captures five major emissions oxidation chemistries on Pt under UHV as well as practically more relevant operating conditions. Nonetheless, it is important to acknowledge the key limitations of the overall approach along with the future work needed to improve the mechanism presented here.

3.6.1 Limitations associated with the reaction mechanism and the uncertainty in kinetic parameters

Current work focuses on the oxidation of five emissions (CO, NO, CH_2O, NH_3, and HCN) only. These species contain only 1 C and/or N atom. After HC-SCR, the exhaust can contain additional secondary

- emissions, such as non-methane hydrocarbons (C_2H_4), aldehydes (CH_3CHO), and nitrogen-containing species (CH_3CN). The emissions oxidation mechanism should be expanded to include such species with more C atoms.

- Beyond the C- and N-containing species, the exhaust also contains S-species, such as SO_2, which originate from the oxidation of sulfur in the diesel fuel. SO_2 can be oxidized on the DOC to SO_3, which in turn could be hydrated (due to the steam in the exhaust) to sulfuric acid. Both, metal and support in the DOC, can interact with the sulfur oxides and sulfuric acid, resulting in catalyst deactivation due to sulfation. [9, 56, 78] The Schneider research group has conducted significant work in sulfur oxide chemistry on Pt using DFT. [238, 238–240] Future work should include such chemistry in the emissions oxidation mechanism.

- Uncertainty in the kinetic parameters originates from the use of various estimation methods and their accuracy. For example, species binding energies and adsorbate-adsorbate interactions estimated using the UHV-TPD experiments can vary to some extent among different experiments. Activation energies for the surface reactions are calculated using the semi-empirical UBI-QEP method. [107] Even though the UBI-QEP method is highly convenient in accounting for coverage effects and ensuring enthalpic consistency, the calculated activation energies need to be verified with first-principles DFT calculations. A number of bond indices are modified in this work to improve the agreement with the experimental data. Agreement between the UBI-QEP and DFT values can be improved by adjusting the bond indices. [241] However, accurate estimates of activation energies and location of transition state along the reaction coordinate are needed to verify the modifications conducted here. Finally, uncertainty in the experimental

measurements (if any) may be translated to the surface reaction mechanism through the adjustment of kinetic parameters.

- The reaction mechanism proposed here utilizes a single temperature exponent to account for equilibrium limitations of NO oxidation in the considered temperature range. As all reactions are theoretically reversible, temperature exponents could be considered for the entire reaction mechanism, consistent with the approaches presented in literature. [101–103] However, out of the five emissions oxidation chemistries studied here, only NO oxidation is reversible in the considered temperature range, whereas all other reactions are practically irreversible. Presence of a large amount of O_2 ($\sim$10-15%) in the diesel exhaust compared to the dilute levels of emissions also drives most of the emissions oxidation reactions toward the oxidized products. To ensure simplicity and practical applicability of the reaction mechanism, we have chosen to include only a single temperature exponent that is necessary for capturing the equilibrium limitations for NO oxidation.

- The mechanism reduction presented here is preliminary compared to more rigorous approaches based on principal component analysis and small parameter asymptotic. [104, 218]

3.6.2 Limitations Associated With the Catalyst and Reactor Modeling

- Catalyst site density used in the simulations (1.5×10^{15} sites/cm^2) is calculated from Pt(111), which is one of the most stable facets of the Pt crystal. However, the actually utilized catalysts are polycrystalline in nature. Multiple types of sites and facets - which may be relevant to the real-life catalyst operation - are not taken into account. Active site density could vary with the catalyst loading, type of support, and catalyst life (deactivation/poisoning); however these effects are not considered in this work

- Catalyst supports, such as Ceria and zirconia, can play an active role in the emissions oxidation kinetics along with Pt. This work primarily focuses on relatively inert supports, such as alumina and titania. Nonetheless, our simplified approach for microkinetic modeling on Pt does not account for the role of support in emissions oxidation kinetics.

- A steady state isothermal PFR model is employed in the simulations. The assumption about isothermality is based on the very small amount of heat generated during the oxidation of dilute concentration levels for the emissions components. Future work will focus on investigating the performance of emissions oxidation mechanism under transient operating conditions for an exhaust containing multiple emissions.

3.7 Conclusion

In this chapter, we have reported the first microkinetic model for the oxidation of five major emissions (CO, NO, CH_2O, NH_3, and HCN) on a Pt-based DOC. The comprehensive microkinetic model contains 124 irreversible (62 reversible) steps and 21 surface species (94 steps and 20 species for the reduced version). Kinetic parameters are extracted using multiple techniques, such as the semi-empirical UBI-QEP method, literature DFT calculations, and simulations of various UHV temperature programmed experiments (TPD/TPR). Parameters extracted/estimated from such techniques are very good initial estimates, but they still require some adjustment to capture and predict the experimental data at practically more relevant operating conditions (atmospheric pressure, high O_2 concentration, dilute level of emissions, high space velocity, monolith- or powder-scale setups, etc.). The microkinetic model shows very good agreement with various sets of experimental data focused on emissions oxidation. The surface reaction mechanism developed in this work provides an excellent starting point for

DOC design and optimization, and could be further expanded by including the chemistry of additional C_2-C_3 species and sulfur impurities in the exhaust.

Chapter 4

Sulfur Oxides Interactions with Diesel Oxidation Catalysts (DOCs)

4.1 Introduction

Sulfur oxides (SO_x) in the diesel engine exhaust are one of the major factors contributing toward deactivation of emissions aftertreatment catalysts. Interactions of SO_x with the catalyst metals and supports can result in sulfate formation. In this chapter, we review various experimental and computational studies regarding SO_x interaction on Pt-Pd/alumina catalysts, which are typically used in Diesel Oxidation Catalysts (DOCs). In addition, we propose a novel microkinetic model for SO_2 oxidation on Pt as a first step toward understanding the DOC-SO_x interactions. The proposed model contains 24 elementary steps (12 reversible) with five surface species. The microkinetic model is validated against experimental data for SO_2 oxidation on Pt. Finally, we discuss the challenges of incorporating sulfur-based deactivation in kinetic modeling, and propose potential directions that could lead to the development of sulfur resistant materials for DOCs.

4.2 Literature Review of DOC-SO_x Interactions

More than 98% of the sulfur in diesel is oxidized to SO_2 during combustion. [71, 72, 242] H_2S has been reported during fuel rich conditions; [242] but in fuel lean conditions for diesel engines, H_2S (if any) would be further oxidized to SO_2 and SO_3 above 300 °C in the presence of a Pt/Pd catalyst. [15, 32, 60] SO_2 and SO_3 subsequently interact with the DOC components, metal oxide and support. DOC sulfation has been widely studied and discussed in the literature. [15, 32, 60, 71, 72, 86, 87, 89, 242] In this section, we present a brief review of the experimental and computational investigations regarding the interactions of sulfur with DOC, that is, metal, metal oxides, as well as the alumina support.

4.3 Experimental Studies

4.3.1 Interaction of SO_x with Pt

Compared to other noble metals, Pt remains in metallic form in the typical oxidizing environment. [243] Pt is very active towards SO_2 oxidation; [79, 243] and various techniques such as Temperature Programmed Desorption (TPD), X-ray Photoelectron Spectroscopy (XPS), Ultraviolet Photoelectron Spectroscopy (UPS), High Resolution Electron Energy Loss Spectroscopy (HREELS), Near Edge X-ray Absorption Fine Structure (NEXAFS) spectroscopy, and Low Energy Electron Diffraction (LEED), have been used to study the interaction of SO_2 with Pt metal. [244–252]

Ultra High Vacuum (UHV) studies show that SO_2 binds strongly (molecular adsorption with a sticking coefficient of $\sim$0.5) on the Pt surface with S and O atoms in η^2-SO_2 configuration (where η^2 represents the number of atoms of adsorbate coordinated to the surface). [245, 246] Astegger and Bechtold [246] reported that SO_2 desorbs at 400, 480, and 580 K (multiple

peaks) in their TPD experiments on Pt(111); however, the peaks at 480 and 580 K were due to molecularly adsorbed SO2, whereas the peak at 400 K was due to saturated SO2 surface. The peak at 400 K appeared only at higher initial coverages suggesting that the peak is from multilayered SO2 adsorption. In the case of co-adsorbed SO_2 and O_2 on Pt(111), a SO_3 desorption peak was observed at 580 K. [246] The SO_2 desorption peak at 480 K decreased and the SO_3 peak at 580 K increased while increasing the oxygen surface coverage. From XPS and HREELS studies, Sun et al. [245] observed that SO_2 also forms sulfur monoxide (SO) and sulfate (SO_4) on Pt at 300 K.

Streber et al. [250] studied the adsorption and reaction of SO_2 on clean and oxygen pre-covered Pt(111) surfaces by in situ high resolution XPS and suggested that SO_2 reacts with oxygen to form SO_3 at 130 K, and subsequently to SO_4, which is stable up to 500 K. The sulfate ions impact the metal sites by deteriorating the chemisorption ability. [251] Many studies suggest that Pt metal is not converted to $PtSO_4$; however, it helps migrating the sulfur species to the support, which subsequently gets sulfated. [32, 252, 253] Based on these studies, the generalized sulfur chemistry on Pt can be summarized as follows.

$$SO_{2(g)} \rightarrow SO_2^* \tag{4.1}$$

$$SO_2^* \rightarrow SO^* + O^* \tag{4.2}$$

$$SO^* \rightarrow S^* + O^* \tag{4.3}$$

$$SO_2^* + O^* \rightarrow SO_3^* \tag{4.4}$$

$$SO_3^* + O^* \rightarrow SO_4 \tag{4.5}$$

Here, subscript (g) and superscript * represent the gas phase and the surface species, respectively.

4.3.2 Interaction of SO_x with PdO

Unlike Pt, in a typical oxidizing environment, Pd is converted to more active oxidized form of PdO. [60, 243, 254] Studies using Scanning Tunneling Microscopy (STM), LEED, Auger Electron Spectroscopy (AES), and TPD suggest a three-step mechanism of PdO formation, that is, chemisorption of oxygen on Pd, diffusion of chemisorbed oxygen into the Pd metal, and formation of the stoichiometric PdO structure. [254] In atmospheric conditions, PdO phase is stable up to ∼800 °C, whereas metallic Pd is stable above ∼800 °C. [61, 254–258]

Based on Fourier Transform Infrared (FT-IR) spectroscopy, Mowrey and McCormick [87] suggested that PdO is active in converting SO_2 to SO_3, which further reacts with PdO to form $PdSO_4$. This is also consistent with the findings of Lampert et al. [81] based on fixed bed and monolith scale experiments. According to Lampert et al. [81], Pd on a sulfating (γ-Al_2O_3) support deactivates more slowly than a non-sulfating (SiO_2) support. The slower deactivation is due to a reservoir type of action of the sulfating support to take SO_2/SO_3. On the other hand, PdO deactivation is faster on a non-sulfating support due to the inability of the support to take SO_2/SO_3 leaving PdO as the only target. Furthermore, they suggested the formation of PdO-SO_3 complex for the decreased activity of the catalyst. Mowrey and McCormick [87] studied PdO sulfation with and without support and suggested that the sulfation was faster in

the absence of a support. Their XPS and FTIR studies showed sulfation of the PdO surface layer and activity loss for methane oxidation.

$$\mathrm{Pd^o} + \frac{1}{2}\mathrm{O_2} \rightarrow \mathrm{PdO} \tag{4.6}$$

$$\mathrm{PdO} + \mathrm{SO_2} \rightarrow \mathrm{Pd^o_{(surface)}} + \mathrm{SO_3} \tag{4.7}$$

$$\mathrm{PdO_{(interior)}} + \mathrm{Pd^o_{(surface)}} \rightarrow \mathrm{Pd^o_{(interior)}} + \mathrm{PdO_{(surface)}} \tag{4.8}$$

4.4 Kinetic Modeling for SO_2-Based Deactivation

Kinetic modeling of sulfur interactions with Pt has received increased attention over the last decade or so [239, 240, 259–262], mostly for Pt-based LNT/NSR applications. [261, 262] Nonetheless, the findings specific to Pt could be relevant for understanding the DOC-SO_x interactions. Olsson et al. [261] developed a global kinetic model for LNT deactivation due to sulfur, which consists of interaction of SO_2 (poisoning and regeneration) on two types of sites, namely, Barium (Ba) and Al_2O_3. For both types of sites, the kinetic model contained two steps, namely, adsorption/binding of SO2 and subsequent oxidation. Furthermore, the model also contained steps for the formation of sulfates on both types of sites during the lean phase and regeneration in the presence of hydrogen. The authors suggested that sulfur poisoning occurs on both types of sites (Ba and Al_2O_3), consistent with the observations by Matsumoto et al. [263]. As all alumina sites are not covered by NO_x, SO_2 adsorption is possible. Similarly, Dowdy *et al.* [262] developed a global mean field kinetic model for SO_2 interaction with NSR (Pt/BaO/Al_2O_3 and BaO/Al_2O_3), which consists of SO_2 storage on NO_x storage sites,

SO_2 storage on bulk sites, SO_2 oxidation, SO_2 interaction with Pt in the presence of H_2, and oxidation of accumulated sulfur compounds on Pt by NO_2. The model is able to predict the decrease in NO_x storage performance due to sulfur accumulation and accumulation of bulk sulfates in $Pt/BaO/Al_2O_3$ after exposure of SO_2 and oxygen. Except for a few studies of sulfur interactions with NO_x reduction/storage catalyst discussed above, details of sulfation kinetics are not available; and therefore, there is an urgent need to understand the complex nature of sulfation kinetics. Along these lines, next we briefly mention the main gaps and challenges in the understanding of DOC-SO_x interactions.

4.5 Microkinetic Modeling for Emissions and SO_2 Oxidation on Pt

In this section, we present a new microkinetic model for SO_2 oxidation on Pt to address the first challenge mentioned in the previous section. It mainly focuses on he development, validation, and analysis of the microkinetic model for SO_2 oxidation on Pt.

4.5.1 Approach for Kinetic Model Development

The overall approach for kinetic model development of SO_2 oxidation on Pt-DOC consists of three major steps, namely, (i) estimation/extraction of kinetic parameters in the surface reaction mechanism, (ii) performance and analysis of the microkinetic model, and (iii) additional validation. In a typical diesel engine exhaust with high O_2 concentration, the primary reaction for SO_2 is its oxidation to SO_3; however, some additional reactions between S and SO_x species are also considered in the reaction mechanism. Based on the information for possible reaction intermediates, pathways, and final products, we have considered 24 irreversible (12 reversible)

catalytic reactions (see Table 4.1) and five surface (adsorbed) species (O^*, S^*, SO^*, $SO_2{}^*$, and $SO_3{}^*$). The overall approach used in microkinetic modeling has some limitations associated with the reaction mechanism, uncertainty in the kinetic parameters, as well as catalyst and reactor modeling, which have been discussed in our earlier work. [264]

Table 4.1 Surface reaction mechanism for SO_2 oxidation on Pt. * indicates an empty (vacant) site, whereas superscript * indicates an adsorbed species. Activation energies in the last column are reported at 300 K; the functional dependence on coverage and temperature originates from Equation 2.1 in the text. $\Delta T = T - T_o$, where T_o is taken as 300 K. Activation energies are computed on-the-fly using the UBI-QEP formalism, as the surface coverages changes in the simulations. Bond index represents the position of the transition state along the reaction co-ordinate. It ranges between 0 (transition state similar to reactants) to 1 (transition state similar to products). Bond index is also used to compute the activation energies according to the UBI-QEP formalism. Additional calculation details are presented in the supplementary material of our earlier work on emissions oxidation on Pt. [264] Shaded reactions in the second column are the least important ones for typical DOC conditions, and can be ignored during the reactor simulations.

No.	**Reactions**	**Bond index (BI) [unitless]**	**Sticking coefficient [unitless] or Pre exponential factor [s^{-1}]**	**Activation energy at 300 K [kcal/mol]**
	Oxygen adsorption/desorption			
R_1	$O + * \rightarrow O^*$	0.5	1	0.0
R_2	$O^* \rightarrow O + *$	0.5	1×10^{13}	86 - 13.3θ_O - 1.5RΔT[173]
R_3	$O_2 + 2* \rightarrow 2O^*$	0.5	0.05[151, 217]	0.0
R_4	$2O^* \rightarrow O_2 + 2*$	0.5	1×10^{13}	52.9 - 26.6θ_O + f(T)
	SO_x adsorption/desorption			
R_5	$S + * \rightarrow S^*$	0.5	1	0.0
R_6	$S^* \rightarrow S + *$	0.5	1×10^{13}	119.53 - 1.5RΔT[265]

R_7	$SO + * \rightarrow SO^*$	0.5	1	0.0
R_8	$SO^* \rightarrow SO + *$	0.5	1×10^{13}	70.99 - 2RΔT[265]
R_9	$SO_2 + * \rightarrow SO_2^*$	0.5	0.5	0.0
R_10	$SO_2^* \rightarrow SO_2 + *$	0.5	1×10^{16}	30.98 - 2.5RΔT[265]
R_{11}	$SO_3 + * \rightarrow SO_3^*$	0.5	1	0.0
R_{12}	$SO_3^* \rightarrow SO_3 + *$	0.5	1×10^{13}	36.01- 2.5RΔT[265]
	SO_x oxidation/reduction			
R_{13}	$SO_3^* + * \rightarrow SO_2^* + O^*$	0.95[a]	1×10^{11}	23.7 + f(θ_O,T)
R_{14}	$SO_2^* + O^* \rightarrow SO_3^* + *$	0.95[a]	2×10^{12}[b]	21.5 + f(θ_O,T)
R_{15}	$SO_2^* + * \rightarrow SO^* + O^*$	0.5	1×10^{11}	22.3 + f(θ_O,T)
R_{16}	$SO^* + O^* \rightarrow SO_2^* + *$	0.5	1×10^{11}	16.6 + f(θ_O,T)
R_{17}	$SO^* + * \rightarrow S^* + O^*$	0.5	1×10^{11}	20.0 + f(θ_O,T)
R_{18}	$S^* + O^* \rightarrow SO^* + *$	0.5	1×10^{11}	30.0 + f(θ_O,T)
R_{19}	$2SO_2^* \rightarrow SO^* + SO_3^*$	0.5	1×10^{11}	13.7 + f(T)
R_{20}	$SO^* + SO_3^* \rightarrow 2SO_2^* + *$	0.5	1×10^{11}	10.2 + f(T)
R_{21}	$S^* + SO_2^* \rightarrow 2SO^*$	0.5	1×10^{11}	25.6 + f(T)
R_{22}	$2SO^* \rightarrow S^* + SO_2^*$	0.5	1×10^{11}	9.9 + f(T)
R_{23}	$SO^* + SO_2^* \rightarrow S^* + SO_3^*$	0.5	1×10^{11}	7.7 + f(T)
R_{24}	$S^* + SO_3^* \rightarrow SO^* + SO_2^*$	0.5	1×10^{11}	19.9 + f(T)

4.5.2 Kinetic Parameters for SO_2 Oxidation Mechanism

Kinetic parameters such as species binding energies (Q) are taken from literature experimental and/or DFT data, [151, 239, 240, 246, 259, 260] whereas the reaction activation energies are calculated using the semi-empirical Unity Bond Index-Quadratic Exponential Potential (UBI-QEP) method [107, 108]. Binding energies are coverage and temperature dependent.

[a]Modified from the initial value of 0.5 to improve the agreement with experimental data.
[b]Modified from the initial value of 10^{11} s^{-1} to improve the agreement with experimental data.

Coverage dependent parameters (adsorbate interactions) are taken from the literature. [173] The temperature dependence is derived from the statistical mechanics based calculations for degrees of freedom lost/gained upon adsorption on the catalyst surface. [101] Coverage and temperature dependent activation energies are calculated on-the-fly using the UBI-QEP method. Sticking coefficients for O_2 and SO_2 are taken from the literature, [151, 217, 246] whereas those for the other species are assumed to be unity. Initial values of pre-exponential factors (A) are taken from Transition State Theory (TST) estimates, which include $10^{13}s^{-1}$ and $10^{11}s^{-1}$ for desorption and the Langmuir-Hinshelwood (L-H) type surface reactions, respectively. [100] For SO_2 desorption, a pre-exponential factor of $1\times10^{16}s^{-1}$ used in this mechanism, which is based on the typically reported high values. [260, 266] A site density of 1.5×10^{15} sites/cm^2 (2.5×10^{-9} mol/cm^2) corresponding to the Pt(111) surface [148] is used in the simulations.

4.5.3 Mechanism Performance and Analysis

Steady state isothermal PFR simulations were carried out using the SO_2 oxidation mechanism to compare its SO_2 conversion performance against experiments conducted with Pt/SiO_2 coated monolith catalysts. The GRI Mech 3.0 gas phase reaction mechanism [109] was used to account for the gas phase chemistry. Transient simulations were performed at the reactor inlet to get the initial surface species coverages. The resulting set of differential and algebraic (DAE) equations were solved using the DDASPK solver. [110]

Figure 4.1 shows that the SO_2 oxidation reaction mechanism captures the experimental data fairly well over the entire temperature range. At high temperatures, the experimental data are limited by SO_2 oxidation equilibrium, which is well captured by our simulations. Only two parameters were adjusted to capture the experimental results. These include (i) pre-exponential of reaction R_{14} ($SO_2{}^* + O^* \rightarrow SO_3{}^* + *$), which was modified to 2×10^{12} s^{-1} (starting from 1×10^{12} s^{-1}), and (ii) bond index of reaction pair R_{13}-R_{14} ($SO_3{}^* + * \leftrightarrow SO_2{}^* + O^*$), which

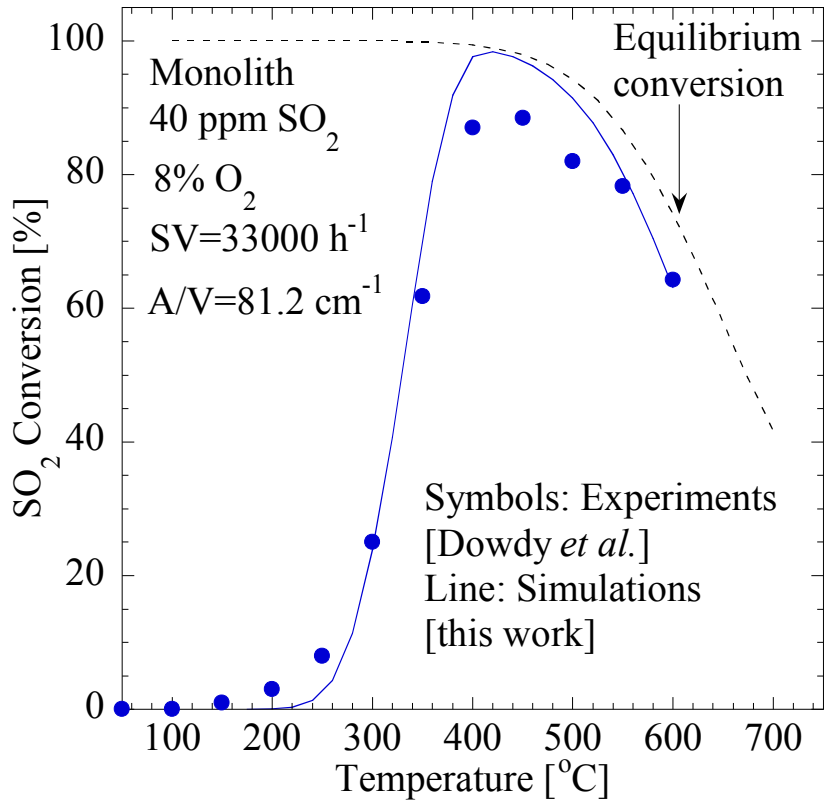

Fig. 4.1 Performance of the microkinetic model for SO_2 oxidation on Pt. Symbols represent experimental data; solid lines represent our simulations; and dashed lines represent the equilibrium calculations using GASEQ software. [230] Operating conditions [262]: Pt/SiO_2 monolith; feed of 40 ppm SO_2, 8% O_2, and ~92% N_2; space velocity of 33,000 h^{-1}; and catalyst area per unit reactor volume of 81.2 cm^{-1}. Simulations are in close agreement with the experimental data.

was modified to 0.95 (starting from 0.5). The bond index modification implemented here is similar to previous work for CO oxidation reaction. [103]

The reaction pair R_{13}-R_{14} (SO_3^* + * $\leftrightarrow$ SO_2* + O^*) was identified as the most important reaction based on sensitivity analysis. The normalized sensitivity coefficient is defined as dlnR/dlnP (i.e., (dR/dP)$\times$(P/R)), where dP is the change in parameter P (pre-exponential factors) and dR is the change in model response R (conversion). Surface reactions with the highest normalized sensitivity coefficients are shown in Figure 4.2. At low temperature (250 $^\circ$C), SO_3 adsorption/desorption pair R_{11}-R_{12} showed the largest sensitivity, but the conversion was very low at this temperature. At 350 $^\circ$C, SO_2 oxidation step R_{13}-R_{14} showed the highest sensitivity. As moderate levels of SO_2 conversion were observed around 350 $^\circ$C, kinetic parameters for the reaction pair R_{13}-R_{14} were adjusted to capture the experimental data in Figure 4.1. At even higher temperatures (e.g., 450 $^\circ$C), as the data become equilibrium limited, none of the the reaction pre-exponentials were sensitive as expected.

Simulated surface coverages at the reactor exit (which are also very close to the average coverage over the reactor length) are shown in Figure 4.3a, whereas Figures 4.3b and 4.3c show the axial coverage profiles of dominant surface species at two representative temperatures: low (350 $^\circ$C) and high (550 $^\circ$C), respectively. At most of the conditions (> 300 $^\circ$C), O^* is the most abundant reaction intermediate (MARI), which is expected given its high concentration in the feed (and also in a typical diesel engine exhaust). The high coverage of O^* also justifies the inclusion of repulsive adsorbate?adsorbate (O^*-O^*) interactions (coverage effects) in our reaction mechanism. At low temperature, the simulations predict some SO_3^* coverage, but negligible coverage of SO_2^*, SO^*, and S^*. This is because SO_2^* is oxidized to SO_3^* even at low temperature, but it is difficult to desorb SO_3^*. At high temperature, SO_3^* desorption becomes easier, resulting in more vacancies and less SO_3^* coverage. Finally, above 500 $^\circ$C, even oxygen also starts to desorb resulting in an increase in vacancies.

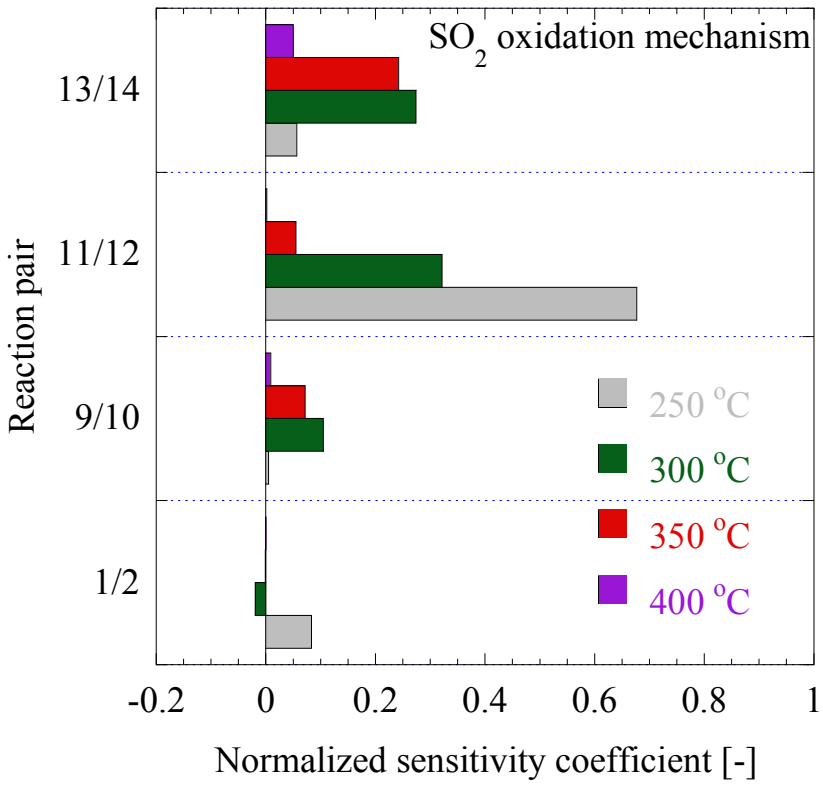

Fig. 4.2 Sensitivity analysis for SO_2 oxidation model responses with respect to the pre-exponential factor pairs in the surface reaction mechanism. Pre-exponentials are modified pairwise without perturbing the equilibrium constant. Only those reaction pairs with the highest normalized sensitivity coefficients (dlnR/dlnP, i.e., (dR/dP)×(P/R)) are shown here. The sensitivity coefficients above 400 °C are negligible (not shown here). Operating conditions are the same as in Figure 4.1.

The reaction path analysis (RPA) is shown in Figure 4.4 at two representative temperatures: low (350 °C, Figure 4.4a) and high (450 °C, Figure 4.4b). At low temperature, SO_2* reacts with oxygen via reaction R_{14}: SO_2* + O* × SO_3* + * to form SO_3*, which subsequently desorbs, resulting in SO_2 conversion (oxidation). This RPA also aligns with the sensitivity analysis in Figure 4.2 and the coverage profiles in Figure 4.3. This observation, albeit on Pt, is also consistent with the experimental results reported by Luckas et al (156) in their HR-XPS studies of SO_2 oxidation on Pd(100) surface. At high temperature, SO_3 readsorbs on the surface, and decomposes via the reverse reaction R_{13}: SO_3* + * → SO_2* + O*, which is consistent with the equilibrium limitations. SO_2* on the surface then follows two separate reaction pathways. The primary pathway (∼94%) is desorption to gas phase SO_2 via reaction R_{10}, whereas the secondary pathway (∼6%) is decomposition to SO* and O* via reaction R_{15}. However, instead of desorbing, SO* further reacts with SO_3* to regenerate SO_2* via reaction R_{20}: SO* + SO_3* → 2SO_2*. Thus, the secondary minor pathway is not important in terms of the overall reaction of SO_3 decomposition at high temperature.

4.5.4 Mechanism Validation

Despite showing good agreement with the monolith experiments, two kinetic parameters in the surface reaction mechanism had to be adjusted to improve the agreement with the experimental data. Therefore, to assess the fidelity of the surface reaction mechanism, we carried out further validation against additional SO_2 oxidation experimental data on Pt/TiO_2 fixed bed, [86] without any further modification of kinetic parameters. Predictions using the microkinetic model are shown in Figure 15, along with the experimental data. This set of experimental data is not very relevant to the DOC operating conditions, as the feed contained an extremely high SO_2 concentration (11%) instead of few ppm, along with an extremely high space velocity.

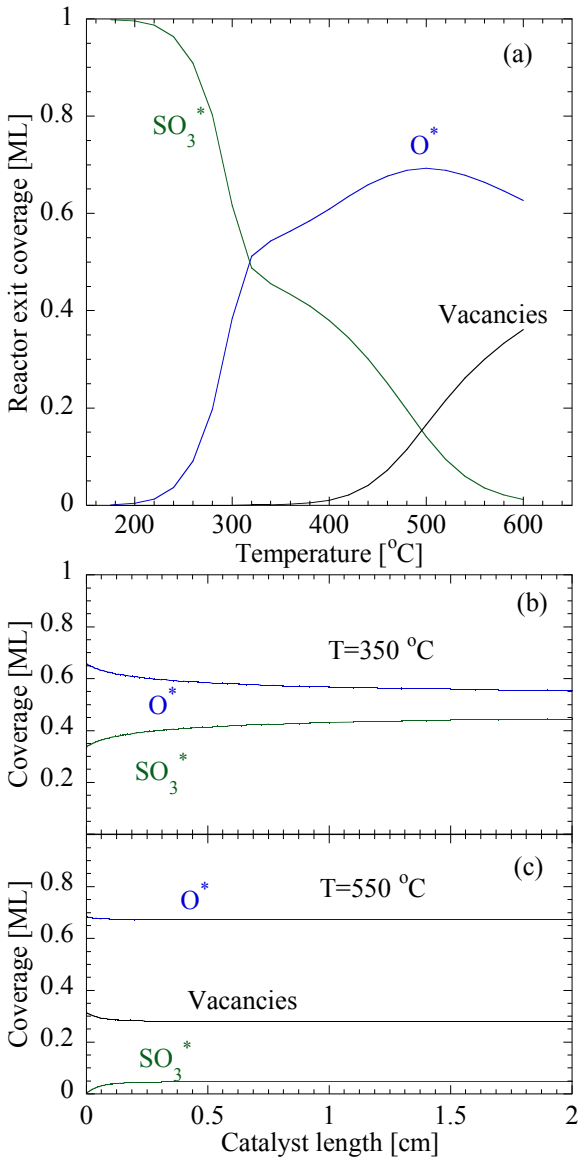

Fig. 4.3 (a) Simulated steady state coverage profiles at reactor exit, (b) simulated axial coverage profiles at 350 °C, and (c) simulated axial coverage profiles at 550 °C. Operating conditions are the same as in Figure 4.1.

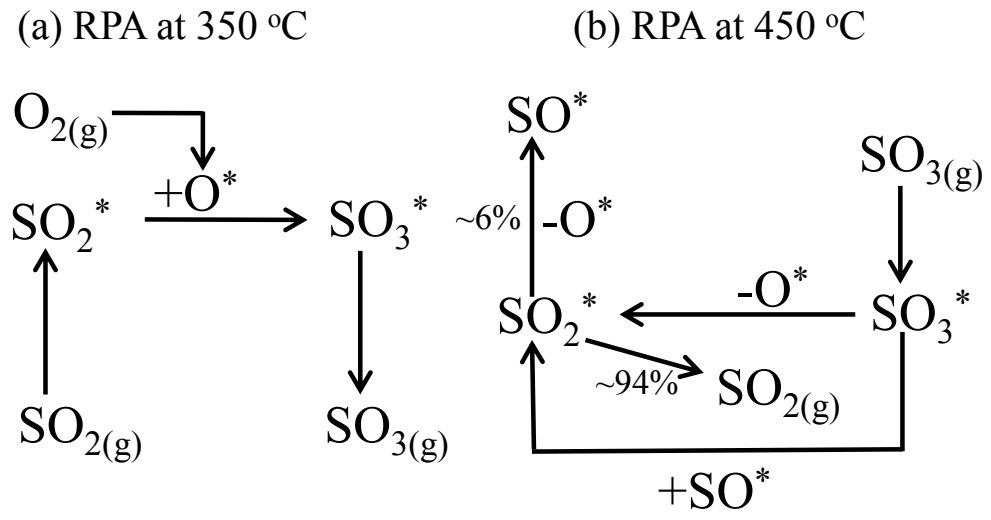

Fig. 4.4 Reaction path analysis at 350 °C (panel a) and 450 °C (panel b) using our microkinetic model for SO_2 oxidation on Pt. Operating conditions are the same as Figure 4.1.

Nonetheless, a fair agreement with experimental data demonstrates the robustness of our SO_2 oxidation surface reaction mechanism on Pt, even under extreme operating conditions.

4.5.5 Mechanism Reduction

Based on the sensitivity analysis, coverage profiles, and RPA, a preliminary mechanism reduction is carried out. Adsorption/desorption of some radicals (O^*, S^*, SO^*) and some surface reactions involving SO^* are not important (shaded reactions in Table 4.1); hence, they can be removed from the mechanism without affecting the simulation results. Finally, a 12-step SO_2 oxidation model is proposed after the mechanism reduction.

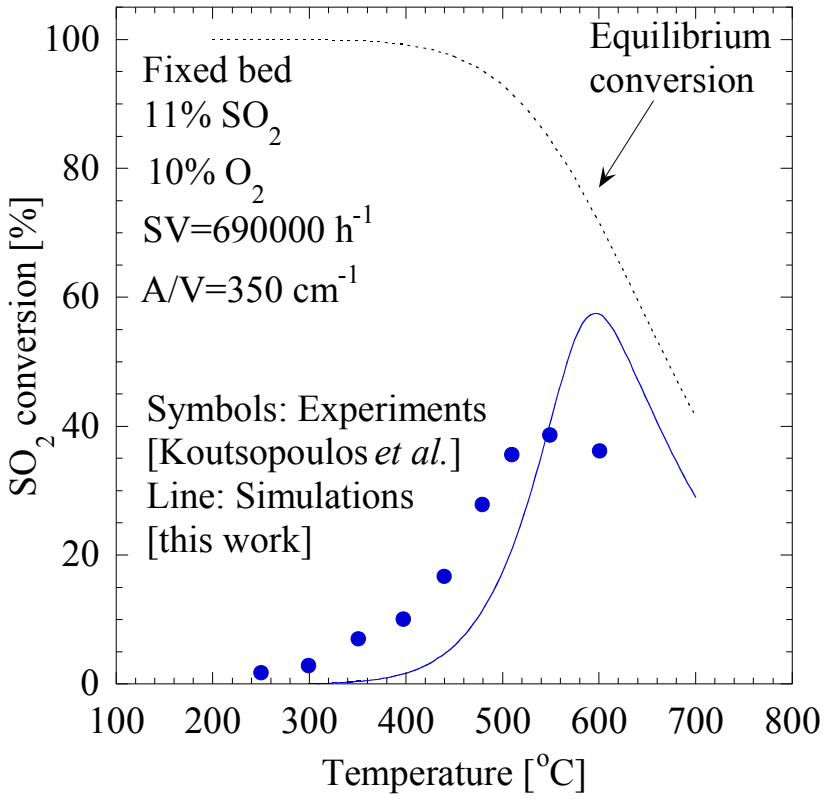

Fig. 4.5 Validation of the microkinetic model for SO_2 oxidation on Pt/TiO_2 fixed bed. Operating conditions [86]: Pt/TiO_2 fixed bed, feed of 11% SO_2, 10% O_2, and 79% N_2, space velocity 690,000 h^{-1}, and catalyst area per unit reactor volume of 350 cm^{-1}

4.6 Conclusions

Sulfation of DOC is a challenging and complex phenomena. Very limited information of this complex chemistry is available in the literature. Details of the SO_x interaction mechanism and kinetics on bimetallic DOC are not available. Similarly, SO_x interaction with supports adds more challenges to the chemistry and kinetics. Therefore, a complete understanding of the sulfation mechanism and kinetics is necessary to predict the DOC deactivation and design sulfur resistant materials, thereby ultimately reducing the cost of operation. Here, we have extended the recently developed microkinetic model for five major emissions oxidation chemistries on Pt to include the SO_2 oxidation chemistry on Pt. The developed mechanism correctly captures experimental data for SO_2 oxidation relevant to DOC operating conditions. This is the first step towards understanding SOx interactions with Pt-Pd/alumina DOCs. In the future, understanding the sulfation mechanism using various approaches discussed here can be crucial to design sulfur resistant catalysts and to make the DOC an efficient and economical component of the diesel engine aftertreatment system.

Chapter 5

SO_x and H_2O Interactions on Pt

5.1 Introduction

Sulfuric acid (H_2SO_4) formation in the diesel engine exhaust is a highly favored phenomenon due to interactions of sulfur oxides (mainly SO_3, in $\sim$1 ppm level due to currently used ultra-low sulfur diesel) and water vapor (concentration up to $\sim$7%) in the engine exhaust. [9, 31, 32] Sulfur in the diesel fuel and lubricants is oxidized to SO_2 in the engine and further oxidized to SO_3 due to the excess oxygen ($\sim$12%) in the exhaust. Once formed, sulfuric acid creates tremendous challenge to the noble metal (Pt and /or Pd) based diesel oxidation catalysts (DOC), increases particulate formation in the engine exhaust and contributes to toxic acid rain formation. [15, 97] Therefore, a complete understanding of the reaction kinetics and pathways of H_2SO_4 formation is required for a better design of the emission aftertreatment catalysts. The overall reaction of H_2SO_4 formation can be given as:

$$SO_3 + H_2O \rightarrow H_2SO_4 \qquad \Delta H = -90 \mathrm{kj\,mol}^{-1} \tag{5.1}$$

Earlier experimental studies have shown that the reaction of SO_3 and H_2O is the primary step for H_2SO_4 formation. [266–269] Phillips et al. suggested the existence of a SO_3-H_2O complex in the gas phase using microwave spectroscopy. [267] Further, the reaction kinetics was reported to be a complex one with rate of the reaction influenced by the H_2O concentration. [268] DFT based studies suggested a decrease in the activation energy for SO_3 and H_2O reaction with an increase in water coverage on the surface. On the other hand, in an ab-initio method based electro-oxidation study of SO_2, Kriek et al. [270] proposed H_2SO_4 formation through an HSO_3 intermediate ($SO_2 + OH \rightarrow HSO_3$) in addition to the SO_3 pathway ($SO_2 + O \rightarrow SO_3$). Prior kinetic modeling attempts have been limited to the oxidation mechanism of SO_2 only to form SO_3. [260, 266, 269] Thus, a complete reaction mechanism and pathways are not fully understood when a complex reaction mechanism involving H_2O and oxygen and sulfur oxides.

In this chapter, we develop a microkinetic model for H_2SO_4 formation on Pt surface with oxidation and H_2O interaction of sulfur oxides (SO_2 and SO_3). We extend our previously developed SO_2 oxidation microkinetic model [31, 271] on Pt to include SO_3 and H_2O interactions and develop a detailed understanding of the reaction pathways en route to the sulfuric acid formation. Furthermore, we analyze the HSO_3 route of H_2SO_4 formation proposed by Kriek et al. [270] Overall, our model predictions show good agreement with the results from experiments operated under practically relevant DOC conditions such as low emissions concentrations (ppm level), high flow rate, and high oxygen and water concentrations.

5.2 Microkinetic Model Development

The reduced surface reaction mechanism for SO_2 oxidation from our previous work was adapted as a starting point. [31, 271] We further extended the reaction mechanism to include the H_2O interactions with SO_x to form H_2SO_4. Based on the information from literature, [270, 272–274]

one can potentially have two paths involving SO_3^* or HSO_3^* intermediate as shown below. Here, * indicates adsorbed species.

PATH A:

$$SO_2^* + O^* \leftrightarrow SO_3^* + * \tag{5.2}$$

$$SO_3^* + H_2O^* \leftrightarrow H_2SO_4^* + * \tag{5.3}$$

PATH B:

$$SO_2^* + OH^* \leftrightarrow HSO_3^* + * \tag{5.4}$$

$$HSO_3^* + OH^* \leftrightarrow H_2SO_4^* + * \tag{5.5}$$

Initially, we considered the following 7 surface species in this mechanism: SO_2^*, SO_3^*, O^*, H_2O^*, OH^*, HSO_3^* and $H_2SO_4^*$. Based on our previous study, [31] surface species S^* and SO^* and their reactions were deemed insignificant. Hence, the reactions involving those surface species are not taken into account here. We considered adsorption/desorption steps of gas phase species (i.e., O_2, SO_2, SO_3, H_2O, and H_2SO_4) and surface reactions for SO_2 oxidation and SO_3 hydration. Our analysis based on the Unity Bond Index-Quadratic Exponential Potential (UBI-QEP)[107] method (see Appendix B) showed that the HSO_3 formation ($SO_2^* + OH^* \rightarrow HSO_3^* + *$) activation barrier is too high ($E_a = \sim 33$ kcal/mol at 300 K) to compete with SO_3 formation ($SO_2^* + O^* \rightarrow SO_3^* + *$, $E_a = \sim 22$ kcal/mol) pathway in the highly oxidizing environment and in the temperature range (< 400 °C) of interest in this study. Thus, inclusion of this pathway has no effect on the mechanism performance for the temperature range and emissions

exhaust conditions considered here. Furthermore, no evidence of formation of HSO_3 and H_2 was reported during the experiments conducted under practically relevant conditions.[275] Similarly, our analysis show that the reaction for water dissociation using oxygen (H_2O^* + $O^* \rightarrow 2OH^*$) also has no effect on the overall model performance even though the reaction is feasible (activation energy, E_a = 9.4 kcal/mol at 300 K [264]) in the temperature range studied here. Therefore, these reactions are not included in our final proposed mechanism. Overall, the reactions considered in this mechanism are chosen based on the reactants, possible intermediates, products, and the experimentally observed/proposed [268, 270] pathways. The proposed final reaction mechanism consists of 14 elementary steps (7 reversible) reactions as listed in Table 5.1.

Parameter estimation was performed using the methodology discussed in Chapter 2 and in previous chapters. Here,the binding energies of HSO_3 and H_2SO_4 on Pt (111) were estimated in this work using DFT implemented in VASP (see Appendix 1 for details). Steady state isothermal plug flow reactor (PFR) modeling was used to simulate the monolith scale experiments conducted in various operating conditions. Isothermal assumption is based on the very small amount of heat generated during the oxidation of very dilute concentration levels of the emissions (ppm levels) in the exhaust. Details of PFR modeling is discussed in Chapter 2.

5.3 Model Performance

It is expected that the microkinetic model should perform well against the experiments operated under practically relevant conditions such as atmospheric pressure, dilute emissions concentrations (ppm level), and short residence times. However, some minor parameter tuning is expected given the pressure gap (UHV vs. atmospheric), materials gap (single crystals vs. polycrystalline and supported catalysts), and uncertainty/error associated with the experimental

Table 5.1 Elementary step reaction mechanism considered to study SO_2 oxidation and H_2SO_4 formation on Pt[a]

No.	Reactions	Bond index[b] (BI) [unitless]	Sticking coefficient [unitless] or Pre exponential factor [s^{-1}]	Activation energy at 300 K [kcal/mol]
	Adsorption/desorption			
R_1	$O_2 + 2* \rightarrow 2O^*$	0.5	0.05 [151, 217]	0.0
R_2	$2O^* \rightarrow O_2 + 2*$	0.5	1×10^{13}	52.9 - 26.6θ_O + f(T)
R_3	$SO_2 + * \rightarrow SO_2{}^*$	0.5	0.5	0.0
R_4	$SO_2{}^* \rightarrow SO_2 + *$	0.5	1×10^{16}	29.3 - 2.5RΔT [265]
R_5	$SO_3 + * \rightarrow SO_3{}^*$	0.5	0.5	0.0
R_6	$SO_3{}^* \rightarrow SO_3 + *$	0.5	1×10^{13}	34.2- 2.5RΔT [265]
R_7	$H_2SO_4 + * \rightarrow H_2SO_3{}^*$	0.5	1	0.0
R_8	$H_2SO_4{}^* \rightarrow H_2SO_4 + *$	0.5	1×10^{13}	2.8- 3.0RΔT
R_9	$H_2O + * \rightarrow H_2O^*$	0.5	1	0.0
R_{10}	$H_2O^* \rightarrow H_2O + *$	0.5	1×10^{13}	10.27- 2.5RΔT
	SO_x oxidation			
R_{11}	$SO_3{}^* + * \rightarrow SO_2{}^* + O^*$	0.97	1.2×10^{11}	23.2 + f(θ_O,T)
R_{12}	$SO_2{}^* + O^* \rightarrow SO_3{}^* + *$	0.97	5×10^{12}	21.3 + f(θ_O,T)
	H_2O reactions			
R_{13}	$SO_3{}^* + H_2O^* \rightarrow H_2SO_4{}^* + *$	0.5	1×10^{11}	0.0 + f(T)
R_{14}	$H_2SO_4{}^* + * \rightarrow SO_3{}^* + H_2O^*$	0.5	1×10^{11}	19.1 + f(T)

[a] θ_O represents the oxygen surface coverage; * indicates a vacant site; whereas the superscript * indicates an adsorbed species. The functional form 'f' in the activation energy includes coverage and temperature dependence. Coverage dependence originates from the use of UBI-QEP for the estimation of activation energies; whereas the temperature dependence is derived from the statistical mechanics based calculations for degrees of freedom lost/gained upon adsorption. $\Delta T = T - T_0$, where T_0 is taken as 300 K.

[b] Bond index represents the position of the transition state along the reaction coordinate, which is also used to compute the activation energies in the UBI-QEP formalism. It is defined for a reaction pair in the forward direction only. It ranges between 0 and 1, with a typical estimate of 0.5.

data. Here, monolith scale experimental data [269, 275] reported in the literature are used to check the microkinetic model performance. Specifically, monolith scale experiments with 3 different types of reactor feed conditions are used: (a) SO_2 and O_2, (b) SO_2, O_2, and SO_3, and (c) SO_2, O_2, and H_2O. Details of the mechanism performance and analysis of reaction paths are presented in next section.

5.3.1 SO_2 Oxidation

Our microkinetic model was validated against experiments [275] conducted using Pt/Al_2O_3 monolith under isothermal and steady state reactor conditions. The model predictions, surface species coverages and reaction path analysis (RPA) at different temperatures are shown in Figure 5.1. Overall, the model captures the experimental data very well over the entire range of temperature considered. At elevated temperature regions (> 350 °C), the conversion of SO_2 decreases (panel a, Figure 5.1), due to equilibrium limited conditions, consistent with the decrease in calculated equilibrium conversion.

Simulated coverage profiles at the reactor exit over a temperature range of 200-500 °C are shown in panel b, Figure 5.1. While SO_3^* coverage is dominant only at low temperature, O^* is the most abundant surface species over wide temperature range (as expected due to high concentration of O_2 in the diesel engine exhaust). In panels c and d in Figure 5.1, we show low temperature (320 °C) and high temperature (520 °C) surface coverage profiles over the reactor length, respectively. In both temperature cases, O^* is the dominant surface species which justifies the inclusion of repulsive adsorbate?adsorbate (O^*-O^*) interactions (coverage effects) in our reaction mechanism. RPA is shown (panel c, Figure 5.1) for two representative temperatures (i.e., 320 oC and 520 oC). It shows that the oxidation of SO_2 (R_{12}, $SO_2^* + O^* \rightarrow SO_3^* + *$) occurs to form SO_3^* on the surface at low temperature which desorbs afterwards.

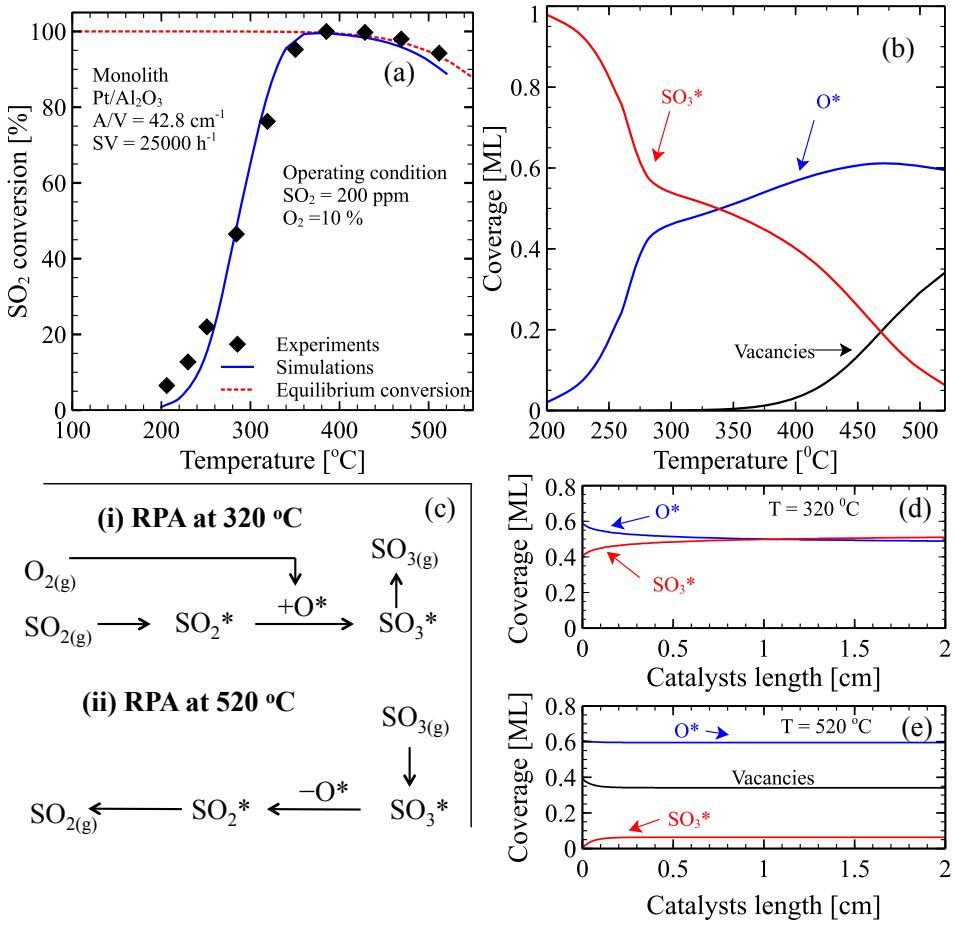

Fig. 5.1 Performance (panel a) and analysis (panels b-e) of the microkinetic model for SO_2 oxidation on Pt/Al_2O_3 monolith. Symbols represent the experimental data, whereas lines represent our simulations. Panel a shows the experimental data, model performance, and the calculated equilibrium conversion profile. Panel b shows the simulated steady state coverage profiles at the reactor exit. Panel c shows the reaction path analysis at 320 °C and 520 °C. Panels d and e show the simulated axial coverage profiles at 320 °C and 520 °C, respectively. Operating conditions: [269, 275] feed of 200 ppm SO_2, 10% O_2, balance N_2; space velocity of 25 000 h^{-1}; Pt loading = 50 g/ft^3 with 6% dispersion; catalyst length = 3.86 cm with a cell density of 325 channels/in^2; and catalyst area per unit reactor volume of 46.8 cm^{-1}; total gas flow rate = 4.6 L/min.

However, SO_3 readsorption and decomposition occurs via reverse reaction (R_{11}, $SO_3^* + * \rightarrow SO_2^* + O^*$), consistent with equilibrium limitations, at higher temperature.

5.3.2 Effect of SO_3 on SO_2 Oxidation

Experimental results suggested that the presence of SO_3 in the feed has negative effect on the oxidation of SO_2, which is accompanied by the increase in apparent activation energy and negative reaction order for SO_3. [269] Due to SO_3 in the feed, the light off temperature of SO_2 oxidation is pushed to higher temperature. Furthermore, SO_2 conversion decreases sharply at the equilibrium-limited region. The phenomenon is well captured by our model as it correctly predicts the experimental conversion profile of SO_2 oxidation in the presence of SO_3 in feed. The model performance against two sets of experimental data [269, 275] (obtained from two different feed concentrations of SO_2 and SO_3) is shown in Figure 5.2 (panel a).

To further evaluate the effect of SO_3 on SO_2 conversion in a highly oxidizing environment, we simulated both experimental data sets without SO_3 in the inlet feed (i.e. hypothetical conditions). The conversion profiles are shown in Figure 5.2 (panel a), as represented by blue and red dotted lines. From the results, we clearly see two distinct features. First, SO_2 concentration has minimal effect on the light off temperature, which is displayed by negligible change in the conversion profiles for 100 ppm (red dotted line) and 149 ppm (blue dotted line) of SO_2 in the feed. Second, the increase in SO_3 concentration results in a large shift in the light off temperature. Furthermore, negative impact on SO_2 conversion was observed in the equilibrium limited region due to presence of SO_3 in the feed.

Panels b and c (Figure 5.2) show the surface coverage profile on the catalysts length at two different temperature scales (at 320 °C and 520 °C). These profiles are very similar to the one without SO_3; however, SO_3^* coverage is slightly higher on the surface for both temperatures and

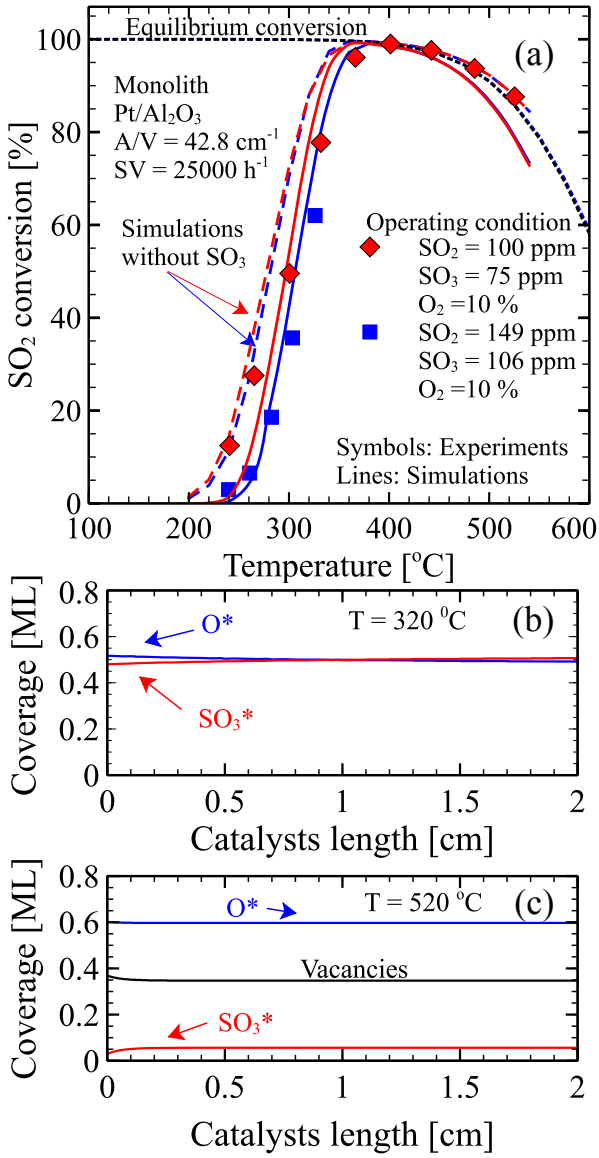

Fig. 5.2 Performance (panel a) and analysis (panels b and c) of the microkinetic model for SO_2 oxidation on Pt/Al_2O_3 monolith. Symbols represent the experimental data, whereas lines represent our simulations. Panel a shows the experimental data, model performance (solid blue and red lines), model simulations without considering SO_3 in the experimental feed compositions (dotted blue and dotted red lines), and the calculated equilibrium conversion profiles. Panels b and c show the simulated axial coverage profiles for the feed composition of 100 ppm SO_2, 75 ppm SO_3, 10% O_2, balance N_2 at 320 °C and 520 °C, respectively. Operating conditions: [269, 275] feed of 100 ppm SO_2, 75 ppm SO_3, 10% O_2, and balance N_2 (red symbols); 149 ppm SO_2, 106 ppm SO_3, 10% O_2, balance N_2 (blue symbols). Reactor and catalysts details are same as in Figure 5.1.

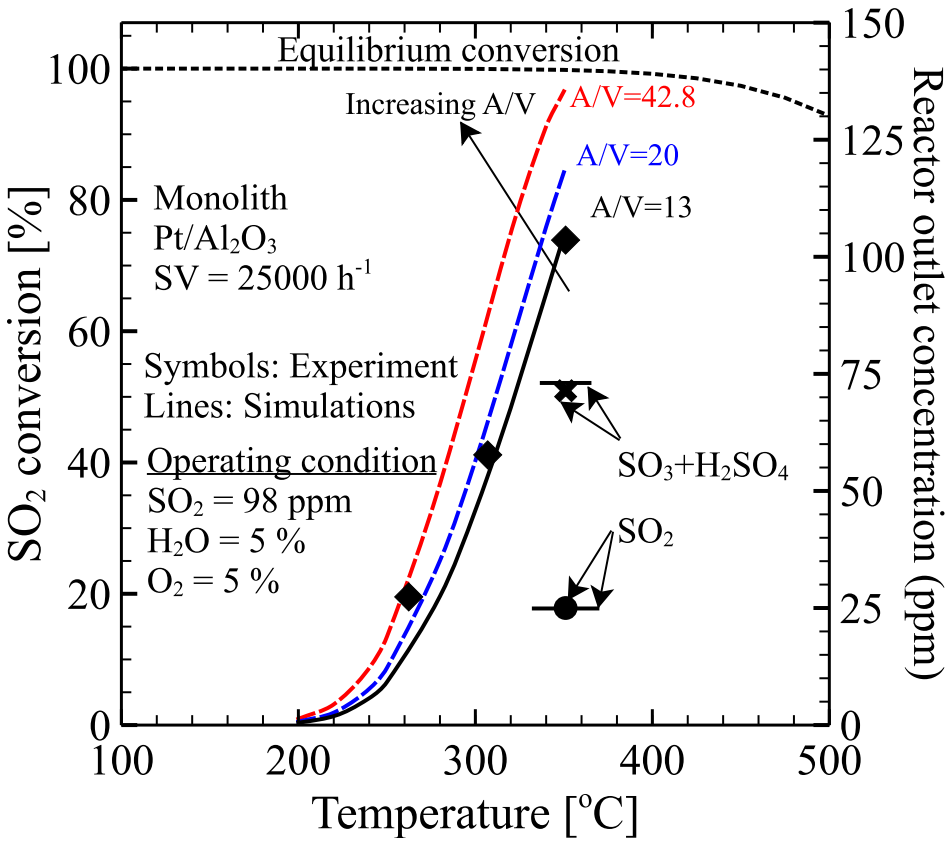

Fig. 5.3 Comparison of the experimental SO_2 conversion and reactor outlet concentrations (at 351 °C) with the predictions of the microkinetic model on Pt/Al_2O_3 monolith. Symbols represent the experimental data, whereas lines represent our simulations. Dotted blue and red lines represent the effect of A/V parameter on the model performance for the prediction of SO_2 conversion data. Experimental data for the reactor outlet concentration of SO_2 and SO_3+H_2SO_4 at 351 °C (symbols) and the model simulated values (horizontal lines) are shown with a y-axis on the right. Operating conditions: [275] feed of 98 ppm SO_2, 5% H_2O, 5% O_2, and balance N_2. Reactor and catalysts details are same as in Figure 5.1.

O^* still remains as the most dominant species on the surface. Overall, the reaction pathways and mechanism remains the same in the presence or absence of SO_3 in the feed.

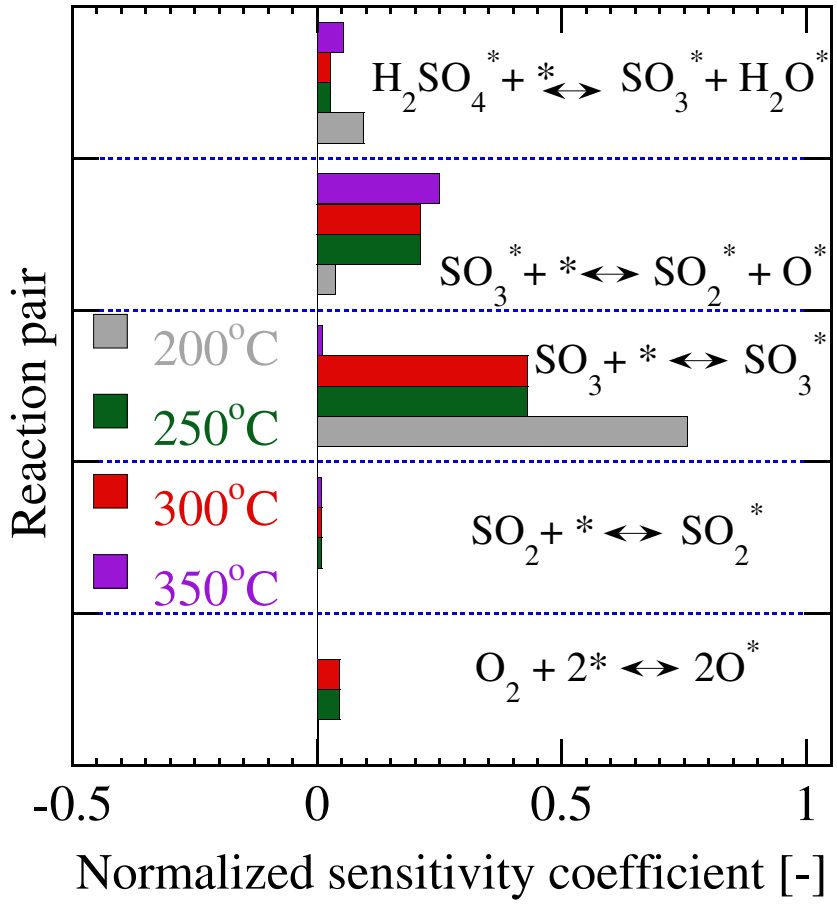

Fig. 5.4 Sensitivity analysis for the microkinetic model responses with respect to the pre-exponential factor pairs in the surface reaction mechanism shown in Table 5.1. Pre-exponentials are modified pairwise without perturbing the equilibrium constant. Only those reaction pairs with the highest normalized sensitivity coefficients [dlnR/dlnP, i.e., (dR/dP)×(P/R)] are shown here. The sensitivity coefficients at four representative temperatures (i.e. 200 °C, 250 °C, 300 °C, and 350 °C) are shown. Sensitivity analysis at the equilibrium-limited regions is not shown here. Operating conditions are the same as in Figure 5.3.

5.3.3 H_2SO_4 Formation

Very limited experimental data are available in the literature for H_2SO_4 formation in the presence of H_2O in engine exhaust conditions due to corrosive and toxic nature of H_2SO_4. Here, we used monolith scale experiments reported by Hamzehlouyan et al. on Pt/Al_2O_3 catalysts. Experimental results showed significant decrease in SO_2 conversion in the presence of H_2O. The decrease in the conversion is also associated with the catalysts poisoning due to H_2SO_4. Our model captures the experimental results; however, with a minor adjustment in the catalyst area per unit volume (A/V) parameter . We also show the simulated conversion profiles using a range of A/V numbers in Figure 5.3. We clearly see the impact of A/V parameters on the SO_2 conversion profile especially at the higher temperature. This observation fits well with the experimental evidence of catalysts active site reduction due to H_2SO_4 poisoning. Furthermore, the plug flow reactor model used here cannot inherently capture any effect due to catalysts poisoning. Thus, the parameter adjustment in our model is reasonable. To further validate the model, we computed the selectivity and compared the model-simulated results against experimentally observed concentrations of the reactants and products as shown in Figure 5.3. Our model captures the reactant (SO_2) concentration and the total product concentration (SO_3 and H_2SO_4) reported at 351 °C. [275]

Next, we looked at the sensitivity of the reaction mechanism. Sensitivity analysis allows us to identify the most sensitive and important reactions. The normalized sensitivity co-efficient is defined as dlnR/dlnP, where dlnP is the change in parameter P (pre-exponential factor) and dlnR is the change in model response R (SO_2 conversion). We performed a pairwise sensitivity analysis by perturbing the pre-exponential factors (of both forward and backward reactions) with same factor. In Figure 5.4, the surface reaction pairs with highest sensitivity coefficients are shown at four different temperatures (range from 200 °C to 350 °C). At low temperature (200 °C), the reaction R_5-R_6 ($SO_3 + * \leftrightarrow SO_3^*$) shows largest sensitivity. At the range of 250

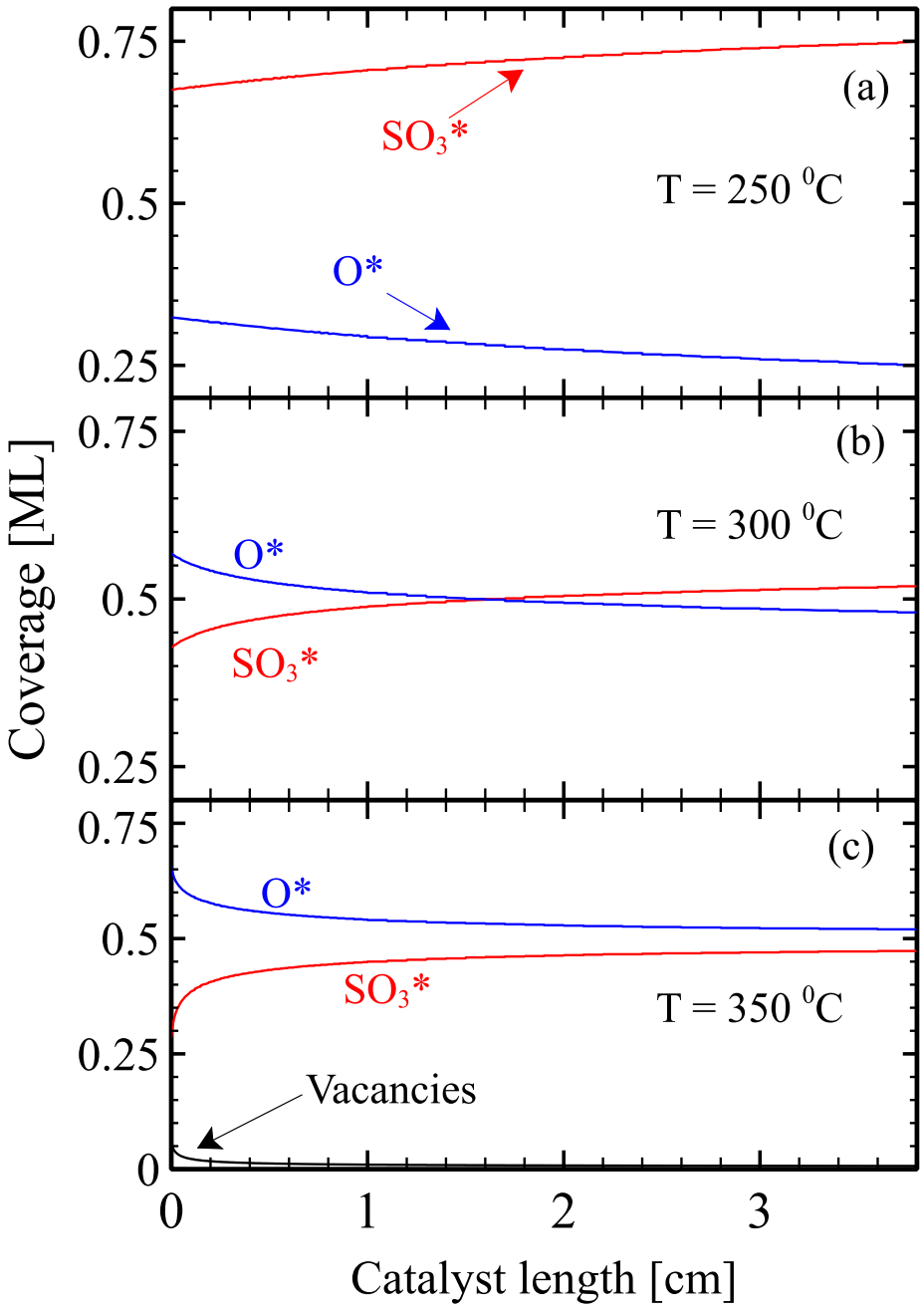

Fig. 5.5 Simulated axial coverage profiles at 250 °C (panel a), 300 °C (panel b), and 350 °C (panel c), respectively. Operating conditions are the same as in Figure 5.3.

°C to 300 °C, reaction pairs R_5-R_6 ($SO_3 + * \leftrightarrow SO_3^*$) and R_{11}-R_{12} ($SO_3^* + * \leftrightarrow SO_2^* + O^*$) show the largest impact on the mechanism. The reaction pair R_{13}-R_{14} ($H_2\,SO_4^* + * \leftrightarrow SO_3^* + H_2\,O^*$) is also one of the important reaction pairs over the range of temperature considered here.

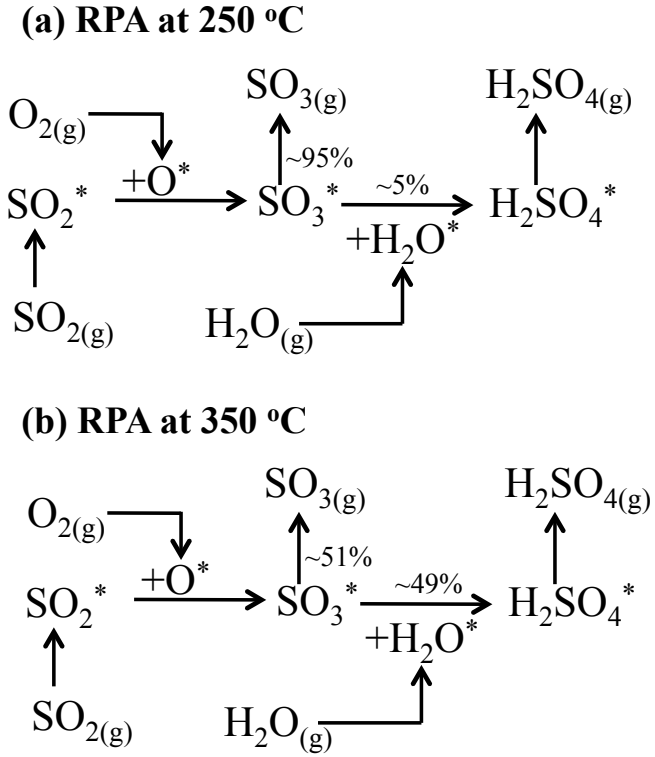

Fig. 5.6 Reaction path analysis at 250 °C (panel a) and 350 °C (panel b) using our microkinetic model for SO_2 oxidation on Pt. Operating conditions are the same as Figure 5.3.

Model simulated surface coverage profiles at three different temperatures (i.e. at 250 °C, 300 °C, and 350 °C) are shown in Figure 5.5 (panels a-c). We observed that the SO_3^* is the most abundant reaction intermediate (MARI) at low temperature (250 °C) which is mainly due to its high sticking coefficient (0.5) compared to that of oxygen (0.05). With the increase in temperature, the SO_3^* coverage gradually decreases while O^* coverage takes over and becomes the MARI. This effect is partly due to the SO_3^* desorption and $H_2SO_4^*$ formation (discussed in

the next paragraph). Furthermore, the binding energy of oxygen is relatively larger than that of SO_3^* which translates to higher temperature desorption phenomena.

Figure 5.6 shows RPA at 250 °C (panel a) and 350 °C (panel b). The lower temperature RPA (at 250 °C) is dominated by the SO_2 oxidation (SO_2^* +O^* $\rightarrow$ SO_3^*+ *) and SO_3 desorption (SO_3^* $\rightarrow$ SO_3+ *) steps. However, the higher temperature RPA (at 350 °C) shows the H_2SO_4 formation (SO_3^* + H_2O^* $\rightarrow$ $H_2SO_4^*$ + *) reaction is one of the major pathway and competing reaction with SO_3 desorption which is also consistent with the sensitivity analysis in Figure 5.4.

5.4 Conclusions

In this chapter, we developed a microkinetic model for H_2SO_4 formation on Pt. The model contains 16 elementary steps (8 reversible pairs) and 5 surface species (i.e. O^*, H_2O^*, SO_2^*, SO_3^*, and $H_2SO_4^*$). Our model captures the available experimental data (from the experiments conducted under realistic DOC conditions such as low emissions concentrations, high oxygen concentrations with presence of water, atmospheric pressure, and high space velocity) and shows good agreement in kinetically and thermodynamically controlled regions. We show the impact of SO_3, consistent with experimental observations, on the SO_2 oxidation light off temperature. Our sensitivity analysis further shows the important reactions in the proposed mechanism. Finally, we show that the interaction of SO_3 and H_2O is the pathway to form H_2SO_4 on the Pt surface.

Chapter 6

SO_x Oxidation Kinetics on Pt(111) and Pd(111)

6.1 Introduction

Sulfur oxides (SO_x) from diesel engine and gas turbine exhaust are detrimental to noble metal (Pt/Pd) based aftertreatment catalysts. [60, 81] For instance, SO_2 can undergo oxidation to SO_3 over the catalyst, and these oxides react with the active catalyst sites, preventing reactant access and modifying the catalyst surface chemistry. [9, 31, 32] More importantly, such interactions lead to the formation of stable sulfates and subsequent deactivation of the catalyst [81, 87]. In addition, reactions of SO_x with steam in the engine exhaust can produce H_2SO_4, which can cause severe catalyst damage. [276] Clearly, fundamental insights on SO_x thermodynamics and kinetics on relevant catalyst surfaces are essential for the development of sulfur-resistant catalysts.

Past work has attempted to uncover the surface chemistry of SO_x on Pt and Pd. [89, 245, 250, 265, 277–280] Experimental studies have confirmed a few stable configurations of SO_2,

and have noted SO_3 and SO_4 formation in the presence of oxygen. [245, 246, 250] Analysis based on the unity bond index-quadratic exponential potential (UBI-QEP) method suggests that SO_2 oxidation, but not decomposition, is favored on various metal surfaces under typical engine exhaust conditions. [107, 281] Available first principles computational studies have also provided critical insights concerning SO_2 binding and oxidation, although predominantly on Pt. [265, 282, 283]

In this chapter, we aim to develop a comprehensive understanding of SO_x ($x = 0 - 4$) chemistry (adsorption/desorption and oxidation) on Pt(111) and Pd(111) surfaces using density functional theory (DFT) calculations coupled with microkinetic modeling. Firstly, a detailed investigation was performed to uncover the binding patterns, coverage dependence of binding strength, charge transfer and redistribution, and orbital interactions upon SO_x adsorption. Secondly, we analyzed several possible reaction pathways and estimated kinetic parameters, including activation barriers and pre-exponential factors of SO_2 and SO_3 oxidation on both metal surfaces. Finally, the kinetic parameters computed using DFT were fed into a microkinetic model developed earlier [31] to predict SO_2 conversion as a function of temperature under several different operating conditions. The predicted conversion compares favorably with available experimental data. [275] The present work thus significantly extends insights that have emerged from past experimental and computational work, and provides a quantitative scheme for the prediction of the performance of catalysts with respect of SO_x chemistry.

6.2 Methods

Our spin-polarized first principles DFT calculations were performed using the Vienna *ab initio* simulation package (VASP), [113] utilizing the Perdew–Burke–Ernzerhof (PBE) [114] functional, and the projector augmented wave (PAW) [284] frozen–core potentials with the

O 2*s*, 2*p*, the S 3*s*, 3*p*, the Pt 5*d*, 6*s* and the Pd 4*d*, 5*s* states treated as the valence states. A plane–wave cut–off energy of 400 eV was used for the plane–wave expansion of the wave functions. The energy of a single atom or molecule was calculated using a $14\times14\times14$ Å^3 cell. Both the Pt(111) and Pd(111) surfaces were represented by a 5–layer slab, and (2×2), (3×3), and (4×4) surface unit cells. The two bottom layers of the slab were fixed and the other layers were allowed to relax. To avoid any periodic image interactions, an intervening 12–14 Å vacuum region was introduced. Monkhorst–Pack [285] grids of $5\times5\times1$, $4\times4\times1$, and $3\times3\times1$ were used for Brillouin zone integration for slabs with (2×2), (3×3), and (4×4) surface unit cells, respectively. For the bulk calculations, Monkhorst-Pack mesh of $10\times10\times10$ was used. The climbing-image nudged elastic band (CI-NEB) [286] method (with a spring constant of -5.0 eV/Å^2) was used to estimate the activation barriers. The true transition states in all activation barrier calculations were confirmed by the identification of a single imaginary frequency, which corresponds to a saddle point on the potential-energy surface.

The binding energy, E_b, of an atom or a molecule on the slab is defined as.

$$E_b = -[E_{slab+ads} - E_{slab} - E_{ads}] \tag{6.1}$$

where $E_{slab+ads}$, E_{slab}, and E_{ads} represent the energy of the slab with the atom/molecule, energy of the clean slab, and the energy of an isolated atom/molecule, respectively. The E_b values are positive numbers, where the increase in positive number indicates the strong binding to the surface.

For each minimum energy path (MEP) from the CI-NEB [286], we calculated the activation energy barrier, E_{act} as.

$$E_{act} = E_{TS} - E_{IS} \tag{6.2}$$

where E_{TS} and E_{IS} represent the energy of the transition state, and energy of initial state (reactants) respectively.

6.3 Results and Discussion

6.3.1 Geometric and electronic structure

Many stable configurations of atomic O and SO_x on Pt(111) and Pd(111) were considered in this work (see Figure 6.1), similar to the past literature studies. [259, 265, 276, 283] Typically, the metal to sulfur bond lengths were relatively shorter on the Pd(111) surface. However, no such pattern was observed for metal-O and S-O bonds. The increase in interatomic bond length was quite large (~10 %) relative to the gas phase values (1.42–1.43 Å), when both the S and O atoms directly attached to the surface. A decrease in bond angle (∠OSO), typically by 8–10 %, was observed relative to the gas phase values of ∠OSO = 119^o–120^o (detailed geometry information of all species considered is provided in Appendix D).

Bader charge analysis suggested that the charge transfer between SO_x and the Pd(111) surface was slightly larger than that on Pt(111). The increase in the number of O atoms in a molecule increased the total charge transfer (i.e. SO_4 acquired the largest negative charge) which explains the larger coverage dependence on binding energy for this case. A molecule with more O atoms attached directly to the metal rendered a larger negative charge on it, a larger positive charge on the attached metal atoms, and a decrease in the net charge on the S atom. This behavior is potentially due to the larger electronegativity of O compared to S. In general, metal surfaces acquired a positive charge while the charge was being accumulated in the adsorbate, which is likely to accelerate catalyst poisoning by depleting the charge from the metal surface and repelling other molecules. [283] Larger charge transfer in Pd systems

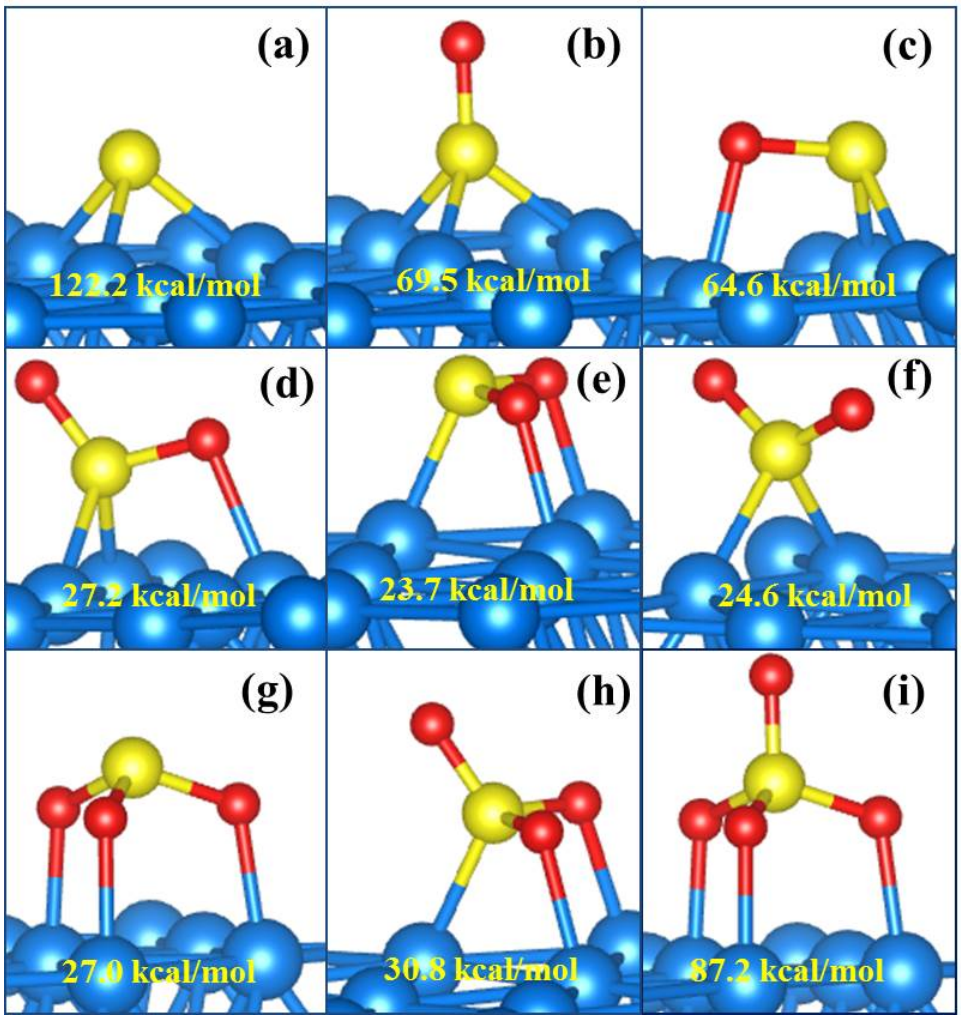

Fig. 6.1 The representative stable configurations of SO_x molecules at the fcc position (unless otherwise stated) of Pt(111) or Pd(111): (a) S (η^1), (b) SO (η^1), (c) SO (η^2), (d) SO_2 (η^2), (e) SO_2 (η^3), (f) SO_2 (bridge, η^1), (g) SO_3 (η^3), (h) SO_3 (η^3), and (i) SO_4 (η^3). The number super-scripted to η represents the number of atoms in a molecule coordinated to the metal (111) surface. Binding energies (in kcal/mol) for the given configurations are shown for a 0.11 ML coverage. Pt(or Pd), S, and O atoms are represented by blue, yellow, and red colors, respectively.

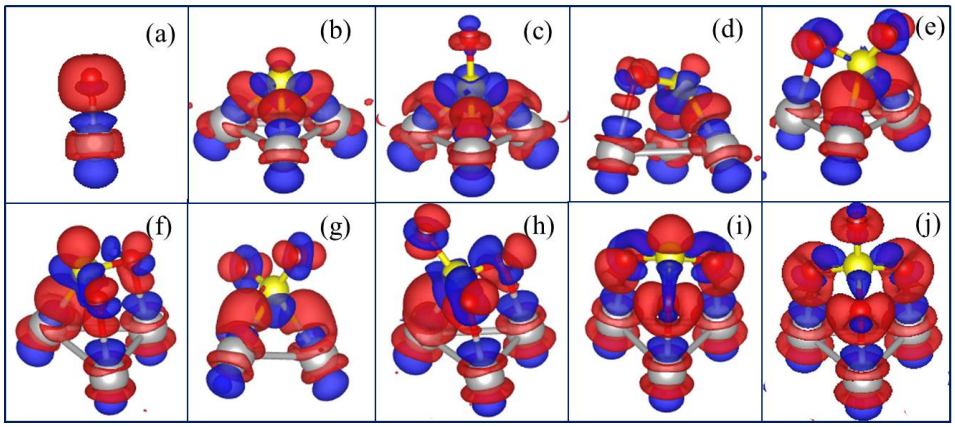

Fig. 6.2 Difference electron density maps highlighting the electron charge density redistribution due to the O and SO_x adsorption at the fcc site (unless otherwise stated) of Pd(111) surface: (a) O (atop, η^1), (b) S (η^1), (c) SO (η^1), (d) SO (η^2), (e) SO_2 (η^3), (f) SO_2 (η^2), (g) SO_2 (bridge, η^1), (h) SO_3 (η^3), (i) SO_3 (η^3), and (j) SO_4 (η^3). An isosurface corresponding to an electron charge density of 0.02 e/Å^3 is shown in each of the panels. Blue and red colors have been used to represent depletion and accumulation of charge, respectively. Silver, yellow, and red spheres represent the Pd, S, and O atoms, respectively.

relative to Pt suggests that the Pd surface is more susceptible to SO_x poisoning, which has been shown in previous experimental investigations. [31] Details of Bader analysis are provided in the Appendix D.

To visualize the charge rearrangements upon SO_x adsorption, we carried out difference electron density. [287] analyses (see 6.2) Hybridization between the d_{z^2} orbital of Pt/Pd atoms with the 3*p* orbital of S and the 2*p* orbitals of O atoms can be noted. Metal d_{xz} and d_{yz} orbitals created charge accumulations, which indicated the presence of a forward-donation and back-donation mechanisms between SO_x and metal surfaces. [265] The charge accumulation between the metal atom and the sp^3 hybridized S atom suggests the presence of some covalent bonding.

To understand the orbital interactions, we examined the density of states (DOS) as shown in Figure 6.3. The DOS analyses revealed the shifting of the active metal *d*-band to lower energy, creating bonding and anti-bonding orbitals. The *d*-band shifting was found to be larger for metal-S interaction compared to metal-O interaction. A remarkable broadening of S and O *p*

orbitals into the metal *d*-band region below the Fermi level was due to back-donation. [259] The S and O *p* orbitals above the Fermi level almost disappeared and shifted to the metal *d*-band region. However, the presence of some residual states suggested the electronic charge donations from the metal, i.e. forward-donation. [259] Generally, the lower energy of S (3*p*) orbitals as compared to O (2*p*) orbitals and the larger shift in the metal *d*-band suggest the strength of metal-S interactions compared to metal-O interactions (see figures and details in Appendix D).

6.3.2 Thermodynamics and kinetics

Binding energy patterns of SO_x was similar on both surfaces, with the order of the binding strength as follows: S > O > SO > SO_4 > SO_3 > SO_2. This result suggests that if S sticks to the surface, which is typically not the case in diesel engine exhaust, it would be extremely difficult to remove. Further, the tetrahedrally coordinated and upright standing molecules at the fcc position exhibited the largest binding energy, which is attributed to the weaker influence from the relatively distant subsurface metal layer. The effect is stronger for the atoms close to the surface. Binding energies of the most stable configurations of SO_x species were in close agreement with other DFT-based studies (see Appendix D). [119, 265, 276, 283, 288]

Moreover, we observed a coverage dependence of the binding energy. Figure 6.4 shows the computed binding energies of the most stable species of SO_x and O for coverages of 0.06–0.25 ML. We considered (2×2), (3×3), and (4×4) surface unit cells with one molecule leading to surface coverages of 0.25 ML, 0.11 ML, and 0.06 ML, respectively. The results suggest that SO_4 and O display the strongest and weakest coverage dependence, respectively. This feature may be associated with the size of the adsorbate and the charge transfer between the surface and the adsorbates.

Figure 6.5 shows a complete picture of the relative energy of SO_x* + (4–x) O* (for x = 0–4) on both surfaces (* indicates that the species is adsorbed on the metal surface). Our

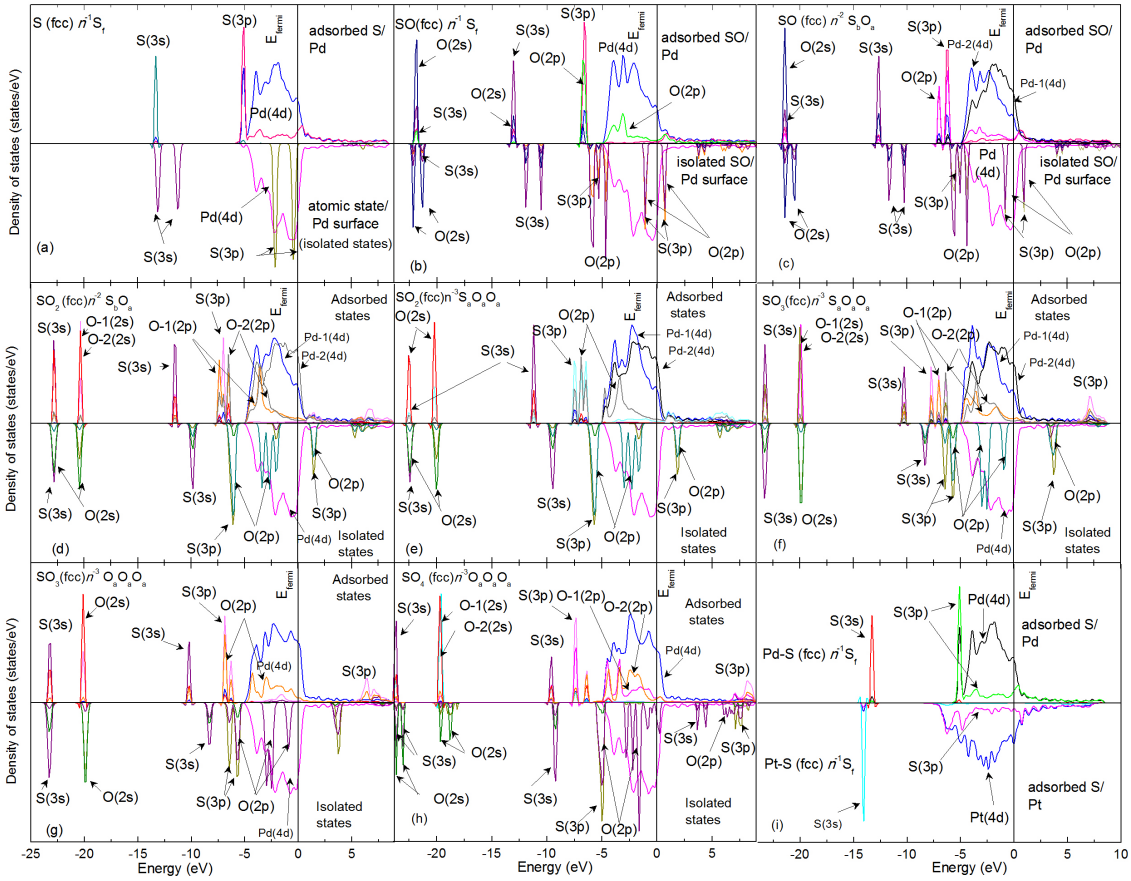

Fig. 6.3 Projected density of states (*P*-DOS) analysis of adsorbed SO_x species on metal surface and comparison to the atomic components in isolated states: (a) S (fcc)η^1–S_f , (b) SO (fcc)η^1–S_f, (c) SO (fcc)η^2–S_bO_a, (d) SO_2 (fcc)η^2–S_aO_a, (e) SO_2 (fcc)η^3–$S_aO_aO_a$, (f) SO_3 (fcc)η^3–$S_aO_aO_a$, (g) SO_3 (fcc)η^3–$O_aO_aO_a$, and (h) SO_4 (fcc)η^3–$O_aO_aO_a$ on Pd(111) surface and (i) S (fcc)η^1–S_f on Pt(111) and Pd(111) surfaces. The lower part each panel (a-h) represents the projected DOS of Pt, S and O atomic orbitals in isolated atomic/molecular/pure slab state and the upper part represents the same in adsorbed state. The O-1 and O-2 represent the oxygen atom attached to Pt (with S) and S atom only. Similarly, Pd-1 and Pd-2 represent the Pd atom attached to S atom and O atom respectively. The Fermi energy (E_{Fermi}) is adjusted to zero in the plot.

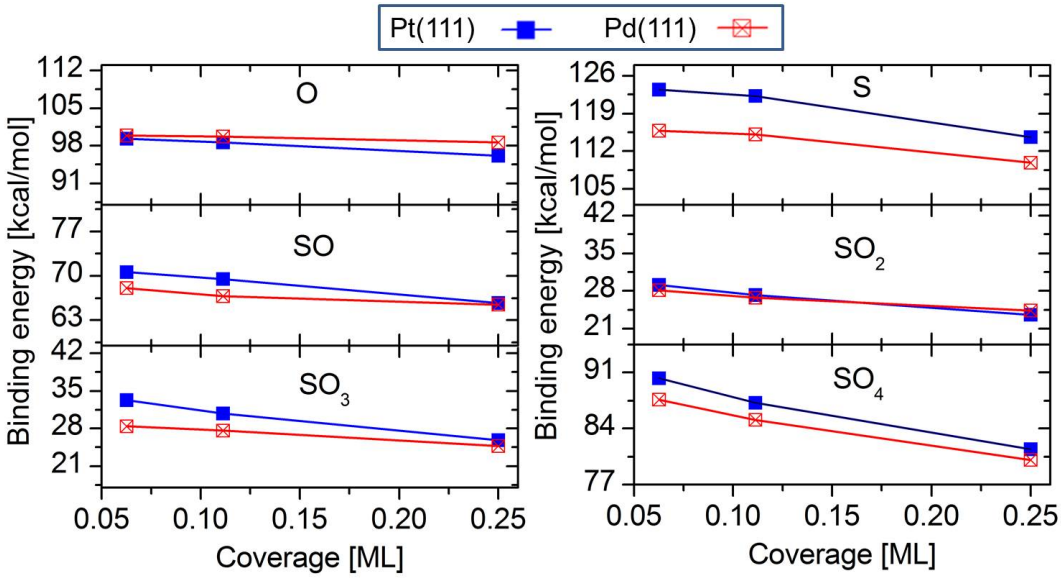

Fig. 6.4 Coverage dependent binding energies (in kcal/mol) of the most stable SO_x species and O atom adsorbed on Pt(111) and Pd(111) surfaces.

thermodynamic analyses based on the binding energies of individual species (i.e., when lateral interactions are excluded) suggest that the relative stability order is as follows: S*+4O* > SO*+3O* > SO_4* > SO_2*+2O* > SO_3*+O* on the Pt(111) surface and S*+4O* > SO*+3O* > SO_2*+2O* > SO_4* > SO_3*+O* on the Pd(111) surface. SO_4* has lower energy compared to SO_3*+O*, which suggests that the sulfates are more stable on the metal surface. The higher exothermicity of SO_3 oxidation suggests that the sulfate, once formed on the catalyst surface, will not decompose easily. Nevertheless, we note that lateral interactions should be taken into consideration when making conclusions regarding energetics. Such interactions were implicitly included in our CI-NEB computations (discussed next) and are reflected in the offset in the energy position of the SO_2*+2O* and SO_3*+O* cases with respect to the positions of the start of the CI-NEB energy profiles.

In addition to thermodynamics, reaction kinetics is critical to understand the sulfation process. Therefore, we investigated the minimum energy paths (MEPs), and estimated activation

energy barriers of the Langmuir-Hinshelwood (L-H) type surface reactions involving SO_2 oxidation to form SO_3, and subsequently SO_4 formation on both surfaces. The MEP analysis revealed three possible pathways (*viz.* paths A, B, and C) of SO_2 oxidation and 2 pathways (*viz.* paths A and B) of SO_3 oxidation as shown in Figure 6.6. In both cases, path A represents the diffusion of the O atom, whereas paths B and C for SO_2 oxidation and path B for SO_3 oxidation involve SO_2 and SO_3 movements, respectively. Our finding pertaining to the SO_2 oxidation reaction MEP (path C) is consistent with the previously reported DFT–based study on the Pt(111) surface. [289]

The activation barriers for paths B and C of SO_2 oxidation were lower ($\geq$ 7–10 kcal/mol) than that for path A and were very similar for both surfaces (see Table 6.1 for activation energies). Hence, neither path can be ruled out from the possible reaction mechanism. As expected, path B of SO_3 oxidation was significantly lower for both surfaces; however the activation barrier was relatively small on the Pd(111) surface. The lower activation barrier may explain the higher sulfation susceptibility of the Pd(111) surface as seen in experimental studies. [32, 276, 277] We note that the binding energy of the O was significantly larger compared to SO_2 and SO_3. Hence, it is easier for those molecules to diffuse towards O and form products on the surface, which is consistent with previous observations. [289]

Our DFT activation barrier for SO_2 oxidation on Pt(111) is in close agreement with experimental results ($\sim$ 23 kcal/mol) [260, 290–292] and with our previous estimate based on the UBI-QEP method (21.5 kcal/mol). [31] Unfortunately, no direct comparison to experimental data can be made for SO_2 oxidation on Pd(111). Nonetheless, similar oxidation behavior of SO_x on the Pd(111) surface is expected and observed as well. [276] The UBI-QEP activation energy estimated using the binding energies from the present work for SO_2 oxidation on the Pd(111) surface is 22.2 kcal/mol, which is close to the DFT estimate. The UBI-QEP procedure to compute the activation energy using a thermodynamic loop is provided in Appendix B. In Table

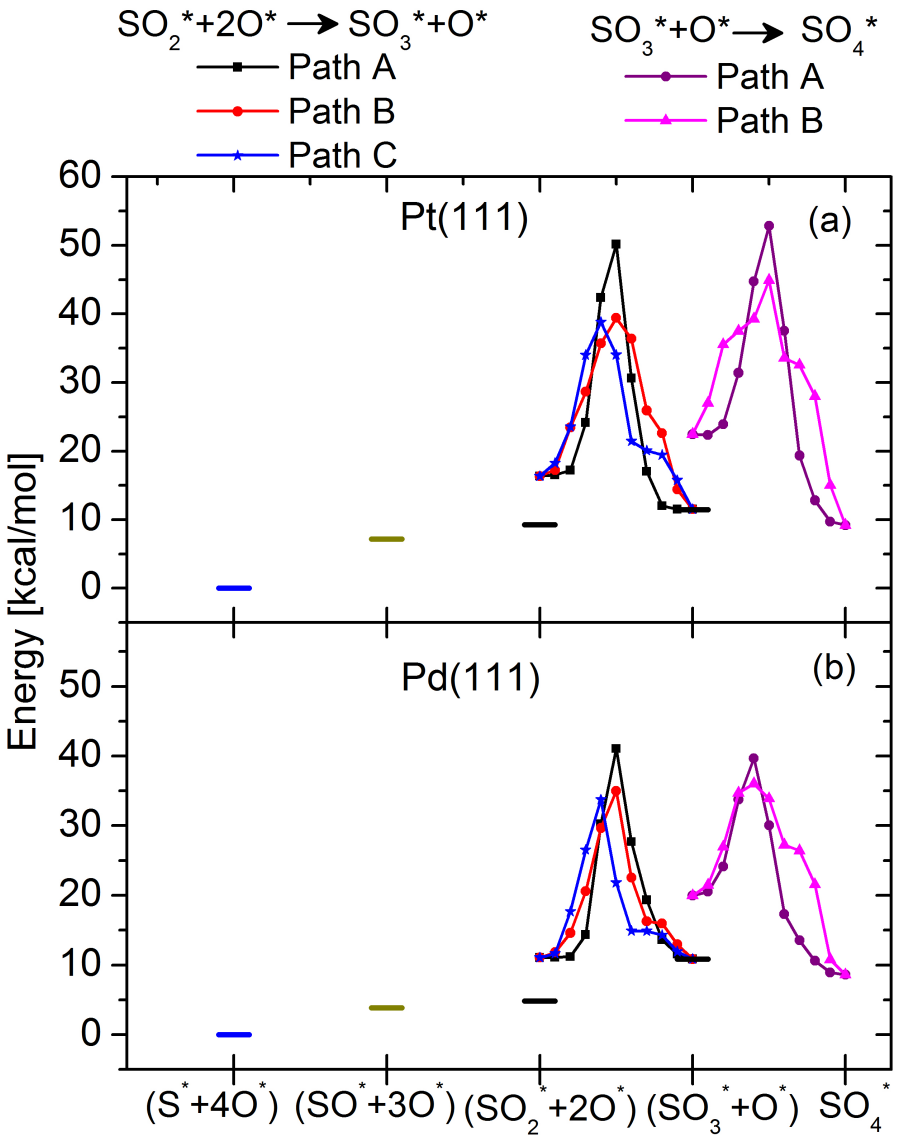

Fig. 6.5 Relative energy of SO_x species on Pt(111) and Pd(111) surfaces without lateral interactions along with CI-NEB computed activation barriers (which include the SO_x + O lateral interactions) for the Langmuir-Hinshelwood type surface reactions (SO_2* + O* $\leftrightarrow$ SO_3* + * and SO_3* + O* $\leftrightarrow$ SO_4* + *) on Pt(111) (a) and on Pd(111) (b). * indicates an adsorbed surface species.

6.1, we also list the pre-exponential factors of both oxidation reactions and the zero-point energy corrections (Δ ZPE) to the activation, which are estimated from the vibrational frequencies of the transition state (TS) and initial state (IS).[168] The pre-exponential factor values (10^{13} s^{-1}) suggest a tight TS. [264] Calculation details are provided in Appendix E.

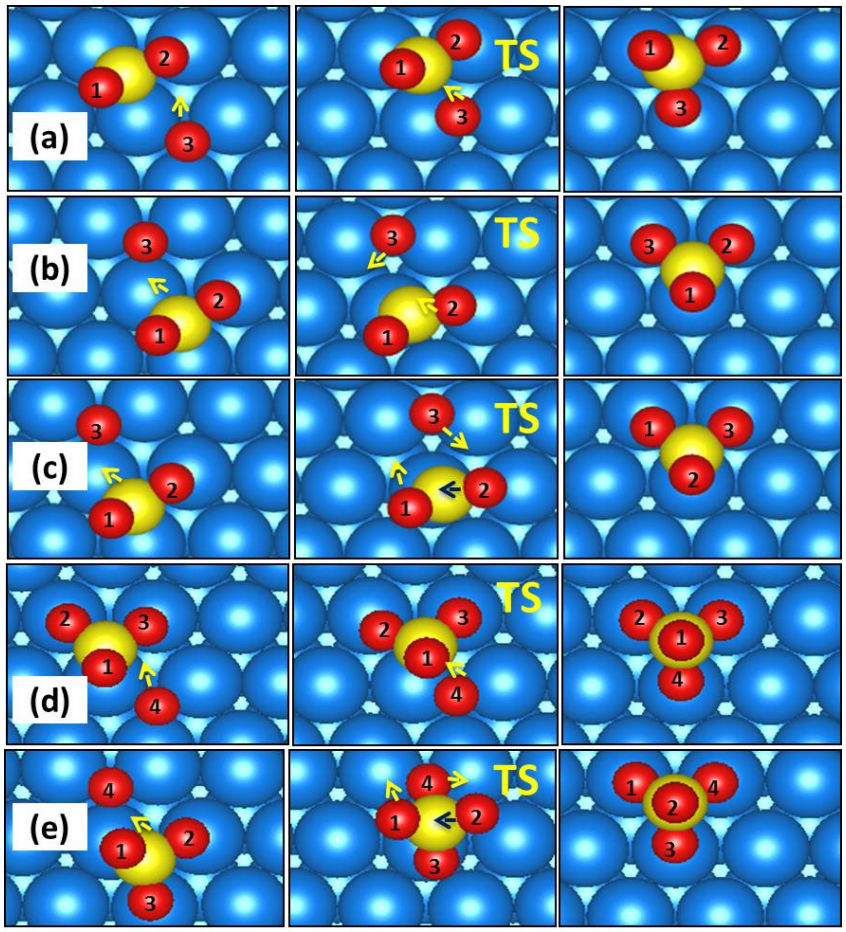

Fig. 6.6 Minimum energy pathways (MEPs) for SO_2 and SO_3 oxidation on the Pt(111) surface. Panel (a–c): SO_2 oxidation paths A, B, and C; panel (c–d): SO_3 oxidation paths A and B. The middle image in each panel represents the transition state. Blue, yellow, and red spheres represent Pt, S, and O atoms, respectively.

Table 6.1 Pre-exponential factors, activation energies, zero-point (Δ ZPE) corrections, and the corrected activation energies (kcal/mol) of SO_2 and SO_3 oxidation on Pt(111) and Pd(111) surfaces computed using DFT for the paths shown in Figure 6.6.

Reaction	**Path**	**Pt(111)**				**Pd(111)**			
		A_o (s^{-1})	E_a (kcal/mol)	Δ ZPE (kcal/mol)	$E_{a,\Delta ZPE}$ (kcal/mol)	A_o (s^{-1})	E_a (kcal/mol)	Δ ZPE (kcal/mol)	$E_{a,\Delta ZPE}$ (kcal/mol)
SO_2* + O* → SO_3*	Path A	2.4×10^{11}	33.8	– 0.3	33.5	5.7×10^{11}	30.0	– 0.2	29.8
	Path B	7.9×10^{11}	23.1	– 0.4	22.7	8.4×10^{11}	23.9	– 0.2	23.7
	Path C	5.0×10^{11}	22.5	– 0.2	22.3	9.0×10^{11}	22.7	– 0.3	22.4
SO_3* + O* → SO_4*	Path A	7.1×10^{12}	30.3	– 1.1	29.2	8.0×10^{12}	19.7	– 0.7	19.0
	Path B	9.6×10^{12}	22.4	– 0.1	22.3	6.2×10^{12}	16.0	– 0.2	15.8

6.3.3 Microkinetic Modeling

The thermodynamic (e.g., binding energies) and kinetic (e.g., activation barriers, pre-exponential factors) information that emerges from DFT computations needs to be coupled with techniques such as microkinetic modeling to assess the relative importance of reaction pathways at various operating conditions. Microkinetic modeling can be used to predict surface coverages, most abundant reaction intermediate(s) (MARI), conversion, and rate determining steps without any *a priori* assumptions about the reactions. [31, 101, 264] Here, we use the present results for the thermodynamic and kinetic parameters as input to our microkinetic model developed earlier. [264] Temperature correction was applied to 0 K DFT binding energies before using in the model at 300 K (given in the last column of Table 6.2). A total of 8 elementary steps (listed in Table 6.2) involving 3 surface species, O*, SO_2*, and SO_3*, are used in this microkinetic model, and the conversion of SO_2 (to SO_3) is predicted at different conditions previously probed experimentally. The model also involved parameters not directly addressed in the DFT part of this work. These include the bond indices, [281] sticking coefficients, desorption pre-exponential factors, and the coverage and temperature dependence of the activation energy

(estimated using the UBI-QEP method), all of which are also listed in Table 6.2. We note that the lateral interactions of the SO_x species are not taken into the microkinetic model. In our previous work, [264] we show that the coverage of SO_x species (particularly SO_3*) on the catalysts surface was relatively small compared to the oxygen. This is also consistent with the typical operating conditions for emissions oxidation, where the gas phase oxygen concentration is $\sim$12%, and the SO_x concentration is only a few ppms. The SO_3* coverage was observed to be slightly higher ($\sim$0.3 ML) at low temperature ($\sim$300 °C), but the coverage was negligible ($\sim$0.045 ML) at higher temperature ($\sim$500 °C). In fact, for most of the conditions, the surface is dominated by oxygen. Therefore, we have included the lateral interactions between oxygen molecules only. Furthermore, the UBI-QEP based activation barriers vary with coverage; however, the variation is negligible if the coverage is low. Activation barriers for R_3 and R_5 (see Table 6.2) are taken as zero, i.e., the adsorption reactions are assumed to be non-activated. Details are provided in Appendix B. The rationale for these choices have been described elsewhere. [31, 264]

Figure 6.7 shows the comparison of microkinetic model predictions against experimental data obtained at 3 different sets of experimental conditions (labeled as Set-A, Set-B, Set-C). [264, 275] Overall, good agreement is observed between the experimental data and the model predictions. In particular, Set-C in Figure 6.7 shows the model performance with SO_3 in the feed. The experimental results show a slight shift of the light-off curve towards high temperature in the presence of SO_3 in the feed. This explains the inhibition effect of SO_3 during SO_2 oxidation, [275] which is also well captured by the model. At high temperature, the presence of SO_3 in the feed further decreases SO_2 conversion due to equilibrium limitations. These results indicate that combining DFT predictions with microkinetic modeling provides a viable way to validate reaction kinetics and experiments.

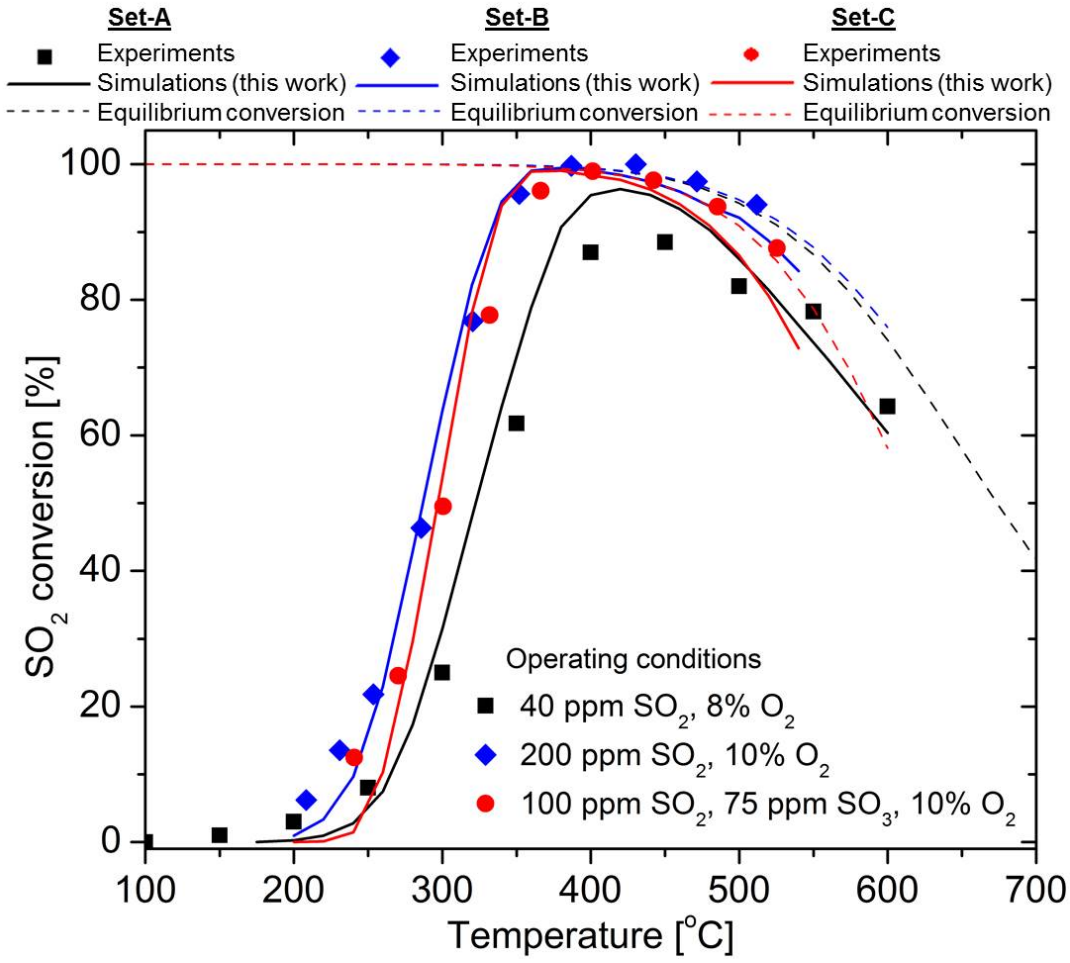

Fig. 6.7 Minimum energy pathways (MEPs) for SO_2 and SO_3 oxidation on the Pt(111) surface. Panel (a–c): SO_2 oxidation paths A, B, and C; panel (c–d): SO_3 oxidation paths A and B. The middle image in each panel represents the transition state. Blue, yellow, and red spheres represent Pt, S, and O atoms, respectively.

Table 6.2 Elementary steps considered to study SO_2 oxidation on Pt. θ_o represents the oxygen surface coverage, * indicates a vacant site, whereas superscript * indicates an adsorbed species. Barriers reported in the fourth and fifth columns correspond to the DFT–computed quantities at 0 K and the temperature and pressure dependent UBI-QEP estimates, respectively.

No.	Reactions	Sticking coefficient	Activation energy [kcal/mol]		Bond index[b]
		[unitless] or	DFT barriers	UBI-QEP barriers[a]	[unitless]
		pre-exponential factor [s^{-1}]	at 0 K		
	O_2 adsorption/desorption [31, 264]				
R_1	$O_2 + 2* \rightarrow 2O^*$	0.05[c]	0.0	0.0	0.5
R_2	$2O^* \rightarrow O_2 + 2*$	1.0×10^{13}[d]	$52.2 - 34.6\theta_o$	$52.2 - 34.6\theta_o$ + f(T)	
	SO_x adsorption/desorption [264]				
R_3	$SO_2 + * \rightarrow SO_2^*$	0.5[c]	0.0	0.0	0.5
R_4	$SO_2^* \rightarrow SO_2 + *$	1×10^{16}[d]	30.8	29.3 – 2.5RΔT	
R_5	$SO_3 + * \rightarrow SO_3^*$	0.5[c]	0.0	0.0	0.5
R_6	$SO_3^* \rightarrow SO_3 + *$	1×10^{13}[d]	35.6	34.1 – 2.5RΔT	
	SO_x oxidation [264]				
R_7	$SO_3^* + * \rightarrow SO_2^* + O^*$	1.2×10^{11}[d]	26.8	23.2 + f(θ_o,T)	0.97
R_8	$SO_2^* + O^* \rightarrow SO_3^* + *$	5.0×10^{11}[d]	22.3	21.3 + f(θ_o,T)	

[a] DFT-based binding energies at 0 K are used as inputs to calculate the binding energies at a given temperature. The functional form 'f' includes coverage and temperature dependence. Coverage dependence originates from the use of UBI-QEP for the estimation of activation energies, whereas the temperature dependence is derived from the statistical mechanics based calculations for degrees of freedom lost/gained upon adsorption [101] (details are discussed in Appendix B). $\Delta T = T - T_o$, where T_o is taken as 300 K. Activation energies are computed on-the-fly using the UBI-QEP formalism, as the surface coverages changes in the simulations. Difference in activation energies for reactions R_7–R_8 primarily originates from the use of UBI-QEP vs. DFT.

[b] Bond index represents the position of the transition state along the reaction coordinate, which is also used to compute the activation energies in the UBI-QEP formalism. It is defined for a reaction pair in the forward direction only (details are discussed in Appendix B). It ranges between 0 and 1, with a typical estimate of 0.5. Bond index for reaction pair R7-R8 was adjusted to 0.97 in the UBI-QEP calculations in order to closely emulate the DFT-computed barriers.

[c] Sticking coefficients for O_2 and SO_2 are taken from Refs. [151] and [246], respectively, whereas that of SO_3 is assumed to be the same as SO_2.

[d] Pre-exponential factors for R_2 and R_6 are based on the typical order-of-magnitude estimate based on Transition State Theory (TST). [101] Pre-exponential factor for R_4 is based on high values (10^{15}–10^{17} s^{-1}) reported in literature. [260, 262] Finally, pre-exponential factors for R_7 and R_8 are based on the DFT calculations from this work.

6.4 Conclusions

In summary, we investigated and compared the stability, morphology, thermodynamics and kinetics of various SO_x species on Pt(111) and Pd(111) surfaces. Our analysis revealed 3 important pathways for SO_2 oxidation and 2 major pathways for SO_3 oxidation, where the lowest activation barrier for both oxidation reaction was due to the diffusion of SO_2 or SO_3 towards an O atom on the surface. In general, oxidation of SO_x and ultimately SO_4 formation is a favorable process on both surfaces, although it appears that Pd is more likely to be sulfated compared to Pt (consistent with experimental findings). Quantities computed using DFT were incorporated in a previously developed microkinetic model to predict SO_2 conversion as a function of temperature for three sets of operating conditions, one of which included SO_3 in the feed. The favorable agreement of the computed results with experiments is indicative of the applicability of the present strategy to obtain quantitative insights pertaining to SO_x chemistry on catalyst surfaces. This can thus lead to the rational design of sulfur-resistant emissions aftertreatment catalysts.

Chapter 7

Why Pt Survives but Pd Suffers From SO_x Poisoning?

7.1 Introduction

Oxides of sulfur, predominantly SO_3 generated from the oxidation of SO_2, poison the noble metal based emissions aftertreatment catalysts such as the Diesel Oxidation Catalysts (DOCs) by altering metal surface properties, blocking other emissions species/adsorbates, changing the reaction selectivity, and forming stable metal sulfates. [9, 31, 32, 72, 276, 277, 293, 294] Traditionally, Pt-based oxidation catalysts have been the most preferred option for the oxidation of diesel engine emissions due to their superior capability to resist sulfation (i.e., formation of $PtSO_4$ or other sulfates). [15, 283, 295] However, the high cost of Pt and its tendency to sinter at the high operating temperatures encountered have forced the inclusion of Pd in the currently used state-of-the-art oxidation catalysts. [31, 32] While Pd by itself is a good oxidation catalyst, has low cost, and resists sintering (unlike Pt), it suffers from sulfur poisoning. [31, 32, 84, 87] Indeed, many experimental and computational studies [9, 15, 87, 283, 293–295] directly point to

the heightened tendency for Pd sulfation –especially, formation of $PdSO_4$. On the other hand, no evidence exists for the formation of $PtSO_4$ even under highly oxidizing and sulfating conditions. Given the chemical similarity between Pt and Pd, the radical divide in their tendencies for sulfation remains a puzzle. A clear understanding of the circumstances (environment, chemical attributes, descriptors, etc.) that contribute to the different sulfation tendencies of Pt and Pd will guide us in rationally designing potentially lower-cost higher-performance sulfur resistant catalysts.

This work aims to provide fundamental insights pertaining to the intrinsic tendency (or lack thereof) of Pt and Pd to undergo sulfation via a comprehensive first principles thermodynamics study. The thermodynamic analysis has resulted in accurate and feature-rich bulk and surface phase diagrams of Pt and Pd when exposed to reservoirs of O_2 and SO_3. This has also aided in the identification of descriptors or key features that make Pt different from Pd. Owing to the complex nature of the sulfation process, capturing a large spectrum of possible bulk and surface phases as a function of the environmental conditions is critical. Figure 7.1 collects the anticipated and known stable phases when Pt or Pd is exposed to oxidizing and/or sulfating conditions (i.e. O_2 and SO_3 environments). This collage of possible phases includes pure bulk metals, bulk oxides and bulk sulfates as well as surface metallic forms, surfaces partially or wholly covered with O and/or SO_3, surface oxides, and surface sulfates. When prior experimental or computational information was available for a particular phase, it was used in our calculations. But, when such information was not available (e.g., in the case of $PtSO_4$), we determined the atomic level structure using a structure search algorithm in the Universal Structure Predictor: Evolutionary Xtallography (USPEX) method. [130, 131]

7.2 Computational Details

Our first principles calculations were carried out using density functional theory (DFT) [111, 296] as implemented in the VASP code [113] with the electronic wave functions expanded in a plane wave basis with a cutoff energy of 400 eV. All calculations were performed utilizing the Perdew-Burke-Ernzerhof (PBE) functional, [114] the projector augmented wave (PAW) frozen-core potentials, and spin polarization method. The structures were relaxed using a conjugate-gradient algorithm until the forces on all atoms were < 0.01 eV/Å. Both the Pt(111) and Pd(111) surfaces were represented by a 5-layer slab, and (2×2), (3×3), and (4×4) surface unit cells. Two bottom layers of the slab were fixed and the remaining top 3 layers were allowed to relax. To avoid any interactions between periodic images, a 12-14 Å thick vacuum region was introduced. Monkhorst-Pack grids of 3×3×1, 4×4×1, and 5×5×1 were used for Brillouin zone integration for slabs with (4×4), (3×3), and (2×2) surface unit cells, respectively. For the Pt surface-oxide models, PtO_2-Pt(111) and Pd surface oxides, PdO-Pd(111), Monkhorst-Pack grids of 5×5×1 and 1×3×1 were used, respectively. Similarly, a Monkhorst-Pack grid of 4×5×1 was used for both Pt and Pd surface-sulfate models with $(3\times\sqrt{3})$ supercell. To search the possible $PtSO_4$ structures, evolutionary structure prediction was performed using the USPEX code [130, 131] in conjunction with *ab-initio* structure relaxations using DFT and methodology as mentioned above.

7.3 First Principles Thermodynamics and Gibbs Free Energy

Once the catalog of possible phases was assembled, the Gibbs free energy of formation of each of the phases with respect to the appropriate reference states was computed using the

density functional theory (DFT) total energies, DFT phonon density of states, and the statistical mechanics of ideal diatomic (O_2) and polyatomic (SO_3) gases. [149, 297, 298] The Gibbs free energy inherently contains temperature and pressure dependence. While the pressure dependence comes entirely through the chemical potentials of the gas phase species ($\mu_{(O_2)}$ and ($\mu_{(SO_3)}$of O_2 and SO_3, respectively), the temperature dependence arises due to the gas phase species as well as due to the vibrational degrees of freedom of the condensed phases. The latter is generally ignored due to the severe computational expense of phonon computations, but it is computed and shown to have no significant impact on outcome of the present work. Hence, the contribution is not included in the phase diagrams shown in this paper. Furthermore, this formulation neglects the configurational entropic contributions since it was found in the past to have no significant impact on the results, especially features of the phase diagrams. [299] The free energies were then used to construct bulk and surface phase diagrams, revealing clear differences between Pt and Pd insofar as their thermodynamic tendencies for both oxidation and sulfation are concerned. Details of the DFT calculations are described later in Computational Methods section. Vibrational modes computations and surface free energy computations are given in the Appendix F.

7.4 Bulk Thermodynamics

A simple yet effective starting point is to consider the bulk phases (metal, oxide and sulfate) shown in panels 1-3 of Figure 7.1. Both Pt and Pd metals are fcc structures (space group 225, Fm3m) with very similar lattice parameters. However, the experimentally known most stable bulk oxides of Pt and Pd are quite different from each other. [300] A dioxide compound PtO_2 (space group 164, P-3m1) is the most stable oxide of Pt, whereas a monoxide compound PdO (space group 131, $P4_2$/mmc) is the only known stable oxide of Pd. In the case of metal

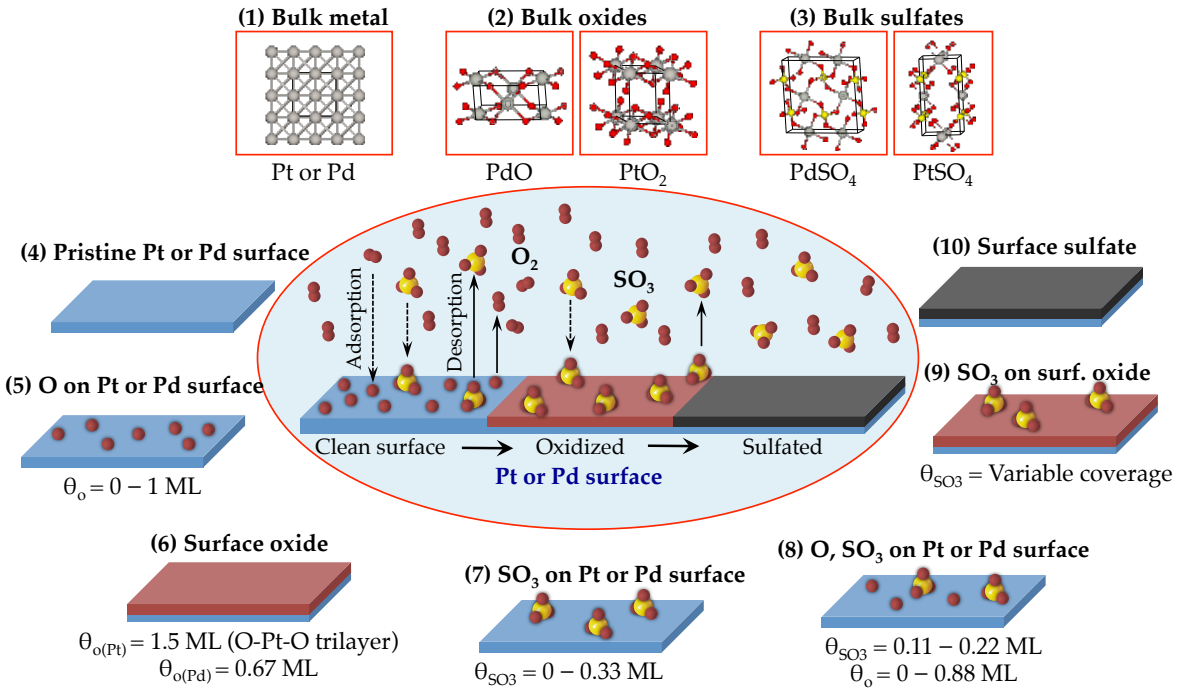

Fig. 7.1 Schematics of the representative stable structures of various bulk and surface phases in the thermodynamic equilibrium containing O_2 and SO_3 for the temperature and pressure range considered in this study. The middle region (inside the circular boundary) represents a catalyst surface exposed to wide ranges of temperature and pressure conditions, where gas phase O2, SO3 along with adsorbed O and SO3 on Pt or Pd surface are also shown. Panels 1-3 at the top represent the bulk phases (i.e., bulk metal, metal oxides, and bulk sulfates), and panels 4-10 represent various possible surface phases of Pt and Pd (i.e., pristine surfaces, O and/ or SO_3 on the metal surfaces, surface oxides, SO_3 on the surface oxides, and surface sulfates) in an anti-clockwise order to the ultimate sulfate phase. The blue, brown, and black colors represent the clean metal surface, surface oxide, and the surface sulfate layer, respectively. Similarly, the silver, red, and yellow spheres represent the Pt or Pd, Oxygen, and Sulfur respectively.

sulfates, $PdSO_4$ (space group 15, C2/c) is well known experimentally; however, no information is available about $PtSO_4$ to the best of our knowledge. Therefore, we have used the USPEX method [130, 131] and have identified a tetragonal $PtSO_4$ phase (space group 84, $P4_2/m$). The dynamical stability of this phase was confirmed via a phonon band structure calculation, which revealed no modes with imaginary frequencies. In order to validate the veracity of the USPEX method for this class of systems, the structure of $PdSO_4$ was also predicted using USPEX. It is reassuring to note that the correct experimentally known ground state structure of $PdSO_4$ is indeed recovered. Details concerning the structure prediction results, as well as the predicted geometries of the selected phases along with comparisons to past experimental and computation work are provided in the Appendix G.

The free energies of the bulk metals, oxides, and sulfates were then used to compute the phase diagrams for both Pt and Pd, which are shown in Figure 7.2. As noted earlier, the free energy depends on the temperature and the O_2 and SO_3 partial pressures. Essentially, this figure shows the most stable phase (i.e., the one with the lowest free energy) for a given choice of the temperature and pressure dependent parts of the O_2 and SO_3 chemical potentials (represented using $\Delta\mu_{O_2}$ and $\Delta\mu_{SO_3}$. For convenience, the O_2 and SO_3 partial pressure ranges for two choices of temperatures (300 K and 700 K) are also shown. It is evident that PdO formation is more favored than PtO2 formation as the onset of the PdO phase region occurs at less oxidizing conditions ($\Delta\mu_{O_2}$ = –1.88 eV) compared to PtO_2 ($\Delta\mu_{O_2}$ = –1.42 eV). More importantly, the $PdSO_4$ phase region is a lot more prominent than the $PtSO_4$ phase region for the same range of chemical potentials or temperature-pressure ranges. In fact, the stability range of $PtSO_4$ lies outside of normal pressure conditions at ambient (300 K) or higher temperatures. This may explain why there is no experimental information available for $PtSO_4$ thus far. [301] The clear thermodynamic resistance for $PtSO_4$ formation (compared to $PdSO_4$) in the bulk form is

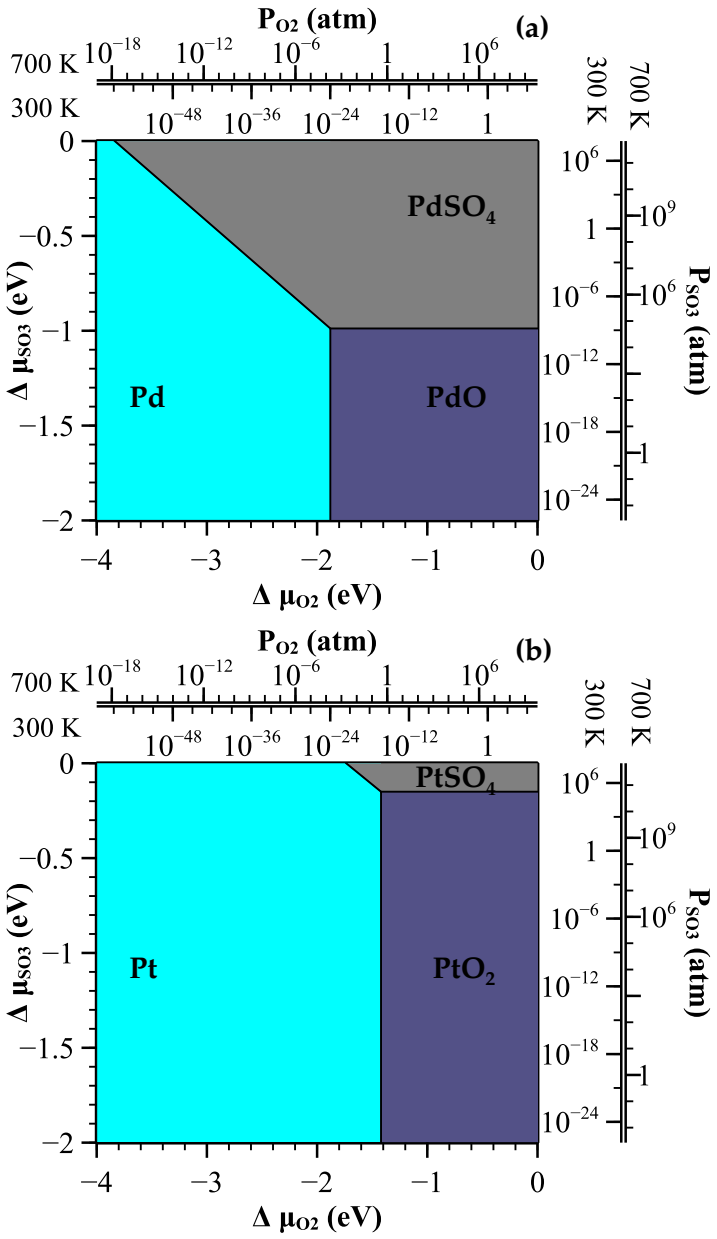

Fig. 7.2 Bulk phase diagrams showing metal, metal oxide and metal sulfate (structures are shown in Figure 7.1) in the given ranges of $\Delta\mu_{SO_3}$and $\Delta\mu_{O_2}$. Panel a: bulk phase diagram with Pd, PdO and $PdSO_4$; and panel b: bulk phase diagram with Pt, PtO_2 and $PtSO_4$. Chemical potential ranges are translated into a pressure range for two representative temperatures (300 K and 700 K). The stability regions of bulk sulfates show the most prominent differences.

indicative of Pt's resistance to sulfur poisoning, and could be used as a screening criterion to identify potentially sulfur resistant catalysts.

7.5 Surface Thermodynamics

While bulk thermodynamics provides a good starting point, catalytically more realistic conditions involve surface phenomena. Therefore, we investigated the possible surface phases on both metal surfaces in oxidizing and sulfating environments. In panels 4-6 of Figure 7.1, we show the stable surface phases while increasing the oxygen partial pressure. Results (discussed later in more details) show greater affinity of Pd surface towards oxygen with highly favored surface oxide formation. Similarly, we show the stable phases of SO3 on clean surface and co-adsorbed oxygen and SO_3 in panels 7 and 8, respectively. Panel 9 shows a more interesting phase of SO_3 on the oxidized surfaces of Pt and Pd. We observed that the affinity of SO_3 is significant on PdO only. Further interaction of SO_3 and the surface oxide could potentially result in a surface sulfate as shown in panel 10, and ultimately in the bulk sulfate in panel 3. These phases are discussed next, resulting in the surface phase diagrams for Pt and Pd surfaces when exposed to O_2 and SO_3.

7.5.1 Oxygen on Pt(111) and Pd(111) Surfaces

Due to significantly high oxygen concentration ($\sim$10%) in realistic exhaust conditions [31, 32], a natural step here is to investigate the oxygen interactions on the surfaces. Experimentally observed stable phases of O on Pt(111) and Pd(111) due to O_2 exposure involve $p(2\times2)$ and $c(2\times2)$ configurations with possibility of higher coverage ($\theta_O \sim$1 ML) when the Pt(111) surface is exposed to NO_2 or O_3. [149, 297] Hence, we investigated the entire range (0 - 1 ML) of O coverage on both surfaces (higher O coverage is possible in surface oxides, as discussed

in the next paragraph). By considering a variety of configurational possibilities (as described in the Appendix H), this approach allowed us to fully capture lateral or adsorbate-adsorbate interactions. In general, we observed very similar oxygen interaction behavior (binding strength and lateral interaction patterns) on both Pt(111) and Pd(111) surfaces. Binding energies of oxygen on both metal surfaces are given in Appendix H.

7.5.2 Surface Oxides

An elevated oxygen concentration on the metal surface can proceed to a partially oxidized phase (i.e., the surface oxide phases shown in panel 6 of Figure 7.1). The surface oxide models for Pt(111) and Pd(111) surfaces considered here are guided by HRCLS, STM, LEED, and XRD experimental observations. [298, 302, 303] Experimental and computational results suggest that the surface oxide layer formation on Pt(111) and Pd(111) surfaces results in different types of arrangements of metal and oxygen atoms. 22-24 A (O-Pt-O) trilayer structure of Pt surface oxide on a (2×2) surface contains only three Pt atoms (unlike four Pt atoms on a clean surface) and six O atoms. LEED patterns show α-PtO_2(0001) (2 × 2) overlayers on the Pt(111) surface. 25 On the other hand, a distinct Pd_5O_4 type (with repetitive structure pattern of five Pd and four O) stable surface oxide layer on Pd(111) was represented by $7\times(Pd_5O_4)$ model. This unique structure corresponds to a 0.67 ML oxygen coverage; it has two types of Pd atoms which are either 2- or 4-fold coordinated to O atoms and two types of O atoms which are either 3-fold (bonded to in-plane Pd atoms) or 4-fold (bonded to in-plane and subsurface Pd atoms) coordinated to Pd atoms. The LEED pattern shows that the structure is commensurate in the $[2\bar{1}\ \bar{1}\ ]$ direction. [304]

We note the existence of possible sub-surface oxygen configurations on both metals. Todorova et al. showed that sub-surface oxygen on transition metals is initially always less stable than on-surface oxygen adsorption. However, with increasing coverage this preference vanishes, and

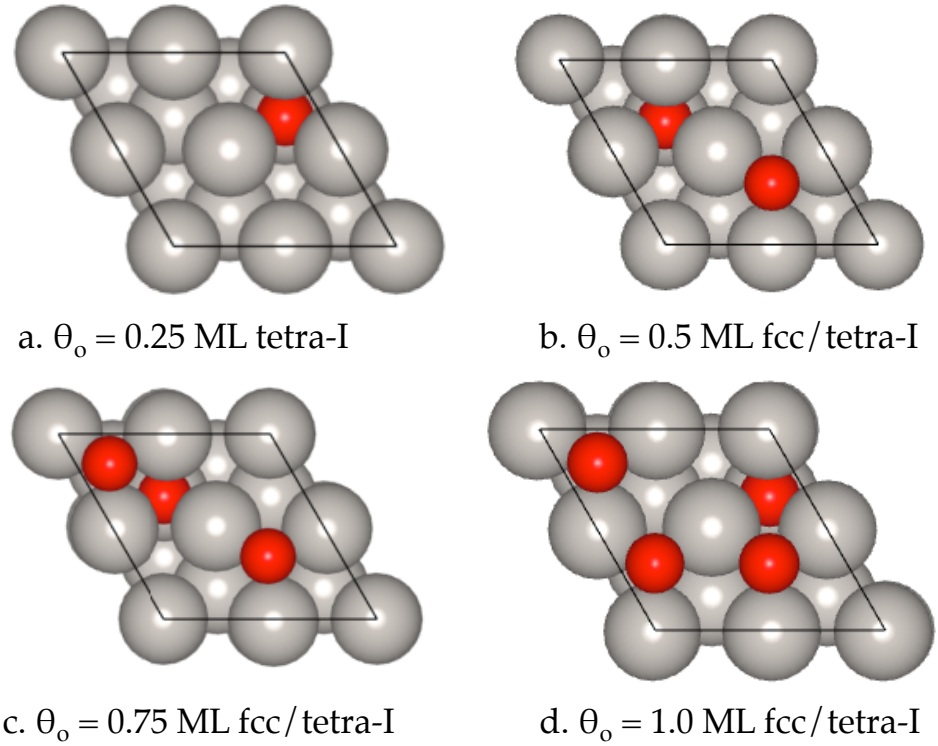

Fig. 7.3 Representative on-surface/sub-surface (fcc/tetra-I) models for oxygen adsorption on the (111) surface with a (2 $\times$2) surface supercell. Panel a: 0.25 ML of oxygen in sub-surface (tetra-I), panel b: 0.5 ML of oxygen with one O atom in on-surface (fcc) and the other on sub-surface (tetra-I) positions, panel c: 0.75 ML of oxygen with two O atoms in on-surface (fcc) and the other on sub-surface (tetra-I) positions, and panel d: 1.0 ML of oxygen with three O atoms in on-surface (fcc) and the one in sub-surface (tetra-I) positions. Silver and red spheres represent the Pt or Pd, and oxygen, respectively.

oxygen incorporation becomes more favorable above coverages of ∼0.5 ML. [118, 305] We considered the most stable/favored sub-surface site tetra-I 29 (i.e. the site directly below the 3-fold hcp position on (111) surface as shown in Figure 7.3) to compute the energetics of the on-surface and sub-surface oxygen adsorption. Our results show that on-surface (fcc)/sub-surface (tetra-I) configuration favors only after on-surface fcc coverage of 0.5 ML on Pd(111), whereas it favors only above the on-surface fcc coverage of 0.75 ML on Pt(111) (in Figure 7.4). The sub-surface only oxygen adsorption (θ_O= 0.25 ML) at tetra-I site was highly endothermic for both Pt(111) and Pd(111). However, the sub-surface/on-surface combination becomes exothermic on/above θ_O= 0.5 ML. This observation clearly shows the favorability of the on-surface oxygen adsorption at the lower coverage. In general, the adsorption of oxygen on the metal surface is followed by the on-surface/sub-surface oxygen configurations, which finally transforms to the fully oxidized metal oxide layers.

While evaluating the stability based on thermodynamics, we observed that the surface oxides phases are thermodynamically more stable than any sub-surface oxygen configurations and even the experimentally known c(2×2)-O (0.5ML) configuration. [306] Thus, they do not appear on the phase diagrams constructed based on thermodynamics. Utilizing the information from oxygen adsorption and surface oxides formation, we created detailed phase diagram of oxygen on both (Pd (111) and Pt(111)) surfaces. Our calculated phase boundaries for various phases of oxygen adsorption on both surfaces are in good agreement with known experimental results. [151, 307–310] Details of the on-surface/sub-surface oxygen adsorption, and phase diagrams are shown in Appendix H.

7.5.3 SO_3 on Pt(111) and Pd(111) Surfaces

Another spectrum of stable phases may arise due to the presence of SO_3 on the surface (panel 7 of Figure 7.1). SO_3 shows a strong affinity towards both surfaces, albeit slightly stronger

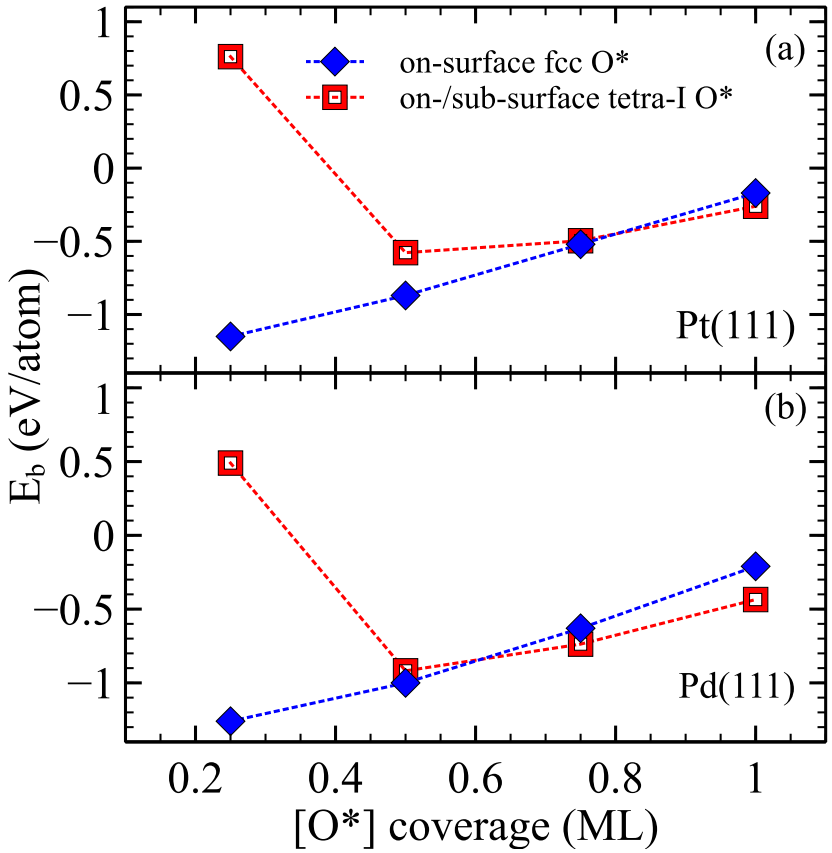

Fig. 7.4 DFT computed average binding energy E_b as a function of total O^* coverage with on-surface fcc and sub-surface tetra-I sites of Pt(111) and Pd(111) shown in panels a and b, respectively. The blue symbols represent the binding energies of oxygen for on-surface fcc sites of (111) surface. The red symbols represent the binding energies of oxygen for fcc/tetra-I combinations. A (2×2) surface supercell was used for the computations. The red symbol at θ_O= 0.25 ML represents the oxygen on sub-surface tetra-I site only and higher coverages (> θ_O = 0.25 ML) represent the combination of O* with one oxygen in sub-surface tetra-I and rest of oxygen on surface fcc sites. Dotted lines are drawn to guide the eyes. On-surface *fcc* O^* coverage below 0.5 ML is always stable on both surfaces.

on Pt(111) as shown by the binding energy numbers in Figure 7.5. An upright standing chair-shaped configuration on fcc sites is the preferred one in both cases. [31, 271] Given the bulky nature of the SO_3 molecule, the maximum coverage on the (111) surface could only reach up to 0.33 ML in a (3×3) surface supercell. Size of the molecule is responsible for the significant lateral interactions between adjacent SO_3 molecules (note the sharp decrease of SO_3 binding energy with coverage in Figure 7.5). We note that the configurational space can be large for a higher coverage; however, the overall outcome due to the selection of our surface models will not change. Four representative stable configurations corresponding to a coverage range of 0.06 ML to 0.33 ML are considered for the generation of phase diagrams (panels 7a-d of Figure 7.6). Computed binding energies and the phase diagrams of SO_3 adsorption in Pt(111) and Pd(111) surfaces are given in the Appendix H.

7.5.4 Co-Adsorption of Oxygen and SO_3 on Pt(111) and Pd(111) Surfaces

A more interesting condition involves the co-adsorbed environment of SO_3 and oxygen on the metal surfaces as shown in panels 8a-c of Figure 7.6. In a (3×3) surface supercell, we investigated two SO_3 coverages (i.e., θ_{SO_3} = 0.11 ML and θ_{SO_3} = 0.22 ML) and possible O coverages (i.e., up to 0.89 ML). For the condition with 1 SO_3 molecule (i.e., θ_{SO_3} = 0.11 ML) on the surface, the maximum stable oxygen coverage was 0.33 ML, whereas the maximum coverage of O decreased to 0.22 ML with 2 SO_3 molecules (i.e., θ_{SO_3} = 0.22 ML) on the surface. Further addition of O on the surface caused destabilization and desorption of the SO_3 molecule from the surface. This is due to the larger binding strength of O on metal (Pt and Pd) surfaces and also due to lateral adsorbate-adsorbate interactions between O and SO_3 as shown in Figure 7.5. It shows the change in binding energies of SO_3 due to oxygen addition on the

Pt(111) and Pd(111) surfaces. Computational details of the co-adsorption and the SO_3^*-O^* cross interactions are given in the Appendix H.

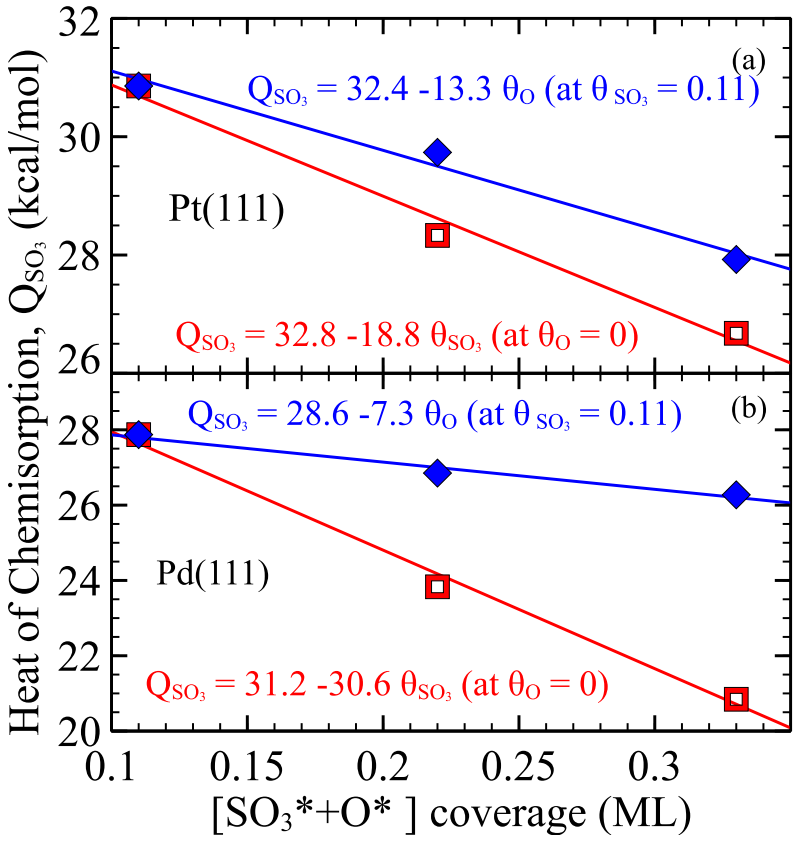

Fig. 7.5 DFT computed heat of chemisorption of SO_3 versus SO_3^* and SO_3^* + O^* coverages on Pt(111) and Pd(111) surfaces shown in panels a and b, respectively. The red lines represent a linear fit to SO_3^* - SO_3^* interactions. The blue lines represent a linear fit for the SO_3^* - O^* interactions as a function of O^* coverage at a fixed θ_{SO_3} = 0.11 ML. A (3×3) surface supercell was used for the energy computations. For the cross-interactions calculations, a fixed surface coverage of SO_3 (at θ_{SO_3} = 0.11 ML) was used while varying the O^* coverage.

7.5.5 Adsorption of Oxygen and SO_3 on the Surface Oxides

With no experimental or computational information on the interactions of O and SO_3 on the oxidized surfaces, it remains an unfamiliar and unexplored territory. This study examined the possible interactions of O and SO_3 on the surface oxides of both Pt and Pd. As expected, both

surface oxides show no affinity towards further O addition. However, we observed a significant difference in the interaction of SO_3 with the oxidized surfaces. The molecular binding energy of SO_3 on Pd vs. Pt surface oxide layers was –0.91 eV and –0.12 eV, respectively, i.e., SO_3 prefers to adsorb on PdO than on PtO_2. This large difference indicates that such interaction is a key descriptor and a pre-requisite for the higher sulfation tendency of Pd than Pt. As expected, our results showed that the co-adsorption SO_3 and O was not favored by both oxidized surfaces, due to the unwelcoming nature of the oxidized metal surface towards additional oxygen. Further details are given in Appendix H.

7.5.6 Surface Sulfates

Interaction of SO_3 and oxidized metal surface could lead to the formation of a surface sulfate layer and ultimately to the bulk sulfate phase. Unlike surface oxide phases of Pt and Pd, we do not have experimental information about the structure/morphology of the surface sulfate phases. Hence, we utilized the structural information of bulk sulfates to create surface sulfate models for both Pt and Pd. From the known structure of $PdSO_4$ and the predicted most stable structure of $PtSO_4$, we created a sulfate layer and placed this on the $(3\times\sqrt{3})$ surface supercell of the (111) surface of Pt or Pd to minimize the lattice strain. The choice of this surface supercell was the best possible compromise considering the size and computational cost restrictions. The structural model of the Pd surface sulfate is shown in panel 10 of Figure 7.6. Further details and other models are provided in the Appendix H.

7.6 Surface Phase Diagram

Assembling the information about the entire spectrum of stable phases discussed above, we have constructed phase diagrams for oxidizing and sulfating conditions on Pd(111) and Pt(111)

surfaces as shown in Figure 7.6. Since the entropic contribution to free energy due to vibrations is negligible and only temperature dependent, we have neglected the contribution to construct the phase diagrams. In this work, the inclusion of vibrational contributions does not alter the outcome of the phase diagram, as the relative magnitude is < 25 meV/Å^2 for the practically relevant temperature range of below 700 K. The impact of including the maximum vibrational contributions results in rather minor changes (up to 0.07 eV shift in O adsorbed phase boundaries and up to 0.16 eV shift in SO_3 adsorbed phase boundaries) to the features of the phase diagrams (most notably, a small shift in the phase boundaries in the phases with SO_3 adsorption). For example: at 300 K, the change of $\Delta\mu_{O_2}$ from –2.64 eV to –2.59 eV corresponds to an incredibly small pressure change of about -2.2×10^{-36} atm. Hence, none of the new stable structures disappears (or appears) from (or into) the phase diagram. While this analysis provides a justification for neglecting the vibrational contribution in many prior studies, [299, 306] we note that the inclusion of such contributions may be useful for complex systems. The computed vibrational contributions for various adsorbed phases are shown in Appendix I.

The surface phase diagram, as portrayed in Figure 7.6, is fairly complex due to possible existence of many phases. The chemical potentials of O_2 and SO_3 (using $\Delta\mu_{O_2}$ and $\Delta\mu_{SO_3}$) represent the x- and y- axes, respectively. Two more intuitive pressure scales (at representative temperatures of 300 K and 700 K) are shown opposite to the chemical potential range. Starting from the lower left corner of the phase diagram (i.e., low chemical potential region of O_2 and SO_3), we observe a stable clean metal surface phase in both cases (Pd and Pt). We clearly see a tendency to get oxidized easily in the case of Pd surface due to the oxygen chemical potential demarcation ($\Delta\mu_{O_2}$ = –2.52 eV for Pd and $\Delta\mu_{O_2}$ = –2.21 eV for Pt in the case of experimentally known $p(2\times2)$ phase) favoring the O adsorption (panel 5b of Figure 7.6). While keeping the SO_3 concentration low and moving towards higher O_2 chemical potential (horizontal direction), we encounter an experimentally observed stable phase of $p(2\times2)$-O overlayer [311] (i.e., θ_O =

0.25 ML, panel 5b of Figure 7.6) on both surfaces after the low coverage phase of θ_O = 0.06 ML. We note that the experimentally observed $c(2\times2)$-O overlayer (i.e., θ_O = 0.5 ML)– most likely a metastable phase before transforming to a more stable surface oxide phase– was not identified as a stable phase in our study. Furthermore, the kinetics will also play a role [306] for the transformation of the $c(2\times2)$-O overlayer structure to the surface oxide phase. Further increase in O_2 chemical potential leads to the formation of stable surface oxide phases (panel 6 of Figure 7.6) on both surfaces. Besides the experimentally observed morphological differences, these two phases deeply contrast in oxidation affinity. The onset of surface oxide formation on Pd(111) surface is from $\Delta\mu_{O_2}$ = –2.38 eV, whereas the onset point for the same on Pt(111) surface is from $\Delta\mu_{O_2}$ = –1.32 eV. As seen experimentally, [31] our results suggest that the oxidized phase of Pd, unlike the more stable metallic state of Pt, is the most prevalent state in relevant catalytic conditions (P $\sim$1 atm and T $\sim$200-500 °C).

Moving toward higher SO_3 chemical potential region while keeping the O_2 chemical potential low (vertical direction), we observed multiple stable phases of SO_3 (represented by a range of θ_{SO_3} = 0.11–0.33 ML, panels 7a-d of Figure 7.6) on both metal surfaces. Further increase in coverage of SO_3 on the metal surface is not stable due to the bulky nature of the molecule, and it falls beyond the realistic temperature and pressure ranges. Stronger binding strength of SO_3 with Pt (111) translates to the higher coverage favorability of SO_3 on Pt(111) than on Pd(111) surface ($\Delta\mu_{SO_3}$ = –0.64 eV for Pd and –1.0 eV for Pt in the case of θ_{SO_3} = 0.33 ML).

Towards the higher chemical potential region along the diagonal (i.e., higher chemical potential for both O_2 and SO_3), we observed quite different behaviors on both metal surfaces. Unlike a single co-adsorbed phase in case of Pd (panel 8a of Figure 7.6), multiple such phases were stable on the Pt surface (panels 8a-c of Figure 7.6). We observed a stable phase of SO_3 on the surface oxide of Pd (panels 9a-e of Figure 7.6), but this feature was absent in the case of Pt

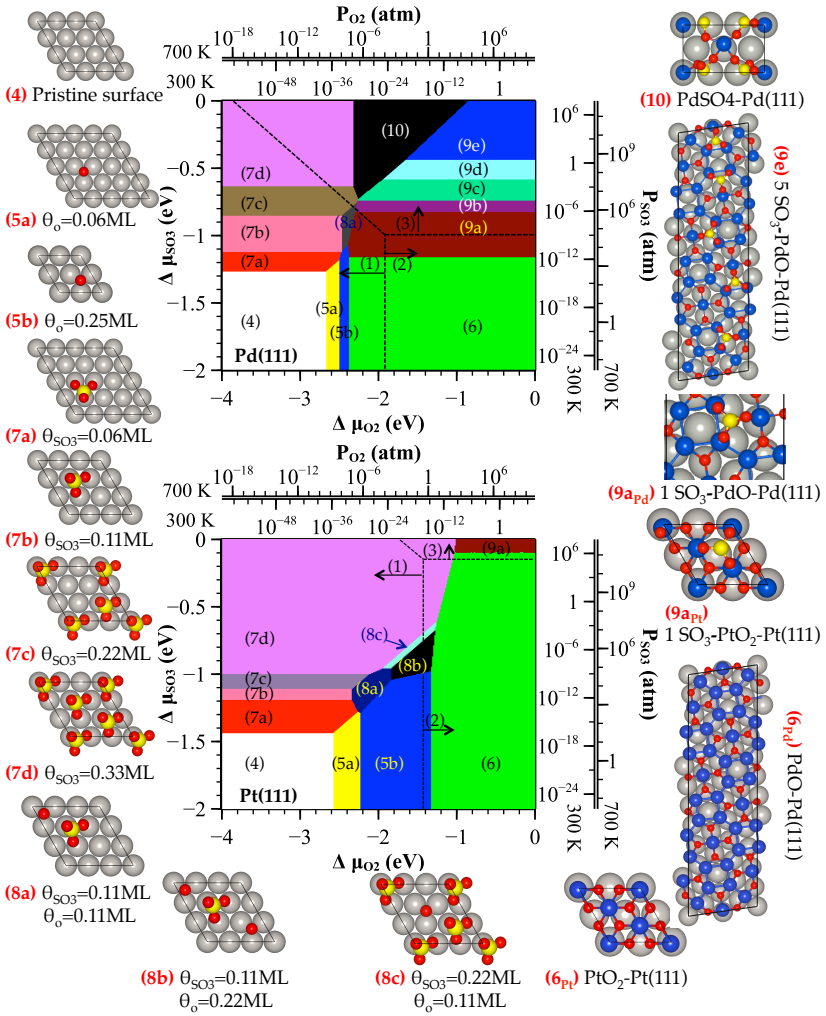

Fig. 7.6 Surface phase diagrams of Pd(111) (top panel) and Pt(111) (bottom panel) surfaces in a constrained thermodynamic equilibrium with SO_3 and O_2. The given chemical potential range of oxygen ($\Delta\mu_{O_2}$) and SO_3 ($\Delta\mu_{SO_3}$) are translated into a pressure range for two representative temperatures (300 K and 700 K). The numbering of the phases in each panel and structural models is adapted according to Figure 7.1. Common structural models for both Pt and Pd phases are represented by a single structure and corresponding structural number, whereas the different structural models of the same phase of Pt and Pd are subscripted (Pt or Pd) in the panel number (e.g., structures 6 and 9a). Structural models for 9b, 9c, and 9d of the top panel are not shown here for brevity, whereas the final structure 9e is shown. Dotted lines represent the bulk phase boundaries. Bulk phases numbering are shown with black arrows showing the respective regions. Bulk structural models are not shown here. Silver, red, and yellow spheres represent the Pt or Pd, Oxygen, and Sulfur respectively. Blue spheres represent the Pt or Pd in the surface oxide or surface sulfate models.

surface oxide at practically relevant temperature and pressure conditions (the phase boundary starts at $\Delta\mu_{SO_3}$ = –1.15 eV for Pd and –0.1 eV for Pt). This result aligns well with the idea of a pre-requisite state to proceed towards the surface sulfate and ultimately the bulk metal sulfate of Pd. We note that the surface sulfate phase (panel 10 of Figure 7.6) for Pd(111) appears at a reasonably low chemical potential, which agrees with the experimental observation of $PdSO_4$ formation under typical operating conditions. In the case of Pt, surface sulfate phase does not appear to be a stable phase. In realistic temperature and pressure conditions, we expect to have co-adsorbed phases of O and SO_3, surface-oxides phases of Pd, surface sulfate phase of Pd, and eventually the bulk sulfate phase of Pd.

Based on the observations so far, we briefly discuss the key insights and outcomes of this study. Figure 7.7 shows a comparison of the key features of the Pd(111) and Pt(111) surfaces. (a) Panel a shows the O_2 chemical potential difference in bulk oxide formation. Clearly, PdO formation is preferred over PtO_2 even at low oxygen chemical potential. (b) Panel b compares the O_2 chemical potential for surface oxide formation. We observe that the surface oxide formation is favored on Pd than Pt. (c) Panel c shows a rather indistinguishable O binding strength on both surfaces. This behavior aligns well with our natural belief of both metals being rather similar due to other physical/morphological properties such as metal-oxygen bond length ($\sim$2 Å), most stable adsorption sites (3-fold fcc), nature of charge transfer between metal-oxygen during adsorption [271] (d) On the other hand, the sulfation behavior is quite different for the two metals. Panel d compares the phase boundary onset of bulk sulfate formation in terms of O_2 and SO_3 chemical potentials (also see Figure 7.2). It is clearly observed that $PdSO_4$ formation is highly favored, unlike $PtSO_4$, under typical operating conditions. (e) Panel e displays the significant difference in SO3 binding strength on both surface oxide layers. SO_3 binds more strongly to PdO than PtO_2. (f) Panel f shows the surface energy comparison of pristine Pt(111) and Pd(111) surfaces. As observed experimentally, [312, 313] lower surface

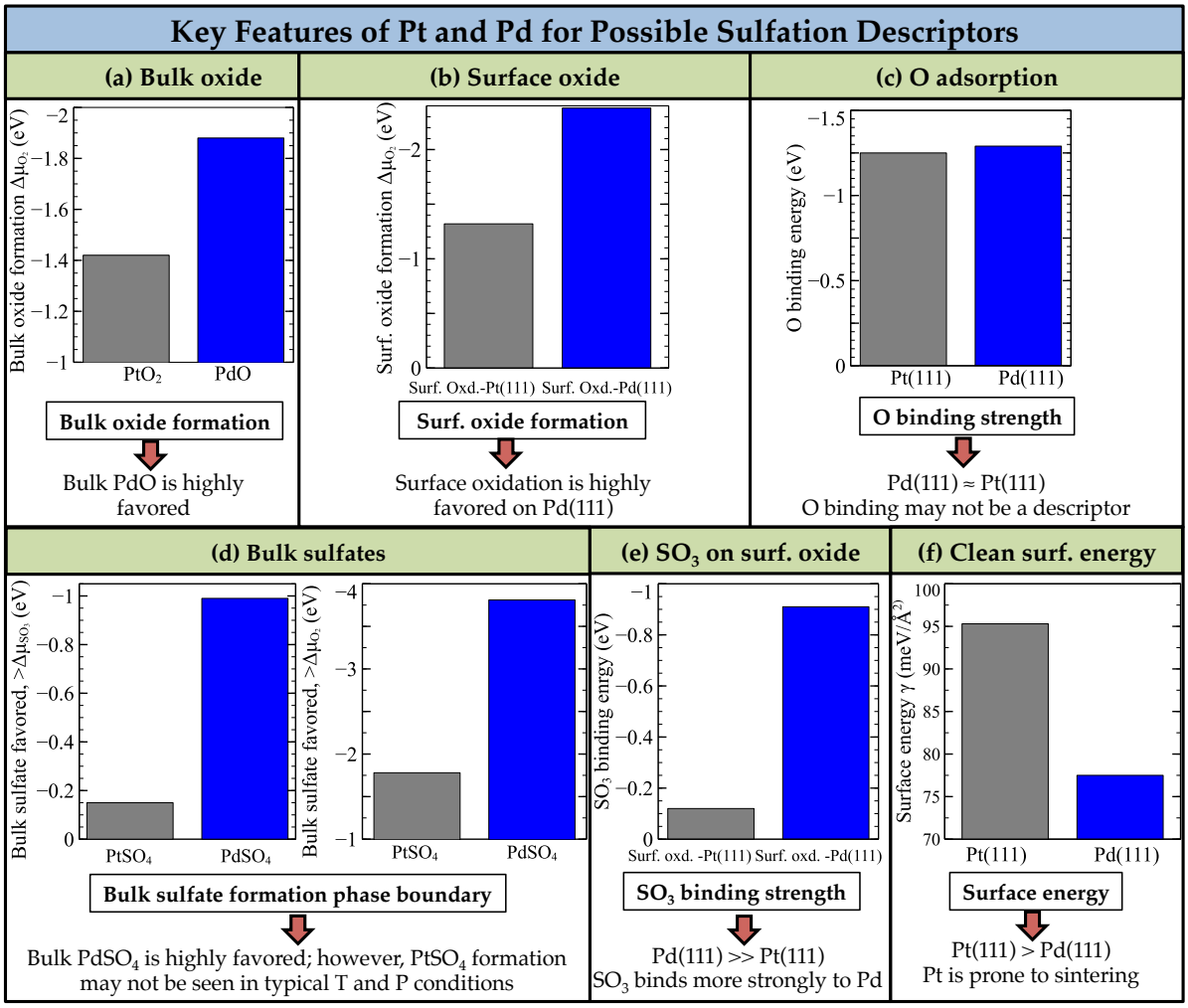

Fig. 7.7 Key descriptors for metal oxidation and sulfation. Panel a: $\Delta\mu_{O_2}$ onset point for bulk oxide formation, panel b: $\Delta\mu_{O_2}$ onset point for surface oxide formation, panel c: oxygen binding energy on the pristine (111) surfaces, panel d: bulk sulfate phase boundary onset point on $\Delta\mu_{O_2}$ and $\Delta\mu_{SO_3}$ scales, panel e: SO_3 binding strength on the surface oxides, and panel f: surface energy of pristine (111) surfaces. Significant differences are seen between Pt and Pd for all features, except in case of panel c (O binding energy).

energy of Pd compared to Pt is associated with the higher stability against sintering. This explains, along with the cost factor, why modern DOCs are bimetallic (Pt/Pd) in nature. Except for oxygen binding, all other key features can serve as descriptors for catalyst sulfation and the resulting deactivation, and hence we believe that they can be utilized for faster and effective screening of the potential sulfur resistant catalysts.

7.7 Limitations and Assumptions

We note that a few assumptions have been made in our work. First, our choice of surface plane is the (111) facet of Pt and Pd. Even though the catalyst nanoparticles contain many types of facets due to polycrystalline nature, the (111) facet is known to be the dominant, most stable and one of the most active surfaces. [314, 315] Second, we do not consider metal-support interactions in this study. The support can have a significant influence in some catalytic systems; however the Al_2O_3 support, typically used in emissions oxidation catalysts, is relatively inert. [264] Hence, we do not expect the support to impact or alter the main conclusions of this work. Third, we have constructed the surface sulfate model by placing bulk sulfate on the metal surface. Nevertheless, we believe our model captures the essence of a surface sulfate phase. Fourth, accuracy of the results presented here will depend on the choice of functional. However, given the number of cases considered and the sizes of systems for each case, considering nonlocal exchange-correlation functionals (e.g., hybrid functionals) would be computational cost prohibitive. Furthermore, we found that the PBE functional is also adequate to address the structure of van der Waals bonded PtO_2 layers. We calculated the energetics of the PtO_2-Pt(111) system with van der Waals interactions using the DFT-D2 functional. [316] The difference in total energy was < 2.2 meV/atom when van der Waals interactions were included. Thus, only the PBE functional was used throughout, and all conclusions were consistently reached using

this functional. It is expected that the qualitative aspects of our results and our main conclusions will not be impacted by the usage of a higher level functional. Finally, we have only considered the thermodynamic aspects in this study. While kinetics also plays an important role during phase transformations, the stability and possibility of the formation of such phases is controlled by thermodynamics, and should be considered first, before kinetic aspects are explored.

7.8 Conclusions

In summary, we have investigated the bulk and surface sulfation phenomena of Pt and Pd under catalytically relevant temperature and pressure conditions using first principles thermodynamics. Bulk and surface phase diagrams were constructed and possible stable phases en route to sulfation were identified. The bulk phase diagrams clearly suggested that the oxidation and sulfation of Pd is highly favored whereas metallic form of Pt is favored under catalytically relevant conditions. The surface phase diagrams clearly showed some remarkable differences between Pt (111) and Pd(111) surfaces in oxidizing and sulfating environments. Our results showed that the oxidized metal surfaces (i.e., surface oxides) are the key to understand sulfation. Pd showed a great affinity to form the surface oxide phase and showed significant SO_3-to-surface oxide binding strength. On the other hand, surface oxide layer formation is relatively less favored and SO_3-to-surface oxide binding strength was significantly smaller for Pt. Furthermore, the surface sulfate phase formation was favored only on Pd(111) in catalytically relevant conditions. The aforementioned key features can be used to screen materials to identify potential candidates for sulfur resistant catalysts.

Chapter 8

Conclusions and Future Work

8.1 Summary

Despite the widespread use and importance of diesel engines, toxic emissions from the diesel engine exhaust create a huge challenge for human health and environment. Some of the important emissions present in the diesel engine exhaust are CO, NO, CO_2, NO_2, SO_2, NH_3, HCN, CH_2O, CH_3CHO, PAHs, SOF, and PM. Many aftertreatment units, such as DOC, DPF, and DeNO$_x$ systems, are being used to control these emissions. Due to increasing stringent regulations to control emissions, the aftertreatment units need to be robust and efficient.

DOC is mainly responsible for oxidation of emissions from the engine as well as toxic byproducts. However, the deactivation of DOC due to sulfur present in the diesel fuel and lubricants creates a tremendous challenge, as DOC is a very expensive unit. Sulfur present in the fuel and lubricants is converted to SO_2 in the diesel engine. This SO_2 is converted to SO_3 due to high oxygen concentration in the engine exhaust. Formation of SO_3 triggers many interactions with metal oxides and supports which leads to the formation of sulfates and subsequent deactivation of the DOC. In addition to the metal and support sulfation, the

presence of H_2O and NH_3 also leads to the production of sulfuric acid and ammonium sulfate, respectively, to hasten the DOC deactivation.

This work mainly focuses on developing a fundamental understanding of the emissions oxidation chemistry and sulfation mechanism. To achieve the main goal, multidimensional and multi-scale approaches have been employed using various research techniques including experimental, microkinetic modeling and the first principles density functional theory methods.

To understand the primary oxidation chemistry on DOC, a detailed 124-step (62 reversible) microkinetic model is developed for five major emission species (i.e. CO, NO, NH_3, CH_2O, and HCN). Kinetic parameters for the detailed microkinetic model are extracted from ultra-high vacuum (UHV) temperature programmed desorption/reaction (TPD/TPR) experiments in literature. Starting with these kinetic parameters as initial estimates, the surface reaction mechanism is extensively tested against practically more relevant operating conditions, such as atmospheric pressure, dilute emissions concentrations, and short residence times, typically experienced by the Diesel Oxidation Catalysts (DOCs). In each of the five oxidation cases, mechanistic analysis is presented to uncover the most important reaction chemistry. The microkinetic model shows very good agreement with multiple experimental data sets on monolith and fixed bed reactor scale, for the oxidation of all five components. For practical implementation, the mechanism is further reduced to 94 steps (47 reversible) using preliminary model reduction.

Next, the model is extended to study SO_2 oxidation on Pt DOC. The developed mechanism correctly captures experimental data for SO_2 oxidation relevant to DOC operating conditions. This is the first step towards understanding SO_x interactions with Pt-Pd/alumina DOCs. This work has been extended further to include more complex chemistry of H_2SO_4 formation in the presence of H_2O and SO_x species.

Given the complexity of the SO_x chemistry with the Pt/Pd catalysts, a DFT based investigation is performed to understand how exactly these SO_x species interact with metal surfaces.

While Pt is more active in SO_2 oxidation than Pd; and no sulfate formation is observed on Pt. Unlike Pt, Pd metal remains in oxidized form (PdO) in the presence of oxygen and forms sulfate on the surface. This work tries to unravel these mysteries about vastly different behaviors of Pt and Pd towards SO_x and sulfation. First, thermodynamic study is performed to understand the binding patterns, binding strengths, and lateral interactions. Then SO_x oxidation minimum energy pathways are identified and the activation barriers are calculated. Here, we are able to show the different behaviors from Pt and Pd towards SO_x.

To understand the sulfation phenomena in realistic situation, temperature and pressure factors need to be considered. Thus, going beyond the traditional zero temperature and pressure DFT computations, this work introduced the first principles thermodynamics approach to mimic the oxidization and sulfation environment for Pt and Pd surfaces. For the first time, the possible sulfation mechanism is discovered which showed drastically different behavior on Pt and Pd. In practically relevant temperatures and O_2 and SO_3 partial pressures, our results show that Pt and Pd show significantly different behavior towards oxidation and sulfation. PdO formation is favored even at low oxygen chemical potential; however, PtO_2 formation is not favorable in catalytically relevant conditions. Similarly, $PdSO_4$, and adsorbed SO_3 and oxygen species on clean and oxidized surfaces are highly favored, whereas $PtSO_4$ formation does not occur at typical temperature and pressure conditions. Finally, several descriptors are identified that correlate to heightened sulfation tendencies, such as the critical O chemical potential for bulk oxide and surface oxide formation, chemical potentials O and SO_3 for bulk sulfate formation, and SO_3 binding strength on metal surface-oxide layers, which can be used to explore promising sulfur resistant catalysts.

8.2 Future Directions

8.2.1 Microkinetic Model Extension

Higher number nitrogen and carbon containing emissions species like acetonitrile and the oxygenates like acetaldehyde can be the immediate extension of our model. While this work lays the foundation of the reactions and mechanism for the mono carbon and nitrogen containing species, the inclusion of those higher C and N containing species should be straightforward using bottom up modeling strategy.

Another aspect of the thesis is to lay out the foundation to include the Hydrocarbons oxidation mechanism on the DOCs. Although this work only involves in the oxidation of C_2 HC species (C_2H_4), many different HCs exist in diesel exhaust, including aromatics, saturated (paraffin), and unsaturated (olefin) components. Generally, ethylene, propylene, ethane and propane are used to model unsaturated HCs and saturated HCs, respectively. Different HCs and mixtures of HCs show different rates of reaction. For example, alkanes tend to show slower reaction rates as the carbon chain length increases because more adjacent sites are required to achieve adsorption of the hydrocarbon chains. While monometallic Pt catalysts have the most efficient light-off performance for hydrocarbons, one can plan to investigate C_3 HC oxidation on Pt to understand the fundamental chemistry on Pt based DOCs and extend the C_2 oxidation chemistry. Further, this mechanism can be expanded easily to include higher hydrocarbon species by utilizing bottom-up mechanism development technique. [317]

8.2.1.1 Support Sulfation

The diffusion of SO_x species into the bulk alumina initiates the support sulfation process. This process is accelerated due the oxidizing environment in the engine exhaust. Kinetics of alumina support sulfation needs be included in the emissions-oxidation model to correctly simulate

DOC deactivation. In this future work, one can investigate the alumina sulfation mechanism and kinetics using DFT. Furthermore, one can conduct Nudged Elastic Band (NEB) calculations using VASP to estimate the activation energy for alumina sulfation. Pre-exponential factor for alumina sulfation can be estimated using vibrational frequency calculations combined with transition state theory (TST). These first-principles DFT calculations involving SO_3, alumina support and aluminum sulfate will provide the theoretical estimates for the kinetic rate constant for alumina support sulfation. Reactor modeling with the support sulfation mechanism will provide more realistic estimation of the DOC sulfation process.

8.2.1.2 Reactor Modeling with Sulfation Kinetics

Predicting DOC performance over time will require a kinetic and reactor modeling framework to incorporate the extent of metal and support sulfation coupled with the emissions-oxidation kinetics. After combining the emissions-oxidation model with the kinetic parameters for catalyst sulfation, one can proceed with PFR modeling to predict the DOC activity/performance over time. Incorporation of catalyst sulfation in reactor modeling is a challenging task, as the extent of metal and support sulfation needs to be coupled with the emissions-oxidation kinetics. We can utilize two prior experimental observations to overcome this challenge: (i) deactivation of metal oxide results in inactive metal sulfate sites and (ii) alumina sulfation results in decreased surface area. Consistent with the first observation, one can propose to implement two types of sites: sulfated inactive sites and non-sulfated active sites. As the extent of metal sulfation increases, the sulfated inactive sites increase relative to the non-sulfated active sites; however, the total site density is conserved. Consistent with the second observation, the overall surface area available for emissions-oxidation chemistry decreases, as the extent of alumina support sulfation increases.

8.2.2 Emissions Oxidation and Sulfation on Bimetallic Pt-Pd Catalysts

The next level of this work may be the exploration of bimetallic nature of the catalysts in DOCs. This can be proceeded with the identification of the stable bimetallic composition under realistic conditions. The first step would be the structure prediction of bimetallic Pt-Pd alloy using USPEX. Then, the stability of the bimetallic catalysts under various condition can be studied using the first principles thermodynamics. Once, thermodynamic stability of the phases are established, the kinetics investigation can be done.

References

[1] The Diesel Technology Forum, Diesel-Powered Machines and Equipment: Essential Uses, Economic Importance and Environmental Performance, Technical Report, The Diesel Technology Forum, 2003.

[2] S. Bensaid, C. J. Caroca, N. Russo, D. Fino, Can. J. Chem. Eng. 89 (2011) 401–407.

[3] R. Prasad, V. R. Bella, Bull. Chem. Reac. Eng. Catal. 5 (2010) 95–101.

[4] C. G. Schneider, L. B. Hill, Diesel and health in america: the lingering threat, Technical Report, Clean Air Task Force (CATF), 2005.

[5] California Energy Commission, California Energy Commission. Petroleum Watch; California Energy Commission: Sacramento, CA, http://energyalmanac.ca.gov, 2011. [Online; accessed 10-July-2012].

[6] U.S. Energy Information Administration, U.S. Energy Information Administration (EIA). diesel fuel explained-use of diesel, http://www.eia.gov/energyexplained/index.cfm?page=diesel_use, 2011. [Online; accessed 10-July-2012].

[7] S. Salomons, Kinetic Models for a Diesel Oxidation Catalyst, Ph.D. thesis, University of Alberta, Canada, 2008.

[8] P. Bera, M. S. Hegde, J. Indian Inst. Sci. 90 (2010) 299–325.

[9] O. Kröcher, M. Widmer, M. Elsener, D. Rothe, Ind. Eng. Chem. Res. 48 (2009) 9847–9857.

[10] K. T. Magara-Gomez, M. R. Olson, T. Okuda, K. A. Walz, J. J. Schauer, Atmos. Environ. 50 (2012) 307–313.

[11] M. C. H. Lim, G. A. Ayoko, L. Morawska, Z. D. Ristovski, E. R. Jayaratne, Atmos. Environ. 39 (2005) 7836–7848.

[12] H.-L. Chiang, Y.-M. Lai, S.-Y. Chang, Atmos. Environ. 47 (2012) 399–406.

[13] J. Jung, J. Lee, S. Song, K. Chun, Int. J. Automot. Technol. 9 (2008) 423–428.

[14] H. Zhao, Y. Ge, X. Wang, J. Tan, A. Wang, K. You, Energy Fuels 24 (2010) 985–991.

[15] G. Corro, React. Kinet. Catal. Lett. 75 (2002) 89–106.

[16] H. Zhao, R. G. Tonkyn, S. E. Barlow, B. E. Koel, C. H. F. Peden, Appl. Catal. B 65 (2006) 282–290.

[17] O. Kröcher, M. Elsener, Appl. Catal. B 92 (2009) 75–89.

[18] A. Macor, F. Avella, D. Faedo, Appl. Energy 88 (2011) 4989–5001.

[19] P.-Q. Tan, Z.-Y. Hu, D.-M. Lou, Fuel 88 (2009) 1086–1091.

[20] J. Rodriguez-Fernandez, F. Oliva, R. A. Vazquez, Energy & Fuels 25 (2011) 2039–2048.

[21] M. Shrivastava, A. Nguyen, Z. Zheng, H.-W. Wu, H. S. Jung, Environmental Science & Technology 44 (2010) 4796–4801.

[22] G. Liu, P.-X. Gao, Catal. Sci. & Technol. 1 (2011) 552–568.

[23] E. Ghzaoui, M. Lindheimer, A. Lindheimer, S. Lagerge, S. Partyka, Colloids Surf., A 233 (2004) 79–86.

[24] C. Y. Lin, J. C. Huang, Ocean Engineering 30 (2003) 1699–1715.

[25] J. Kašpar, P. Fornasiero, N. Hickey, Catal. Today 77 (2003) 419–449.

[26] S. Jelles, SAE Technical Paper 1999-01-0113 (1999).

[27] S. Kumar, M. Nayek, A. Kumar, A. Tandon, P. Mondal, P. Vijay, U. D. Bhangale, D. Tyagi, Am. Chem. Sci. J. 1 (2011) 1–27.

[28] M. Zheng, G. T. Reader, J. G. Hawley, Energy Convers. and Manage. 45 (2004) 883–900.

[29] R. M. Heck, R. J. Farrauto, S. T. Gulati, Catalytic air pollution control: commercial technology, John Wiley sons, USA, 3 edition, 2009.

[30] J. P. A. Neeft, M. Makkee, J. A. Moulijn, Fuel Process. Technol. 47 (1996) 1–69.

[31] H. N. Sharma, S. L. Suib, A. B. Mhadeshwar, Interactions of Sulfur Oxides With Diesel Oxidation Catalysts (DOCs), volume 1132 of *Novel Materials for Catalysis and Fuels Processing*, American Chemical Society, Washington, DC, pp. 117–155.

[32] A. Russell, W. S. Epling, Catal. Rev. 53 (2011) 337–423.

[33] S. Williams, Surface intermediates, mechanism, and reactivity of soot oxidation, Ph.D. thesis, University of Toronto, 2008.

[34] T. M. V., Catal. Today 163 (2011) 33–41.

[35] A. Yezerets, N. W. Currier, D. H. Kim, H. A. Eadler, W. S. Epling, C. H. F. Peden, Appl. Catal. B 61 (2005) 120–129.

[36] B. Azambre, S. Collura, P. Darcy, J. M. Trichard, P. D. Costa, A. García-Garcia, A. Bueno-López, Fuel Process. Technol. 92 (2011) 363–371.

[37] B. R. Stanmore, V. Tschamber, J. F. Brilhac, Fuel 87 (2008) 131–146.

[38] F. Jacquot, J. Brilhac, R. Noirot, SAE Technical Paper 2004-01-1943 (2004).

[39] Retrofit, What is a diesel particulate filter, http://www.emissionsretrofit.com, 2015. Accessed: 2015-02-30.

[40] F. Basile, G. Fornasari, A. Grimandi, M. Livi, A. Vaccari, Appl. Catal. B 69 (2006) 58–64.

[41] J. F. Kelly, M. Stanciulescu, J.-P. Charland, Fuel 85 (2006) 1772–1780.

[42] V. Houel, P. Millington, R. Rajaram, A. Tsolakis, Appl. Catal. B 73 (2007) 203–207.

[43] A. Grossale, I. Nova, E. Tronconi, Catal. Today 136 (2008) 18–27.

[44] E. Tronconi, I. Nova, C. Ciardelli, D. Chatterjee, B. Bandl-Konrad, T. Burkhardt, Catal. Today 105 (2005) 529–536.

[45] J. R. H. Carucci, K. Arve, S. Bartova, K. Eranen, T. Salmi, D. Y. Murzin, Catal. Sci. Technol. 1 (2011) 1456–1465.

[46] K. Arve, H. Backman, F. Klingstedt, K. Eranen, D. Y. Murzin, Appl. Catal. A 303 (2006) 96–102.

[47] J.-S. Choi, W. P. Partridge, C. S. Daw, Appl. Catal. A 293 (2005) 24–40.

[48] S. S. Mulla, N. Chen, W. N. Delgass, W. S. Epling, F. H. Ribeiro, Catal. Lett. 100 (2005) 267–270.

[49] W. S. Epling, L. E. Campbell, A. Yezerets, N. W. Currier, J. E. Parks, Catal. Rev. Sci. Eng. 46 (2004) 163–245.

[50] M. Colombo, I. Nova, E. Tronconi, Chem. Eng. Sci. 75 (2012) 75–83.

[51] A. Scheuer, W. Hauptmann, A. Drochner, J. Gieshoff, H. Vogel, M. Votsmeier, Appl. Catal. B 111-112 (2012) 445–455.

[52] A. Scheuer, A. Drochner, J. Gieshoff, H. Vogel, M. Votsmeier, Catal. Today 188 (2012) 70–79.

[53] A. Scheuer, O. Hirsch, R. Hayes, H. Vogel, M. Votsmeier, Catal. Today 175 (2011) 141–146.

[54] M. Votsmeier, A. Scheuer, A. Drochner, H. Vogel, J. Gieshoff, Catal. Today 151 (2010) 271–277.

[55] K. Kamasamudram, A. Yezerets, X. Chen, N. Currier, M. Castagnola, H. Chen, SAE Technical Paper 2011-01-1314 (2011).

[56] J.-Y. Luo, D. Kisinger, A. Abedi, W. S. Epling, Appl. Catal. A 383 (2010) 182–191.

[57] T. J. Wallington, C. K. Lambert, W. C. Ruona, Energy Policy 54 (2011) 47–53.

[58] H. Oh, J. Luo, W. Epling, Catal. Lett. 141 (2011) 1746–1751.

[59] A. Morlang, U. Neuhausen, K. V. Klementiev, F. W. Schütze, G. Miehe, H. Fuess, E. S. Lox, Appl. Catal. B 60 (2005) 191–199.

[60] A. K. Neyestanaki, F. Klingstedt, T. Salmi, D. Y. Murzin, Fuel 83 (2004) 395–408.

[61] W. Majewski, M. Khair, SAE Technical Paper (2006).

[62] K. Hauff, U. Tuttlies, G. Eigenberger, U. Nieken, Appl. Catal. B 100 (2010) 10–18.

[63] J. Matthey, Palladium use in diesel oxidation catalysts, 2009.

[64] Diesel oxidation catalysts, http://www.preciousmetals.umicore.com, 2015. Accessed: 2015-02-30.

[65] A. Setiabudi, M. Makkee, J. A. Moulijn, Appl. Catal. B 50 (2004) 185–194.

[66] C. J. Tighe, M. V. Twigg, A. N. Hayhurst, J. S. Dennis, Combust. Flame 159 (2012) 77–90.

[67] H. Miessner, K.-P. Francke, R. Rudolph, Appl. Catal. B 36 (2002) 53–62.

[68] G. Centi, S. Perathoner, Selective catalytic reduction(SCR) processes on metal oxides, Metal Oxides: Chemistry And Applications, Taylor & Francis, Boca Raton, Florida, USA, pp. 661–682.

[69] C. S. Sampara, Global Reaction Kinetics for Oxidation and Storage in Diesel Oxidation Catalysts, Ph.D. thesis, University of Michigan, 2008.

[70] R. M. Heck, R. J. Farrauto, Appl. Catal. A 221 (2001) 443–457.

[71] C. H. Bartholomew, R. J. Farrauto, Fundamentals of Industrial Catalytic Processes, volume 2, John Wiley & Sons, Hoboken, New Jersey, 2006.

[72] C. H. Bartholomew, Appl. Catal. A 212 (2001) 17–60.

[73] Fuels and fuel additives:diesel fuel, http://www.epa.gov/OTAQ/fuels/dieselfuels, 2006. [Online; accessed 10-July-2012].

[74] CDFA, Clean diesel fuel alliance, http://www.clean-diesel.org/, 2012. [Online; accessed 1–Aug-2012].

[75] ENVIRONMENTAL PROTECTION AGENCY, Environmental protection agency: Technical amendments to the highway and nonroad diesel regulations, Federal Register Volume 71, Number 83 (Monday, May 1, 2006), 2006.

[76] M. Lemmetty, T. Rönkkö, A. Virtanen, J. Keskinen, L. Pirjola, Aerosol Science and Technology 42 (2008) 916–929.

[77] P. Bielaczyc, J. Keskinen, J. Dzida, R. Sala, T. Ronkko, T. Kinnunen, P. Matilainen, P. Karjalainen, M. J. Happonen, SAE Technical Paper 2012-01-0366 (2012).

[78] T. Kolli, M. Huuhtanen, A. Hallikainen, K. Kallinen, R. Keiski, Catal. Lett. 127 (2009) 49–54.

[79] E. Xue, K. Seshan, J. R. H. Ross, Appl. Catal. B 11 (1996) 65–79.

[80] G. A. Stratakis, Experimental Investigation of Catalytic Soot Oxidation and Pressure Drop Characteristics in Wall-Flow Diesel Particulate Filters, Ph.D. thesis, University of Thessaly, 2004.

[81] J. K. Lampert, M. S. Kazi, R. J. Farrauto, Appl. Catal. B 14 (1997) 211–223.

[82] A. Russell, C. Henry, N. W. Currier, A. Yezerets, W. S. Epling, Appl. Catal. A 397 (2011) 272–284.

[83] J. A. Rodriguez, J. Hrbek, Acc. Chem. Res. 32 (1999) 719–728.

[84] T. Truex, SAE Technical Paper 1999-01-1543 (1999).

[85] E. Xue, K. Seshan, J. G. van Ommen, J. R. H. Ross, Appl. Catal. B 2 (1993) 183–197.

[86] S. Koutsopoulos, S. B. Rasmussen, K. M. Eriksen, R. Fehrmann, Appl. Catal. A: Gen. 306 (2006) 142–148.

[87] D. L. Mowery, R. L. McCormick, Appl. Catal. B: Env. 34 (2001) 287–297.

[88] G. Corro, A. Velasco, R. Montiel, Catal. Commun. 2 (2001) 369–374.

[89] J. H. P. no, J. T. Miller, S. S. Mulla, W. N. Delgass, F. H. Ribeiro, J. Catal. 282 (2011) 13–24.

[90] M.-V. Mathieu, M. Primet, Appl. Catal. 9 (1984) 361–370.

[91] R. H. Hammerle, T. J. Truex, Am. Chem. Soc. 21 (1976) 769–783.

[92] S. Matsumoto, Catal. Today 90 (2004) 183–190.

[93] G. Corro, C. Cano, J. L. G. Fierro, J. Mol. Catal. A: Chem. 315 (2010) 35–42.

[94] T. Kolli, T. Kanerva, M. Huuhtanen, M. Vippola, K. Kallinen, T. Kinnunen, T. Lepistò, J. Lahtinen, R. L. Keiski, Catal. Today 154 (2010) 303–307.

[95] J. Gieshoff, M. Pfeifer, A. Schäfer-Sindlinger, P. Spurk, G. Garr, T. Leprince, SAE Technical Paper 2001-01-0514 (2001).

[96] P. Zelenka, W. Cartellieri, P. Herzog, Appl. Catal. B 10 (1996) 3–28.

[97] R. J. Farrauto, K. E. Voss, Appl. Catal. B 10 (1996) 29–51.

[98] J. D. Herner, S. Hu, W. H. Robertson, T. Huai, M. C. O. Chang, P. Rieger, A. Ayala, Env. Sci. Technol. 45 (2011) 2413–2419.

[99] B. Ramachandran, R. G. Herman, S. Choi, H. G. Stenger, C. E. Lyman, J. W. Sale, Catal. Today 55 (2000) 281–290.

[100] J. A. Dumesic, D. F. Rudd, L. M. Aparicio, J. E. Rekoske, A. A. Trevino, The Microkinetics of Heterogeneous Catalysis, American Chemical Society, 1 edition, 1993.

[101] A. B. Mhadeshwar, H. Wang, D. G. Vlachos, J. Phys. Chem. B 107 (2003) 12721–12733.

[102] A. B. Mhadeshwar, J. R. Kitchin, M. A. Barteau, D. G. Vlachos, Catal. Lett. 96 (2004) 13–22.

[103] A. B. Mhadeshwar, D. G. Vlachos, Combust. Flame 142 (2005) 289–298.

[104] M. Salciccioli, M. Stamatakis, S. Caratzoulas, D. G. Vlachos, Chem. Eng. Sci. 66 (2011) 4319–4355.

[105] D. A. Hansgen, D. G. Vlachos, J. G. Chen, Nat. Chem. 2 (2010) 484–489.

[106] W. Hauptmann, M. Votsmeier, J. Gieshoff, D. Vlachos, A. Drochner, H. Vogel, Top. Catal. 52 (2009) 1925–1928.

[107] E. Shustorovich, H. Sellers, Surf. Sci. Reports 31 (1998) 1–119.

[108] E. Shustorovich, Advances in Catalysis 37 (1990) 101–164.

[109] G. P. Smith, D. M. Golden, M. Frenklach, N. W. Moriarty, B. Eiteneer, M. Goldenberg, C. T. Bowman, R. K. Hanson, S. Song, W. C. Gardiner, V. V. Lissianski, Z. Qin, Gri-mech 3.0, 1999.

[110] S. Li, L. Petzold, Design of new DASPK for sensitivity analysis, 1999.

[111] W. Kohn, L. J. Sham, Phys. Rev. 140 (1965) A1133–A1138.

[112] P. Hohenberg, W. Kohn, Phys. Rev. 136 (1964) B864–B871.

[113] G. Kresse, J. Furthmüller, Phys. Rev. B 54 (1996) 11169.

[114] P. E. Blöchl, Phys. Rev. B 50 (1994) 17953–17979.

[115] A. E. Mattsson, R. Armiento, P. A. Schultz, T. R. Mattsson, Phys. Rev. B 73 (2006) 195123.

[116] Q. Fu, J. Yang, Y. Luo, - J. Phys. Chem. C 115 (2011) 6864–6869.

[117] A. Eichler, F. Mittendorfer, J. Hafner, Phys. Rev. B 52 (2000) 4744–4755.

[118] M. Todorova, K. Reuter, M. Scheffler, J. Phys. Chem. B 108 (2004) 14477–14483.

[119] D. R. Alfonso, Surf. Sci. 596 (2005) 229–241.

[120] V. Branger, V. Pelosin, K. F. Badawi, P. Goudeau, Thin Solid Films 275 (1996) 22–24.

[121] C. Kittel, Introduction to Solid State Physics, volume 8, Wiley, 2004.

[122] B. E. Nieuwenhuys, W. M. H. Sachtler, Surf. Sci. 34 (1973) 317–336.

[123] J. Speight, Lange's Handbook of Chemistry, volume 16, McGraw-Hill Professional, Boston, MA, 2004.

[124] N. E. Singh-Miller, N. Marzari, Phys. Rev. B 80 (2009) 235407.

[125] M. Scheffler, C. Stampfl, Theory of adsorption on metal substrates, volume 2 of *Handbook of Surf. Sci.*, Elsevier, Amsterdam, pp. 285–356.

[126] C. Stampfl, A. Soon, S. Piccinin, H. Z. Hongqing Shi and, J. Phys. Condens. Matter 20 (2008) 184021.

[127] de Walle van, G. Ceder, J. Phase Equilib. 23 (2002) 348–359.

[128] A. R. Oganov, S. Ono, Nature 430 (2004) 445–448.

[129] X. Gong, J. Huang, Y. Chen, M. Wu, G. Liu, X. Lei, J. Liang, H. Cao, F. Tang, B. Xu, C. Ouyang, Int. J. Electrochem. Sci. 8 (2013) 10549–10556.

[130] C. W. Glass, A. R. Oganov, N. Hansen, Comput. Phys. Commun. 175 (2006) 713–720.

[131] A. R. Oganov, C. W. Glass, J. Chem. Phys. 124 (2006).

[132] A. R. Oganov, C. W. Glass, J. Chem. Phys. 124 (2006) 244704.

[133] A. R. Oganov, A. O. Lyakhov, M. Valle, Acc. Chem. Res. 44 (2011) 227–237.

[134] X.-F. Zhou, X. Dong, A. R. Oganov, Q. Zhu, Y. Tian, H.-T. Wang, Phys. Rev. Lett. 112 (2014).

[135] A. O. Lyakhov, A. R. Oganov, H. T. Stokes, Q. Zhu, Comp. Phys. Comm. 184 (2013) 1172–1182.

[136] Q. Zhu, L. Li, A. R. Oganov, P. B. Allen, Phys. Rev. B 87 (2013) 195317.

[137] V. Sharma, C. C. Wang, R. G. Lorenzini, R. Ma, Q. Zhu, D. W. Sinkovits, G. Pilania, A. R. Oganov, S. Kumar, G. A. Sotzing, S. A. Boggs, R. Ramprasad, Nat. Comm. 5 (2014) 4845.

[138] Q. Zhu, V. Sharma, A. R. Oganov, R. Ramprasad, J. Chem. Phys. 141 (2014) 154102.

[139] J. L. Gland, E. B. Kollin, The J. Chem. Phys. 78 (1983) 963–974.

[140] A. L. Gerrard, J. F. Weaver, The J. Chem. Phys. 123 (2005) 224703.

[141] A. S. Ivanova, E. M. Slavinskaya, R. V. Gulyaev, V. I. Zaikovskii, O. A. Stonkus, I. G. Danilova, L. M. Plyasova, I. A. Polukhina, A. I. Boronin, Appl. Catal. B 97 (2010) 57–71.

[142] A. Manasilp, E. Gulari, Appl. Catal. B 37 (2002) 17–25.

[143] N. Rankovic, A. Nicolle, P. D. Costa, J. Phys. Chem. C 114 (2010) 7102–7111.

[144] N. Rankovic, A. Nicolle, D. Berthout, P. D. Costa, Catal. Commun. 12 (2010) 54–57.

[145] M. Crocoll, S. Kureti, W. Weisweiler, J. Catal. 229 (2005) 480–489.

[146] L. Olsson, H. Persson, E. Fridell, M. Skoglundh, B. Andersson, J. Phys. Chem. B 105 (2001) 6895–6906.

[147] W. Hauptmann, M. Votsmeier, J. Gieshoff, A. Drochner, H. Vogel, Appl. Catal. B 93 (2009) 22–29.

[148] R. J. Gorte, L. D. Schmidt, J. L. Gland, Surf. Sci. 109 (1981) 367–380.

[149] D. H. Parker, M. E. Bartram, B. E. Koel, Surf. Sci. 217 (1989) 489–510.

[150] J. F. Weaver, J.-J. Chen, A. L. Gerrard, Surf. Sci. 592 (2005) 83–103.

[151] C. T. Campbell, G. Ertl, H. Kuipers, J. Segner, Surf. Sci. 107 (1981) 220–236.

[152] J. L. Gland, B. A. Sexton, Surf. Sci. 94 (1980) 355–368.

[153] V. P. Zhdanov, B. Kasemo, Surf. Sci. 415 (1998) 403–410.

[154] C. Panja, Chemisorption on the (111) and (100) faces of platinum-tin bimetallic surfaces, Ph.D. thesis, University of Southern California, 2000.

[155] M. T. Paffett, S. C. Gebhard, R. G. Windham, B. E. Koel, J. Phys. Chem. 94 (1990) 6831.

[156] B. E. Hayden, A. M. Bradshaw, J. Electron. Spectrosc. Relat. Phenom. 30 (1983) 51.

[157] N. K. Ray, A. B. Anderson, Surf. Sci. 119 (1982) 35–45.

[158] Y. Ishikawa, M.-S. Liao, C. R. Cabrera, Surf. Sci. 463 (2000) 66–80.

[159] C. Daniel, M.-O. Clartè, S. P. Teh, O. Thinon, H. Provendier, A. C. V. Veen, B. J. Beccard, Y. Schuurman, C. Mirodatos, J. Catal. 272 (2010) 55–64.

[160] M. Rinnemo, D. Kulginov, S. Johansson, K. L. Wong, V. P. Zhdanov, B. Kasemo, Surf. Sci. 376 (1997) 297–309.

[161] M. Lynch, P. Hu, Surf. Sci. 458 (2000) 1–14.

[162] M. Stamatakis, Y. Chen, D. G. Vlachos, J. Phys. Chem. C 115 (2011) 24750–24762.

[163] Y. Li, L. Xu, X. Yao, T. Luo, G. Li, J. Phys. Conf. Ser. 339 (2012) 1–8.

[164] R. W. McCabe, L. D. Schmidt, Surf. Sci. 65 (1977) 189–209.

[165] S. K. Desai, M. Neurock, K. Kourtakis, J. Phys. Chem. B 106 (2002) 2559.

[166] J. Greeley, M. Mavrikakis, J. Am. Chem. Soc. 126 (2004) 3910.

[167] S. Alayoglu, A. U. Nilekar, M. Mavrikakis, B. Eichhorn, Nat. Mater. 7 (2008) 333.

[168] A. A. Gokhale, S. Kandoi, J. P. Greeley, M. Mavrikakis, J. A. Dumesic, Chem. Eng. Sci. 59 (2004) 4679–4691.

[169] S. C. Gebhard, B. E. Koel, J. Phys. Chem. 96 (1992) 7056.

[170] H. Zhu, W. Guo, R. Jiang, L. Zhao, X. Lu, M. Li, D. Fu, H. Shan, Langmuir 26 (2010) 12017–12025.

[171] D. C. Ford, A. U. Nilekar, Y. Xu, M. Mavrikakis, Surf. Sci. 604 (2010) 1565–1575.

[172] G. B. Fisher, J. L. Gland, Surf. Sci. 94 (1980) 446–455.

[173] L. C. Grabow, A. A. Gokhale, S. T. Evans, J. A. Dumesic, M. Mavrikakis, J. Phys. Chem. C 112 (2008) 4608–4617.

[174] J. Kua, W. A. Goddard, J. Am. Chem. Soc. 121 (1999) 10928–10941.

[175] Y. Zhai, D. Pierre, R. Si, W. Deng, P. Ferrin, A. U. Nilekar, G. Peng, J. A. Herron, D. C. Bell, H. Saltsburg, M. Mavrikakis, M. Flytzani-Stephanopoulos, Science 329 (2010) 1633–1636.

[176] J.-H. Meng, C. A. Menning, M. B. Zellner, J. G. Chen, Surf. Sci. 604 (2010) 1845–1853.

[177] G. Psofogiannakis, Ab-initio DFT Modeling of the Oxidation of Methane on Transition Metal Catalysts, Ph.D. thesis, University of Ottawa, 2007.

[178] A. Picolin, C. Busse, A. Redinger, M. Morgenstern, T. Michely, J. Phys. Chem. C 113 (2009) 691–697.

[179] J. M. Gohndrone, C. W. Olsen, A. L. Backman, T. R. Gow, E. Yagasaki, R. I. Masel, J. Vac. Sci. Technol., A 7 (1989) 1986–1990.

[180] J. L. Gland, E. B. Kollin, Surf. Sci. 104 (1981) 478–490.

[181] W. D. Mieher, W. Ho, Surf. Sci. 322 (1995) 151–167.

[182] A. Scheuer, M. Votsmeier, A. Schuler, J. Gieshoff, A. Drochner, H. Vogel, Topics in Catalysis 52 (2009) 1847–1851.

[183] J. L. Gland, Surf. Sci. 71 (1978) 327–350.

[184] D. C. Ford, Y. Xu, M. Mavrikakis, Surf. Sci. 587 (2005) 159–174.

[185] G. Novell-Leruth, Catalytic Ammonia Oxidation on Nobel Metal Surfaces: A Theoretical Study, Ph.D. thesis, Universitat Rovira I Virgili, 2009.

[186] G. Novell-Leruth, A. Valcàrcel, J. Pèrez-Ramìrez, J. M. Ricart, J. Phys. Chem. C 111 (2007) 860–868.

[187] W. K. Offermans, A. P. J. Jansen, R. A. van Santen, G. Novell-Leruth, J. M. Ricart, J. Perez-Ramirez, J. Phys. Chem. C 111 (2007) 17551–17557.

[188] W. K. Offermans, A. P. J. Jansen, R. A. van Santen, Surf. Sci. 600 (2006) 1714–1734.

[189] K. Rasim, M. Bobeth, W. Pompe, N. Seriani, J. Mol. Catal. A: Chem. 325 (2010) 15–24.

[190] H. Ibach, S. Lehwald, Surf. Sci. 76 (1978) 1–12.

[191] F. Gobal, S. Azizian, Langmuir 13 (1997) 5999–6000.

[192] S. Ovesson, B. I. Lundqvist, W. F. Schneider, A. Bogicevic, Phys. Rev. B 71 (2005) 115406.

[193] M. E. Bartram, R. G. Windham, B. E. Koel, Langmuir 4 (1988) 240.

[194] D. Mei, J. Du, M. Neurock, nd. Eng. Chem. Res. 49 (2010) 10364–10373.

[195] M. E. Bartram, R. G. Windham, B. E. Koel, Surf. Sci. 184 (1987) 57–74.

[196] R. B. Getman, W. F. Schneider, J. Phys. Chem. C 111 (2007) 389–397.

[197] D. Mei, Q. Ge, M. Neurock, L. Kieken, J. Lerou, Mol. Phys. 102 (2004) 361–369.

[198] P. L. Hagans, X. Guo, I. Chorkendorff, A. Winkler, H. Siddiqui, J. T. Y. Jr., Surf. Sci. 203 (1988) 1–16.

[199] H. Celio, P. Mills, D. Jentz, Y. I. Pae, M. Trenary, Langmuir 14 (1998) 1379–1383.

[200] E. Herceg, M. Trenary, J. Phys. Chem. B 109 (2005) 17560.

[201] M. A. Henderson, G. E. Mitchell, J. M. White, Surf. Sci. 188 (1987) 206–218.

[202] J. R. Kingsley, J. C. Hemminger, Langmuir 2 (1986) 460–464.

[203] J. M. Lindquist, J. P. Ziegler, J. C. Hemminger, Surf. Sci. 210 (1989) 27–45.

[204] F. P. Netzer, Surf. Sci. 61 (1976) 343–354.

[205] M. E. Bridge, R. M. Lambert, Surf. Sci. 63 (1977) 315–324.

[206] R. B. Getman, W. F. Schneider, ChemCatChem 2 (2010) 1450–1460.

[207] E. V. Rebrov, M. H. J. M. de Croon, J. C. Schouten, Chem. Eng. J. 90 (2002) 61–76.

[208] N. M. Abbas, R. J. Madix, Appl. Surf. Sci. 3 (1981) 241–275.

[209] X. Guo, A. Winkler, I. Chorkendorff, P. L. Hagans, H. R. Siddiqui, J. T. Y. Jr., Surf. Sci. 203 (1988) 17–32.

[210] C. L. Levoguer, R. M. Nix, J. Chem. Soc., Faraday Trans. 92 (1996) 4799.

[211] J. R. Kingsley, J. C. Hemminger, Surf. Sci. 181 (1987) L156–L162.

[212] K. Mudiyanselage, C.-W. Yi, J. Szanyi, J. Phys. Chem. C 113 (2009) 5766.

[213] M. E. Bartram, B. E. Koel, E. A. Carter, Surf. Sci. 219 (1989) 467–489.

[214] G. A. Attard, H. D. Ebert, R. Parsons, Surf. Sci. 240 (1990) 125–135.

[215] W. Gao, J. A. Keith, J. Anton, T. Jacob, Dalton Trans. 39 (2010) 8450–8456.

[216] E. M. Shustovovich, A. V. Zeigarnik, Russ. J. Phys. Chem. 80 (2006) 665–666.

[217] Y. Y. Yeo, L. Vattuone, D. A. King, J. Chem. Phys. 106 (1997) 392–401.

[218] A. B. Mhadeshwar, D. G. Vlachos, Catal. Today 105 (2005) 162–172.

[219] A. V. Myshlyavtsev, V. P. Zhdanov, Langmuir 9 (1993) 1290–1298.

[220] G. Estiu, S. A. Maluendes, E. A. Castro, A. Arvia, J. Phys. Chem. 92 (1988) 2512–2516.

[221] A. B. Mhadeshwar, D. G. Vlachos, Ind. Eng. Chem. Res. 46 (2007) 5310–5324.

[222] A. Michaelides, P. Hu, Theoretical Aspects of Heterogeneous Catalysis, pp. 199–215.

[223] Y. Chen, D. G. Vlachos, J. Phys. Chem. C 114 (2010) 4973–4982.

[224] K. Arnby, A. Tòrncrona, B. Andersson, M. Skoglundh, J. Catal. 221 (2004) 252–261.

[225] P.-A. Carlsson, M. Skoglundh, Appl. Catal. B 101 (2011) 669–675.

[226] R. J. H. Grisel, J. J. Slyconish, B. E. Nieuwenhuys, Top. Catal. 16-17 (2001) 425–431.

[227] A. Bourane, D. Bianchi, J. Catal. 209 (2002) 126–134.

[228] BenchCAT, Benchcat, altamira instruments, http://www.altamirainstruments.com, 2012. [Online; accessed 10-May-2013].

[229] D. Bhatia, R. W. McCabe, M. P. Harold, V. Balakotaiah, J. Catal. 266 (2009) 106–119.

[230] C. Morley, Gaseq- a chemical equilibrium program for windows, http://www.gaseq.co.uk, 2012. [Online; accessed 10-July-2012].

[231] M. A. Marques, H. E. Troiani, M. Miki-Yoshida, M. Jose-Yacaman, A. Rubio, Nano Letters 4 (2004) 811–815.

[232] S. Appari, V. M. Janardhanan, S. Jayanti, L. Maier, S. Tischer, O. Deutschmann, Chem. Eng. Sci. 66 (2011) 5184–5191.

[233] C. Zhang, H. He, K. ichi Tanaka, Appl. Catal. B 65 (2006) 37–43.

[234] J. Peng, S. Wang, Appl. Catal. B 73 (2007) 282–291.

[235] R. W. McCabe, D. F. McCready, Chem .Phys. Lett. 111 (1984) 89–93.

[236] H. Parsson, http://www.chemeng.lth.se/exjobb/044.pdf, 2012. [Online; accessed 10-July-2012].

[237] J. M. Bradley, A. Hopkinson, D. A. King, J. Phys. Chem. 99 (1995) 17032–17042.

[238] X. Lin, N. J. Ramer, A. M. Rappe, K. C. Hass, W. F. Schneider, B. L. Trout, J. Phys. Chem. B 105 (2001) 7739–7747.

[239] X. Lin, K. C. Hass, W. F. Schneider, B. L. Trout, J. Phys. Chem. B 108 (2002) 250–265.

[240] X. Lin, K. C. Hass, W. F. Schneider, B. L. Trout, J. Phys. Chem. B 106 (2002) 12575.

[241] M. Maestri, K. Reuter, Angew. Chem. Int. Ed. 50 (2011) 1194–1197.

[242] M. Kozak, J. Merkisz, TEKA Kom. Mot. Energ. Roln. 5 (2005) 96–106.

[243] Johnson Matthey, Palladium use in diesel oxidation catalysts, http://www.platinum.matthey.com/uploaded_files/int_2008/09special_featurepdindieselcatalysts.pdf, 2009.

[244] M. P. cik, L. Wilde, J. Haase, B. Brena, G. Comelli, G. Paolucci, Surf. Sci. 381 (1997) L568–L572.

[245] Y. M. Sun, D. Sloan, D. J. Alberas, M. Kovar, Z. J. Sun, J. M. White, Surf. Sci. 319 (1994) 34–44.

[246] S. Astegger, E. Bechtold, Surf. Sci. 122 (1982) 491–504.

[247] U. Köhler, H. W. Wassmuth, Surf. Sci. 126 (1983) 448–454.

[248] M. Höfer, S. Hillig, H.-W. Wassmuth, Vacuum 41 (1990) 102–104.

[249] A. F. Lee, K. Wilson, A. Goldoni, R. Larciprete, S. Lizzit, Surf. Sci. 513 (2002) 140–148.

[250] R. Streber, C. Papp, M. P. A. Lorenz, O. Höfert, E. Darlatt, A. Bayer, R. Denecke, H. P. Steinröck, Chem .Phys. Lett. 494 (2010) 188–192.

[251] F. C. Galisteo, R. Mariscal, M. L. Granados, M. D. Z. Poves, J. L. G. Fierro, V. Kröger, R. L. Keiski, Appl. Catal. B 72 (2007) 272–281.

[252] H. C. Yao, H. K. Stepien, H. S. Gandhi, J.Catal. 67 (1981) 231–236.

[253] C. C. Chang, J. Catal. 53 (1978) 374–385.

[254] J. Han, Kinetic and Morphological Studies of Palladium Oxidation in O2-CH4 Mixtures, Ph.D. thesis, Worchester Polytechnical Institute, 2004.

[255] G. Bayer, H. G. Wiedemann, Thermochimica Acta 11 (1975) 79–88.

[256] W. E. Bell, R. E. Inyard, M. Tagami, J. Phys. Chem. 70 (1966) 3735–3736.

[257] M. Lyubovsky, L. Pfefferle, Appl. Catal. A 173 (1998) 107–119.

[258] C. Mallika, O. M. Sreedharan, J. B. Gnanamoorthy, Journal of the Less Common Metals 95 (1983) 213–220.

[259] X. Lin, K. C. Hass, W. F. Schneider, B. L. Trout, J. Phys. Chem. B 106 (2002) 12575–12583.

[260] W. Benzinger, A. Wenka, R. Dittmeyer, Appl. Catal. A 397 (2011) 209–217.

[261] L. Olsson, M. Fredriksson, R. J. Blint, Appl. Catal. B 100 (2010) 31–41.

[262] J. Dawody, M. Skoglundh, L. Olsson, E. Fridell, J. Catal. 234 (2005) 206–218.

[263] S. Matsumoto, Y. Ikeda, H. Suzuki, M. Ogai, N. Miyoshi, Appl. Catal. B 25 (2000) 115–124.

[264] H. N. Sharma, A. B. Mhadeshwar, Appl. Catal. B 127 (2012) 190–204.

[265] X. Lin, W. F. Schneider, B. L. Trout, J. Phys. Chem. B 108 (2004) 250–264.

[266] J. Dawody, M. Skoglundh, L. Olsson, E. Fridell, Appl. Catal. B 70 (2007) 179–188.

[267] J. A. Phillips, M. Canagaratna, H. Goodfriend, K. R. Leopold, J. Phys. Chem. 99 (1995) 501–504.

[268] E. R. Lovejoy, J. Curtius, K. D. Froyd, J. Geophys. Res. D: Atmos. 109 (2004) – D08204.

[269] T. Hamzehlouyan, C. Sampara, J. Li, A. Kumar, W. Epling, Appl. Catal. B 152-153 (2014) 108–116.

[270] R. J. Kriek, J. Rossmeisl, S. Siahrostami, M. E. Bjorketun, Physical Chemistry Chemical Physics 16 (2014) 9572–9579.

[271] H. N. Sharma, V. Sharma, T. Hamzehlouyan, W. Epling, A. B. Mhadeshwar, R. Ramprasad, J. Phys. Chem. C (2014).

[272] H. Somnitz, G. Gleitsmann, R. Zellner, in: Proceedings of the AAC-Conference, pp. 19–24.

[273] B. M. Penetrante, R. M. Brusasco, B. T. Merritt, G. E. Vogtlin, Sulfur Tolerance of Selective Partial Oxidation of NO to NO2 in a Plasma, Technical Report 1999-01-3687, Lawrence Livermore National Laboratory, 1999.

[274] J. M. Standard, I. S. Buckner, D. H. Pulsifer, J. Mol. Struct. THEOCHEM 673 (2004) 1–16.

[275] T. Hamzehlouyan, C. Sampara, J. Li, A. Kumar, W. Epling, So_2 oxidation over Pt/Al_2O_3 catalysts, http://cleers.org/workshops/workshop2013/index.php, 2013. Accessed: 2013-09-30.

[276] N. Luckas, F. Viñes, M. Happel, A. Desikusumastuti, J. Libuda, A. Gòrling, J. Phys. Chem. C 114 (2010) 13813–13824. Cited By (since 1996): 3.

[277] D. L. Mowery, M. S. Graboski, T. R. Ohno, R. L. McCormick, Appl. Catal. B: Env. 21 (1999) 157–169.

[278] S. Terada, T. Yokoyama, M. Sakano, M. Kiguchi, Y. Kitajima, T. Ohta, Chem .Phys. Lett. 300 (1999) 645–650.

[279] C.-H. Yeh, J.-J. Ho, ChemPhysChem 13 (2012) 3194–3203.

[280] K. Gotterbarm, N. Luckas, O. Hofert, M. P. A. Lorenz, R. Streber, C. Papp, F. Vines, H.-P. Steinruck, A. Gorling, The J. Chem. Phys. 136 (2012) 094702.

[281] H. Sellers, E. Shustorovich, Surf. Sci. 356 (1996) 209–221.

[282] C. Suzuki, Y. Yamada, T. Nakagiri, Appl. Surf. Sci. 256 (2009) 862–869.

[283] M. Happel, N. Luckas, F. Viñes, M. Sobota, M. Laurin, A. Gòrling, J. Libuda, J. Phys. Chem. C 115 (2011) 479–491.

[284] G. Kresse, D. Joubert, Phys.Rev. 59 (1999) 1758. A1:.

[285] H. J. Monkhorst, J. D. Pack, Phys. Rev. B 13 (1976) 5188–5192.

[286] G. Henkelman, B. P. Uberuaga, H. Jonsson, The J. Chem. Phys. 113 (2000) 9901–9904.

[287] G. Pilania, R. Ramprasad, Surf. Sci. 604 (2010) 1889–1893.

[288] D. O. Demchenko, G. M. Sacha, M. Salmeron, L. W. Wang, Interactions of oxygen and hydrogen on pd(111) surface, 2008.

[289] X. Lin, W. F. Schneider, B. L. Trot, J. Phys. Chem. B 108 (2004) 13329–13340.

[290] H. Nagoshi, A study of sulfur dioxide oxidation on platinum, Master's thesis, University of Minnesota, MN, 1972.

[291] G. Ertl, H. Knìzinger, F. Scùhth, J. Weitkam, Handbook of Heterogeneous Catalysis, volume 4, Wiley, 1997.

[292] V. Dupont, J. M. Jones, S.-H. Zhang, A. Westwood, M. V. Twigg, Chem. Eng. Sci. 59 (2004) 17–29.

[293] J. C. Summers, Environ. Sci. Technol. 13 (1979) 321–325.

[294] K. C. Taylor, Product R&D 15 (1976) 264–268.

[295] B. McAllister, P. Hu, J. Chem. Phys. 122 (2005) 084709–1–084709–6.

[296] P. Hohenberg, W. Kohn, Phys. Rev. 136 (1964) B864–B871.

[297] N. A. Saliba, Y. L. Tsai, C. Panja, B. E. Koel, Surf. Sci. 419 (1999) 79–88.

[298] S. A. Krasnikov, S. Murphy, N. Berdunov, A. P. McCoy, I. K Radican and, Nanotechnology 21 (2010) 335301.

[299] H. Zhu, C. Tang, R. Ramprasad, Phys. Rev. B 82 (2010).

[300] A. Dianat, N. Seriani, M. Bobeth, W. Pompe, L. C. Ciacchi, J. Phys. Chem. C 112 (2008) 13623–13628.

[301] M. Derzsi, A. Hermann, R. Hoffmann, W. Grochala, Eur. J. Inorg. Chem. 2013 (2013) 5094–5102.

[302] H. Gabasch, W. Unterberger, K. Hayek, B. Klötzer, G. Kresse, C. Klein, M. Schmid, P. Varga, Surf. Sci. 600 (2006) 205–218.

[303] D. Zemlyanov, B. Aszalos-Kiss, E. Kleimenov, D. Teschner, S. Zafeiratos, M. Hävecker, A. Knop-Gericke, R. Schlögl, H. Gabasch, W. Unterberger, K. Hayek, B. Klötzer, Surf. Sci. 600 (2006) 983–994.

[304] E. Lundgren, A. Mikkelsen, J. Andersen, G. Kresse, M. Schmid, P. Varga, J. Phys. Condens. Matter 18 (2006) R481–R499.

[305] M. Todorova, W. X. Li, M. Ganduglia-Pirovano, C. Stampfl, K. Reuter, M. Scheffler, Phys. Rev. Lett. 89 (2002) 096103.

[306] J. Rogal, K. Reuter, M. Scheffler, Phys. Rev. B 75 (2007).

[307] E. H. Voogt, A. J. M. Mens, O. L. J. Gijzeman, J. W. Geus, Surf. Sci. 373 (1997) 210–220.

[308] H. H. Kan, J. F. Weaver, Surf. Sci. 602 (2008) L53–L57.

[309] U. Engström, R. Ryberg, Phys. Rev. Lett. 82 (1999) 2741–2744.

[310] F. P. Leisenberger, G. Koller, M. Sock, S. Surnev, M. G. Ramsey, F. P. Netzer, B. Klötzer, K. Hayek, Surf. Sci. 445 (2000) 380–393.

[311] J. L. Gland, Surf. Sci. 93 (1980) 487–514.

[312] J. J. Spivey, J. B. Butt, Catal. Today 11 (1992) 465–500.

[313] L. L. Hegedus, J. C. Summers, J. C. Schlatter, K. Baron, J. Catal. 56 (1979) 321–335.

[314] J. Solla-Gullon, F. J. Vidal-Iglesias, J. M. Feliu, Annu. Rep. Prog. Chem., Sect. C: Phys. Chem. 107 (2011) 263–297.

[315] A. M. Gómez-Martín, R. Rizo, J. M. Feliu, Beilstein J. Nanotechnol. 4 (2013) 956–967.

[316] S. Grimme, J. Comput. Chem. 27 (2006) 1787–1799.

[317] A. Mhadeshwar, A Hierarchical Multiscale Approach for Predictive Microkinetic Modeling of Hydrogen Production, Ph.D. thesis, University of Delaware, Newark, DE, 2005.

[318] B. Hammer, J. K. Nörskov, Theoretical Surf. Sci. and catalysis-calculations and concepts, volume Volume 45 of *Advances in Catalysis*, Academic Press, pp. 71–129.

[319] S. Kandoi, J. Greeley, M. A. Sanchez-Castillo, S. T. Evans, A. A. Gokhale, J. A. Dumesic, M. Mavrikakis, Top. Catal. 37 (2006) 17–28.

[320] O. Muller, R. Roy, Journal of the Less Common Metals 16 (1968) 129–146.

[321] N. Seriani, W. Pompe, L. C. Ciacchi, J. Phys. Chem. B 110 (2006) 14860–14869.

[322] J. Waser, H. A. Levy, S. W. Peterson, Acta Cryst. 6 (1953) 661–663.

[323] H. T. Stokes, D. M. Hatch, J. Appl. Cryst. 38 (2005) 237–238.

[324] M. D. Ackermann, Operando SXRD: a new view on catalysis, Ph.D. thesis, University of Leiden and ESRF Grenoble, 2007.

Appendix A

Experimental Study of Carbon Black and Diesel Engine Soot Oxidation Kinetics Using Thermogravimetric Analysis

energy&fuels

Article

pubs.acs.org/EF

Experimental Study of Carbon Black and Diesel Engine Soot Oxidation Kinetics Using Thermogravimetric Analysis

Hom N. Sharma,[†,‡] Lakshitha Pahalagedara,[§] Ameya Joshi,[∥] Steven L. Suib,[§] and Ashish B. Mhadeshwar*[,†,‡]

[†]Department of Chemical, Materials, and Biomolecular Engineering, University of Connecticut, 191 Auditorium Road, Unit 3222, Storrs, Connecticut 06269, United States

[‡]Center for Clean Energy Engineering, University of Connecticut, 44 Weaver Road, Unit 5233, Storrs, Connecticut 06268, United States

[§]Department of Chemistry, University of Connecticut, 55 North Eagleville Road, Unit 3060, Storrs, Connecticut 06269, United States

[∥]Corning, Incorporated, Science Center Road, SP TD 01-1, Corning, New York 14831, United States

ABSTRACT: Non-catalytic oxidation kinetics of diesel engine soot and more than a dozen commercial carbon black samples was investigated using non-isothermal and isothermal thermogravimetric analysis (TGA) experiments. The effect of various operating parameters, such as oxygen flow rate, initial sample mass, oxygen partial pressure, crucible type, and ramp rate, on the oxidation rate was investigated. Three types of TGA experiments (non-isothermal single-ramp rate, non-isothermal multiple-ramp rates, and isothermal) were conducted and analyzed to extract the kinetic parameters for oxidation. Activation energies for oxidation of carbon black samples ranged from 125 to 257 kJ/mol, whereas that for soot oxidation was ∼155 kJ/mol. Furthermore, oxidation rate trends were explained on the basis of structural characteristics, such as scanning electron microscopy (SEM)-based average particle size and Brunauer−Emmett−Teller (BET) surface area. In general, a low particle size and high surface area were associated with a higher oxidation rate and vice versa. A thorough understanding of the non-catalytic oxidation kinetics developed in this work along with the correlation of the oxidation rate with the structural parameters may assist in efficient oxidation of diesel engine soot during the regeneration of diesel particulate filters.

1. INTRODUCTION

More than 13 million diesel vehicles are responsible for transportation of 94% of the goods in the U.S. and use ∼4 million barrels of diesel per day.[1−3] In the European market, 53% of the passenger cars run on diesel.[4] Diesel engines are the workhorses for industrial, commercial, and personal transportation and also play a vital role in power generation, because of the highly efficient combustion, excellent fuel economy, torque, durability, reliability, and low operating costs.[5−7] However, emissions from diesel engines contain fine particles produced during high-temperature pyrolysis or combustion. Diesel particulate matter (PM), also known as soot, is primarily composed of carbon along with some organic compounds, inorganic compounds (ash), sulfur compounds, and traces of metals from unburnt fuel and lubricating oil. PM formation is a complex phenomenon, which depends upon the engine operating conditions, fuel type, and lubricating oil, resulting in a wide range of particle sizes and chemical compositions.[8−11] PM emissions are responsible for various human health and environmental problems, such as asthma, bronchitis, lung cancer, air pollution, and global warming.[5,12,13] Diesel particulate filter (DPF) is the most popular aftertreatment technology to meet the stringent PM emission standards.[14,15] DPFs need to be periodically regenerated through oxidation of soot; otherwise, the accumulated soot can cause backpressure, resulting in decreased fuel economy and possible engine and/or filter failure.[16,17] Given the complexity and variability in the soot structure as well as the need for periodic DPF regeneration, there is an urgent need to develop a comprehensive understanding for the kinetics of soot oxidation.

This work focused on developing such an understanding through a comprehensive investigation of 15 carbonaceous samples (diesel engine soot provided by Corning, 13 commercial carbon black samples, and graphite). The effect of various parameters, such as the oxidizer flow rate, initial sample mass, partial pressure of oxygen, crucible type, and ramp rate, was studied using temperature-programmed oxidation (TPO) thermogravimetric experiments. The paper is organized as follows. First, experimental details are provided in section 2, followed by a description of the data analysis methods in section 3. In section 4, we discuss the effect of various operating conditions in non-isothermal experiments, followed by kinetic parameter extraction. The results are compared to isothermal experiments presented in section 5. Summary and concluding remarks are presented in the end.

2. EXPERIMENTAL SECTION

2.1. Materials. A total of 15 different samples studied included a diesel engine soot sample provided by Corning, 13 commercial carbon black samples obtained from various manufacturers, and a graphitic carbon sample. The samples were as follows: (1) diesel soot (Corning), (2) graphite (Fisher Scientific), (3) Mogul-E (Cabot), (4) Monarch 1300 (Cabot), (5) Monarch 1400 (Cabot), (6) Monarch 280 (Cabot),

Received: May 24, 2012
Revised: August 2, 2012
Published: August 3, 2012

dx.doi.org/10.1021/ef3009025 | Energy Fuels 2012, 26, 5613−5625

(7) N 120 (Continental carbon), (8) N 339 (Continental carbon), (9) N 762 (Continental carbon), (10) Printex-G (Orion), (11) Printex-U (Orion), (12) Printex-XE2B (Orion), (13) Regal 330 R (Cabot), (14) Regal 400 R (Cabot), and (15) VulcanXC72R (Cabot). Throughout the paper, the samples are referred in this order. Two of the samples (Monarch 1300 and Monarch 1400) contained 7% moisture, as compared to negligible moisture (0−0.6%) in the other samples.

2.2. Thermogravimetric Analysis (TGA). A TGA Q5000 IR thermogravimetric analyzer from TA Instruments was used for all of the experiments. This is a thermal weight-change analysis instrument, used in conjunction with a controller computer and associated software to make up a thermal analysis system. This TGA is also equipped with an autosampler for multiple sample loadings. In this work, we developed mixed methods consisting of non-isothermal and isothermal steps. Instrumental specifications and experimental protocol details are given in Table 1.

Table 1. Details of the TGA Instrument and Experimental Protocols

Technical Specifications[79]	
weighting capacity	100 mg
weighting precision	±0.01%
sensitivity	<0.1 μg (1 ppm)
signal resolution	0.002 μg
temperature range	ambient to 1200 °C
furnace type	infrared heating with a built-in electromagnetic coil for automated temperature calibration
isothermal temperature accuracy	±1 °C
isothermal temperature precision	±0.1 °C
linear heating rates	0.1−500 °C/min in 0.01 °C/min increments
special heating mode	hi-res TGA and modulated TGA
autosampler	16 sample carousel with automated pan punching

Experimental Protocol for Non-isothermal Tests		
step	description	stage
1	flow of oxidant gas with nitrogen	initial
2	ramp to 800 °C with ramp rate β = 5−20 °C/min	heating
3	hold at 800 °C for 15 min	isothermal
4	cool to room temperature	cooling

Experimental Protocol for Isothermal Tests		
step	description	stage
1	flow of nitrogen (balance and purge gases)	initial
2	ramp to $T_{isothermal}$ with β = 20 °C/min	heating
3	flow of oxidant gas with nitrogen	isothermal
4	hold at $T_{isothermal}$ for 120 min	isothermal
5	cool to room temperature	cooling

In all of the experiments, the oxidizer gas (UHP air or 10% O_2 in Ar from Airgas) flow rate was 60 mL/min and N_2 was used as a purge gas with a flow rate of 40 mL/min. The initial mass of the carbon black samples was ∼10−12 mg. However, because of the low density of diesel soot, an initial mass of only ∼2.5 mg was used. For the non-isothermal experiments, the samples were heated in a platinum (Pt) crucible (the Pt crucible was inert, as discussed later in section 2.3.4) from room temperature to 800 °C at a chosen ramp rate (5−20 °C/min), followed by a 15 min hold at 800 °C, and then cooling back to room temperature. For the isothermal experiments, first, the samples were heated to the desired temperature with a ramp rate of 20 °C/min, and then, the samples were kept at the isothermal point for 2 h under oxidizing environment, followed by cooling back to room temperature. Non-isothermal tests are typically preferred over isothermal tests for two reasons: (i) an isothermal test always consists of a finite non-isothermal heating time, as a result of which strictly isothermal tests are not possible,[18] and (ii) multiple experiments are required for extraction of kinetic parameters from isothermal tests.[19,20] On the other hand, isothermal tests provide information about the characteristic profile of the reaction and, hence, provide an idea about the appropriate kinetic model.[18] In this work, we conducted isothermal tests for selected samples to extract the kinetic parameters and to validate the parameters obtained from the non-isothermal experiments.

Finally, the oxidation rate is defined on the basis of the temperature required for a certain level of fractional conversion. For example, T_{10}, T_{50}, and T_{90} represent the temperatures required to achieve 10, 50, and 90% mass loss, respectively. T_{10} is also referred to as the light-off temperature.

2.3. Factors Affecting TGA Experiments. *2.3.1. Oxygen Flow Rate.* The overall efficiency of the gas−solid reactions can be greatly affected by the gas flow rate and, hence, mass-transfer limitations or limiting reactants.[19−23] For the oxidation of carbon black or soot, the availability of oxygen is critical; otherwise, the observed oxidation efficiency may be lower because of the lack of sufficient oxygen. This is particularly important at high temperatures, where the soot oxidation rate is high and the lack of oxygen can limit the overall soot oxidation rate. To ensure that the TGA experiments reported here were not affected by such limitations because of insufficient availability of oxygen in the oxidizer gas, we conducted a series of experiments with various oxidizer gas flow rates while maintaining other parameters the same. Figure 1 shows the mass loss profile of Printex-U for various levels

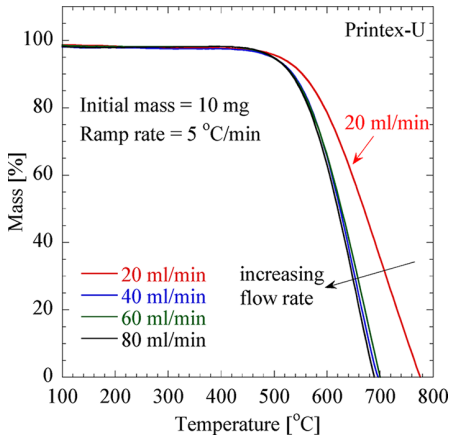

Figure 1. Oxidation profile of Printex-U with different flow rates of air. Operating conditions: non-isothermal experiment, initial mass of 10 mg, and ramp rate at 5 °C/min. Data indicate that the gas flow rate must be at least 40 mL/min to avoid the limitations associated with the availability of oxygen.

of air flow rates (20−80 mL/min). The oxidation rate at a gas flow rate of 20 mL/min was lower than that at a gas flow rate of 40 mL/min or higher, but the rate stayed constant for gas flow rates of 40 mL/min and higher. Therefore, the oxidizer gas flow rate must be at least 40 mL/min to avoid the scenario in which oxygen becomes the limiting reactant. On the basis of these experiments, we used an oxidizer gas flow rate of 60 mL/min in all of the TGA experiments reported in this paper.

2.3.2. Initial Sample Mass. TGA analysis is also affected, to some extent, by the initial sample mass used in the experiment.[23,24] A large initial mass may be associated with diffusional limitations,[24−27] whereas a small initial mass may result in increased uncertainty along with low reproducibility.[20] Furthermore, a large initial mass may cause self-heating (exothermic) and self-cooling (endothermic), producing a large deviation from the programmed heating rates.[28] The temperature gradient could be created as a result of the low thermal conductivity of the samples, producing regions with different temperatures.[28] As shown in Figure 2, we conducted multiple experiments with different initial masses and ramp rates (5−20 °C/min) for Printex-U (panel a, 2−20 mg) and Printex-XE2B (panel b, 8−14 mg; panel c, 4−14 mg; and

dx.doi.org/10.1021/ef3009025 | Energy Fuels 2012, 26, 5613−5625

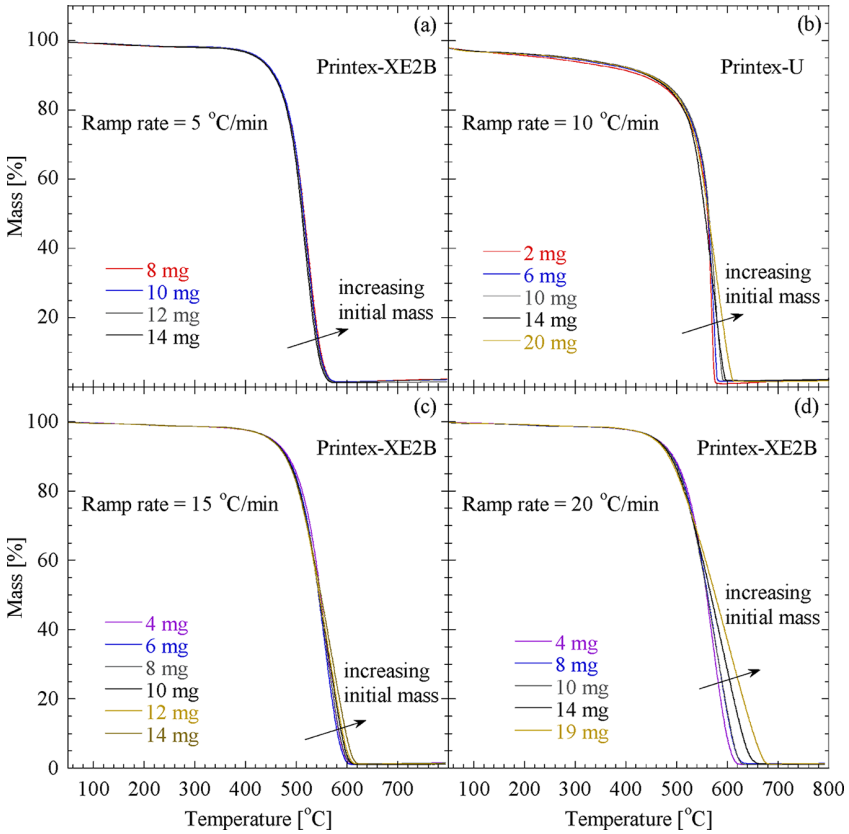

Figure 2. Effect of the initial sample mass and ramp rate on the oxidation of (a) Printex-XE2B with a ramp rate of 5 °C/min and an initial mass of 8−14 mg, (b) Printex-U with a ramp rate of 10 °C/min and an initial mass of 2−20 mg, (c) Printex-XE2B with a ramp rate of 15 °C/min and an initial mass of 4−14 mg, and (d) Printex-XE2B with a ramp rate of 20 °C/min and an initial mass of 4−19 mg. Operating conditions: non-isothermal experiment, air oxidant, and flow rate at 60 mL/min.

panel d, 4−19 mg). We observed that large initial masses were affected by diffusional limitations, as evident from the delayed oxidation rate. On the basis of these experiments, we selected moderate initial masses of 10−12 mg for each sample, except for diesel soot (~2.5 mg), which had a much lower density.

2.3.3. Ramp Rate. The effect of the ramp rate on gas−solid reactions is well-documented in the literature.[29−34] High ramp rates are typically associated with heat- and mass-transfer limitations.[33] On the other hand, experiments conducted with low ramp rates are not influenced by such limitations.[35] Our results in Figure 2 for different initial masses and ramp rates showed delayed oxidation rates in the case of large initial masses and high ramp rates as a result of their combined effect (e.g., Figure 2d). However, in general, the effect of the initial mass was negligible in the considered initial mass range, with a ramp rate of 5−15 °C/min. On the basis of these experiments, we have chosen a low ramp rate of 5 °C/min for most of the experiments.

2.3.4. Crucible. The crucible shape in the TGA experiments can significantly influence the oxidation kinetics because of mass-transfer limitations.[20,23,26,27,36] A large crucible height can lead to a large stagnant volume (space available in the crucible above the sample) and, hence, diffusion limitations.[20,23,27,36] Therefore, short and wide crucibles are typically recommended for such studies.[23,37] In this work, we used short and wide crucibles (D = 10 mm, h = 2 mm, and h/D = 0.2, with actual sample h/D < 0.2) to avoid such limitations. Furthermore, to ensure that the Pt crucible is inert in the oxidation experiments, we conducted additional experiments with an alumina crucible in identical operating conditions. As shown in Figure 3, results with both crucibles were almost identical for two samples (panel a, Printex-XE2B; panel b, Printex-U); hence, the Pt crucible could be considered as inert in the subsequent experiments.

2.3.5. Diffusion Limitations. Diffusion limitations in soot oxidation kinetics during TGA experiments have been discussed in the literature,[20,23−25,27,30,36,38−43] and such limitations can impact kinetic parameter estimation.[24,27,38,40,43] As discussed earlier, diffusion limitations can be avoided or minimized by selecting an appropriate initial sample mass, ramp rate, crucible shape, sample packing, bed height, and stagnation volume.[23,24,27,36,38,44] Internal mass-transfer limitations could also be important and could differ for each sample because of different pore sizes. Such limitations have been estimated in the literature using the effectiveness factor and Thiele modulus;[40,45,46] however, they were not considered in the scope of our work presented here.

2.4. Experimental Reproducibility. Prior to discussing the results and data analysis from the TGA experiments for multiple samples and various operating conditions, it was important to ensure that the experiments had good reproducibility. Figure 4 shows an example of the experimental reproducibility over three runs for the oxidation of diesel soot (panel a) and Printex-XE2B (panel b). As observed from the overlapping profiles, the TGA experiments were highly reproducible.

3. DATA ANALYSIS FOR KINETIC PARAMETER EXTRACTION

Three methods were used for the TGA data analysis: (a) non-isothermal single-ramp rate, (b) non-isothermal multiple-ramp rates, and (c) isothermal. A majority of the results presented in this work are focused around the non-isothermal single-ramp rate method, whereas the other two methods are demonstrated for additional validation or comparison. Next, we discuss the details of the data analysis for the three methods.

dx.doi.org/10.1021/ef3009025 | *Energy Fuels* 2012, 26, 5613−5625

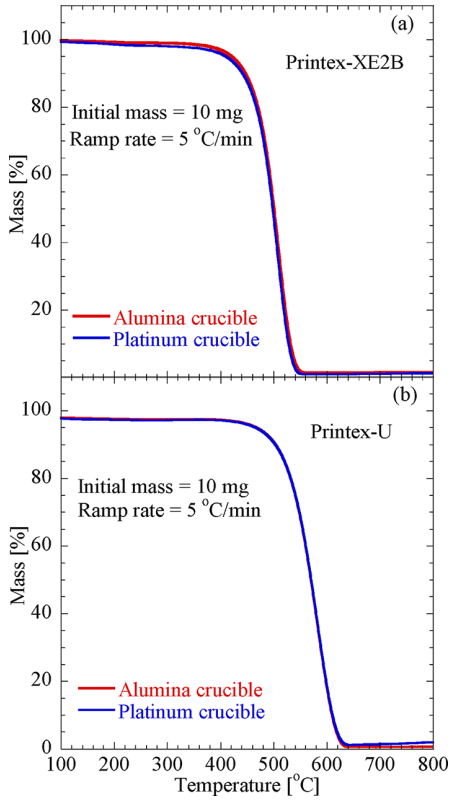

Figure 3. Effect of the crucible type on the oxidation of (a) Printex-XE2B with a ramp rate of 5 °C/min and an initial mass of 10 mg and (b) Printex-U with a ramp rate of 5 °C/min and an initial mass of 10 mg. Operating conditions: non-isothermal experiment, air oxidant, and flow rate at 60 mL/min.

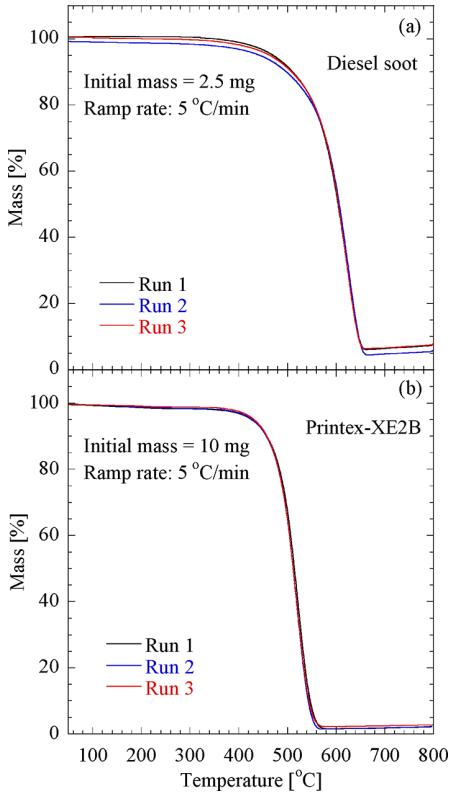

Figure 4. Reproducibility of the TGA experiments for (a) diesel soot with an initial mass of 2.5 mg and (b) Printex-XE2B with an initial mass of 10 mg. Operating conditions: non-isothermal experiment, air oxidant, flow rate at 60 mL/min, and ramp rate at 5 °C/min.

3.1. Method A: Non-isothermal Single-Ramp Rate Method. Estimation of kinetic parameters from TGA data can be performed using various approaches, as recommended by the Kinetics Committee of the International Confederation for Thermal Analysis and Calorimetry (ICTAC).[18] However, the most widely used approach for kinetic parameter estimation from soot or carbon black oxidation is based on the Arrhenius equation format[20,47,48]

$$-\frac{dm}{dt} = km^n p_{O_2}{}^r = A\exp\left(-\frac{E_a}{RT}\right)m^n p_{O_2}{}^r \quad (1)$$

where m is the instantaneous sample mass at time t, k is the reaction rate constant, A is the pre-exponential factor, E_a is the activation energy, T is the operating temperature, p_{O_2} is the partial pressure of oxygen, and n and r are the reaction orders for carbon and oxygen, respectively. It is known that the surface area of the carbonaceous samples increases during oxidation.[9] However, any change in the surface area and pore size effects is not accounted for in the simplified kinetic expression. Furthermore, most literature studies for carbon black or soot oxidation show reaction orders close to unity[20,25,39,40] (see section 5 for the validity of this assumption). In that case, the above equation can be rearranged as

$$\ln\left(-\frac{dm}{mdt}\right) = \ln(Ap_{O_2}) - \frac{E_a}{RT} \quad (2)$$

where E_a and A can be estimated from the slope and intercept of a $\ln(-dm/mdt)$ against $1/T$ plot. In this method, TGA data at a single-ramp rate are sufficient for the analysis and kinetic parameter extraction.

3.2. Method B: Non-isothermal Multiple-Ramp Rate Method. To delineate the effect of the ramp rate from the kinetic parameters, they can also be estimated using a fractional conversion α [where $\alpha = 1 - (m/m_0)$] in the non-isothermal experiments conducted at different ramp rates β. This analysis is based on the Flynn–Wall–Ozawa method[49−52] and Doyle's approximation.[53,54] Equation 1 can be written in terms of fractional conversion α as

$$\frac{d\alpha}{dt} = -\frac{1}{m_0}\frac{dm}{dt} = A\exp\left(-\frac{E_a}{RT}\right)\frac{m}{m_0}p_{O_2} = A\exp\left(-\frac{E_a}{RT}\right)(1-\alpha)p_{O_2} \quad (3)$$

With a linear ramp rate $\beta = dT/dt$, eq 3 can be written as

$$\frac{d\alpha}{dT} = \frac{A}{\beta}\exp\left(-\frac{E_a}{RT}\right)(1-\alpha)p_{O_2} \quad (4)$$

Integrating this equation from a very low temperature (zero conversion) to the final temperature T, corresponding to a final degree of conversion α, and using $x = E_a/RT$ gives

$$-\ln(1-\alpha) = \frac{Ap_{O_2}E_a}{\beta R}\int_x^\infty \frac{e^{-x}}{x^2}dx = \frac{Ap_{O_2}E_a}{\beta R}I(x) \quad (5)$$

dx.doi.org/10.1021/ef3009025 | Energy Fuels 2012, 26, 5613−5625

The integral $I(x)$ is approximated as[28,51]

$$\log I(x) \approx -2.315 - 0.457x \tag{6}$$

When eqs 5 and 6 are combined and rearranged, we obtain

$$\log \beta = \log\left(\frac{Ap_{O_2}E_a/R}{-\ln(1-\alpha)}\right) - 2.315 - 0.457\frac{E_a}{RT} \tag{7}$$

The activation energy E_a for different conversion values α can be calculated from the slope of a $\log \beta$ versus $1/T$ plot.

3.3. Method C: Isothermal Method. Isothermal tests provide another way of studying the kinetics of gas−solid reactions occurring in carbon black or soot oxidation.[12,23,30,55−57] Starting from eq 1, under isothermal conditions, one can write

$$\begin{aligned}\ln(1-\alpha) &= \ln\left(\frac{m}{m_0}\right)\\ &= \int_{m_0}^{m}\frac{dm}{m}\\ &= \int_0^t -A\exp\left(-\frac{E_a}{RT}\right)p_{O_2}dt\\ &= -A\exp\left(-\frac{E_a}{RT}\right)p_{O_2}t\end{aligned} \tag{8}$$

When eq 8 is rearranged, we obtain

$$-\ln t = \ln\left[\frac{Ap_{O_2}}{-\ln(1-\alpha)}\right] - \frac{E_a}{RT} \tag{9}$$

A plot of $-\ln t$ versus $1/T$ at a chosen value of α gives the activation energy E_a from the slope and pre-exponential factor A from the intercept.[28]

Given the assumptions associated with eqs 1 and 2, the kinetic parameters (activation energies and pre-exponential factors) estimated using the aforementioned methods should be treated as apparent parameters only.

4. OXIDATION KINETICS USING NON-ISOTHERMAL EXPERIMENTS

4.1. Effect of the Oxygen Partial Pressure. Soot could be oxidized using the oxygen present in the diesel engine exhaust (5−15% oxygen[58,59]) or using air. Although the oxygen content in air is higher than that in the typical diesel engine exhaust, literature studies have commonly used air to test the oxidation of soot samples.[20,55,60] Therefore, we conducted the TGA experiments with both oxidizers: (i) 10% O_2 in Ar and (ii) air. Experimental protocol details are provided in Table 1. Mass loss profiles for all 15 samples with these two oxidizers are shown in Figures 5 and 6, respectively, with a constant ramp rate of 5 °C/min. The diesel soot sample in this study was collected under real diesel engine exhaust conditions [engine type, light duty; engine swept volume, 2 L; revolutions per minute (rpm), 3250 min^{-1}; torque, 50 N m; power, 17 kW; and exhaust gas flow rate, 253 kg/h]. It contained metal oxides and ash particles, which were not burnt off during the oxidation experiments. A very small amount of ash particles was observed in the crucible after the diesel soot experiments, which was not the case with other carbon black samples. Therefore, the diesel soot conversion was not 100%, even at high temperatures, as observed in Figures 5 and 6. The negligible deviation from

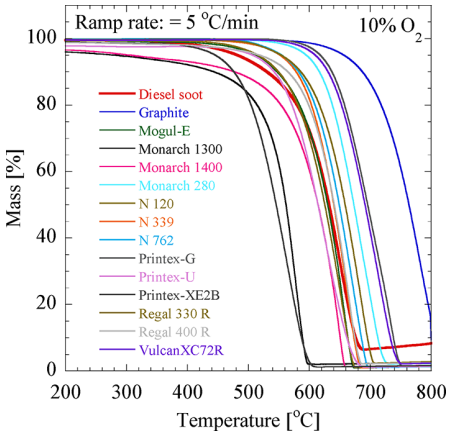

Figure 5. Mass loss profiles of all samples with 10% O_2. Operating conditions: non-isothermal experiment, initial mass range of 2.5−12 mg, flow rate at 60 mL/min, and ramp rate at 5 °C/min. Diesel soot showed incomplete conversion because of the presence of metal oxides and ash particles.

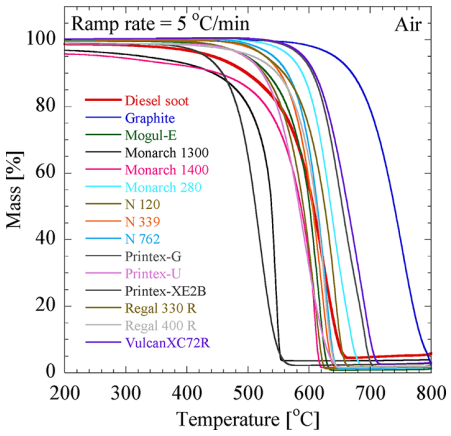

Figure 6. Mass loss profiles of all samples with air. Operating conditions: non-isothermal experiment, initial mass range of 2.5−12 mg, flow rate at 60 mL/min, and ramp rate at 5 °C/min. Diesel soot showed incomplete conversion because of the presence of metal oxides and ash particles.

100% conversion for other samples and the slight increase in diesel soot mass with the temperature (at high temperatures) could be associated with experimental uncertainty in measuring very small quantities.

Details of T_{10}, T_{50}, and T_{90} are reported in Table 2. The T_{50} values for the most commonly studied samples, such as Printex-U and VulcanXC72R, were in close agreement with the literature data (e.g., reported T_{50} of Printex-U = 606 °C and T_{50} of VulcanXC72R = 683 °C by Atribak et al.[61] and reported T_{50} of Printex-U = 607 °C and T_{50} of VulcanXC72R = 667 °C by Hinot[62]). In general, there were three major groups in the considered samples: (i) Monarch 1300, Monarch 1400, and Printex-XE2B had low light-off temperatures (T_{10} < 500 °C) and, hence, the highest oxidation rate; (ii) Printex-G, Monarch 280, VulcanXC72R, and graphite showed high light-off temperatures (T_{10} > 600 °C) and, hence, the lowest oxidation rate; and (iii) all other samples had a moderate oxidation rate, with a T_{10} ranging between 500 and 600 °C. The trend was similar for T_{50} and T_{90} (see Table 2). Monarch 1300 and Monarch 1400 contained 7% moisture, as compared to

dx.doi.org/10.1021/ef3009025 | Energy Fuels 2012, 26, 5613−5625

Table 2. Light-Off Temperature Data from Non-isothermal Experiments

		10% O_2, β = 5 °C/min			air, β = 5 °C/min		
sample number	sample name	T_{10} (°C)	T_{50} (°C)	T_{90} (°C)	T_{10} (°C)	T_{50} (°C)	T_{90} (°C)
1	diesel soot	541	640	685	499	607	647
2	graphite	687	764	800	671	740	784
3	Mogul-E	548	630	663	532	601	623
4	Monarch 1300	444	562	590	444	539	550
	Monarch 1300	482[a]	563[a]	590[a]	468[a]	539[a]	550[a]
5	Monarch 1400	478	615	651	452	587	612
	Monarch 1400	513[a]	616[a]	651[a]	496[a]	589[a]	612[a]
6	Monarch 280	617	674	713	543	609	650
7	N 120	550	626	663	526	591	617
8	N 339	579	641	674	553	606	631
9	N 762	583	649	686	565	614	636
10	Printex-G	637	696	738	606	655	693
11	Printex-U	543	615	662	524	584	625
12	Printex-XE2B	479	547	589	459	512	545
13	Regal 330 R	587	659	696	559	626	651
14	Regal 400 R	565	641	675	548	612	635
15	VulcanXC72R	631	692	733	610	664	701

[a]Data without moisture (see the text for details).

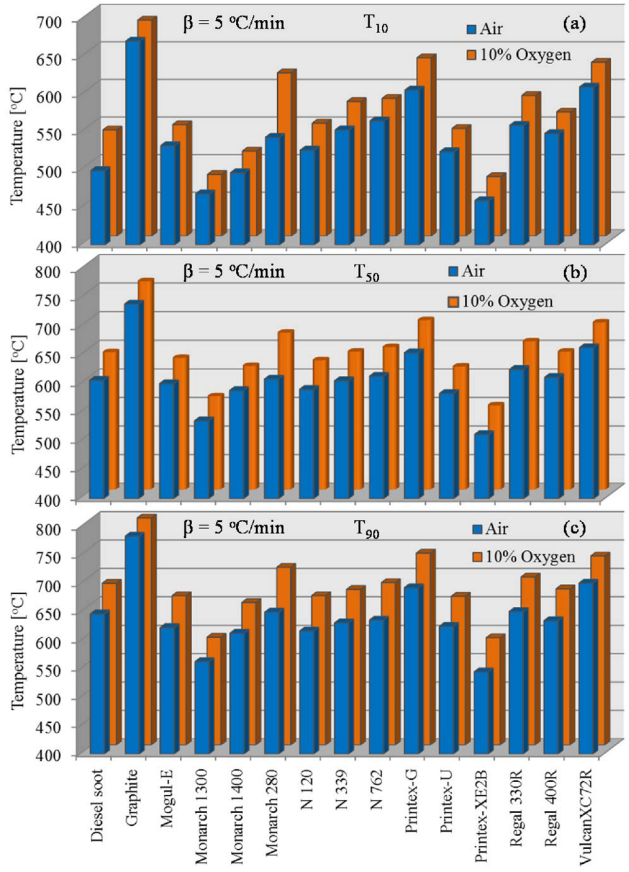

Figure 7. Comparison of T_{10}, T_{50}, and T_{90} values for all samples with 10% O_2 and air. Oxidation is faster with air. The operating conditions are the same as in Figures 5 and 6.

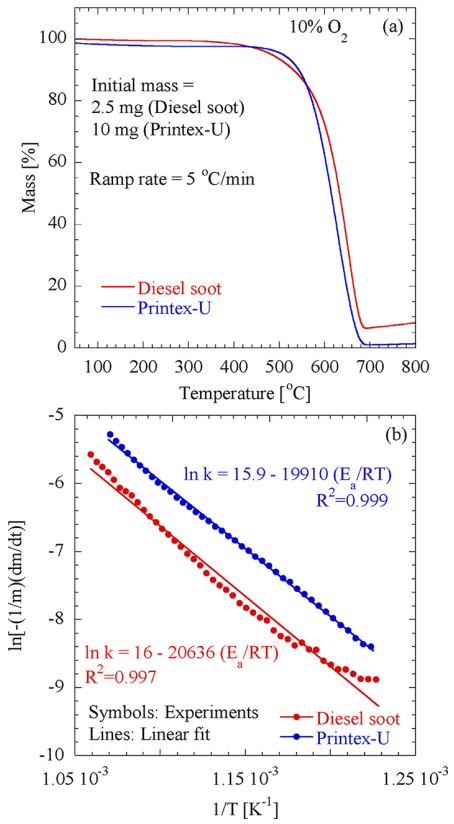

Figure 8. (a) Mass loss profiles and (b) Arrhenius plots for diesel soot and Printex-U samples using method A. The operating conditions are the same as in Figure 5.

negligible moisture (0−0.6%) in the other samples. Therefore, oxidation data for Monarch 1300 and Monarch 1400 are reported with and without considering the moisture content (see Table 2). To calculate the conversion without considering the moisture content, the conversion (~4−5%) of those two samples just before reaching 200 °C was used to compute the "corrected" initial mass without moisture. As expected, the T_{10} values were significantly affected by the moisture content, but the T_{50} and T_{90} values were not.

Figure 7 compares the T_{10}, T_{50}, and T_{90} values for all samples with 10% O_2 and air. The T_{10}−T_{90} values of all samples were lower in the case of oxidation with air than those with 10% O_2.

dx.doi.org/10.1021/ef3009025 | Energy Fuels 2012, 26, 5613−5625

Table 3. Apparent Kinetic Parameters from Non-isothermal and Isothermal Experiments[a]

		10% O_2							air						
sample number	samples	range (%)	R^2	E (kJ/mol)	A (Pa^{-1} s^{-1})	k_{550} (Pa^{-1} s^{-1})	k_{600} (Pa^{-1} s^{-1})	k_{650} (Pa^{-1} s^{-1})	range (%)	R^2	E (kJ/mol)	A (Pa^{-1} s^{-1})	k_{550} (Pa^{-1} s^{-1})	k_{600} (Pa^{-1} s^{-1})	k_{650} (Pa^{-1} s^{-1})
1	diesel soot	10−90	0.991	154−172[b]	1.0×10^2−9.4×10^2[b]	1.1×10^{-8}	4.8×10^{-8}	1.7×10^{-7}	10−90	0.985	152−169[b]	1.0×10^2−8.5×10^2[b]	1.6×10^{-8}	6.6×10^{-8}	2.3×10^{-7}
		10−90	0.898	155−198[c]	2.4×10^2 − 3.4×10^5[c]	2.2×10^{-8}[c]	8.6×10^{-8}[c]	2.9×10^{-7}[c]	10−90	0.872	121−163[c]	2.3×10^0−5.0×10^2[c]	2.2×10^{-8}[c]	8.3×10^{-8}[c]	2.7×10^{-7}[c]
		20−90	0.956	112−142[d]	3.3×10^{-1}− 2.6×10^1[d]	2.3×10^{-8}[d]	6.9×10^{-8}[d]	1.8×10^{-7}[d]	20−90	0.683	133−155[d]	6.2×10^0−1.8×10^2[d]	2.2×10^{-8}[d]	7.9×10^{-8}[d]	2.4×10^{-7}[d]
2	graphite	10−80	0.995	226	3.7×10^4	1.7×10^{-10}	1.1×10^{-9}	5.9×10^{-9}	10−90	0.999	229	4.8×10^4	1.4×10^{-10}	9.6×10^{-10}	5.3×10^{-9}
3	Mogul-E	10−75	0.980	186	9.4×10^3	1.5×10^{-8}	7.0×10^{-8}	2.8×10^{-7}	10−60	0.958	214	5.9×10^5	1.6×10^{-8}	9.4×10^{-8}	4.6×10^{-7}
4	Monarch 1300	10−80	0.945	164	2.9×10^3	1.2×10^{-7}	4.6×10^{-7}	1.5×10^{-6}	10−80	0.870	197	4.7×10^5	1.5×10^{-7}	7.8×10^{-7}	3.4×10^{-6}
		5−80[e]	0.932[e]	145[e]	1.9×10^2[e]	1.1×10^{-7}[e]	3.7×10^{-7}[e]	1.1×10^{-6}[e]	5−80[e]	0.861[e]	156[e]	8.6×10^2[e]	1.0×10^{-7}[e]	4.0×10^{-7}[e]	1.3×10^{-6}[e]
		20−90	0.897	93−117[d]	1.5×10^{-1} −1.9×10^0[d]	9.0×10^{-8}[d]	2.3×10^{-7}[d]	5.2×10^{-7}[d]							
5	Monarch 1400	10−80	0.971	144	3.6×10^1	2.6×10^{-8}	8.9×10^{-8}	2.6×10^{-7}	10−80	0.940	146	5.2×10^1	2.9×10^{-8}	9.7×10^{-8}	2.9×10^{-7}
		5−80[e]	0.952[e]	125[e]	2.6×10^0[e]	3.1×10^{-8}[e]	8.9×10^{-8}[e]	2.3×10^{-7}[e]	5−80[e]	0.933[e]	133[e]	7.6×10^0[e]	2.8×10^{-8}[e]	8.5×10^{-8}[e]	2.3×10^{-7}[e]
6	Monarch 280	10−90	0.989	220	2.4×10^5	2.6×10^{-9}	1.6×10^{-8}	8.5×10^{-8}	10−90	0.994	180	3.8×10^3	1.4×10^{-8}	6.5×10^{-8}	2.5×10^{-7}
7	N 120	10−90	0.980	195	3.5×10^4	1.5×10^{-8}	7.6×10^{-8}	3.2×10^{-7}	10−80	0.996	203	1.5×10^5	2.0×10^{-8}	1.0×10^{-7}	5.1×10^{-7}
8	N 339	10−80	0.993	222	9.4×10^5	7.7×10^{-9}	4.9×10^{-8}	2.6×10^{-7}	10−80	0.991	243	2.6×10^7	1.0×10^{-8}	7.7×10^{-8}	4.7×10^{-7}
9	N 762	10−80	0.994	206	8.5×10^4	7.2×10^{-9}	4.0×10^{-8}	1.9×10^{-7}	10−80	0.992	257	1.3×10^8	6.3×10^{-9}	5.4×10^{-8}	3.7×10^{-7}
10	Printex-G	10−80	0.990	187	1.9×10^3	2.6×10^{-9}	1.2×10^{-8}	4.9×10^{-8}	10−80	0.987	207	3.8×10^4	2.8×10^{-9}	1.6×10^{-8}	7.5×10^{-8}
11	Printex-U	10−90	0.999	87−165[b]	1.2×10^{-2}−8.2×10^2[b]	2.8×10^{-8}	1.1×10^{-7}	3.8×10^{-7}	10−90	0.999	143−182[b]	3.8×10^1−1.0×10^4[b]	2.9×10^{-8}	1.3×10^{-7}	5.2×10^{-7}
		10−90	0.959	78−142[c]	1.7×10^{-2} −3.8×10^1[c]	7.5×10^{-8}[c]	1.7×10^{-7}[c]	3.6×10^{-7}[c]	10−90	0.902	136−170[c]	1.4×10^3 −1.2×10^5[c]	4.0×10^{-8}[c]	1.5×10^{-7}[c]	4.8×10^{-7}[c]
		20−90	0.987	107−136[d]	1.2×10^{-1} −1.4×10^1[d]	2.7×10^{-8}[d]	7.6×10^{-8}[d]	1.9×10^{-7}[d]	20−90	0.832	135−153[d]	6.2×10^0 −1.5×10^2[d]	2.1×10^{-8}[d]	7.3×10^{-8}[d]	2.2×10^{-7}[d]
12	Printex-XE2B	10−90	0.993	155	6.1×10^2	8.9×10^{-8}	3.2×10^{-7}	1.0×10^{-6}	10−90	0.997	196	1.1×10^6	4.1×10^{-7}	2.1×10^{-6}	9.2×10^{-6}
13	Regal 330 R	10−80	0.992	207	3.4×10^4	2.4×10^{-9}	1.4×10^{-8}	6.5×10^{-8}	10−80	0.984	171	1.6×10^3	2.2×10^{-8}	9.4×10^{-8}	3.4×10^{-7}
14	Regal 400 R	10−80	0.990	211	2.1×10^5	8.5×10^{-9}	5.0×10^{-8}	2.4×10^{-7}	10−80	0.987	249	5.8×10^7	9.1×10^{-9}	7.3×10^{-8}	4.7×10^{-7}
15	VulcanXC72R	10−90	0.988	210	1.9×10^4	9.3×10^{-10}	5.4×10^{-9}	2.6×10^{-8}	10−90	0.983	223	2.7×10^5	1.9×10^{-9}	1.2×10^{-8}	6.5×10^{-8}
		20−90	0.888	144−156[d]	4.6×10^0−4.6×10^1[d]	4.1×10^{-9}[d]	1.5×10^{-8}[d]	4.6×10^{-8}[d]	20−90	0.903	188−223[d]	2.8×10^3−1.6×10^5[d]	1.6×10^{-9}[d]	1.0×10^{-8}[d]	5.0×10^{-8}[d]

[a]The kinetic parameters correspond to method A with ramp rate β of 5 °C/min, unless specified otherwise. [b]Method A was applied for different ramp rates (β = 5−20 °C/min). For the given range, the first value is for 20 °C/min experiments and the second value is for 5 °C/min experiments. [c]Method B: non-isothermal experiments with multiple-ramp rates. Activation energies and pre-exponential factors are given for the fractional conversion α range of 0.1−0.9, whereas the rate constants k are reported for α of 0.5. [d]Method C: isothermal experiments. Activation energies and pre-exponential factors are given for the fractional conversion α range of 0.2−0.9, whereas the rate constants k are reported for α of 0.5. [e]Without moisture (see the text for details).

dx.doi.org/10.1021/ef3009025 | Energy Fuels 2012, 26, 5613−5625

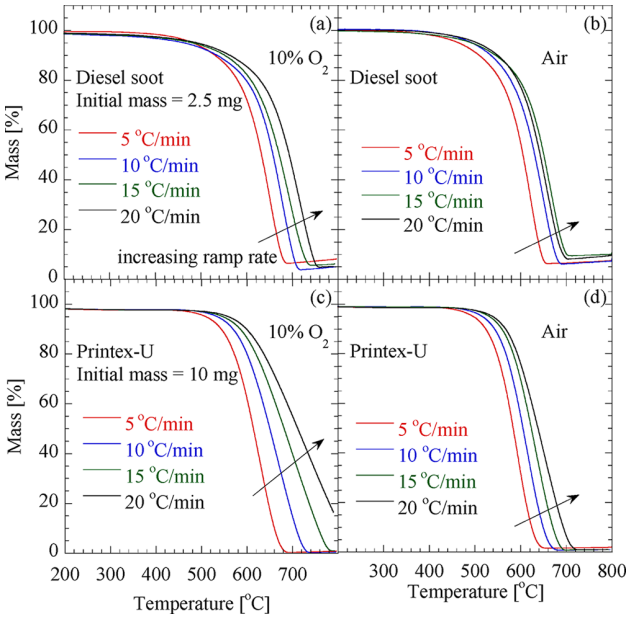

Figure 9. Effect of the ramp rate and oxygen partial pressure on the oxidation of diesel soot (initial mass of 2.5 mg) and Printex-U (initial mass of 10 mg). Ramp rates of 5, 10, 15, and 20 °C/min are used. (a) Diesel soot with 10% O_2, (b) diesel soot with air, (c) Printex-U with 10% O_2, and (d) Printex-U with air. Operating conditions: non-isothermal experiment and flow rate at 60 mL/min.

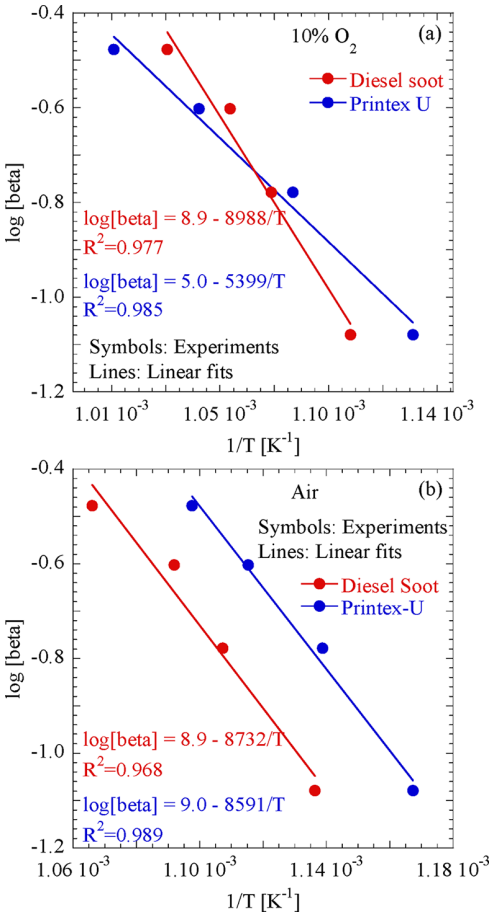

Figure 10. Kinetic parameter extraction for diesel soot (initial mass of 2.5 mg) and Printex-U (initial mass of 10 mg) oxidation with (a) 10% O_2 and (b) air using method B for a fractional conversion α of 0.5. Operating conditions are the same as in Figure 9.

Therefore, the oxidation of carbon black and soot samples with air was faster than with 10% O_2. Because the oxidation profiles in Figures 5 and 6 showed similar trends for both cases, the decrease in $T_{10}-T_{90}$ values for air was due to the higher concentration of O_2 in air (21%).

Method A discussed in section 3.1 was used to extract the apparent activation energies and pre-exponential factors. Figure 8 shows an example of data analysis for diesel soot and Printex-U. First, data in panel a confirmed that the oxidation behavior of diesel soot and Printex-U was quite similar, which explains why Printex-U is commonly used as a surrogate for diesel soot.[30,40,42,59,63−65] Second, we used a much wider range of conversion profile (from 10 to ∼90%) for data analysis in panel b compared to the literature studies,[42,66] which ensured the validity of the estimated kinetic parameters over almost the complete oxidation process. Third, as shown in panel b, the $\ln(-dm/mdt)$ versus $1/T$ plots for diesel soot and Printex-U are almost straight lines with $R^2 > 0.99$, which agrees with the assumption of first-order kinetics. A similar analysis was conducted for all samples for both oxidizer gases (10% O_2 and air), and the kinetic parameters (along with the considered conversion ranges and R^2 values) are reported in Table 3. Oxidation reaction rate constants at different temperatures (k_{550}, k_{600}, and k_{650}) are also given in Table 3 for both cases (10% O_2 and air), which indicated that oxidation with air was faster than with 10% O_2.

In general, the range of activation energies reported in the literature for the oxidation of carbon black and soot samples is 100−300 kJ/mol.[9,21,30,34,40,42,43,47,60,64,66−69] However, the typically reported activation energies for diesel engine soot oxidation are in the range of 120−180 kJ/mol.[30,59,60,68,70−72] Neeft et al.[59] suggested that the activation energy increased in the following sequence: soot < activated carbon < carbon and chars < graphite, which was also observed in our experiments, with graphite showing the largest activation energy and the smallest rate constant. Given the comprehensive nature of our study, literature data were not available for direct comparisons for all of the samples studied; however, the activation energies estimated from our TGA experiments were in close agreement with those reported in the literature. For example, the activation energy for diesel soot oxidation with oxygen was reported to be 164 kJ/mol by Higgins et al.[60] and Darcy et al.,[68] and 177 kJ/mol by Lee et al.,[70] which compare well to our estimate of 172 kJ/mol. Similarly, the activation energy for Printex-U oxidation was reported to be 168 kJ/mol by Neeft et al.[59] and 161 kJ/mol by Tang et al.[42] with 10% O_2 and 160 kJ/mol by Hinot[62] with 20% O_2, which compare well with our estimates of 165 kJ/mol with 10% O_2 and 182 kJ/mol with air. Despite the agreement with the literature, it is important to note that the estimated kinetic parameters should ideally not change with the O_2 partial pressure. As alluded to earlier, this fundamental limitation most likely stems from the simplified kinetic expressions (eqs 1 and 2), where the change in the surface area during oxidation and the pore size effects were ignored and the reaction order with respect to O_2 was assumed to be unity. Therefore, we emphasize that the estimated activation energies (and pre-exponential factors) should be considered as apparent kinetic parameters only.

dx.doi.org/10.1021/ef3009025 | Energy Fuels 2012, 26, 5613−5625

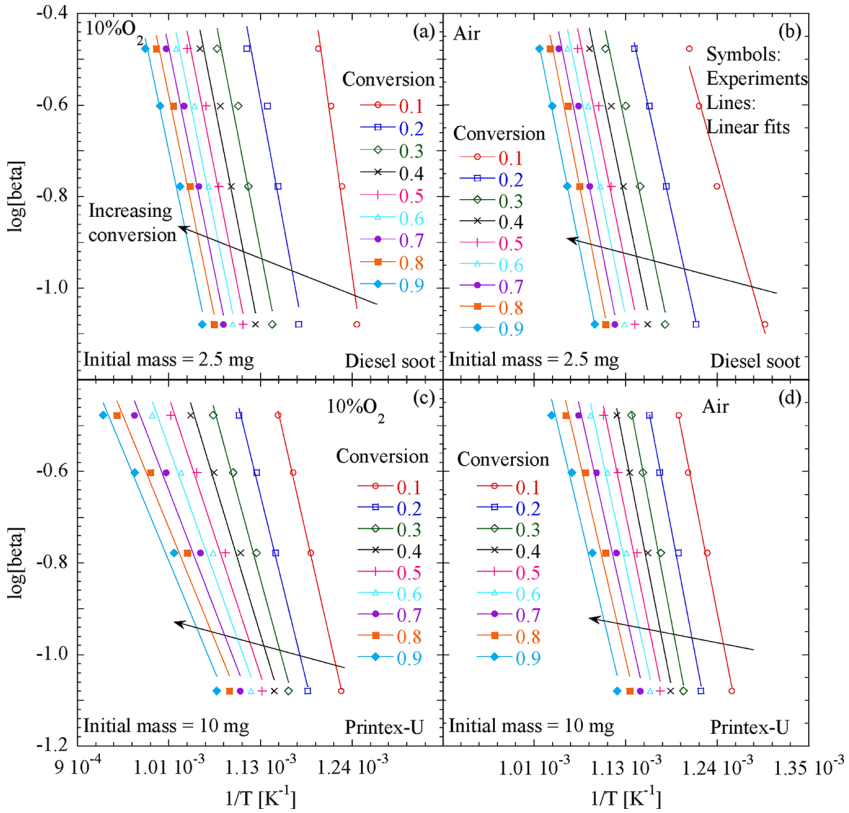

Figure 11. Flynn–Wall–Ozawa plot for diesel soot (initial mass of 2.5 mg) and Printex U (initial mass of 10 mg) oxidation. (a) Diesel soot with 10% O_2, (b) diesel soot with air, (c) Printex-U with 10% O_2, and (d) Printex-U with air, using method B for a fractional conversion α range of 0.1–0.9. Operating conditions are the same as in Figure 9.

To understand the variation of the oxidation rate for the different carbon black and soot samples, they were characterized using scanning electron microscopy (SEM) and Brunauer–Emmett–Teller (BET) surface area.[73] SEM analysis indicated that the average particle size (over ~200 particles) varied over a wide range (20.9–74 nm). Similarly, the BET surface area varied over a wide range as well (43–1005 m^2/g). The oxidation rate of carbon black and soot samples is a complex function of various structural factors and operating conditions; however, the large variations in average particle size and surface area may be used to explain some of the trends in the oxidation rate.[73] Monarch 1400, Monarch 1300, and Printex-XE2B had the smallest average particle size (20.9–26.7 nm), whereas Printex-G, Monarch 280, and Mogul-E had the largest particle size (69.7–74 nm). Surface areas of Monarch 1400, Monarch 1300, and Printex-XE2B were in the higher range of 342–1005 m^2/g, whereas those of Printex-G, Monarch 280, and Mogul-E were in the lower range of 45–49 m^2/g. The higher rate of Monarch 1400, Monarch 1300, and Printex-XE2B ($T_{50}^{O_2}$ range of 547–616 °C) could be attributed to the smaller particle size and higher surface area. Similarly, the lower rate of Printex-G, Monarch 280, and Mogul-E ($T_{50}^{O_2}$ range of 630–674 °C) could be attributed to the larger particle size and lower surface area.

4.2. Effect of the Ramp Rate. The ramp rate β is another operating parameter that typically shows a large impact on the oxidation profile.[20,30] To validate the activation energies estimated in the previous section, we conducted TGA experiments with 10% O_2 and air using four ramp rates (5, 10, 15, and 20 °C/min) for diesel soot and Printex-U samples. Experimental protocol details are provided in Table 1. As shown in Figure 9, the oxidation rate shifted to higher temperatures with an increase in the ramp rate. A higher ramp rate reduces the overall reaction time in an experiment for a given temperature range, and less mass loss occurs at the same temperature point compared to a lower ramp rate case.[31] For example, for heating from 600 to 800 °C, it takes only 10 min with 20 °C/min, whereas it takes 40 min with 5 °C/min. Kalogirou and Samaras suggested that the higher ramp rates could also be associated with diffusional limitations, which are more prominent in the case of low oxygen concentrations.[30] Our experimental results with different ramp rates and oxygen partial pressures were consistent with this observation. For example, when the 10% O_2 versus air profiles in Figure 9 are compared, the delay in the oxidation rate with an increased ramp rate was higher for 10% O_2 compared to that for air. This also justifies the 5 °C/min ramp rate used in section 4.1 (method A) for kinetic parameter estimation. On the other hand, data analysis presented in this section could be affected by diffusional limitations to some extent at higher ramp rates but provide a reasonably good validation of the kinetic parameters.

Results obtained from diesel soot and Printex-U oxidation with 10% O_2 and air for various ramp rates (5–20 °C/min) were analyzed using method B discussed in section 3.2. Figure 10 shows a plot of log β versus $1/T$ for diesel soot and Printex-U for both 10% O_2 (panel a) and air (panel b) for a selected fractional conversion α of 0.5. The estimated kinetic parameters are reported in Table 3. With 10% O_2, the estimated activation energies for diesel soot and Printex-U oxidation were in the range of 155–198 and 78–142 kJ/mol, respectively (these ranges were based on applying method B at different fractional conversions),

dx.doi.org/10.1021/ef3009025 | Energy Fuels 2012, 26, 5613–5625

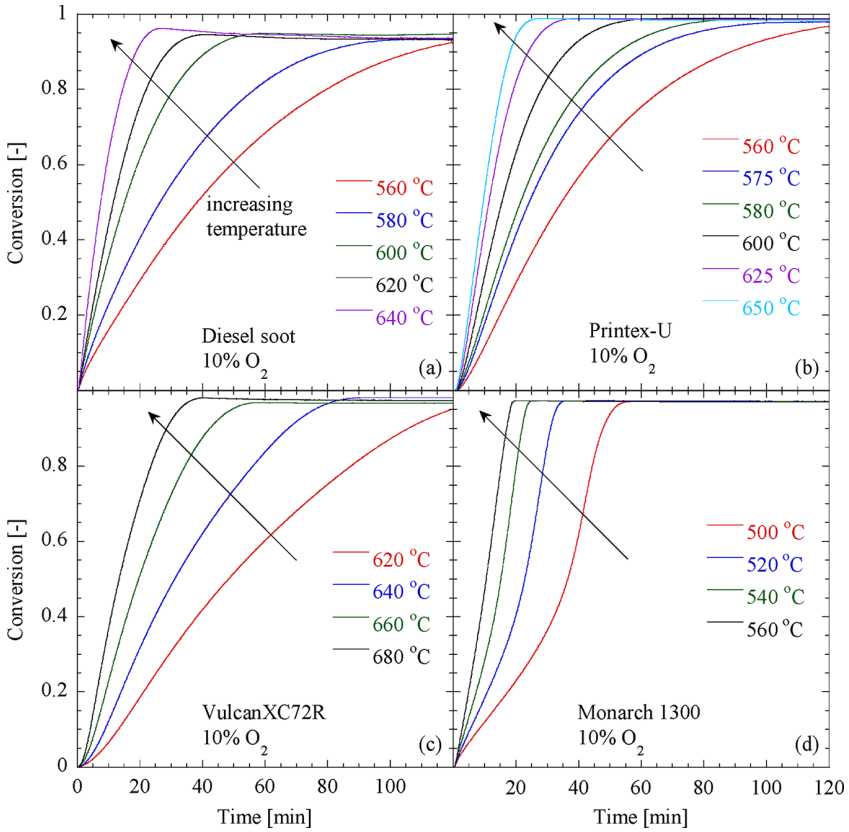

Figure 12. Isothermal conversion profiles of (a) diesel soot (initial mass of 2.5 mg), (b) Printex-U (initial mass of 10 mg), (c) VulcanXC72R (initial mass of 5 mg), and (d) Monarch 1300 (initial mass of 12 mg). Operating conditions: isothermal experiment, 10% O_2 oxidant, flow rate at 60 mL/min, and ramp rate to reach isothermal temperature at 20 °C/min.

which were comparable to the numbers estimated from method A (154−172 and 87−165 kJ/mol, respectively; these ranges were based on applying method A at different ramp rates). Similarly, with air, the estimated activation energies for diesel soot and Printex-U oxidation were in the range of 121−163 and 136−170 kJ/mol, respectively (these ranges were based on applying method B at different fractional conversions), which were also comparable to the numbers estimated from method A (152−169 and 143−182 kJ/mol, respectively; these ranges were based on applying method A at different ramp rates). A larger deviation was observed in the case of 10% O_2 than air, which could be due to the diffusional limitations associated with larger ramp rates and a low oxygen concentration. However, the rate constants calculated using method B at any particular temperature (see k values in Table 3 for $\alpha = 0.5$) showed excellent agreement with the rate constants calculated using method A.

Before moving on to the isothermal experiments in the next section, we note that the kinetic parameters estimated using method B are dependent upon the fractional conversion α. For example, parameter estimation analysis was carried out for a wider range of fractional conversion values ($\alpha = 0.1-0.9$), as shown in Figure 11 for diesel soot and Printex-U. The activation energies varied with the fractional conversion (diesel soot, 155−198 kJ/mol for 10% O_2 and 121−163 kJ/mol for air; Printex-U, 78−142 kJ/mol for 10% O_2 and 136−170 kJ/mol for air). Overall, the analysis based on method B provided excellent validation for the kinetic parameters estimated using method A. Nonetheless, we recommend experiments with lower ramp rates to avoid any influence of heat- and mass-transfer limitations.

5. KINETICS FROM ISOTHERMAL TESTS

Apart from the non-isothermal experiments reported thus far, we also conducted isothermal tests for selected samples (diesel soot, Printex-U, Monarch 1300, and VulcanXC72R) to further validate the kinetic parameters. The four samples were selected to cover the range from low to high oxidation rates from the non-isothermal experiments. For each sample, we conducted isothermal experiments at multiple temperature points with the same initial mass. After reaching the set point (isothermal temperature), the sample was kept at the set point for 2 h. Experimental protocol details are provided in Table 1. Method C discussed in section 3.3 was used for the analysis of the isothermal experiments.

Figure 12 shows the mass loss profiles of the four selected samples. Plots of conversion α versus time t suggest that the reaction profiles or kinetic curves of diesel soot and commercial carbon black samples are of the decelerating type, in which the rate is maximum at the beginning and decreases continuously with the extent of conversion.[18] Reaction order models are generally used for gas−solid reactions of the decelerating type. First-order reaction kinetics was used for the analysis of these data to extract the kinetic parameters, consistent with the methods A and B discussed earlier. The estimated kinetic parameters are reported in Table 3.

In general, the activation energies estimated using method C (isothermal) were slightly lower than those estimated using

dx.doi.org/10.1021/ef3009025 | Energy Fuels 2012, 26, 5613−5625

methods A and B (non-isothermal). Similarly, the pre-exponential factors calculated using method C (isothermal) were lower than those estimated using methods A and B (non-isothermal). On the other hand, the reaction rate constants computed at 550, 600, and 650 °C for α of 0.5 showed good agreement with the corresponding rate constants estimated from the non-isothermal experiments. This indicated that the activation energies estimated using method C could be affected by the compensation effect between activation energies and pre-exponential factors. The compensation effect is a commonly reported phenomenon, in which change in the activation energy is compensated by change in the pre-exponential factor.[28,74−76] Analysis conducted at different fractional conversion values for diesel soot oxidation with 10% O_2 and air is shown in Figure 13a. The activation

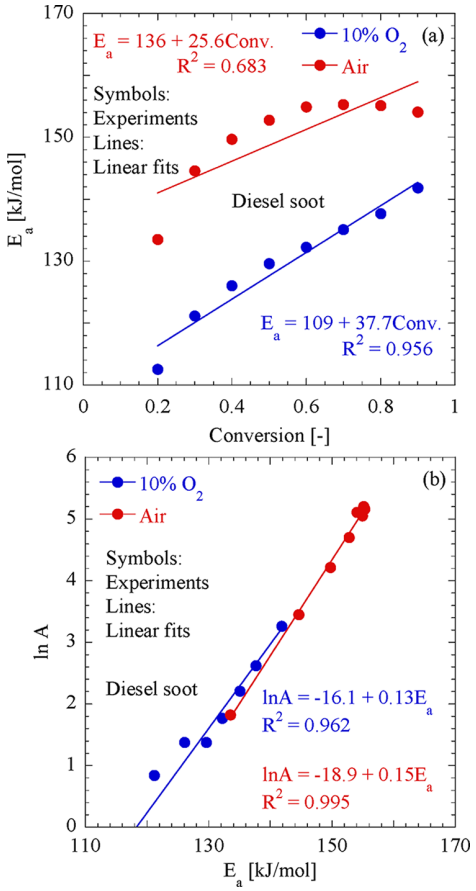

Figure 13. Isothermal kinetics of diesel soot oxidation using method C. (a) Variation of the activation energy with fractional conversion α (range of 0.2−0.9) using both 10% O_2 and air. (b) Compensation effect of activation energies and pre-exponential factors. Operating conditions are the same as in Figure 12.

energy varied with fractional conversion, consistent with literature reports on solid-state reaction kinetics.[18,76−78] For example, the estimated activation energy ranged over fractional conversion α of 0.2−0.9 for diesel soot (112−142 kJ/mol for 10% O_2 and 133−155 kJ/mol for air) and Printex-U (107−136 kJ/mol for 10% O_2 and 135−153 kJ/mol for air), and corresponding variation in pre-exponential factors confirmed the existence of the compensation effect. Figure 13b shows the variation in activation energy with the pre-exponential factor. Complex or multiple-step reaction kinetics of soot oxidation was ruled out because of the absence of multiple peaks and/or shoulders in the reaction rate curve.[18] Despite this limitation, method C (isothermal) provided a reasonably good validation of the kinetic parameters estimated using methods A and B (non-isothermal).

To verify the assumption of first-order kinetics with respect to O_2, we estimated the reaction order (n_{O_2}) based on the isothermal experiments with 10% O_2 and air for the four samples studied here (diesel soot, Printex-U, Monarch 1300, and VulcanXC72R). The estimated n_{O_2} was 1 for diesel soot, whereas it was close to 1 for the other carbon black samples (0.95 for Printex-U, 0.88 for Monarch 1300, and 0.90 for VulcanXC72R). Finally, to demonstrate the validity of effective models used here, Figure 14 shows how the apparent kinetic

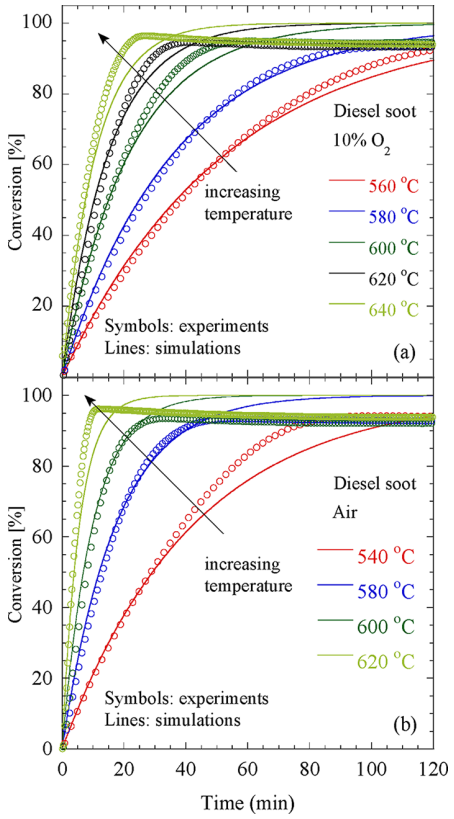

Figure 14. Validation of estimated apparent kinetic parameters and the effective model against experimental results in Figure 12a and also against isothermal experiments with air. Simulations were conducted using apparent activation energies and pre-exponential factors at fractional conversion α of 0.5 from the isothermal experiments for diesel soot with (a) 10% O_2 and (b) air. A reaction order n_{O_2} of 1 was used. Diesel soot showed incomplete conversion in the experiments because of the presence of metal oxides and ash particles.

parameters extracted at nominal conditions (fractional conversion α = 0.5) along with first-order kinetics with respect to O_2 can adequately capture the entire range of experimental data; i.e., the compensation effect between the apparent activation energy and pre-exponential factors was not critical for the effective models considered here.

6. CONCLUSION

In this work, we conducted non-isothermal and isothermal TGA experiments for more than a dozen carbon black samples and a diesel engine soot sample with 10% O_2 and air to

dx.doi.org/10.1021/ef3009025 | Energy Fuels 2012, 26, 5613−5625

investigate the effect of operating conditions on the oxidation rate and to extract the corresponding apparent kinetic parameters. Limitations associated with the availability of oxygen were avoided by conducting experiments in sufficient oxidizer gas flow rate conditions. The partial pressure of oxygen and ramp rates showed significant effects on the oxidation rate. Oxidation with air was faster than with 10% O_2, because of the higher concentration of oxygen in air. The activation energy for the oxidation of carbon black samples ranged from 125 to 257 kJ/mol, whereas that for soot oxidation was ∼155 kJ/mol. Oxidation rate trends were explained on the basis of structural characteristics, such as SEM-based average particle size and BET surface area. In general, a low particle size and high surface area were associated with a higher oxidation rate and vice versa. Kinetic parameters extracted using the non-isothermal experiments at a single-ramp rate (method A) were further validated using additional non-isothermal experiments with multiple-ramp rates (method B) and isothermal experiments (method C). The overall agreement for kinetic parameters estimated using the three methods (consisting of separately conducted experiments) was remarkable; however, the analysis in methods B and C indicated that the extracted parameters could be affected by a compensation effect between activation energies and pre-exponential factors as they change with the extent of conversion. Overall, the comprehensive understanding developed in this work for oxidation of carbon black and soot samples could be beneficial for the improved design and optimization of DPF operation and regeneration protocols.

■ AUTHOR INFORMATION

Corresponding Author

*Telephone: 1-443-523-8609 . Fax: 1-860-486-2959. E-mail: ashish.mhadeshwar@gmail.com.

Notes

The authors declare no competing financial interest.

■ ACKNOWLEDGMENTS

This work was supported by Corning, Inc. and the Department of Energy (DOE) through Award DE-EE0003226 ("Improving Reliability and Durability of Efficient and Clean Energy Systems"). Hom N. Sharma also acknowledges the Department of Education GAANN Fellowship for funding. The authors thank Laura Pinatti from the Institute of Materials Science (IMS) at the University of Connecticut for access to the TGA equipment.

■ REFERENCES

(1) Schneider, C. G.; Hill, L. B. *Diesel and Health in America: The Lingering Threat*; Clean Air Task Force: Boston, MA, 2005; http://www.catf.us/resources/publications/files/Diesel_Health_in_America.pdf.

(2) U.S. Energy Information Administration (EIA). *Diesel Fuel Explained—Use of Diesel*; EIA: Washington, D.C., 2011; http://www.eia.gov/energyexplained/index.cfm?page=diesel_use (accessed Feb 5, 2012).

(3) California Energy Commission. *Petroleum Watch*; California Energy Commission: Sacramento, CA, 2011; http://energyalmanac.ca.gov/petroleum/petroleum_watch/2011-09-16_Petroleum_Watch.pdf (accessed Feb 5, 2012).

(4) Bensaid, S.; Caroca, C. J.; Russo, N.; Fino, D. *Can. J. Chem. Eng.* **2011**, *89* (2), 401−407.

(5) Prasad, R.; Bella, V. R. *Bull. Chem. React. Eng. Catal.* **2010**, *5* (2), 69−86.

(6) Fino, D. *Sci. Technol. Adv. Mater.* **2007**, *8* (1−2), 93−100.

(7) Xi, J.; Zhong, B. J. *Chem. Eng. Technol.* **2006**, *29* (6), 665−673.

(8) Vander Wal, R. L.; Bryg, V. M.; Hays, M. D. *J. Aerosol Sci.* **2010**, *41* (1), 108−117.

(9) Yezerets, A.; Currier, N. W.; Kim, D. H.; Eadler, H. A.; Epling, W. S.; Peden, C. H. F. *Appl. Catal., B* **2005**, *61* (1−2), 120−129.

(10) Jones, C. C.; Chughtai, A. R.; Murugaverl, B.; Smith, D. M. *Carbon* **2004**, *42* (12−13), 2471−2484.

(11) Clague, A. D. H.; Donnet, J. B.; Wang, T. K.; Peng, J. C. M. *Carbon* **1999**, *37* (10), 1553−1565.

(12) Prasad, R.; Bella, V. R. *Bull. Chem. React. Eng. Catal.* **2010**, *5* (2), 95−101.

(13) Hoyer, M.; Foureman, G.; Valcovic, L.; Grant, L.; McGrath, J.; Koppikar, A.; Pepelko, W.; Chen, C.; Ris, C. *Health Assessment Document for Diesel Engine Exhaust*; United States Environmental Protection Agency (U.S. EPA): Washington, D.C., 2002; http://www.epa.gov/ttn/atw/dieselfinal.pdf (accessed March 14, 2012).

(14) United States Environmental Protection Agency (U.S. EPA). *National Ambient Air Quality Standards (NAAQS)*; U.S. EPA: Washington, D.C., 2011; http://epa.gov/air/criteria.html (accessed Jan 12, 2012).

(15) Ecopoint, Inc. *Emissions Standards*; Ecopoint, Inc.: Mississauga, Ontario, Canada, 2011; http://www.dieselnet.com/standards/eu/hd.php (accessed Feb 15, 2012).

(16) Williams, S. Surface intermediates, mechanism, and reactivity of soot oxidation. Ph.D. Thesis, University of Toronto, Toronto, Ontario, Canada, 2008.

(17) Maricq, M. *J. Aerosol Sci.* **2007**, *38* (11), 1079−1118.

(18) Vyazovkin, S.; Burnham, A. K.; Criado, J. M.; Pérez-Maqueda, L. A.; Popescu, C.; Sbirrazzuoli, N. *Thermochim. Acta* **2011**, *520* (1−2), 1−19.

(19) Song, J.; Alam, M.; Boehman, A. L. *Combust. Sci. Technol.* **2007**, *179* (9), 1991−2037.

(20) Rodriguez-Fernandez, J.; Oliva, F.; Vazquez, R. A. *Energy Fuels* **2011**, *25* (5), 2039−2048.

(21) Kalogirou, M.; Samaras, Z. *J. Therm. Anal. Calorim.* **2010**, *99* (3), 1005−1010.

(22) López-Fonseca, R.; Elizundia, U.; Landa, I.; Gutiérrez-Ortiz, M. A.; González-Velasco, J. R. *Appl. Catal., B* **2005**, *61* (1−2), 150−158.

(23) Zouaoui, N.; Brilhac, J.; Mechati, F.; Jeguirim, M.; Djellouli, B.; Gilot, P. *J. Therm. Anal. Calorim.* **2010**, *102* (3), 837−849.

(24) Neeft, J. P. A.; Hoornaert, F.; Makkee, M.; Moulijn, J. A. *Thermochim. Acta* **1996**, *287* (2), 261−278.

(25) Gilot, P.; Bonnefoy, F.; Marcuccilli, F.; Prado, G. *Combust. Flame* **1993**, *95* (1−2), 87−100.

(26) Stanmore, B. R.; Gilot, P. *Thermochim. Acta* **1995**, *261*, 151−164.

(27) Gilot, P.; Brillard, A.; Stanmore, B. R. *Combust. Flame* **1995**, *102* (4), 471−480.

(28) Khawam, A.; Flanagan, D. R. *J. Pharm. Sci.* **2006**, *95* (3), 472−498.

(29) Liu, C.; Yu, J.; Sun, X.; Zhang, J.; He, J. *Polym. Degrad. Stab.* **2003**, *81* (2), 197−205.

(30) Kalogirou, M.; Samaras, Z. *J. Therm. Anal. Calorim.* **2009**, *98* (1), 215−224.

(31) Castaldi, M. J.; Kwon, E. Thermo-gravimetric analysis (TGA) of combustion and gasification of styrene−butadiene copolymer (SBR). *Proceedings of the 13th North American Waste to Energy Conference*; Orlando, FL, May 23−25, 2005; NAWTEC13-3149.

(32) Costache, M. C.; Wang, D.; Heidecker, M. J.; Manias, E.; Wilkie, C. A. *Polym. Adv. Technol.* **2006**, *17*, 272−280.

(33) Gašparovič, L.; Koreňová, Z.; Jelemenský, L'. Kinetic study of wood chips decomposition by TGA. *Proceedings of the 36th International Conference of Slovak Society of Chemical Engineering*; Tatranské Matliare, Slovakia, May 25−29, 2009; p 178.

(34) López-Fonseca, R.; Landa, I.; Elizundia, U.; Gutiérrez-Ortiz, M. A.; González-Velasco, J. R. *Combust. Flame* **2006**, *144* (1−2), 398−406.

(35) Skreiberg, A.; Skreiberg, Ø.; Sandquist, J.; Sørum, L. *Fuel* **2011**, *90* (6), 2182−2197.

(36) Ollero, P.; Serrera, A.; Arjona, R.; Alcantarilla, S. *Fuel* **2002**, *81* (15), 1989−2000.
(37) López-Fonseca, R.; Landa, I.; Elizundia, U.; Gutiérrez-Ortiz, M. A.; González-Velasco, J. R. *Chem. Eng. J.* **2007**, *129* (1−3), 41−49.
(38) Gómez-Barea, A.; Ollero, P.; Arjona, R. *Fuel* **2005**, *84* (12−13), 1695−1704.
(39) Brilhac, J. F.; Bensouda, F.; Gilot, P.; Brillard, A.; Stanmore, B. *Carbon* **2000**, *38* (7), 1011−1019.
(40) Stanmore, B. R.; Brilhac, J. F.; Gilot, P. *Carbon* **2001**, *39* (15), 2247−2268.
(41) Stanmore, B.; Gilot, P.; Prado, G. *Thermochim. Acta* **1994**, *240*, 79−89.
(42) Tang, J.; Song, Q.; He, B.; Yao, Q. *Sci. China, Ser. E: Technol. Sci.* **2009**, *52* (6), 1535−1542.
(43) Yezerets, A.; Currier, N. W.; Eadler, H. A.; Suresh, A.; Madden, P. F.; Branigin, M. A. *Catal. Today* **2003**, *88* (1−2), 17−25.
(44) López-Fonseca, R.; Landa, I.; Gutiérrez-Ortiz, M. A.; González-Velasco, J. R. *J. Therm. Anal. Calorim.* **2005**, *80* (1), 65−69.
(45) Leistner, K.; Nicolle, A.; Berthout, D.; da Costa, P. *Combust. Flame* **2012**, *159* (1), 64−76.
(46) Salvador, S.; Commandré, J. M.; Stanmore, B. R. *Fuel* **2003**, *82* (6), 715−720.
(47) Hartman, J. R.; Beyler, A. P.; Riahi, S.; Beyler, C. L. *Fire Mater.* **2012**, *36* (3), 177−184.
(48) Yang, S.; Lee, K.; Chong, H. *SAE Tech. Pap. Ser.* **2010**, DOI: 10.4271/2010-01-2166.
(49) Flynn, J. H.; Wall, L. A. *J. Polym. Sci., Polym. Phys.* **1966**, *4* (5), 323−328.
(50) Ozawa, T. *Bull. Chem. Soc. Jpn.* **1965**, *38* (11), 1881−1886.
(51) Li, Y.; Xu, L.; Yao, X.; Luo, T.; Li, G. *J. Phys.: Conf. Ser.* **2012**, *339* (1), 1−8.
(52) Chen, X.; Yu, J.; Guo, S. *J. Appl. Polym. Sci.* **2007**, *103* (3), 1978−1984.
(53) Doyle, C. D. *Nature* **1965**, *207* (4994), 290−291.
(54) Doyle, C. D. *J. Appl. Polym. Sci.* **1961**, *5* (15), 285−292.
(55) Azambre, B.; Collura, S.; Darcy, P.; Trichard, J. M.; Da Costa, P.; García-García, A.; Bueno-López, A. *Fuel Process. Technol.* **2011**, *92* (3), 363−371.
(56) Tighe, C. J.; Twigg, M. V.; Hayhurst, A. N.; Dennis, J. S. *Combust. Flame* **2012**, *159* (1), 77−90.
(57) Kalogirou, M.; Pistikopoulos, P.; Ntziachristos, L.; Samaras, Z. *J. Therm. Anal. Calorim.* **2009**, *95* (1), 141−147.
(58) Neeft, J. P. A.; Makkee, M.; Moulijn, J. A. *Fuel Process. Technol.* **1996**, *47* (1), 1−69.
(59) Neeft, J. P. A.; Nijhuis, T. X.; Smakman, E.; Makkee, M.; Moulijn, J. A. *Fuel* **1997**, *76* (12), 1129−1136.
(60) Higgins, K. J.; Jung, H.; Kittelson, D. B.; Roberts, J. T.; Zachariah, M. R. *J. Phys. Chem. A* **2002**, *96* (1), 96−103.
(61) Atribak, I.; Bueno-López, A.; García-García, A. *Combust. Flame* **2010**, *157* (11), 2086−2094.
(62) Hinot, K. Catalytic soot oxidation by platinum on sintered metal filters: Influence of the platinum quantity, particle size and location, and investigation of the platinum−soot contact. Ph.D. Thesis, Universität Karlsruhe, Karlsruhe, Germany, 2006.
(63) Setiabudi, A.; Makkee, M.; Moulijn, J. A. *Appl. Catal., B* **2004**, *50* (3), 185−194.
(64) Wang-Hansen, C.; Kamp, C. J.; Skoglundh, M.; Andersson, B.; Carlsson, P. *J. Phys. Chem. C* **2011**, *115* (32), 16098−16108.
(65) Jung, H.; Kittelson, D. B.; Zachariah, M. R. *Combust. Flame* **2004**, *136* (4), 445−456.
(66) Stratakis, G. A.; Stamatelos, A. M. *Combust. Flame* **2003**, *132* (1−2), 157−169.
(67) Du, Z.; Sarofim, A. F.; Longwell, J. P.; Mims, C. A. *Energy Fuels* **1991**, *5* (1), 214−221.
(68) Darcy, P.; Da Costa, P.; Mellottée, H.; Trichard, J.; Djéga-Mariadassou, G. *Catal. Today* **2007**, *119* (1−4), 252−256.
(69) Messerer, A.; Niessner, R.; Pöschl, U. *Carbon* **2006**, *44* (2), 307−324.
(70) Lee, J.; Lee, H.; Song, S.; Chun, K. *SAE Tech. Pap. Ser.* **2007**, DOI: 10.4271/2007-01-1270.
(71) Otto, K.; Sieg, M.; Zinbo, M.; Bartosiewicz, L. *SAE Tech. Pap. Ser.* **1980**, DOI: 10.4271/1980-02-01.
(72) Fredrik Ahlström, A.; Ingemar Odenbrand, C. U. *Carbon* **1989**, *27* (3), 475−483.
(73) Pahalagedara, L. R.; Sharma, H. N.; Kuo, C.; Dharmarathna, S.; Joshi, A. V.; Suib, S. L.; Mhadeshwar, A. B., *submitted to Energy & Fuels,* **2012**.
(74) Galwey, A. K. *Thermochim. Acta* **2003**, *399* (1−2), 1−29.
(75) Galwey, A. K.; Brown, M. E. *Thermochim. Acta* **1997**, *300* (1−2), 107−115.
(76) Vyazovkin, S.; Wight, C. A. *Annu. Rev. Phys. Chem.* **1997**, *48* (1), 125−149.
(77) Vyazovkin, S. *Int. Rev. Phys. Chem.* **2000**, *19* (1), 45−60.
(78) Vyazovkin, S.; Sbirrazzuoli, N. *Macromol. Rapid Commun.* **2006**, *27* (18), 1515−1532.
(79) TA Instruments. *Q500 Series Thermogravimetric Analyzer*; TA Instruments: New Castle, DE, 2012; http://www.tainstruments.com/product.aspx?id=20&n=1&siteid=11 (accessed March 22, 2012).

Appendix B

Functional Dependence of Activation Energies

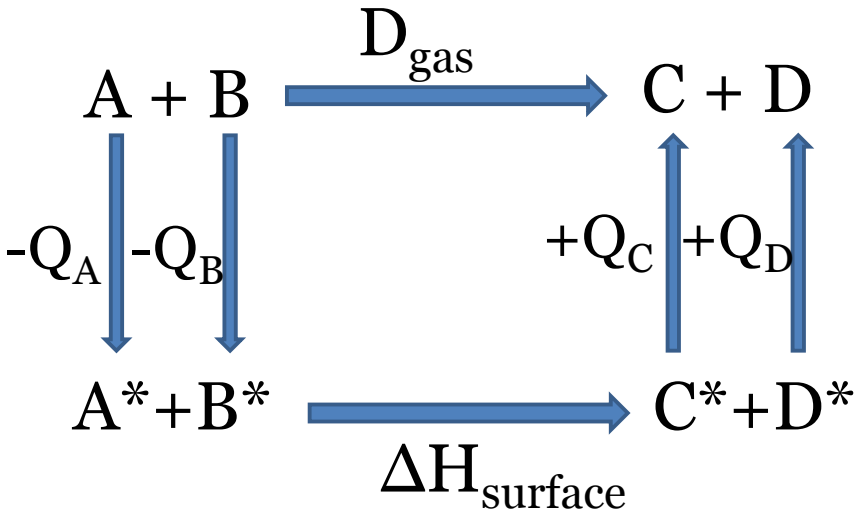

Fig. B.1 Schematic of a reaction loop with gas phase and surface reactions.

To calculate activation energies using the UBI-QEP method [107], a reaction loop with gas phase and surface reactions is considered here for all reactions. The gas phase bond dissociation energy D_{gas} is calculated from enthalpies of the reactants and the products as,

$$D_{gas} = \sum H_{products} - \sum H_{reactants} \tag{B.1}$$

The reaction is written in the endothermic direction (for gas phase), i.e., Dgas ≥ 0. Here, the standard state molar enthalpy is temperature dependent and it is given by,

$$H^{o} = \int_{0}^{T} C_{p}^{o} dT \tag{B.2}$$

The specific heats C_p can be calculated using Eq. C.4 in Appendix C. Alternatively, polynomial form of Eq. C.5 in Appendix A can be used to compute the enthalpy. The polynomial coefficients for each species are used from thermodynamic databases (e.g., GRI-Mech 3.0 thermodynamic database) [109].

For the reaction loop considered, heat of surface reaction can be calculated as,

$$\Delta H_{surf} = D_{gas} + Q_A + Q_B - Q_C - Q_D \tag{B.3}$$

Here, Q is the binding energy, which is temperature dependent based on the calculations for degrees of freedom lost/gained upon adsorption, as described by Mhadeshwar et al. [101]. Q can also be species coverage dependent, as described in Chapter 2. This makes the heat of surface reaction coverage and temperature dependent.

UBI-QEP formalism is then used to compute the forward (E_f) and backward (E_b) activation energies for the reactions. Note that activation energies are related to the heat of surface reaction as,

$$\Delta H_{surf} = E_f - E_b \tag{B.4}$$

Therefore, the activation energies are coverage and temperature dependent as well. Formulas for the activation energy calculation vary depending on the reaction type [101, 107]. Only the types relevant to our surface reaction mechanism are discussed next.

B.1 Non-activated Atomic or Non-dissociative Mol. Adsorption

Here, the adsorption is non-activated; hence the forward activation energy is zero. As there is no bond breaking, the gas phase dissociation energy is also zero. Example:

$$CO + * \leftrightarrow CO^*, \tag{B.5}$$

here, E_f = 0,

D_{gas} = 0,

ΔH_{surf} = –Q_{CO}, and

$$E_b = Q_{CO}. \tag{B.6}$$

B.2 Non-activated Dissociative Adsorption

Here, the adsorption is non-activated; hence the forward activation energy is zero. However, the bond dissociation energy is non-zero. Example:

$$O_2 + 2* \leftrightarrow 2O^*, \tag{B.7}$$

here, $E_f = 0$,

$\Delta H_{surf} = D_{gas}$ - 2 Q_O, and

$$E_b = -\Delta H_{surf}. \tag{B.8}$$

B.3 Activated Dissociative Adsorption

Here, the adsorption is activated; hence the forward activation energy is non-zero. Furthermore, the bond dissociation energy is also non-zero. Example:

$$N_2 + 2* \leftrightarrow 2N^*, \tag{B.9}$$

$\Delta H_{surf} = D_{gas}$ - 2 Q_N,

$E_f = \omega \left[\Delta H_{surf} - Q_{N_2} + 0.5\ Q_N \right]$, and

$$E_b = E_f - \Delta H_{surf}. \tag{B.10}$$

Here, ω is the bond index.

B.4 Surface Dissociation

Here, the surface species undergoes dissociation. Example:

$$OH + * \leftrightarrow O^* + H^*, \tag{B.11}$$

ΔH_{surf} = D_{gas} + Q_{OH} - Q_O - Q_H,
$E_f = \omega \left[\Delta H_{surf} + (Q_O\ Q_H)/(Q_O+Q_H) \right]$, and

$$E_b = E_f - \Delta H_{surf}. \tag{B.12}$$

B.5 Surface Disproportionation

Here, the surface species undergo disproportionation. Example:

$$CO_2 + H^* \leftrightarrow CO^* + OH^*, \tag{B.13}$$

ΔH_{surf} = D_{gas} + Q_{CO_2} + Q_H - Q_{CO} - Q_{OH},
$E_f = \omega \left[\Delta H_{surf} + (Q_{CO}\ Q_{OH})/(Q_{CO}+Q_{OH}) \right]$, and

$$E_b = E_f - \Delta H_{surf}. \tag{B.14}$$

B.6 Temperature Dependence on Binding energy

Next, we discuss the generalized assumptions to calculate the temperature dependence to the binding energy of a molecule due to degrees of freedom lost/gained during adsorption: (a) Each translational, rotational, and vibrational degree of freedom (DOF) corresponds to $0.5R_gT$,

$0.5R_gT$, and R_gT, respectively. (b) Upon adsorption, all translational and rotational DOF are converted into vibrational DOF. For example, in SO_2 and SO_3 molecules, with a vertical axis through the adsorbed atom, one of the gained vibrational DOF is assumed to be a free internal rotor (rigid rotor (RR) approximation) and counts as $0.5R_gT$. [317] So, the total change in degrees of freedom ($2.5R_gT$) of SO_2 and SO_3 for the temperature dependence can be calculated as:

$$-3F_T - 3F_R + F_{RR} + 4F_V \tag{B.15}$$

Here F_T, F_R, and F_V represent the translational, rotational, and vibrational degrees of freedom. F_{RR} represents that the vibrational DOF is assumed to be a free internal rotor. The "+" and "–" signs indicate gain and loss of DOF, respectively.

Appendix C

Thermodynamic data for cyanogen (C_2N_2)

HCN oxidation chemistry on Pt contains C_2N_2 as a recombination product, as reported by Guo et al. [209]. In order to conduct reactor simulations, thermodynamic data of specific heat coefficients are determined here in ChemKin format, based on the thermodynamic data reported on the NIST webbook website. The website reports gas phase heat capacity data using Shomate equation, as given below.

$$C_p^o = A + Bt + Ct^2 + Dt^3 + \frac{E}{t^2} \tag{C.1}$$

$$H^o - H^o_{298.15} = A + B\frac{t^2}{2} + C\frac{t^3}{3} + D\frac{t^4}{4} - \frac{E}{t} + F - H \tag{C.2}$$

$$S^o = A\ln(t) + Bt + C\frac{t^2}{2} + D\frac{t^3}{3} - \frac{E}{2t^2} + G \tag{C.3}$$

Here, $C_p{}^o$ is the Heat capacity (J/molK), H^o is the standard enthalpy (kJ/mol), S^o is the standard entropy (J/molK), and t is the normalized temperature (K)/1000. Table C.1shows the reported thermodynamic coefficients A to H.

Table C.1 Reported coefficients for C_2N_2 thermodynamic data.

Temperature [K]	**Low-Mid temperature range 298-1300 K**	**Mid-High temperature range 1300-6000 K**
A	51.6929	83.01014
B	36.79351	2.209166
C	-12.46154	-0.419735
D	0.701803	0.027676
E	-0.428743	-9.308648
F	290.6951	264.0342
G	291.2884	315.7192
H	309.0725	309.0725

The thermodynamic data was fitted with the following equations, separately at the low and high temperature ranges.

$$\frac{C_p^o}{R} = a_1 + a_2T + a_3T^2 + a_4T^3 + a_5T^4 \tag{C.4}$$

$$\frac{H^o}{RT} = a_1 + \frac{a_2}{2}T + \frac{a_3}{3}T^2 + \frac{a_4}{4}T^3 + \frac{a_5}{5}T^4 + \text{fraca}_6T \tag{C.5}$$

$$\frac{S^o}{R} = a_1\ln T + a_2T + \frac{a_3}{2}T^2 + \frac{a_4}{3}T^3 + \frac{a_5}{4}T^4 + a_7 \tag{C.6}$$

Here, T is the temperature (K) and a_1 to a_7 are the polynomial coefficients. Table C.2 shows the calculated coefficients.

Table C.2 Calculated coefficients for C2N2 thermodynamic data in ChemKin format.

Coefficients	**Low-Mid temperature range 298-1300 K**	**Mid-High temperature range 1300-6000 K**
a1	4.00801541E+00	7.65682428E+00
a2	1.33682724E-02	2.33702677E-03
a3	-1.57983027E-05	-7.77839287E-07
a4	1.03107335E-08	1.17450503E-10
a5	-2.71547695E-12	-6.64325037E-15
a6	3.54050000E+04	3.42500000E+04
a7	2.85184990E+00	-1.61912162E+01

Appendix D

Adsorption of SO_x on Pt and Pd surfaces

D.1 Binding energy and adsorption geometry

Table D.1 contains the computed structural parameters of SO_x (x = 0–4) species on both surfaces. In the conformation notation, the number super-scripted to η represents the number of atoms in a molecule coordinated to the metal (111) surface, and the subscripts a, b, f, and h stand for the atoms on atop sites, bridge sites, fcc hollow sites, and hcp hollow sites, respectively. The η^1–S$\perp$ notation represents the S atom in SO_2 molecule with 2 O atoms attached only with S atom (unbound to the metal surface). From Table S1, it has been observed that the metal to sulfur (M-S) bond lengths were relatively shorter in for the Pd(111) surface. However, no such pattern was observed for metal to oxygen (M-O) and sulfur to oxygen (S-O) bonds. The increase in interatomic bond length was quite large when both atoms directly attached to the surface compared to the case when one atom is attached. The shortest metal sulfur bond (2.20 Å) was for SO molecule where S is attached to 3 metal atoms in fcc position. The S-O bond (O unbound to the metal) increased slightly (1.43 Å – 1.46 Å) from the gas phase bond length of 1.42 Å; however, the bond length increased tremendously (1.51 Å – 1.55

Å) in the case when both S and O atoms are attached. The bond angle (∠OSO) decreased from the gas phase values (SO_2(∠OSO) = 119.5^o and SO_3(∠OSO) = 120^o)). An interesting configuration, SO_2(bridge)η^1–S⊥, has both oxygen atoms unbounded to the metal surface, showed the minimal decrease in bond length (∠OSO) = 117^o) from the gas phase ∠OSO bond angle. Furthermore, the computed binding energies of various SO_x species are compared with the available DFT based results (see ***Table D.2***).

Table D.1 Bond lengths (Pt/Pd-S, Pt/Pd-O, S-O), bond angles (OSO), and binding energies of the stable configurations of oxygen (O), and sulfur oxides (SO_x) adsorbed on Pt(111) and Pd(111) Surfaces. Total number of identical bond lengths and bond angles of that particular configuration are reported in parentheses, which arises from the symmetry of the adsorbed molecule.

Molecule	**Conformation**	**Pt(111) surface**					**Pd(111) surface**				
		Bond length(Å)			Bond angle(^{o})	Binding energy	Bond length(Å)			Bond angle(^{o})	Binding energy
		Pt–O	Pt–S	S–O	∠OSO	(kcal/mol)	Pd–O	Pd–S	S–O	∠OSO	(kcal/mol)
SO_4	(fcc)η^3–$O_aO_aO_a$	2.09(×3)		1.43	108.6(×3)	87.2	2.09(×3)		1.44	108.6(×3)	85.1
				1.53(×3)	110.3(×3)				1.53(×3)	110.3(×3)	
SO_4	(hcp)η^3–$O_aO_aO_a$	2.10(×3)		1.43	108.5(×3)	87.2	2.09(×3)		1.43	108.5	85.1
				1.53(×3)	110.3(×3)				1.53(×3)	110.4(×3)	
SO_3	(fcc)η^3–$S_aO_aO_a$	2.13(×2)	2.28	1.44	106.6	30.8	2.18	2.25	1.45	109.3	27.6
				1.54(×2)	111.0				1.52(×2)	112.7	
SO_3	(hcp)η^3–$S_aO_aO_a$	2.13(×2)	2.27	1.44	107.0	30.3	2.19(×2)	2.25	1.45	109.5	27.4
				1.55(×2)	111.1				1.52(×2)	112.6	
SO_3	(fcc)η^3–$O_aO_aO_a$	2.11(×3)		1.55(×3)	107.1(×3)	27.0	2.11(×3)		1.54(×3)	107.4(×3)	26.9
SO_3	(hcp)η^3–$O_aO_aO_a$	2.11(×3)		1.55(×3)	107.0(×3)	27.0	2.11(×3)		1.54(×3)	107.5(×3)	26.8
SO_2	(fcc)η^2–S_aO_a	2.32	2.27	1.45	114.5	27.2	2.32	2.28	1.46	113.6	26.7
				1.51					1.50		
SO_2	(hcp)η^2–S_aO_a	2.33	2.28	1.45	114.6	25.2	2.33	2.27	1.46	114.5	26.1
				1.51					1.52		
SO_2	(bridge)η^1–S⊥		2.29	1.46(×2)	117.3	24.6		2.26	1.47(×2)	116.7	26.2
SO_2	(fcc)η^3–$S_aO_aO_a$	2.16(×2)	2.30	1.54(×2)	108.1	23.7	2.22(×2)	2.28	1.52(×2)	111.2	23.9
SO_2	(hcp)η^3–$S_aO_aO_a$	2.17(×2)	2.30	1.54(×2)	108.5	23.1	2.22(×2)	2.28	1.51(×2)	111.2	23.8
SO	(fcc)η^1–S_f		2.24(×3)	1.46		69.5		2.20(×3)	1.47		66.8
SO	(hcp)η^1–S_h		2.24(×3)	1.46		66.8		2.20(×3)	1.47		66.2
SO	(fcc)η^2–S_bO_a	2.15	2.27(×2)	1.56		64.6	2.19	2.22(×2)			60.2
SO	(hcp)η^2–S_bO_a	2.16	2.27(×2)	1.57		63.5	2.20	2.23(×2)			59.5
S	(fcc)η^1–S_f		2.27(×3)			122.2		2.23(×3)			115.1
S	(hcp)η^1–S_h		2.27(×3)			117.7		2.24(×3)			107.6
O	(fcc)η^1–O_f	2.05(×3)				98.6	2.00(×3)				99.7
O	(hcp)η^1–O_h	2.04(×3)				90.2	2.00(×3)				95.3
O	(atop)η^1–O_a	1.82(×3)				69.7	1.81(×3)				64.3

Typically, the increase in surface coverage of an adsorbate decreases the binding strength of that adsorbate on the metal surface. In this work, we explored the effect of coverage on

Table D.2 Comparison of binding energies (kcal/mol) for the most stable configurations of SO_x species on Pt(111) and Pd(111) surfaces. Surface coverage of 0.11 ML is considered for the comparison.

Molecule	**Conformation**	**Pt(111) surface**		**Pd(111) surface**	
		This work	Other DFT	This work	Other DFT
SO_4	(fcc)η^3–$O_aO_aO_a$	87.2	86.5[283], 81.6[265]	85.1	–
SO_3	(fcc)η^3–$S_aO_aO_a$	30.3	27.5[283], 33.0[265]	27.4	–
SO_2	(fcc)η^2–S_aO_a	27.2	24.4[283], 28.1[265]	26.7	28.9[276]
SO	(fcc)η^1–S_f	69.5	68.1[283], 68.0[265]	66.8	–
S	(fcc)η^1–S_f	122.2	118.7[283]	115.1	111.84[119]
O	(fcc)η^1–O_f	98.6	100.6[283]	99.7	108.1[288]

Table D.3 Coverage dependent binding energy (kcal/mol) of the most stable SO_x species and O atom adsorbed on Pt(111) and Pd(111) surfaces.

Molecule	**Conformation**	**Pt(111) surface**				**Pd(111) surface**			
		$p(2\times2)$	$p(3\times3)$	$p(4\times4)$	estimated	$p(2\times2)$	$p(3\times3)$	$p(4\times4)$	estimated
		0.25 ML	0.11 ML	0.06 ML	0 ML	0.25 ML	0.11 ML	0.06 ML	0 ML
SO_4	(fcc)η^3–$O_aO_aO_a$	81.4	87.2	90.3	92.8	80.1	85.1	87.6	89.8
SO_3	(fcc)η^3–$S_aO_aO_a$	25.8	30.8	33.3	35.6	24.7	27.6	28.4	29.8
SO_2	(fcc)η^2–S_aO_a	23.6	27.2	29.1	30.8	24.4	26.7	28.1	29.1
SO	(fcc)η^1–S_f	65.7	69.5	70.6	72.4	65.5	66.8	68.1	68.7
S	(fcc)η^1–S_f	114.6	122.2	123.4	126.9	109.8	115.1	115.8	118.3
O	(fcc)η^1–O_f	96.1	98.6	99.3	100.4	98.6	99.6	99.9	100.5

binding energies of SO_x and O on both surfaces. The computed binding energies of the most stable species of SO_x are given for the coverage range from 0.25 ML to zero coverage (see ***Table D.3***). The zero coverage binding energies are estimated from linear interpolation of the DFT–computed binding energies.

D.2 Bader Charge Analysis

Bader charge analysis, purely based on the electronic charge density, was performed to calculate the net charge transfer from/to molecules to/from catalysts surface. The Bader analysis results are presented in **Table D.4** , where we report the net charge transfer to the molecule from the slab (Q_{mol}), the net charge acquired by the metal atoms (Q_{Pt} or Q_{Pd}) directly attached to the atom/molecule, and the net charge acquired by the sulfur atom (Q_S) in the molecule.

Among the different configurations of a molecule, the one with higher number of O atoms attached directly to the metal rendered larger negative charge on the molecule and larger positive charge on attached Pt atoms; however, it exhibited decrease in the net charge on S atom. For example, the Q_{mol}, Q_{Pd}, and the Q_S of SO_3 (fcc)η^3–$S_aO_aO_a$ on Pd(111) were -0.696, +0.424, and +4.714 respectively; however, those for SO_3 (fcc)η^3–$O_aO_aO_a$ changed to -0.957, +0.585, and +4.316 respectively producing ~27% difference in charge transfer between two configurations of a molecules. An interesting behavior was observed for SO_2(bridge)η^1–S$\perp$ molecule, where Q_{mol} and Q_{Pt} (or Q_{Pd}) were remarkably low but the Q_S was higher compared to other SO_2 configurations.

D.3 Density of states analysis

We decomposed the electron density and wave function into contributions from atomic orbitals, i.e. *s*, *p* and *d* orbitals centered on each atom. ***Figure 6.3*** shows the *p*-DOS of various SO_x molecules on Pd(111) and Pt(111) surfaces. In ***Figure 6.3***, each panel (a-h) shows the projected atomic DOS of atom/molecule in a isolated state along with the pure slab surface in the lower part and the adsorbed states of those in the upper part. Further, comparison of DOS of S adsorption on Pd(111) and Pt(111) surfaces is given in ***Figure 6.3***(i). We observed the shifting of active metal *d* band to lower energy after adsorption of atom/molecule in all cases. The

Table D.4 Bader charge analysis of O and SO_x adsorption on Pt(111) and Pd(111)surfaces. Charge (au) in the molecule (Q_{mol}), surface metal atoms (Q_{Pt}), and sulfur atom (Q_S) represents the total charge acquired after adsorption.

Molecule	**Conformation**	**Pt(111) surface**			**Pd(111) surface**		
		Q_{mol}	Q_{Pt}	Q_S	Q_{mol}	Q_{Pd}	Q_S
SO_4	(fcc)η^3–$O_aO_aO_a$	–1.010	+0.700	+6.000	–1.070	+0.670	+6.000
SO_4	(hcp)η^3–$O_aO_aO_a$	–1.000	+0.690	+6.000	–1.070	+0.671	+6.000
SO_3	(fcc)η^3–$S_aO_aO_a$	–0.656	+0.412	+4.60	–0.696	+0.424	+4.714
SO_3	(hcp)η^3–$S_aO_aO_a$	–0.652	+0.414	+4.614	–0.694	+0.411	+4.697
SO_3	(fcc)η^3–$O_aO_aO_a$	–0.891	+0.646	+4.280	–0.957	+0.585	+4.316
SO_3	(hcp)η^3–$O_aO_aO_a$	–0.920	+0.685	+4.263	–0.937	+0.466	+4.313
SO_2	(fcc)η^2–S_aO_a	–0.330	+0.189	+3.325	–0.369	+0.258	+3.334
SO_2	(hcp)η^2–S_aO_a	–0.327	+0.157	+3.336	–0.373	+0.201	+3.361
SO_2	(bridge)η^1–S$\perp$	–0.272	+0.023	+3.475	–0.353	+0.114	+3.403
SO_2	(fcc)η^3–$S_aO_aO_a$	–0.443	+0.341	+2.997	–0.471	+0.362	+3.095
SO_2	(hcp)η^3–$S_aO_aO_a$	–0.439	+0.317	+2.999	–0.469	+0.343	+3.098
SO	(fcc)η^1–S_f	–0.196	+0.152	+1.693	–0.195	+0.152	+1.693
SO	(hcp)η^1–S_h	–0.163	+0.142	+1.700	–0.151	+0.202	+1.701
SO	(fcc)η^2–S_bO_a	–0.236	+0.057	+1.434	–0.267	+0.165	+1.469
SO	(hcp)η^2–S_bO_a	–0.232	+0.056	+1.451	–0.303	+0.163	+1.146
S	(fcc)η^1–S_f	–0.125	+0.076	–0.125	–0.256	+0.244	–0.256
S	(hcp)η^1–S_h	–0.081	+0.060	–0.081	–0.256	+0.228	–0.256
O	(fcc)η^1–O_f	–0.772	+0.622		–0.773	+0.752	
O	(hcp)η^1–O_h	–0.757	+0.633		–0.764	+0.714	
O	(atop)η^1–O_a	–0.599	+0.484		–0.604	+0.386	

d band shifting was larger in the case of sulfur metal interaction compared to oxygen metal interaction. Panel c, d, e, and f (in **Figure 6.3**) show the difference in *d* band shifting, where Pd-1 shows larger shift (M-S interaction) then Pd-2 (M-O interaction). Along the same line, we found very similar characteristics of DOS in the case of Pt(111) surface. Nonetheless, we showed the DOS of S adsorption (see **Figure 6.3**(i)) on both surfaces for the comparison. We note that the oxygen 2*p* orbitals attached to metal and sulfur atom (denoted as O-1 in **Figure 6.3**) showed more broadening with a spike at -7 eV, whereas the oxygen 2*p* orbitals attached only with sulfur atom (denoted as O-2 in **Figure 6.3**) showed relatively smaller broadening with a spike at -6eV. Furthermore, we observed strong interactions of *p* orbitals of S and O with each other and with metal *d* band in this reason (-5 to -8 eV) We note that the *d* band was larger and extend to lower energy in Pt(111) along with broadening and larger separation of bonding and antibonding states of *p* orbitals, which can be assigned to comparatively stronger SO_x binding to Pt(111) surface observed in this study. Finally, we also observed diffused metal *s* orbitals and provided some contribution to total DOS (not shown here); however, the contribution was negligible compared to metal *d* orbitals. [318].

Appendix E

Computation of Pre-exponential Factors From Vibrational Modes

Pre-exponential factors are important kinetics parameters for the study of various catalytic process, which can be calculated rigorously using DFT. For an example, the elementary step surface reaction of SO_2 oxidation on the Pt/Pd surfaces, the reaction rate constant k is given as:

$$k_i = A_o exp(\frac{-E_{a,i}}{K_B T}) \tag{E.1}$$

Where A_o, $E_{a,i}$, K_B, and T represent the pre-exponential factor, reaction activation energy, Boltzmann's constant, and temperature respectively. The pre-exponential factor A_o can be given as:

$$A_o = \frac{K_B T}{h} exp(\frac{\Delta {S^o}_i^{\ddagger}}{K_B}) \tag{E.2}$$

Where h is the Planck's constant and $\Delta\ {S^o}_i^{\ddagger}$ represents the standard state entropy change accompanying the formation of transition state and calculated as:

$$\Delta {S^o}_i^{\ddagger} = {S^o}_{TS}^{\ddagger} - {S^o}_{IS} \tag{E.3}$$

Where ${S^o}_{TS}^{\ddagger}$ and ${S^o}_{IS}$ represent the transition state entropy and the initial state entropy. The entropies can be calculated from the analysis of vibrational modes of the species as follows, [168, 319]

$$S_{vib} = K_B \sum_{i}^{no.of modes} \left(\frac{x_i}{e^{x_i} - 1} - ln(1 - e^{-x_i}) \right) \tag{E.4}$$

Where x_i represents the each vibrational mode and calculated from the vibrational frequency ν_i as:

$$x_i = \frac{h\nu_i}{K_B T} \tag{E.5}$$

The lowest possible energy at ground state, zero-point energy (ZPE) accounts for the energy at zero Kelvin. The difference in zero-point energy, i.e. ΔZPE can be calculated as: [319]

$$\Delta ZPE = \left(\sum_{i}^{no.of modes} \frac{h\nu_i}{2} \right)_{TS} - \left(\sum_{i}^{no.of modes} \frac{h\nu_i}{2} \right)_{IS} \tag{E.6}$$

The vibrational frequencies, except the single imaginary mode in each transition state, are utilized to compute the pre-exponential factors and zero-point energy. The frequencies are listed in ***Table E.1***.

Table E.1 List of the vibrational frequencies (cm^{-1}) of initial state and transition state of SO_2 oxidation (SO_2* + O* $\rightarrow$ SO_3*) and SO_3 oxidation (SO_3* + O* $\rightarrow$ SO_4*) on Pt(111) and Pd(111) surfaces.

Reaction	**Path**	**Frequencies (cm^{-1})**			
		Pt(111)		**Pd(111)**	
		Initial state	Transition state	Initial state	Transition state
SO_2* + O* $\rightarrow$ SO_3*	Path A	1173, 957, 491, 434, 404, 347	1197, 889, 496, 479, 312, 268	1167, 953, 482, 414, 365	1202, 962, 483, 441, 325, 279
		306, 149, 87, 81, 44, 21	194, 156, 153, 87, 50	361, 175, 120, 96, 81, 63, 27	165, 153, 131, 71, 30
	Path B		1220, 1017, 486, 476, 370, 197		1224, 1006, 490, 443, 384, 163
			180, 108, 95, 62, 58		154, 144, 92, 60, 53
	Path C		1261, 1063, 505, 482, 365, 200		1247, 1053, 495, 448, 400, 165
			183, 127, 100, 53, 41		162, 150, 125, 46, 42
SO_3* + O* $\rightarrow$ SO_4*	Path A	1219, 871, 802, 582, 504, 457, 439	1213, 876, 741, 502, 485, 440, 416	1196, 914, 823, 561, 488, 439, 434	1240, 1051, 856, 484, 472, 426
		410, 360, 285, 259, 217, 148, 103, 92	329, 232, 183, 166, 153, 127, 112	401, 352, 258, 228, 150, 127, 82, 53	390, 323, 227, 144,130, 95, 90, 78
	Path B		1307, 1190, 951, 500, 498, 404, 336		1307, 1256, 970, 494, 490, 422, 372
			323, 183, 163, 149, 94, 66		361, 328, 147, 117, 101, 86, 67

Appendix F

First Principles Thermodynamics

F.1 Surface and Bulk Free Energy

Surface energy of a surface model system in equilibrium with the surrounding gas phase reservoir can be expressed as follows.

$$\gamma(\mathrm{T},\mathrm{p}\{\mathrm{i}\}) = \frac{1}{\mathrm{A}}\left[\mathrm{G}^{\mathrm{surf}} - \sum_{\mathrm{i}=1}^{\mathrm{n}} \mathrm{N_i}\mu_{\mathrm{i}}(\mathrm{T},\mathrm{p_i})\right] \tag{F.1}$$

where, G^{surf}, A, μ_i, n, and N_i represent the Gibbs free energy, surface area of the slab, individual gas species in the system, number of gas species, number of atoms/molecules of gas species, respectively. For the stability comparison between multiple models (with SO_3 and O on the surface), we take the clean slab as a common reference. Then, the relative surface energy can be computed as:

$$\Delta\gamma_{(\mathrm{T},\mathrm{SO_3},\mathrm{O})} = \frac{1}{\mathrm{A}}\left[\mathrm{G}^{\mathrm{surf}}_{\mathrm{SO_3,O+slab}} - \mathrm{G}^{\mathrm{surf}}_{\mathrm{slab}} - \frac{\mathrm{N_O}}{2}\mu_{\mathrm{O_2}} - \mathrm{N}_{\mathrm{SO_3}}\mu_{\mathrm{SO_3}}\right] \tag{F.2}$$

The Gibbs free energy can be further simplified in terms of DFT computed energy [299] and expressed as:

$$\Delta\gamma_{(\mathrm{T,SO_3,O})} = \frac{1}{\mathrm{A}}\left[\Delta \mathrm{E}^{\mathrm{DFT}}_{\mathrm{SO_3,O}} + \Delta \mathrm{F}^{\mathrm{Vib}}_{\mathrm{SO_3,O}} - \frac{\mathrm{N_O}}{2}\Delta\mu_{\mathrm{O_2}} - \mathrm{N_{SO_3}}\Delta\mu_{\mathrm{SO_3}}\right] \tag{F.3}$$

where $\Delta F^{Vib}_{SO_3,O}$ ($\Delta F^{Vib}_{SO_3,O}$=$F^{Vib}_{SO_3,O+slab} - F^{Vib}_{slab}$) represents the vibrational contributions to the free energy. $\Delta E^{DFT}_{SO_3,O}$ is the average binding energy of SO_3 and O (the DFT energy difference slab+ adsorbates and clean slab) which can be obtained from DFT calculations as follows:

$$\Delta \mathrm{E}^{\mathrm{DFT}}_{\mathrm{SO_3,O}} = \left[\mathrm{E}^{\mathrm{DFT}}_{\mathrm{SO_3,O+slab}} - \mathrm{E}^{\mathrm{DFT}}_{\mathrm{slab}} - \Delta \mathrm{N_{Pt/Pd}}\mathrm{E_{Pt/Pd}} - \frac{\mathrm{N_O}}{2}\mathrm{E}^{\mathrm{DFT}}_{\mathrm{O_2}} - \mathrm{N_{SO_3}}\mathrm{E}^{\mathrm{DFT}}_{\mathrm{SO_3}}\right] \tag{F.4}$$

where $E^{DFT}_{SO_3,O+slab}$ and E^{DFT}_{slab} represent the total energy of the slab+adsorbates and the slab only, respectively. The $\Delta N_{Pt/Pd}$ represents the condition if the number of Pt/Pd atoms of the slab+adsorbates are not equal to the one in clean slab, i.e. $N^{slab+ads.}_{Pt/Pd} \neq N^{slab}_{Pt/Pd}$ as in the case of surface oxides of Pt and Pd. The excess/deficiency of metal atoms are taken from/ put into a bulk reservoir can be represented by the bulk phase chemical potential $\mu^{bulk}_{Pt/Pd}$. The chemical potential of the gas species (i.e. μ_{SO_3} and μ_{O_2}) can be represented as a combination of total energy and the temperature and pressure dependent function as:

$$\mu_{\mathrm{O_2}}(\mathrm{T,P_{O_2}}) = \mathrm{E}^{\mathrm{DFT}}_{\mathrm{O_2}} + \Delta\mu_{\mathrm{O_2}}(\mathrm{T,P_{O_2}}) \tag{F.5}$$

where $E^{DFT}_{O_2}$ represents the DFT energy of an isolated O_2 molecule and the $\Delta\mu_{O_2}(T,P_{O_2})$ represents the temperature and pressure dependent chemical potential term (computation details are given in supporting information). Similarly, chemical potential of SO_3 can be calculated as:

$$\mu_{\mathrm{SO_3}}(\mathrm{T,P_{SO_3}}) = \mathrm{E}^{\mathrm{DFT}}_{\mathrm{SO_3}} + \Delta\mu_{\mathrm{SO_3}}(\mathrm{T,P_{SO_3}}) \tag{F.6}$$

Which also contains the DFT computed energy of an isolated SO_3 molecule and chemical potential with temperature and pressure dependence. Computations details and results are shown in supporting information. Further, we define the binding energy per atom (or molecule) O (or SO_3) on the surface as:

$$\mathrm{E_O^{bind}} = \frac{1}{\mathrm{N_O}}\left[\mathrm{E_{O+slab}^{DFT}} - \mathrm{E_{slab}^{DFT}} - \frac{\mathrm{N_O}}{2}\mathrm{E_{O_2}^{DFT}}\right] \tag{F.7}$$

Adsorption of O (or SO_3) on the surface oxides of Pt/Pd is slightly different case compared to the adsorption on the clean surface. Here, we define the binding energy taking the oxidized surface as a reference. For example, the adsorption of SO_3 on the surface oxide is given as:

$$\mathrm{E_{SO_3}^{bind}} = \frac{1}{\mathrm{N_{SO_3}}}\left[\mathrm{E_{SO_3+surf.oxd.}^{DFT}} - \mathrm{E_{surf.oxd.}^{DFT}} - \mathrm{N_{SO_3}E_{SO_3}^{DFT}}\right] \tag{F.8}$$

The Phase diagrams are created by plotting the relative surface energy vs. the chemical potentials of oxygen and SO_3 ($\Delta\mu_{O_2}$ and $\Delta\mu_{SO_3}$) in x and y-axis respectively. As mentioned in the main text, we see little effect of the vibrational contributions to the free energy; however, the outcome and stability of the phases do not change.

To establish the stability of bulk phases, Gibbs free energy is computed which can be written as:

$$\Delta\mathrm{G} = \left[\mathrm{E_{SO_3+surf.oxd.}^{DFT}} - \frac{\mathrm{N_O}}{2}\Delta\mu_{\mathrm{O_2}} - \mathrm{N_{SO_3}}\Delta\mu_{\mathrm{SO_3}}\right] - \mathrm{E_{bulk(metal)}^{DFT}} \tag{F.9}$$

where $\mathrm{E}_{bulk(sulfateoroxide)}^{DFT}$ and $\mathrm{E}_{bulk(metal)}^{DFT}$ represent the DFT computed energy of the bulk sulfate or oxide species and the corresponding bulk metal. Theμ_{O_2} and μ_{SO_3} are computed as shown above.

F.2 Vibrational Contributions to the Free Energy

The Gibbs free energy consists of the contribution from atomic/ molecular vibration as:

$$\mathrm{G(T,P) = E^{total} + F^{vib} - TS^{conf} + pV} \tag{F.10}$$

where E^{total}, S^{conf}, p and V represent the total energy of the system, configurational entropy, pressure, and volume terms respectively. The contribution to Gibbs free energy from pV term and configurational entropy are negligible for the adsorption process, hence discarded in this study. Thus, we incorporate this contribution through harmonic normal mode analysis of the adsorbates and the substrate layers involved in the case of surface models using Bose-Einstein model approximations. The approximation is computed as, [129]

$$\mathrm{F^{vib} = \frac{1}{2}\sum_{i} 3N\varepsilon_i + K_B T \sum_{i} 3N \ln(1 - e^{-\beta\varepsilon_i})} \tag{F.11}$$

where $\varepsilon_i = h\nu$ represents the phonon energy at different vibrational modes, ν_i represents the vibrational frequency and $\beta = (K_B T)^{-1}$.

Appendix G

Bulk Parameters and USPEX Predictions

G.1 Bulk Parameters of Oxides and Sulfates of Pt and Pd

We considered various bulk structures (clean metals, metal oxides, and metal sulfates) in this study. In Table G.1, we show the computed lattice parameters of the structures considered.

G.2 USPEX Predictions

In this study, we predict the structure of $PtSO_4$ using an evolutionary algorithm based method USPEX. [131] We explored the configurational space of $PtSO_4$ using up to 4 formula unit supercell. Multiple independent USPEX run were performed to avoid confining in a local minimum. The most stable structure of $PtSO_4$ was predicted to be a tetragonal structure with space group P42/m (84). To validate our prediction, we performed the USPEX calculation on $PdSO_4$, which showed the P42/m (84) structure is the lowest energy phase along with the previously known monoclinic C2/c (15) structure [301] being a competing structure. We show the relative energies and atomic arrangements of a few USPEX predicted structures of $PtSO_4$

Table G.1 Structural parameters of the various bulk phases considered in this study. Available experimental parameters are given inside brackets below the computed values. Space groups were determined using FINDSYM software.

S.N.	Structure	Lattice parameters						Space group
		a [Å]	**b** [Å]	**c** [Å]	α [°]	β [°]	γ[°]	
1	Pt	3.97 (3.92)[a]	3.97 (3.92)[a]	3.97 (3.92)[a]	90	90	90	Fm3m (225)
2	Pd	3.94 (3.89)[b]	3.94 (3.89)[b]	3.94 (3.89)[b]	90	90	90	Fm3m (225)
3	PtO_2	3.12 (3.10)[c]	3.12 (3.10)[c]	3.60 (3.10)[c]	90	90	120	P-3m1 (164)
4	PdO	3.05 (3.03)[d]	3.05 (3.03) d	5.40 (5.33)[d]	90	90	90	P42/mmc (131)
5	$PtSO_4$	4.14	4.14	8.89	90	90	90	P42/m (84)[e]
6	$PdSO_4$	7.49	6.32	7.77	90	100.5	90	C2/c (15)

[a] references [117, 120]
[b] references [117, 121]
[c] references [320, 321]
[d] references [322]
[e] predicted structure

and $PdSO_4$ in Figure G.1. Results suggested that many structures are common in both $PdSO_4$ and $PtSO_4$. We used Density Functional theory (DFT) [111] implemented in VASP [113] for the first principles computations with the USPEX. Relative energetics of the four selected structures is shown in Figure G.1 and lattice parameters information for the structures given in Table G.2.

Table G.2 DFT computed lattice parameters of USPEX predicted bulk $PtSO_4$ and $PdSO_4$.

S.N.	Structure	Lattice parameters						Space group
		a [Å]	**b** [Å]	**c** [Å]	α [°]	β [°]	γ[°]	
1	$PtSO_4$	4.15	4.15	8.86	90	90	90	Tetragonal, P42/m (84)
2		7.05	6.99	7.68	90	104.9	90	Monoclinic, C2/c (15)
3		4.11	9.46	8.87	90	90	90	Orthorhombic, Ibam (72)
4		6.20	6.20	4.90	90	90	90	Tetragonal, P4/n (85)
1	$PdSO_4$	4.44	4.44	8.85	90	90	90	Tetragonal, P42/m (84)
2		7.49	6.32	7.77	90	100.5	90	Monoclinic, C2/c (15)
3		6.19	6.19	4.94	90	90	90	Tetragonal, P4/n (85)
4		4.09	9.47	8.93	90	90	90	Orthorhombic,Ibam (72)

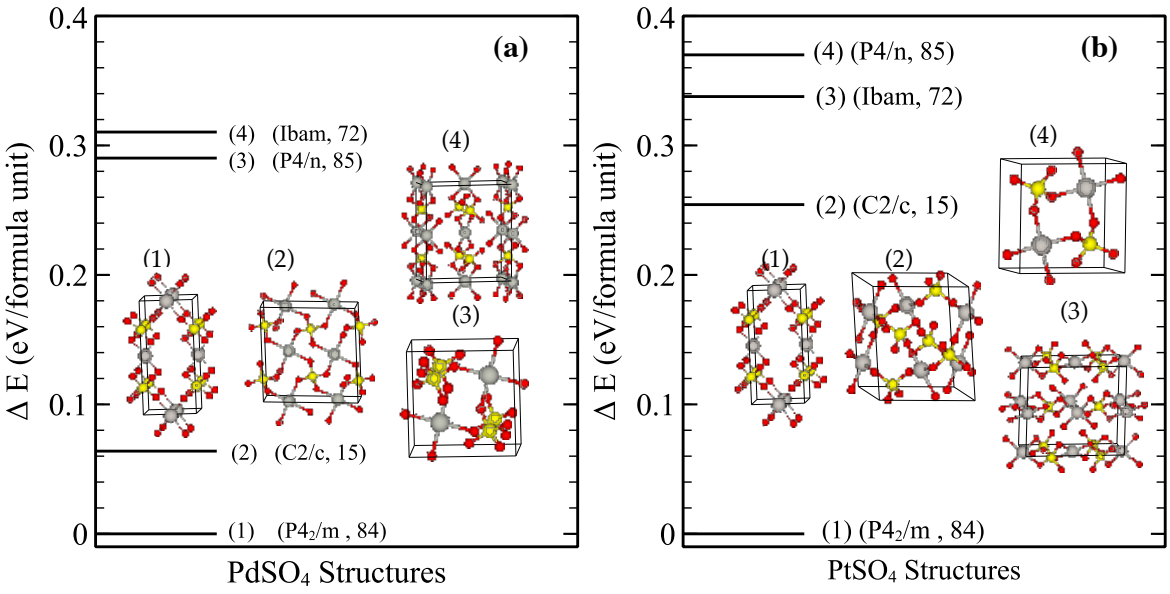

Fig. G.1 Relative energetics and structures predicted using USPEX method. Panel a: relative energetics of $PdSO_4$ structures and panel b: relative energetics of $PtSO_4$ structures, compared to the most stable $P4_2/m$, 84. Predicted structural models for both sulfates are shown in the respective panels. Space-group of the structure was determined using FINDSYM [323] software.

Appendix H

Oxygen and SO_3 on Pt(111) or Pd(111) Surfaces and Sub-Surfaces

H.1 Oxygen on Pt/Pd Surfaces and Sub-Surfaces

Experimental studies suggest that the adsorption of oxygen is favored on 3-fold hollow fcc sites on both Pt(111) and Pd(111) surfaces. Most commonly reported structures include a p(2×2) and a c(2×2) configurations corresponding the coverage of 0.25 ML and 0.5 ML, respectively. In this study, we considered a coverage range of 0.06 ML to 1 ML coverage of oxygen on both surfaces. For 0.06 ML (in a (4×4) surface supercell) and 0.25 ML (in a (2×2) surface supercell) coverage of oxygen, all fcc sites (most stable sites) are equivalent; however, adsorption of further oxygen on the surface could produce hundreds of possible surface configuration combinations. To avoid the calculation for all possible configurations, we employ few constrains to our models. First, we only consider fcc sites for the configuration. Second, too close positions of the atom/molecule on the surface are unphysical due to immense lateral interactions. Hence, we avoid such close unphysical combinations by considering the distance

between two atoms/molecules greater than the two adjacent fcc sites. Our results shows that the 3-hold hollow fcc sites are in fact the most stable adsorption sites even for higher oxygen coverages.

To study the sub-surface oxygen adsorption favorability and transition over on-surface adsorption, we considered the most stable/favored sub-surface site tetra-I (site directly below 3-fold hcp site on (111) surface). A (2×2) surface supercell was considered and the coverage was varied from 0.25 Ml to 1 ML (see Figure S2). The 0.25 ML coverage of sub-surface oxygen corresponds to an only O at sub-surface tetra-I position. Then, the rest of the oxygen coverage for sub-surface/on-surface combination contain one sub-surface oxygen at tetra-I site and rest on the on-surface fcc sites.

The adsorption behavior is similar for both Pt(111) and Pd(111) surfaces considered here; however, the binding strength of oxygen on Pd(111) is slightly greater compared to the same on Pt(111) surface. This is also true for on-surface/sub-surface oxygen configurations. Binding energies for the most stable and metastable configurations considered are given in the Table H.1. The decrease in the binding energy, computed as given by Equation H.1, with the increase the oxygen coverage indicates the presence of lateral interaction.

$$\mathrm{E_O^{bind}} = \frac{1}{\mathrm{N_O}}\left[\mathrm{E_{O+slab}^{DFT}} - \mathrm{E_{slab}^{DFT}} - \frac{\mathrm{N_O}}{2}\mathrm{E_{O_2}^{DFT}}\right] \tag{H.1}$$

Figure H.1 shows a comparative picture of the oxygen adsorption on Pt(111) and Pd(111) surfaces. The upper panels (panel a and b, Figure H.1) show the change of surface energy with respect to the oxygen chemical potential. We provide more intuitive quantity (i.e. p_{O_2}) corresponding to the oxygen chemical potential at 300 K and 900 K. At very low chemical potential $\Delta\mu_{O_2} \approx$ -2.5 eV), clean surface is stable in both cases. With the increase in oxygen chemical potential, various surface structures can be seen as stable phases before a surface

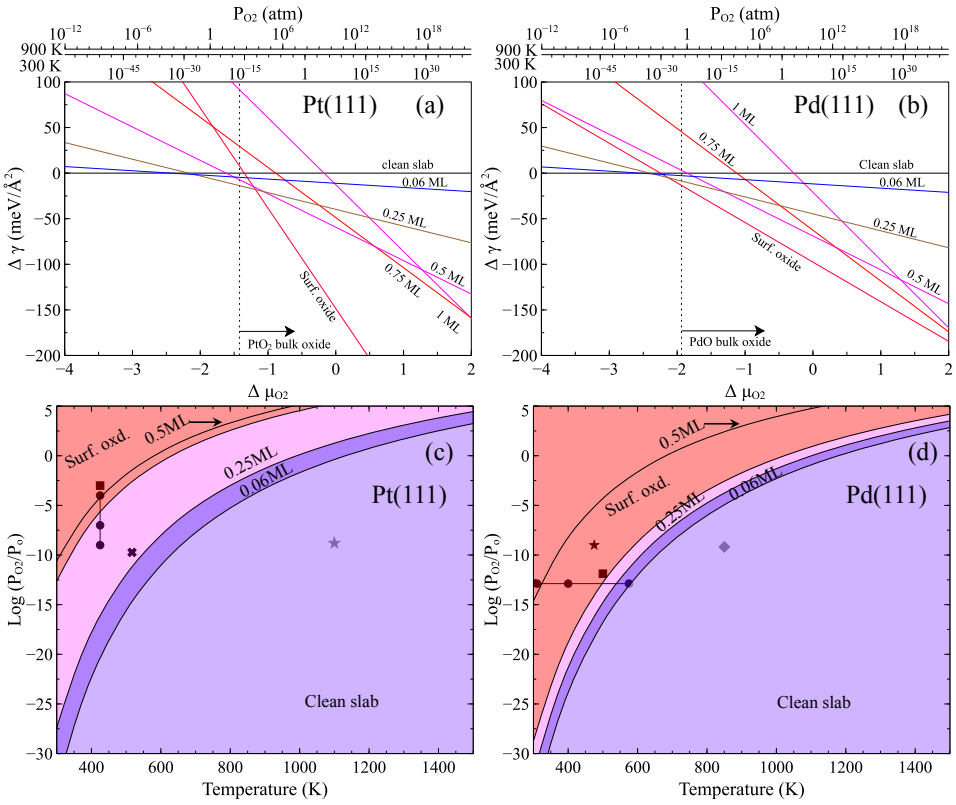

Fig. H.1 Relative surface energy as a function of $\Delta\mu_{O_2}$ and phase diagrams of oxygen adsorption on Pt(111) and Pd(111) surfaces. Pressure scales (in atm) at two representative temperatures (300K and 900K) are given opposite to the chemical potential scale in two upper panels. Symbols in the lower panels represent the experimental data available for the various phases in the given temperature-pressure conditions. Panel a: relative surface energy ($\Delta\gamma$) vs relative oxygen chemical potential ($\Delta\mu_{O_2}$) for Pt(111); panel b: relative surface energy ($\Delta\gamma$) vs relative oxygen chemical potential ($\Delta\mu_{O_2}$) for Pd(111); panel c: phase diagram of O adsorption on Pt(111) for the range of temperature and pressure conditions. Symbol ★ represents the experimentally observed [309] clean slab condition, symbol ✖ represents the temperature and pressure conditions [151] for surface coverage of 0.25 ML, symbols ● represent the pressure conditions [324] at constant temperature (425 K) where surface coverage of 0.25 ML was observed, and symbol ■ represents the surface oxide condition [324] observed; panel d: phase diagram of O adsorption on Pd(111) for the range of temperature and pressure conditions. Symbol ♦ represents the experimentally observed [310] clean slab condition, symbols ● represent the experimental condition of constant pressure and range of temperatures for the surface coverage of 0.25 ML, and symbols ■ and ★ represent the condition of surface oxide phase (PdO on Pd(111)) observed experimentally [307, 308]. Sub-surface oxygen phases were not shown in panel a and b.

Table H.1 DFT computed binding energies per atom of the most stable phases of O for on-surface and on-surface/sub-surface combinations on Pt(111) and Pd(111) surfaces using Equation 3.2.

Structure (fcc)	Coverage (ML)	Binding energy (eV) Pt(111)	Pd(111)
1 O on (4×4)	0.06	-1.25	-1.29
1 O on (2×2)	0.25	-1.15	-1.26
2 O on (2×2)	0.50	-0.87	-1.00
3 O on (2×2)	0.75	-0.52	-0.63
4 O on (2×2)	1.00	-0.17	-0.21
Tetra-I, 1 O on (2×2)	0.25	0.76	0.48
Tetra-1/fcc, 2 O on (2×2)	0.5	-0.57	-0.92
Tetra-1/fcc, 3 O on (2×2)	0.75	-0.49	-0.74
Tetra-1/fcc, 4 O on (2×2)	1.00	-0.26	-0.43

oxide becomes more stable. Results show that the surface oxides become more stable before the oxygen surface coverage of 0.5 ML; however, the Pd surface oxide formation is highly favored. The thermodynamic stability range of bulk oxides are also marked on the plot for corresponding metal bulk oxides. Furthermore, we show the surface phase diagrams (panel c and d, Figure H.1) of oxygen on Pt(111) and Pd(111) surfaces in a wide range of temperature and pressure conditions. The surface phase diagram confirms the higher oxidation affinity of Pd(111) surface compared to Pt(111) surface. For the comparison, we plotted various experimental data obtained from literature to our phase diagrams. Various experimental points fall on the stable phase regions predicted in this study. In general, we observed a larger oxygen affinity and lower surface energy of Pd(111) surfaces suggesting that the Pd(111) surface is more stable.

H.2 SO_3 on Pt/Pd Surfaces

The upright standing chair-shaped configuration was the most stable SO_3 configuration on the surface plane considered here. The binding energies of the most stable phases are given in the

Table H.2. Unlike oxygen, results suggest that the binding strength of SO_3 on Pt(111) surface is stronger compared to SO_3 on Pd(111) surface

We compared the SO_3 adsorption behavior on both Pt(111) and Pd(111) surfaces in Figure H.2. In panels a and b, we show the change in surface energy vs. SO_3 chemical potential. Results show that the SO_3 adsorption is favored more on Pt(111) surface. Unlike oxygen, adsorbed SO_3 phases are not stable in 1 atm pressure and at 600 K conditions. Further, we show the phase diagram of SO3 adsorption on both surfaces for a wide temperature and pressure range (see panel c and d in Figure H.2). The surface phase diagram also shows a relatively higher affinity of Pt(111) towards SO_3.

Table H.2 DFT computed binding energies per molecule of the most stable phases of SO_3 on Pt(111) and Pd(111).

Structure (fcc)	**Coverage (ML)**	**Binding energy (eV)**	
		Pt(111)	**Pd(111)**
1 SO_3 on (4×4)	0.06	-1.45	-1.23
1 SO_3 on (3×3)	0.11	-1.33	-1.16
2 SO_3 on (3×3)	0.22	-1.22	-1.07
3 SO_3 on (3×3)	0.33	-1.15	-0.90

H.3 SO_3 and O on Pt(111) or Pd(111) Surfaces

Two SO_3 coverages (i.e. 0.11 ML and 0.22 ML) were considered along with a range of oxygen coverages on (3×3) surface. As mentioned earlier, we contained the possible configurations of SO_3 and oxygen to the most stable fcc sites and avoided unphysical adsorption condition. For the 0.11 ML SO_3 condition, oxygen coverage up to 0.33 ML found to be stable; however, oxygen coverage up to 0.22 ML was found to be stable for the 0.22 ML SO_3 condition. Total binding energy of the adsorbates (SO_3 and O) is computed for those stable cases are given in Table H.3.

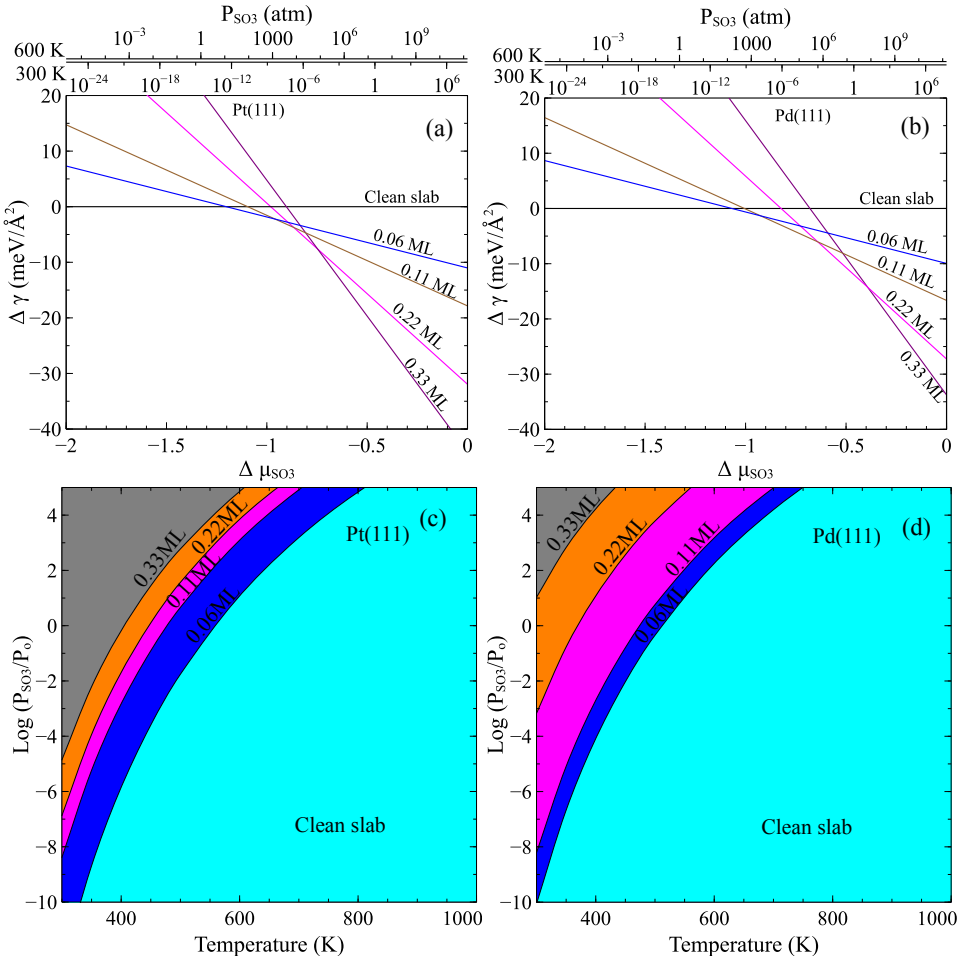

Fig. H.2 Relative surface energy as a function of $\Delta\mu_{SO_3}$ and phase diagrams of SO_3 adsorption on Pt(111) and Pd(111) surfaces.

Table H.3 DFT computed total binding energies of the most stable phases of SO_3 and O on Pt(111) and Pd(111).

Structure (fcc)	**Coverage (ML)**	**Binding energy (eV)**	
		Pt(111)	**Pd(111)**
1 SO_3 + 1 O on (4×4)	0.22	-2.49	-2.44
1 SO_3 + 2 O on (3×3)	0.33	-3.42	-3.49
1 SO_3 + 3 O on (3×3)	0.44	-3.77	-3.97
2 SO_3 + 1 O on (3×3)	0.33	-3.47	-3.16
2 SO_3 + 2 O on (3×3)	0.44	-3.48	-3.21

H.4 Estimation of Cross-interactions of SO_3^* and O^*

In this work, we used a surface unit cell of (3×3) to investigate the cross-interactions (inter-species lateral interactions) between SO_3^* and O^* on Pt(111) and Pd(111) surfaces. For a generalized surface supercell (p×q), the maximum occupancy (available sites) for 1ML coverage can be written as pq(=N). For a (3×3) surface supercell, the maximum occupancy is 9. At the given all adsorbates coverage of θ, we can define the adsorption energy as,

$$\mathrm{E}_{\mathrm{ads}}^{\theta} = \mathrm{E}_{\mathrm{slab}}^{\theta=0} + \sum_{\mathrm{i}=1}^{\mathrm{N}} \mathrm{E}_{\mathrm{gas,i}} - \mathrm{E}_{\mathrm{total}}^{\theta} \tag{H.2}$$

where,

$\mathrm{E}_{ads}^{\theta}$ = Total adsorption energy of all adsorbates at a coverage θ

$\mathrm{E}_{slab}^{\theta=0}$ = Energy of the slab

$\mathrm{E}_{gas,i}$ = Gas phase energy

$\mathrm{E}_{total}^{\theta}$ = Energy of the slab + adsorbates

Adsorbate-adsorbate interactions and zero-coverage heat of chemisorption are denoted as I and $\mathrm{Q}_{ads}^{(\theta=0)}$, respectively and can be extracted by fitting heat of chemisorption $\mathrm{Q}_{ads}^{\theta}$ (Adsorption energy $\mathrm{E}_{ads}^{\theta}$ per adsorbate) as a function of surface coverages θ. I_{AA} and I_{AB} denote self-interactions and cross-interactions, respectively. For different species adsorption, we use $\mathrm{E}_{(j,k)}$

and $Q_{(j,k)}$ representing E^{θ}_{ads} and Q^{θ}_{ads}, respectively, where j and k are the kinds of adsorbates. For a simple case of self-interactions, heat of chemisorption Q^{θ}_{ads} is computed as,

$$Q^{\theta}_{\mathrm{ads}} = \frac{E^{\theta}_{\mathrm{ads}}}{\mathrm{m}}, \qquad \text{form} = 1, ..., \mathrm{N}. \tag{H.3}$$

For the cross interactions I_{AB} computations, A is fixed at the minimum coverage (i.e.θ_A=1/N ML) and B is varied from 0 to the maximum occupancy of (1-N). We assume a pairwise additivity in the case of effects in energy due to adsorption. For example, 1 atom/molecule of B is added next to 1 atom/molecule of A, the interactions result due to ?the change in energy of A due to B? and ?the change in energy of B due to A?. Similarly, if another atom/molecule of B is added next to A and B system, the interactions result from ?change in energy of A due to second B?, ?change in energy of 1st B due to 2nd B?, and ?change in energy of 2nd B due to A and 1st B?. We further assume that the effect of A on B is equivalent to the effect of B on A. Hence, a generalized formula for the heat of chemisorption at any coverage of B is given as [317]

$$Q_{(1,\mathrm{k})} = Q_{(1,\mathrm{k}-1)} - \frac{E_{(1,\mathrm{k}-1)} + E_{(0,1)} - E_{(1,\mathrm{k})} - 2 \times \frac{(\mathrm{k}-1)I_{\mathrm{BB}}}{\mathrm{N}}}{2} \tag{H.4}$$

Here, we keep occupancy of A to a minimum (i.e. 1), and k varies form 1 to (1-N). We estimate the $E_{(1,k-1)}$, $E_{(0,1)}$, and $E_{(1,k)}$ using DFT. When we fit Q as a function of $?_B$, we can estimate the cross-interaction I_{AB}. Table H.4 shows the calculated parameters for Pt(111) and Pd(111) surfaces.

Table H.4 computations of $SO_3{}^*$-O^* interactions on Pt(111) and Pd(111). For Pt(111): O^*-O^* interactions of 30.44 kcal/mol/ML and $E_{ads}^{(\theta_O=0.11)}$ = E(0,1) of 98.6 kcal/mol are used and for Pd(111): O^*-O^* interactions of 32.49 kcal/mol/ML and $E_{ads}^{(\theta_O=0.11)}$ = E(0,1) of 99.7 kcal/mol are used.

θ_O**ML** (**at** θ_{SO_3} **= 0.11**	**k**	**E(1,k) (kcal/mol)**		**Q(1,k)(kcal/mol)**	
		Pt(111)	**Pd(111)**	**Pt(111)**	**Pd(111)**
0	0	30.85	27.87	30.85	27.87
0.11	1	127.22	125.53	29.73	26.85
0.22	2	218.02	217.14	29.21	26.40

H.5 SO_3 and O on the Surface Oxides of Pt(111) or Pd(111) Surfaces

As expected, PtO_2/Pt(111) surface seems to be relatively passive. In this passive structure, each Pt is coordinated to 6 O atoms and each O atom is coordinated to 3 adjacent Pt atoms. Further addition of O atom on top position of Pt on the surface was not favored. A SO_3 molecule on the O atom of the surface oxide layer was barely stable. Higher coverages of SO_3 or O, and co-adsorption conditions were not stable. Surface oxide model of Pd showed significant affinity towards SO_3. Here, co-adsorption of SO_3 and O was not favored. We explored possible adsorption configurations of O and/or SO_3 on the surface. For SO_3, a 3-fold coordinated O on the surface was the most favored site. Co-adsorption configuration was constructed based on the information about the most stable sites for each species. Higher coverage configurations were not explored due to extremely large supercell size. The binding energy of O (or SO_3) adsorption on the surface oxides is given as:

$$E_O^{\text{bind}} = \frac{1}{N_O}\left[E_{O+\text{surf}-\text{oxd}}^{\text{DFT}} - E_{\text{surf}-\text{oxd}}^{\text{DFT}} - \frac{N_O}{2}E_{O_2}^{\text{DFT}}\right] \tag{H.5}$$

The binding energy definition here is different from the Equation H.1 since this is referenced with the surface oxide (not the clean surface) and also contains the energetic changes due to the formation of the surface oxides. The binding energies are given in Table H.5.

Table H.5 DFT computed binding energies of O/SO_3 adsorption on PtO_2-Pt(111) and PdO-Pd(111) surfaces. Binding energy per atom/molecule is given in case of mono species adsorption. Total binding energies are given for the co-adsorption (mixed O and SO_3) cases.

Structure	**Binding energy (eV)**	
(fcc)	**PtO_2-Pt(111)**	**PdO-Pd(111)**
1 O	2.55 (top, Pt)	0.99 (top, Pd-3f)
1 SO_3	-0.12 (top, O)	-0.91 (top, O-3f)
2 SO_3	Unstable	-0.86
3 SO_3	-	-0.82
4 SO_3	-	-0.86
5 SO_3	-	-0.69
1 SO_3 + 1 O	Unstable	-0.80 (O-3f, Pd-3f)

H.6 Surface Sulfate Models

To create the surface sulfate model on the (111) surface of Pt and Pd, we choose the $(3\times\sqrt{3})$ surface supercell. Then, bulk structures of $PtSO_4$ and $PdSO_4$ (both $P4_2/m$ and C2/c phases) are used to create an overlayer of sulfate on the clean slab. We observed no significant difference in energetics of the surface sulfate model created using two bulk sulfates phases. For example, the surface sulfate model of Pt(111) using $P4_2/m$ bulk $PtSO_4$ was lower in energy by -0.05 eV compared to the model created using C2/c bulk $PtSO_4$. Hence, the choice of the model had no real impact on the phase diagrams. The surface sulfate models used in this work are shown in Figure H.3.

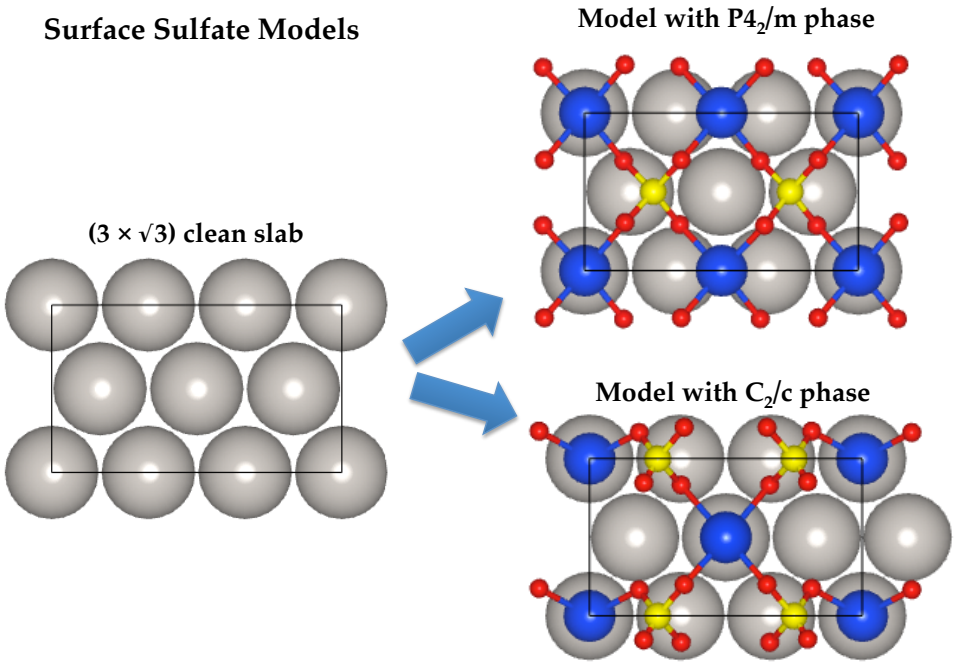

Fig. H.3 Representative surface sulfate models from bulk sulfates on the (111) surface with a $(3\times\sqrt{3})$ surface supercell. Silver, red, and yellow spheres represent the Pt or Pd, Oxygen, and Sulfur respectively. Blue spheres represent the Pt or Pd in the surface sulfate models.

Appendix I

Computation of Free Energies due to Vibrational Contributions

Here the relative vibrational contributions are shown, taking clean surface as a reference, to free energy due to oxygen adsorption (see Figure I.1) and SO_3 adsorption (see Figure I.2) on Pt(111) and Pd(111) surfaces. Only adsorbates and the top metal surface layer are allowed, as appropriate, to vibrate since the vibration of atoms away from the surface (sub-surface atoms) are assumed to cancel out in the computation of ΔF^V. We observed that the adsorption of SO_3 shows slightly larger impact on free energy change compared to O adsorption on both surfaces. In oxygen adsorption, the relative free energy (ΔF^V/A) remains positive below $\sim$750 K and it goes to negative range at higher temperature. The shift from positive to negative values of relative free energy occurs at $\sim$580 K in the case of SO_3 adsorption. Overall, the vibrational contribution to free energy remains < 25 meV/Åfor the catalytically important range of temperature. Hence, it will not have any significant impact on the overall results.

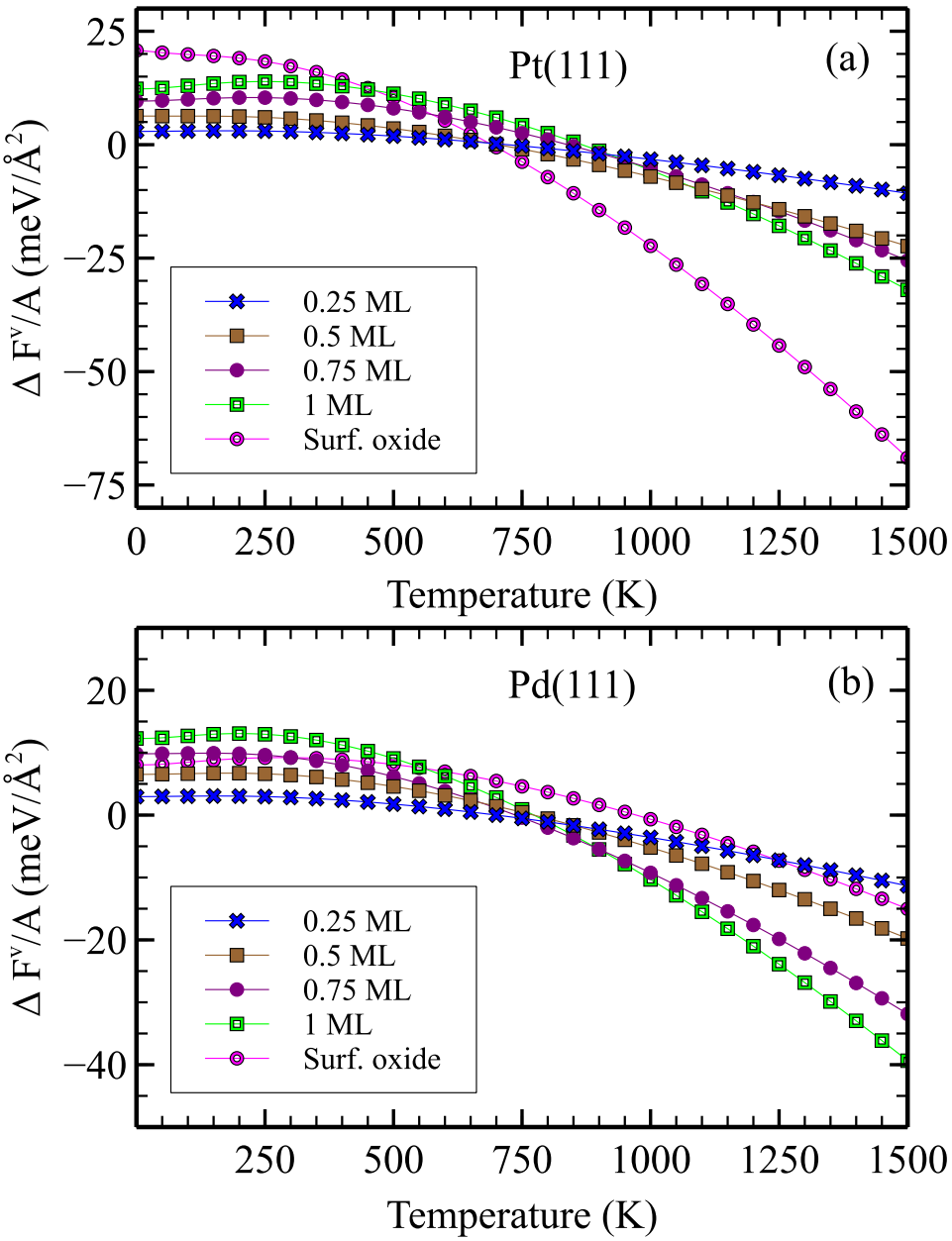

Fig. I.1 Vibrational contributions to the relative free energy ($\Delta F^V/A$) due to oxygen adsorption on Pt(111) and Pd(111) surfaces. Panel a: O adsorption on Pt(111) surface; panel b: O adsorption on Pd(111) surface. Relative change in free energy due to adsorption for a range of 0.25 ML to 1ML surface coverage and the surface oxide models are shown here.

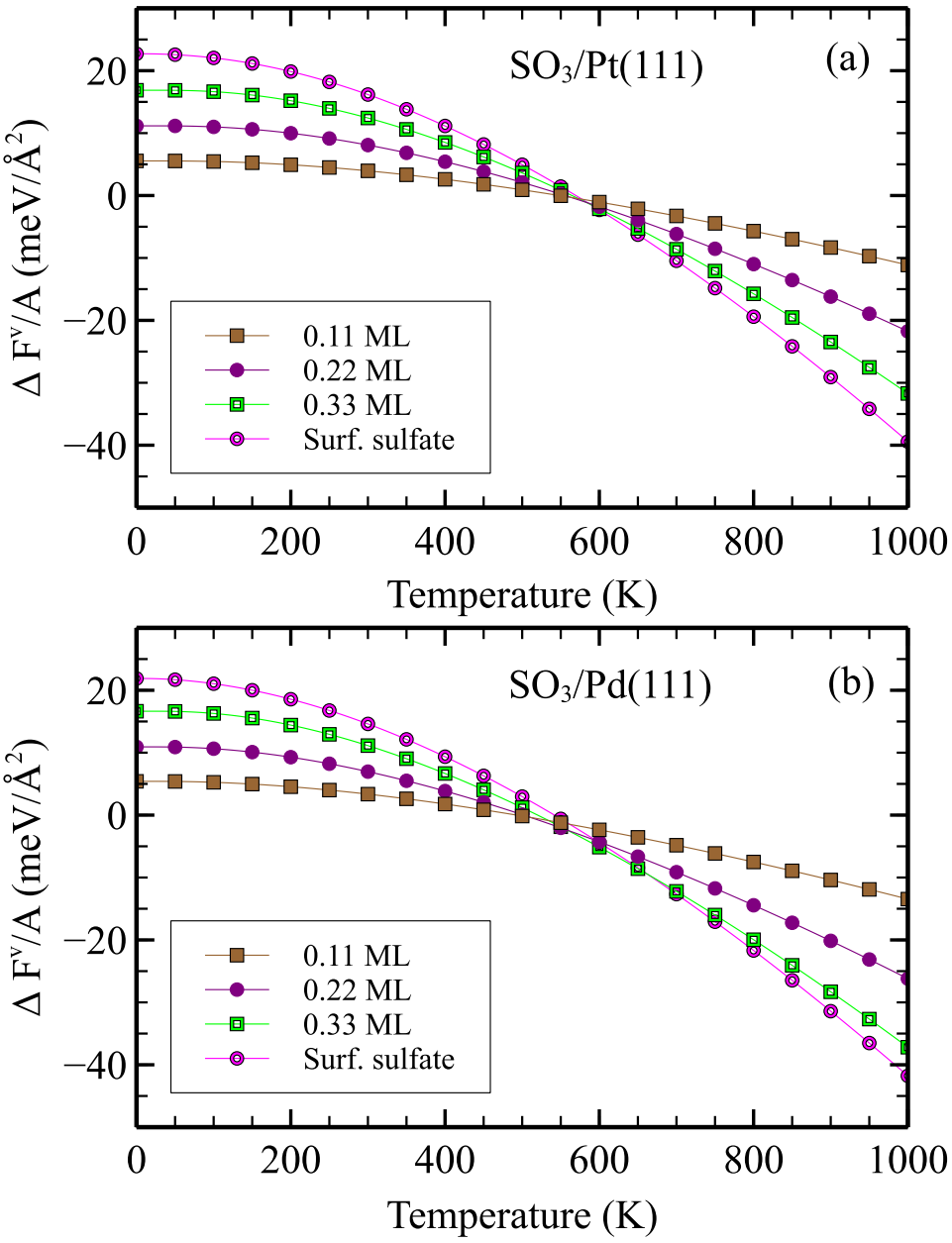

Fig. I.2 Vibrational contributions to the relative free energy ($\Delta F^V/A$) as a function of temperature due to SO_3 adsorption on Pt(111) and Pd(111) surfaces. Panel a: SO_3 adsorption on Pt(111) surface; panel b: SO_3 adsorption on Pd(111) surface. Relative change in free energy due to adsorption for a range of 0.11 ML to 0.33 ML surface coverage and the surface sulfate models are shown here.

Appendix J

Density Functional Theory: Background

J.1 Density Functional Theory (DFT)

There are many flavors of *ab-initio* methods, which are being used to compute the properties of the material. In this thesis, the main focus will be on one particular flavor, or more correctly, combination of methodologies and approximations. That is the plane-wave pseudopotential method, within density functional theory, employing a gradient corrected functional to describe the exchange-correlation energy. Few key concepts are given below, which is required for the practical implementation of the DFT.

J.1.1 The Schrödinger Equation

The Schrödinger's equation is the fundamental equation of physics for describing quantum mechanical behavior of a given non-relativistic physical system. The time independent Schrödinger equation is:

$$\hat{\mathrm{H}}\psi_{\mathrm{i}} = \mathrm{E}_{\mathrm{i}}\psi_{\mathrm{i}} \tag{J.1}$$

where $\hat{H}$ is the hamiltonian operator for a system of nuclei and electrons in the absence of electric and magnetic fields. ψ_i represents the wave function of the i^{th} state of the system. and contains the sum of all information about the system. E is the energy of the state described by the ψ_i. Virtually all of the physical properties of the interest can be obtained by the identification of the ground state energy E_o.

The wavefunction depends on the three spatial coordinates of each electrons and the nuclei, and one spin coordinate of each electron (i.e. $\pm 1/2$). The wavefunction is not a observable quantity, but the square of the wavefunction $\int |\psi(\bar{r})|^2 \, d\bar{r}$ is the probability of the electron with wave function $\psi(\bar{r})$ that will be found within a given volume element $d\bar{r}$. The complete hamiltonian $\hat{H}$ for a system with N nuclei and n electrons can be written as:

$$\hat{H} = -\frac{1}{2}\sum_{i=1}^{n}\nabla_i^2 - \frac{1}{2}\sum_{A=1}^{N}\frac{1}{M_A}\nabla_i^2 - \sum_{i=1}^{n}\sum_{A=1}^{N}\frac{Z_A}{r_{iA}} + \sum_{i=1}^{n}\sum_{i\neq j}^{n}\frac{1}{r_{ij}} + \sum_{A=1}^{N}\sum_{A\neq B}^{N}\frac{Z_A Z_B}{R_{AB}} \qquad \text{(J.2)}$$

where the subscripts i and j represent the n electrons in the system and the subscript A and B represent the N nuclei in the system. M_A and Z_A are the mass and the charge, respectively, of the nucleus A. The spatial coordinates of the electrons and nuclei ate $\vec{r}_i$ and $\vec{R}_A$, and the distance between particles i and A, is $r_{iA} = |\vec{r}_i - \vec{R}_A|$. the first two terms representing the kinetic energy $\hat{T}$ of the electrons and nuclei, respectively, and the last three terms representing the electrostatic potential energy due to electron-nucleus attraction $\hat{V}_{Ne}$, electron-electron repulsion $\hat{V}_{ee}$, and nucleus-nucleus repulsion $\hat{V}_{NN}$,respectively.

J.1.2 The Born-Oppenheimer Approximation

Since the nuclei are much heavier than the electrons, their motion will be relatively much slower than the electrons. In the limit of stationary nuclei (referred to variously as the Born-Oppenheimer, adiabatic, or clamped-nuclei approximation) the electrons are thought of as

moving in the field of fixed nuclei. The result of this is that the kinetic energy terms can be separated and $\hat{V}_{NN}$ becomes a constant. Then a simplified electronic Schrödinger equation is solved for the electronic wavefunction,

$$\hat{\mathrm{H}}_{\mathrm{elec}} = \hat{\mathrm{T}} + \hat{\mathrm{V}}_{\mathrm{Ne}} + \hat{\mathrm{V}}_{\mathrm{ee}}, \text{and} \tag{J.3}$$

$$\hat{\mathrm{H}}_{\mathrm{elec}}\,\psi_{\mathrm{elec}} = \mathrm{E}_{\mathrm{elec}}\,\psi_{\mathrm{elec}} \tag{J.4}$$

The total energy of the system is:

$$\mathrm{E}_{\mathrm{total}} = \mathrm{E}_{\mathrm{elec}} + \mathrm{E}_{\mathrm{nuc}} \tag{J.5}$$

where

$$\mathrm{E}_{\mathrm{nuc}} = \sum_{\mathrm{A}=1}^{\mathrm{N}} \sum_{\mathrm{A}\neq\mathrm{B}}^{\mathrm{N}} \frac{\mathrm{Z}_{\mathrm{A}}\mathrm{Z}_{\mathrm{B}}}{\mathrm{R}_{\mathrm{AB}}} \tag{J.6}$$

The Born-Oppenheimer approximation does not capture certain features like electronic conduction where electronic and nuclear dynamics are important. Time dependent Schrödinger equation can be solved precisely for single electron systems like Hydrogen atom. The introduction of another electron creates the complexity due to electrostatic interactions between them.

J.1.3 Hartree-Fock Approximation

In 1930's, Douglas Hartree and Vladimir Fock developed a method called Hartree-Fock approximation which assumes the total wavefunction is separable by the coordinates of each individual electron. Even though this assumption is not absolutely correct, it is able to approximately solve

for the individual one-electron wavefunctions ψ_i, which are then combined to obtain the total electronic wavefunction,

$$\psi\left(\overrightarrow{x_1}, \overrightarrow{x_2}, ..., \overrightarrow{x_n}\right) = \psi_1(\overrightarrow{x_1})\,\psi_2(\overrightarrow{x_2})...\psi_{\mathrm{n}}(\overrightarrow{x_n}) \tag{J.7}$$

It ignores all the important effects of exchange symmetry and so, instead of a simple product, an antisymmetrized product is used. The antisymmetrized product of n one-electron wavefunctions is approximately equal to the true n-electron wavefuction ψ_0 (called Slater determinant Φ_{SD}). The individual one electron wave function which consists it are called spin orbitals. Because the instantaneous electrostatic repulsion does not enter into one electron potential V_{HF}(i), electrons get too close to one another, and this causes the energy (E_{HF}) to be higher than the true ground state energy (E_0). This energy is termed as the correlation energy, E_C.

$$\mathrm{E_C} = \mathrm{E_0} - \mathrm{E_{HF}} \tag{J.8}$$

J.1.4 Development of DFT

The wavefunction itself is not directly observable. The attraction of density functional theory is that it depends on the observable electron density, $\rho(\vec{r})$, with only three spatial coordinates regardless of the size of the system. The electron density is the square of the wavefunction.

J.1.5 Hohenberg-Kohn Theorems

In 1964 Hohenberg and Kohn presented a mathematical proof that the electron density could uniquely determine the Hamiltonian, and hence the ground state energy. According to the first theorem, there is a one to- one mapping between the electronic wavefunction, ψ, and the electron density, ρ. The second theorem states that the ground state electron density corresponds

to the density that minimizes the energy of the system. Thus the electron density contains all the necessary information (uniquely, as the proof demonstrates) to determine $\hat{H}$. So, the ground state energy E_0 can be written as the function of ground state electron density, ρ_0.

$$E_0[\rho_0] = T[\rho_0] + E_{ee}[\rho_0] + E_{ne}[\rho_0] \tag{J.9}$$

where the components and their subscripts have the same meaning as above and are themselves functionals of the electron density. This expression is separable into components which depend on the system under consideration (i.e., on $\vec{R_A}$, Z_A and n), the electrostatic attraction between nuclei and electrons, and the non-system-specific components, T $[\rho_0]$ and $E_{ee}[\rho_0]$. These system-independent components are grouped together into a single term, the Hohenberg-Kohn functional, $F_{HK}[\rho_0]$. Hohenberg and Kohn did not provide specific guidance for how to actually solve the problem and the functional form of $F_{HK}[\rho]$ is a total mystery. Later, Kohn and Sham introduced an approach to solving for the electron density and ground state energy that was more general, beginning with the next landmark paper in DFT history by Kohn and Sham (1965).

J.1.6 Kohn-Sham Equations

Kohn and Sham extended the work of Hohenberg and Kohn and showed how $F_{HK}[\rho]$ can be calculated. This was done by calculating $F_{HK}[\rho]$ exactly as much as possible, and leaving the remainder in one smaller unknown term. This resembles aspects of the Hartree-Fock approximation of one-electron wavefunctions. As in Hartree-Fock theory, the n-electron system is reduced to a set of n non-interacting one-electron systems. In Hartree-Fock theory this is the basic approximation upon which the solution is built, but in DFT it is simply a tool to calculate the exact component of an unknown term. For this non-interacting electron system, the

wavefunction is a Slater determinant and the kinetic energy for this (T_{HF}) is known exactly. The Slater determinant, Φ_S, consists of orbitals, $\phi_i(\vec{x}_i$, termed Kohn-Sham orbitals (to distinguish them from the spin orbitals of Hartree-Fock theory).

$$\hat{f}^{KS}\phi_i = \varepsilon_i\phi_i \qquad\qquad i = 1,2,.....,n \tag{J.10}$$

where ε_i are the energies of the Kohn-Sham orbitals,ϕ_i, and the Kohn-Sham operator, $\hat{f}^{KS}$, is the one-electron Hamiltonian of the fictitious non-interacting system of electrons, which depends on the kinetic energy of the electrons and an effective one-electron potential, V_S.

$$\hat{f}^{KS} = -\frac{1}{2}\nabla^2 + V_S(\overrightarrow{r}) \tag{J.11}$$

V_S is chosen to make the connection between model and reality by obtaining the electron density, $\rho_S(\vec{r})$, same as the ground state density,$\rho_0(\vec{r})$, in the true system of interacting electrons.

$F_{HK}[\rho]$ also contains the term $V_{ee}[\rho]$ and can be split into a Coulomb term, J[ρ], which is known exactly, and another term, $E_{ncl}[\rho]$, which describes all of the non-classical interaction between electrons, such as exchange and correlation. So, the Coulomb terms, J[ρ], and the noninteracting part of the kinetic energy, $T_C[\rho]$, have been found exactly. A small part of the kinetic energy, T_C, is influenced by correlation effects, and cannot be found by the method described above.The remainder, which cannot be treated exactly, is called the Exchange correlation energy, E_{XC}, equal to TC[ρ] + $E_{ncl}[\rho]$. Then the $V_S(\vec{r})$ is now $V_{eff}(\vec{r})$

$$V_{eff}(\overrightarrow{r}) = \int \frac{\rho(\overrightarrow{r_2})}{r_{12}} d\overrightarrow{r_2} + V_{XC}(\overrightarrow{r_1}) - \sum_A^N \frac{Z_A}{r_{1A}} \tag{J.12}$$

where

$$V_{XC} = \frac{\delta E_{XC}}{\delta \rho} \tag{J.13}$$

and the final Kohn-Sham equation becomes,

$$\Big[-\frac{1}{2}\nabla^2 + \mathrm{V_{eff}}(\overrightarrow{r})\Big]\phi_\mathrm{i} = \varepsilon_\mathrm{i}\phi_\mathrm{i} \qquad\qquad \mathrm{i} = 1,2,.....,\mathrm{n} \tag{J.14}$$

with the electron density,

$$\rho = \sum_\mathrm{i}^\mathrm{n} < \phi_\mathrm{i}|\phi_\mathrm{i} > \tag{J.15}$$

The DFT is a SCF theory as Kohn-Sham equations are solved iteratively where $\mathrm{V}_{eff}(\vec{r})$ depends on the electron density, therefore on the orbitals. Everything except the functional form of E_{XC} is known exactly, and this is the major difference between density functional theory and wavefunction theory. In wavefunction theory, the approximation appears at the outset, in the assumption that the real wavefunction is a Slater determinant. In density functional theory, the approximation appears in the final step - the search for a suitable expression for the exchange-correlation energy.

J.1.7 Exchange-Correlation Functionals

The Exchange-Correlation Functionals provide the estimate for exchange and exchange and correlations energies of electrons. The physical contributions are: kinetic energy correction due to the hypothetical, non-interacting electron system, exchange interaction for electrons of like spin, due to Pauli exclusion principle, which forbids electrons of like spin from occupying the same orbital, correlation of electrons of different spin, due to Coulomb interactions that prevent electrons of unlike spin from coinciding in space, which is otherwise allowed by the Pauli exclusion principle, and correction for the interaction of each electron with itself (self-interaction) artificially created by use of the classical Coulomb potential for a point charge (electron) with the entire electron density, ρ(r), including itself. Much of the work has been

done over the years to find reasonable estimates to the ?true? functional, without which DFT cannot provide exact solutions.

The simplest way of approximating the exchange-correlation energy, introduced by Kohn and Sham, is called the local-density approximation (LDA). In this scheme the value of E_{XC} per electron is taken to be the same as that of an electron in a uniform 'gas' of electrons.The use of the term 'local' means that the exchange-correlation energy at $\vec{r}$ in this approximation depends only on the electron density at $\vec{r}$. In other words, contributions to E_{XC} from inhomogeneities in the real electron density at a distance from $\vec{r}$ (i.e., non-local contributions) are not considered.

$$V_{XC} = f\big[(\rho(\overrightarrow{r})\big] \tag{J.16}$$

Their performance in most areas of solid state studies was a significant improvement over the Hartree-Fock approximation. However, some of the poor performances are: binding energies are almost always overestimated, the wrong ground state is sometimes predicted to be stable (e.g. a non-magnetic hcp structure of iron), insulating systems which exhibit strong correlation effects (e.g., NiO) are predicted to be metallic, and weak bonds, such as hydrogen bonds, are not well described, and van der Waals forces are not accounted for.

Incorporating non-local correlation effects partially achieved by introducing a dependence on the gradient in the electron density around the location r, and this is known as the generalized gradient approximation (GGA):

$$V_{XC} = f\big[(\rho(\overrightarrow{r}), \nabla(\rho(\overrightarrow{r})\big] \tag{J.17}$$

GGA tend to undo the overbinding effect, though in some cases this leads to severe underbinding. Noble gas cryocrystals, and molecular cryocrystals like N_2, are not predicted to be bound at all by some GGA's. However, the correct magnetic and structural ground state is found for

metals like iron, chromium and manganese. Further extension of the XC functional are the Hybrid functionals which incorporate aspects of the Hartree-Fock method and does calculate the electron exchange energy exactly. New functionals are proposed and tested frequently to address specific shortcomings of the standard LDA and GGA approaches. In this work, we mostly use PBE GGA functional.

J.1.8 Self-Consistency and Basis Functions

Kohn-Sham equations must be solved with a self-consistent, iterative approach as the Hamiltonian requires knowledge of the electron density where an initial electron density (usually some type of guess based on the particular atoms involved) is applied, then solutions for a new electron density obtained. This is then used to update the Hamiltonian to solve for yet another, improved electron density and it is repetitive. The self-consistency is reached when the energy (typically) fall below a predetermined threshold, or convergence criterion. Since the actual functional form of the electron density and electron wavefunctions are unknown, these are approximated by linear combinations of known functions, known as basis functions.

$$\psi_{\mathrm{i}} = \sum_{\sigma} \mathrm{c}_{\mathrm{i},\sigma} \phi_{\mathrm{i},\sigma} \tag{J.18}$$

The weighting coefficient, $\mathrm{c}_{i,\rho}$ of each basis function, $\phi_{i,\rho}$ determines the contribution to the overall wavefunction, ψ_i. The optimal set of coefficients for a given choice of basis functions are solve rather than solving for the actual functional from. The cost of obtaining a solution increases with the number of basis functions used. Thus, it is most efficient to use basis functions that behave similarly to the wavefunction they are being used to approximate. For atom-centered basis functions, gaussian functions are commonly used due to their computational efficiency, but more expensive exponential functions are also used as basis functions because of

their similarities to actual wavefunctions, thus requiring fewer basis functions to achieve the same level of accuracy.

J.1.9 Periodic Supercell Implementation

In this case, by the implementation of periodic boundary condition, a relatively smaller supercell is repeated infinitely in directions. Due to the periodic nature of the system, basis functions are chosen which are also periodic and will therefore be able to capture the correct behavior more efficiently. An infinite system means infinite number of electrons and wavefunctions. Wavefunctions can be indexed based on a measure of the periodicity of the system, called the reciprocal lattice vector, k. The k vector can take on any value, but only a small set of values are unique, and these are referred to as the first Brillouin zone. Bloch?s theorem states that for periodic systems the wavefunction can always be written as the combination of a periodic part, indexed by k and a part internal to the supercell, χ.

$$\tilde{\psi^{\mathrm{k}}} = \sum_{\mathrm{n}} \mathrm{e}^{\mathrm{ikna}} \chi_{\mathrm{n}} \tag{J.19}$$

where the integer n indexes an infinite sum over all multiples of the lattice constant, a, and k ranges between $\pm$a. In DFT calculations, integration over values of k numerically done, and the specification of reciprocal-space grid points for this integration is referred to as the k-point grid. An automatically generating an evenly-spaced k-point grid was developed by Monkhorst and Pack.

Planewave basis functions are essentially combinations of sine and cosine functions of the form

$$\phi_{\rho}(\mathrm{x}) = \mathrm{e}^{\mathrm{ip}\rho\mathrm{x}} \tag{J.20}$$

where p is chosen accordingly to make the periodicity of the basis function commensurate with the supercell. These are used to expand the supercell-invariant portion of Bloch?s theorem in terms of periodic functions. The planewave expansion must be truncated at some point. This cutoff can be expressed in terms of an energy and it is termed as cutoff energy. By setting a cutoff energy, the basis set is completely specified for a given supercell geometry.

Appendix K

Hydrocarbon Emissions Oxidation on Platinum Based Diesel Oxidation Catalysts (DOC): A Combined Study Using Experiments and Microkinetic Modeling

Hydrocarbon Emissions Oxidation on Platinum Based Diesel Oxidation Catalysts (DOC): A Combined Study Using Experiments and Microkinetic Modeling

Hom Sharma[1], Zheng Ren[2, 3], Yanbing Gao[2, 3], Pu-Xian Guo[2, 3], Rampi Ramprasad[2, 3], and Ashish Mhadeshwar[1*]

[1]Department of Chemical and Biomolecular Engineering, University of Connecticut, 191 Auditorium Road, Unit 3222, Storrs, CT 06269.

[2]Institute of Material Science, University of Connecticut, 97 Eagleville Road, Storrs, CT 06269

[3]Department of Material Science and Engineering, University of Connecticut, 97 Eagleville Road, Storrs, CT 06269

[*]Corresponding author.

Email: ashish.mhadeshwar@gmail.com Tel: 443-523-8609. Fax: 860-486-2959.

Abstract

In this work, a comprehensive 52-step (26 reversible) microkinetic model is developed for C_2H_4 oxidation on Pt. Kinetic parameters for the detailed microkinetic model are extracted from ultra-high vacuum (UHV) temperature programmed desorption/reaction (TPD/TPR) experiments in literature and calculated using density functional theory (DFT). Starting with these kinetic parameters as initial estimates, the surface reaction mechanism is extensively tested against the experiments conducted under practically more relevant operating conditions, such as atmospheric pressure, dilute emissions concentrations, and short residence times, typically experienced by the Diesel Oxidation Catalysts (DOCs). C_2H_4 oxidation experiments are conducted using a fixed bed reactor for various operating conditions. Mechanistic analysis is presented to uncover the most important reaction chemistry. The microkinetic model shows very good agreement with multiple experimental data sets on monolith and fixed bed reactor scale.

1. Introduction

Hydrocarbons (HC) emission from fossil fuel based engines including diesel engines pose a serious threat to human health and environment. [1-4] Wide range of HC species (i.e. unsaturated, saturated, aromatic, and poly-aromatic hydrocarbons (PAH)) are present in the diesel engine exhaust. [1, 3, 5] A typical range of HC emission from diesel engines is 50−500 ppm C_1.[4] To meet mandatory HC emissions standards set by the Environment Protection Agency (EPA) in the USA and European commission in Europe, Pt/Pd/Pt-Pd blend based diesel oxidation catalysts (DOCs) are employed in the engine emissions aftertreatment units. [3, 4] However, tremendous challenge lingers in optimal and robust design of DOC due to increasingly stringent emissions standards and exponential price hike of noble metal catalysts over the years. Thus, a fundamental understanding of HC oxidation chemistry on DOC is paramount.

Many experimental and computational studies in the past investigated the oxidation of C_2H_4 on Pt.[6-14] Some notable experimental studies involve the ultra-high vacuum (UHV) TPD/TPR studies on various single crystal plane,[15, 16] X-ray based studies,[10] and fixed bed reactor type experiments[8, 13] to understand the oxidation mechanism. Steininger *et al.* suggested that H_2O and CO_2 are the final oxidation products along with H_2 and CO formation.[16] Further, no indication for reaction intermediates containing carboxyl or hydroxyl groups was found from their high-resolution electron energy loss spectroscopy (EELS) and temperature programmed thermal desorption spectroscopy (TPDS) experiments. However, ethylidyne (CH_3CH) intermediate was observed during C_2H_4 only TPD experiments.[16] Similar observations about the oxidation products and intermediates were reported by Berlowitz *et al.* Stable

intermediates as a decomposition and oxidation products.[7, 14, 17]On the other hand, in fixed a bed type experiments in atmospheric pressure condition, Imanaka *et. al.*[13] observed complete conversion of C_2H_4 at 120 °C on Pt/Al_2O_3 catalysts.

Kinetic modeling of C_2H_4 oxidation has been reported by Sant *et al.* [6] on Pt based catalysts; however, the model consisted some global reactions without detailed intermediate steps and radical species. An oxidation mechanism at relatively high temperature (600 K - 900 K) and high pressure (60 bar) conditions was proposed by Lopez *et al.* [18] On the other hand, Stegelmann and Stoltze proposed a microkinetic model of C_2H_4 oxidation on Ag catalysts with ethylene oxide (C_2H_4O) and acetic acid (CH_3CHO) species as intermediates. [19] In general, previously reported kinetic models were unable to include many intermediate species and elementary steps, which can be crucial to capture reaction pathways correctly. Furthermore, a detailed mechanism of C_2H_4 oxidation on DOC, particularly relevant to the diesel engine exhaust condition, is not available and requires an attention.

This work investigates the detail mechanism of C_2H_4 oxidation, as representative HC oxidation from diesel engine exhaust, on Pt based DOC using a combinatorial approach including experiments, density functional theory (DFT), and microkinetic modeling. More specifically, we consider practically relevant operating conditions experienced by a typical DOC, i.e. ppm level of emissions concentration, high oxygen concentration (10 - 15 %), short residence time, and atmospheric pressure environment. Microkinetic modeling is used to predict surface coverages, most abundant reaction intermediate(s) (MARI), conversion, and rate determining steps without any *a priori* assumptions; however, it requires good initial parameters. Those parameters can come

either from experiments or from first principle DFT computations. In this study, we extract the kinetic parameters from the simulations of TPD/TPR experiments and from DFT calculation. Parameters, mostly for the radicals and reaction intermediates, are not always available from experimental studies. In that case, DFT studies can provide those parameters; however, the temperature/pressure dependent kinetic parameters cannot be obtained. Thus, we implement semi-empirical unity bond-index quadratic exponential potential (UBI-QEP) [20] method to compute coverage and temperature dependent quantities such as activation barriers. Finally, we conducted fixed bed reactor experiments in practically realistic DOC operating conditions for the validation of our model. The global reaction mechanism of C_2H_4 oxidation on Pt is given as:

$$C_2H_4 + 3O_2 \rightarrow 2CO_2 + 2H_2O. \quad [1]$$

This paper is organized as follows. First, we discuss the methodology for the development of emissions oxidation chemistry in Section 2. In Section 3, we discuss the estimation of kinetic parameters from ultra-high vacuum (UHV) temperature programmed desorption/reaction (TPD/TPR) experiments in literature. Performance of the reaction mechanism is demonstrated in Section 4 at practically more relevant operating conditions. Preliminary mechanism reduction is discussed in Section 5. Finally, we discuss the overall limitations of this work in Section 6, followed by conclusions.

2. Methodology

2.1 DFT calculation

Our first principles DFT calculations were performed using the Vienna ab initio simulation package (VASP) [21, 22] utilizing the Perdew-Burke-Ernzerhof (PBE) [23]

functional, and the projector augmented wave (PAW) [24] frozen-core potentials. Plane-wave cut-off energy of 500 eV was used for the plane-wave expansion of the wave functions. The energy of a single atom or molecule was calculated using a 14×14×14 $Å^3$ cell. A 5-layer slab and a (3 ×3) surface unit cell was considered to represent a Pt(111) surface. The two bottom layers of the slab were fixed and the other layers were allowed to relax. To avoid any periodic image interactions, an intervening 12-14 Å vacuum region was introduced. Monkhorst-Pack grids[25] of 4 × 4 × 1 were used for Brillouin zone integration for the slab with (3 ×3) surface unit cell. For the Pt bulk calculations, Monkhorst-Pack mesh of 10 × 10 × 10 was used. The binding energy E_b of an atom or a molecule on the slab is defined as:

$$E_b = -[E_{slab+adsorbate} - E_{slab} - E_{sdsorbate}] \quad [2]$$

where $E_{slab+adsorbate}$, E_{slab}, and $E_{sdsorbate}$ represent the energy of the slab with the atom/molecule, energy of the clean slab, and the energy of an isolated atom/molecule, respectively. E_b values are positive numbers, where an increase in positive number indicates the strong binding to the surface.

2.2 Experimental

2.2.1 Catalysts characterization

Powder Pt/Al_2O_3 catalysts with 1% Pt loaded on alumina was purchased directly from Sigma-Aldrich. Platinum loading in the range of 0.70 - 1.30 % was confirmed by the company through ICP. The catalytic oxidation performance data was tested after a simple pretreatment. Figure 1 shows the characterization of Pt/Al_2O_3 using N_2 adsorption/desorption and SEM analysis. The isothermal N_2 adsorption and desorption

analysis of the Pt/Al_2O_3 powder catalysts is shown in Figure 1a. The BET surface area was calculated in the linear relative pressure range from 0.05 to 0.3. The typical hysteresis loop between the adsorption and desorption branches in figure 1a indicates that the existence of large amount of mesopores in the powder catalysts. The BJH desorption pore size distribution was also shown in Figure 1b, which revealed that the mesopores in the catalysts have a narrow size distribution with an average pore size around 10 nm. In panel c and d (**Figure 1**), SEM image and the elemental composition are shown confirming the Pt loading in the catalyst sample used in this study.

2.2.2 Catalytic performance tests

A fixed-bed type reactor, BenchCAT reactor from Altamira Instruments, was used for C_2H_4 oxidation experiments using Pt/Al_2O_3 powder catalysts. The reaction was carried out on 100 mg of Pt/Al_2O_3 catalyst loaded in a 0.34 cm i.d. quartz tube reactor inside a temperature-controlled furnace. Dycor Dymaxion mass spectrometer and Agilent Micro GC were used for the gas species analysis in the product stream. Effects of O_2 partial pressure (6 – 14 %), C_2H_4 concentration (500 – 3000 ppm), and space velocity (20000 – 60000 h^{-1}) on catalytic performance were tested for the temperature range of 50-300 °C. Ar was used as a balance gas in the experiments. All experiments were performed at near atmospheric pressure condition.

2.3 C_2H_4 oxidation chemistry development strategy

Microkinetic modeling of C_2H_4 oxidation consists of three major steps. First, elementary step reaction mechanism is developed for the oxidation chemistry based on reactants, intermediates, possible reaction pathways, and final products. Second, kinetic parameters

for the proposed reactions are extracted/estimated from literature surface science experiments, semi-empirical methods, and DFT calculations. Third, the surface reaction mechanism, combined with reactor modeling, is validated against multiple fixed bed experiments conducted in practically relevant operating conditions of DOC.

We note that some uncertainty may be associated with the microkinetic modeling due to various factors such as choice of reaction mechanism, kinetic parameters, experimental methods, and reactor modeling. Uncertainties due to the choice of reactions and species may be reduced with mechanism complexity; however, it reduces the practical usability. A good set of initial kinetic parameters is crucial for the microkinetic modeling. However, the kinetic parameters are inherently associated with some uncertainty due to the accuracy of estimation methods. Similarly, uncertainty may come from experimental methods due to products and intermediate identification techniques, availability of range of temperature, and species concentration profiles etc. On the other hand, reactor model uncertainty involves the role of diffusion vs. kinetics, representation of experimental non-uniformity with uniform mean field performance. [26] In general, many uncertainties come from various sources; nonetheless, provide justification for some parameter adjustment in the model.

2.3.1 Surface reaction mechanism development

Elementary step surface reaction mechanism of C_2H_4 oxidation consists of following 15 surface species: H*, O*, OH*, H_2O*, C*, CO*, CO_2*, COOH*, CH*, CH_2*, CH_3*, C_2H_2*, C_2H_3*, C_2H_4*, C_2H*, and CCH_2*. We considered the complete oxidation products such as CO_2 and H_2O as well as the other stable products such as CO, H_2, and C_2H_2.

Various cross-interactive reaction pathways such as CO and H_2 oxidation, CO oxidation and carbon formation/oxidation, C_2H and CCH_2 oxidation chemistries are included in this work. In total, 52 elementary step reactions (26 reversible pairs) are considered in this study. Detail reaction mechanism is given in **Table 2**.

2.3.2 Kinetic parameter estimation/extraction

Kinetic parameters for the proposed mechanism were estimated/extracted using various methods, i.e. simulations of UHV temperature programmed surface science experiments in literature, semi-empirical UBI-QEP method[20], and first principles DFT calculations. For each stable species in the reaction mechanism, we have considered multiple TPD experimental data on Pt facets to extract the species binding energies (Q) and adsorbate-adsorbate interactions (α). Resulting parameters from the TPD simulations are shown in **Table 1** and **Figure 3**. Detailed information about the experimental conditions and the experimental vs. model predicted peak temperatures is given in Section 3. Various TPR experimental data sets in the literature are used to extract the activation energies (E_a and bond indices (BI) for the reactions. Details of the TPR simulations are discussed in Section 3.

DFT calculations are carried out to estimate binding energies (Q) and adsorbate-adsorbate interactions (α) parameters of various intermediates and radicals along with stable species. Such calculations will reduce the inherent error introduced to the model due to parameters, as all parameters are computation with same level of theory and accuracy. The semi-empirical UBI-QEP method is used to estimate the coverage and temperature dependent activation energies on-the-fly in these simulations. Functional

forms to compute the activation energies using UBI-QEP formalism are discussed elsewhere. [2] In UBI-QEP formalism, temperature and coverage dependence to compute activation barriers are introduced through binding energy as shown in equation 3.

$$Q(T) = Q_o - \alpha\theta - \gamma R(T - T_o) \quad [3]$$

where, α is the coverage dependence coefficient (kcal/mol/ML), θ is the coverage of species (ML), γ is the temperature dependence coefficient for binding energies (unitless), R is the universal gas constant (kcal/mol/K), and T is the temperature (K). ML stands for monolayer. T_o is taken as 300 K. The temperature dependence (γ) is derived from the statistical mechanics based calculations for degrees of freedom lost/gained upon adsorption. [27] Bond index represents the position of the transition state along the reaction coordinate, which is also used to compute the activation energies in the UBI-QEP formalism. [27, 28] It is defined for a reaction pair in the forward direction only. It ranges between 0 and 1, with a typical initial estimate of 0.5 is used here.

Pre-exponential factors are taken either from literature (if available) or taken as initial estimates based on transition state theory (TST), e.g., $10^{13}s^{-1}$ for desorption and $10^{11}s^{-1}$ for Langmuir-Hinshelwood type surface reactions. Sticking coefficients for the adsorption reactions are taken from values reported in literature, otherwise taken as unity. Site density σ of 1×10^{15}sites/cm^2 (2.5×10^{9}mol/cm^2) is used in the simulations based on the typical estimate for the most stable Pt(111) facet.[29]

2.3.3 Mechanism performance and validation at more realistic conditions

Validation of the developed model is crucial as the operating conditions experienced by the DOCs are significantly different from the UHV conditions for temperature programmed experiments or the zero-temperature conditions used in first principles calculations. Therefore, it is important to ensure that the microkinetic model developed with such parameters also works in the practically more relevant conditions, such as atmospheric pressure, dilute emissions concentrations (few tens to hundreds of ppm), and short residence times. In this work, fixed bed reactor experiments were conducted to obtain C_2H_4 oxidation data in realistic DOC conditions. The results obtained from our experiments are used to validate the developed model. Details of the mechanism performance and analysis of reaction paths are presented in Section 4.

Gas phase chemistry is taken into account through the GRI-Mech 3.0[30] reaction mechanism. Steady state isothermal PFR simulations were carried out using the developed oxidation mechanism performance against experimental results. Transient simulations were performed at the reactor inlet to get the initial surface species coverages. The resulting set of differential and algebraic (DAE) equations was solved using the DDASPK solver.

3. Results and discussions

3.1 C_2H_4 oxidation experiments

Figure 2 shows the essence of experimental results obtained for the C_2H_4 oxidation on Pt/Al_2O_3 catalyst. In panel a, we show the effect of C_2H_4 concentration on light off temperature. With the total flow rate of 50 sccm, we considered four different concentration (500 ppm – 3000 ppm) of C_2H_4 and 10% O_2 to see the effect. We clearly

see a huge shift in light off temperature ($T_{50,}$ 50% conversion) as it moves from ~80 ^{o}C (for 500 ppm of C_2H_4) to ~140 ^{o}C (for 3000 ppm of C_2H_4). Our results are consistent with the experimental results of C_2H_4 complete conversion at 145 ^{o}C by Imanaka *et al.*[13], while considering 1% C_2H_4 and 4% O_2. The effect of O_2 concentration is shown in panel b (Figure 2). Unlike the C_2H_4 effect, we observed significantly lesser impact on light of temperature due to oxygen concentration considered here (6-14%). This is due to the fact that even 6% oxygen is already in excess compared to the ppm level of C_2H_4 concentrations considered here. In the light of oxygen concentration information on diesel engine exhaust, we see no significant impact of O_2 alone. We note that the outcome may be different while the concentration of oxygen is being relatively low (for example, engine in rich conditions). To depict the change in driving conditions (accelerating/decelerating), we conducted experiments with varying total flow rate (50 – 150 sccm) for 1000 ppm C_2H_4 and 10% O_2. Surprisingly, the effect on light off temperature was small even with the large variation in space velocity (~20000 - 60000 h^{-1}) (see Panel c, Figure 2).

3.2 TPD simulations

From TPD simulations, we extracted the binding energy of C_2H_4 (17.9 kcal/mol) and C_2H_6 (8.1 kcal/mol) along with adsorbate interactions $\alpha_{C_2H_4}$= 1.9 kcal/mol/ML and $\alpha_{C_2H_6}$= 0.9 kcal/mol/ML). The estimated binding energies are within the range of values reported in the literature (range of $Q_{C_2H_4}$ = 14 - 20 kcal/mol and $Q_{C_2H_6}$ = 6 - 10 kcal/mol). We have used the binding energies and adsorbate interactions of other stable species (for example: CO, H_2O, H_2, O_2 etc) obtained from TPD simulations in our previous work.[2]

Here, we discuss the C_2H_4 TPD, which results in decomposition and formation of various products. Heating of C_2H_4 to higher temperature leads to the decomposition and formation of C_2H_6 and H_2 along with molecular desorption of C_2H_4. Our simulations correctly capture the products peaks as well as the molecular desorption of C_2H_4. In order to capture the experimental results, bond index of $C_2H_4^* + * \leftrightarrow C_2H_3^* + H^*$ and $C_2H_3^* + * \leftrightarrow C_2H_2^* + H^*$ were modified to 0.75 and 0.76 respectively (starting from 0.5). With these minor adjustments, **Figure 3c** shows the agreement of model simulations and experimental peaks. Further, the simulated coverage profile in **Figure 3d** shows the dominant surface species. At low temperature, we see the decomposition of $C_2H_4^*$ and formation of H_2 and $C_2H_3^*$. The $C_2H_3^*$is stable up to 500 K and further decomposes to form CH* on the surface. The decomposition of CH* was not seen, although expected, due to the range of temperature considered. The kinetic parameters estimated from these TPD simulations are incorporated in the mechanism for further investigations through TPR and PFR simulations.

3.3 TPR simulations

Ultra high vacuum TPR experimental data from Steininger et al.[16] was taken to simulate the oxidation mechanism of C_2H_4 on Pt(111) surface. Figure 4a shows the peaks for C_2H_4 oxidation products (i.e. CO, CO_2, H_2, and H_2O) and excess C_2H_4 desorption rate from the C_2H_4 oxidation TPR on Pt(111) and Figure 4b shows the model simulated coverage profiles with various surface species such as $C_2H_4^*$, $C_2H_3^*$, OH*, C_2H^*, and CH* over the range of temperature. The initial coverage include 0.35 ML of $C_2H_4^*$ and 0.23 ML of O* on the surface. Bond index (UBI-QEP parameter) of the reaction pair Rx

($C_2H_4^* + O^* \leftrightarrow C_2H_3^* + OH^*$) was modified to 0.9 (starting from 0.5) to correctly capture the experimental peak temperature.

RPA suggests that the oxidation and decomposition starts at low temperature with the formation of C_2H_3*, H*, and OH* on the surface as seen in figure 4b. Excess of C_2H_4* starts desorbing at ~200 K (peak at ~280 K, Figure 4a). At the same time, H_2O formation and simultaneous desorption occurs due to the reactions $H_2O^* + * \leftrightarrow OH^* + H^*$ and $H_2O^* + O^* \leftrightarrow 2OH^*$ resulting in a peak at ~290 K. At ~ 400 K, two experimental peaks of H_2O and CO_2 were observed. RPA shows that the H_2O formation is mostly due to the reactions $C_2H_2^* + H_2O^* \leftrightarrow C_2H_3^* + OH^*$ and $C_2H_2^* + OH^* \leftrightarrow C_2H^* + H_2O^*$(~80 % combined) and partly due to the reactions $H_2O^* + * \leftrightarrow OH^* + H^*$ and $H_2O^* + O^* \leftrightarrow 2OH^*$ (~20% combined). The CO_2 formation is mainly due to the reactions $COOH^* + * \leftrightarrow CO_2^* + H^*$ and $CO_2^* + H^* \leftrightarrow CO^* + OH^*$, where CO* formation is primarily due to the reaction $CH^* + CO^* \leftrightarrow C_2H^* + O^*$. Once CO_2* is formed on the surface, it desorbs immediately resulting a peak at ~400 K (Figure 4a). Finally, the last two peaks appear at ~500 K, i.e. experimental desorption peaks of CO and H_2. RPA suggests that the CO peak at this temperature range is primarily due to desorption of CO* from the surface due to sufficient energy at the elevated temperature. Formation of H* on the surface is due to the reaction $C_2H_3^* + * \leftrightarrow C_2H_2^* + H^*$, which desorbs as H_2 immediately. The C_2H_2* species further decompose into CH* on the surface, which can be seen in the coverage profile (**Figure 4b**). With no oxygen on the surface, the increase in temperature will leads to the decomposition of CH* species into C* and H* (not shown here).

3.4 Model performance under practically relevant operating conditions

The developed mechanism performed well against the experimental data from UHV conditions. However, the realistic condition (i.e. DOC operating condition) is significantly different as discussed in **Section 2.3.3**. Thus, we performed C_2H_4 oxidation experiments (discussed earlier in **Section 3.1**). Next, we discuss the validation/performance of the model using the data obtained from our fixed-bed reactor experiments.

3.4.1 Effect of C_2H_4 concentration

First, we show the model performance to capture the concentration effect of C_2H_4 (concentration 500-3000 ppm) on the light off temperature using 10% O_2. As discussed earlier, the impact of increasing C_2H_4 concentration on the light off temperature was quite large, which is captured by our model nicely for the entire temperature range. As expected, the conversion profile reaches complete conversion quite rapidly. The model performance is shown in **Figure 6**. We show the simulated coverage profile for different initial C_2H_4 feed concentrations at 100 ^oC. we clearly see the dominant coverage of CH* and CO* species on the surface. O* coverage was not seen at lower temperature range; however, it becomes a MARI above $\sim 150\,^oC$ (not shown here).

We have adjusted the bond index of the reaction pair R_{29}-R_{30}($C_2H_4^* + O^* \leftrightarrow C_2H_3^* + OH^*$) to 0.65 to capture the low temperature profile correctly. We note that the adjustment was slightly different in TPR simulations. This modification is justified as some parameter refinement is generally required for the transition from UHV simulations to practically more relevant atmospheric pressure simulations on polycrystalline or supported catalysts. At higher temperature, abrupt change in coverage profiles was

observed while achieving the complete conversion state. This aligns well with the experimental observation as the complete conversion occurred in few degrees range after achieving ~50% C_2H_4 conversion.

3.4.2 Effect of O_2 concentration

The effect of O_2 concentration of the light off temperature was predicted without modifying any kinetic parameters of the model. This model was able to capture our experimental data well. The effect of oxygen concentration was not as big as compared to the effect of C_2H_4 concentration. Our model performance against the experimental data is shown in **Figure 6**.

3.4.3 Effect of flow rates

Our microkinetic model performed well and captured our experimental data well. In this case, varying the flow rate up to 300% showed no such drastic impact on the light off temperature. Our model performance against the experimental data is shown in **Figure 7.**

3.5 Sensitivity analysis

Sensitivity analysis was performed to identify the important reaction in the mechanism. The normalized sensitivity coefficient is defined as dlnP/dlnR (i.e., (dP/dR)×(R/P)), where dP is the change in parameter P (pre-exponential factors) and dR is the change in model response R (conversion). **Figure 8** shows the most sensitive reaction pairs (10 pairs are shown here). The reaction pair R_{29}-R_{30} ($C_2H_4^* + O^* \leftrightarrow C_2H_3^* + OH^*$) was the most sensitive reaction in our analysis.

4. Conclusions

In this study, we performed a detailed study of C_2H_4 oxidation on Pt based DOC using multiple methods including fixed bed experiments, DFT computations, and microkinetic modeling. Our experimental results suggested that the concentration of C_2H_4 has the most impact on the light off temperature. This suggests that the slight fluctuation on the O_2 concentration and the total exhaust flow rate have no significant impact on the DOC performance. DFT computations are performed to obtain the kinetic parameters for our microkinetic model for C_2H_4 oxidation on Pt. Our model performs well against all the experimental data. Finally we propose a 52 elementary step model for the oxidation of C_2H_4 on Pt.

5. Acknowledgements

HNS acknowledges the United States EPA STAR graduate fellowship for funding support. This publication (article) was made possible by EPA fellowship number FP917501. Its contents are solely the responsibility of the fellow and do not necessarily represent the official views of the EPA. Furthermore, the EPA does not endorse the purchase of any commercial products or services mentioned in the publication.

References

[1] H.N. Sharma, L. Pahalagedara, A. Joshi, S.L. Suib, A.B. Mhadeshwar, Energy and Fuels. 26 (2012) 5613-5625.

[2] H.N. Sharma, A.B. Mhadeshwar, Appl. Catal. B-Environ. 127 (2012) 190-204.

[3] A. Russell, W.S. Epling, Catal. Rev. Sci. Eng. 53 (2011) 337-423.

[4] H.N. Sharma, S.L. Suib, A.B. Mhadeshwar, in: Bravo-Suarez, J.J., Schwartz, V. and Kidder, M.K. (Eds.), Novel Materials for Catalysis and Fuels Processing, ACS, 2013, pp. 117-155.

[5] H. Oh, I.S. Pieta, J. Luo, W.S. Epling, Top. Catal. 56 (2013) 1916-1921.

[6] R. Sant, D.J. Kaul, E.E. Wolf, AIChE J. 35 (1989) 267-278.

[7] R.M. Watwe, R.D. Cortright, M. Mavrikakis, J.K. Nørskov, J.A. Dumesic, J. Chem. Phys. 114 (2001) 4663-4668.

[8] M.A. Peña, D.M. Carr, K.L. Yeung, A. Varma, Chem. Eng. Sci. 53 (1998) 3821-3834.

[9] D.I. Iordanoglou, A.S. Bodke, L.D. Schmidt, J. Catal. 187 (1999) 400-409.

[10] D.J. Burnett, A.M. Gabelnick, D.A. Fischer, A.L. Marsh, J.L. Gland, J. Phys. Chem. B. 109 (2005) 5659-5666, doi: 10.1021/jp048106u.

[11] J.R. Hawkins, S.E. Wanke, Can. J. Chem. Eng. 57 (1979) 621-626.

[12] B.C. Michael, D.N. Nare, L.D. Schmidt, Chem. Eng. Sci. 65 (2010) 3893-3902.

[13] N. Imanaka, T. Masui, A. Terada, H. Imadzu, Chem. Lett. 37 (2008) 42-43.

[14] H.A. Aleksandrov, L.V. Moskaleva, Z. Zhao, D. Basaran, Z. Chen, D. Mei, N. Rösch, J. Catal. 285 (2012) 187-195.

[15] J.E. Demuth, Surf. Sci. 84 (1979) 315-328.

[16] H. Steininger, H. Ibach, S. Lehwald, Surf. Sci. 117 (1982) 685-698.

[17] T. Jacob, W.A. Goddard, J. Phys. Chem. B. 109 (2005) 297-311.

[18] J.G. Lopez, C.L. Rasmussen, M.U. Alzueta, Y. Gao, P. Marshall, P. Glarborg, Proceedings of the Combustion Institute. 32 (2009) 367-375.

[19] C. Stegelmann, P. Stoltze, J. Catal. 226 (2004) 129-137.

[20] E. Shustorovich, H. Sellers, Surface Science Reports. 31 (1998) 1-119.

[21] G. Kresse, J. Furthmüller, Comput. Mater. Sci. 6 (1996) 15-50, doi: 10.1016/0927-0256(96)00008-0.

[22] G. Kresse, J. Furthmüller, Phys. Rev. B. 54 (1996) 11169.

[23] J.P. Perdew, K. Burke, M. Ernzerhof, Phys. Rev. Lett. 77 (1996) 3865-3868.

[24] P. Blöchl, Phys. Rev. B. 50 (1994) 17953-17979.

[25] H.J. Monkhorst, J.D. Pack, Phys. Rev. B. 13 (1976) 5188-5192.

[26] M. Koehle, A. Mhadeshwar, Chem. Eng. Sci. 78 (2012) 209-225.

[27] A.B. Mhadeshwar, H. Wang, D.G. Vlachos, - J. Phys. Chem. B. 107 (2003) - 12721-12733.

[28] A.B. Mhadeshwar, D.G. Vlachos, Combust. Flame. 142 (2005) 289-298, doi: 10.1016/j.combustflame.2005.01.019.

[29] R.J. Gorte, L.D. Schmidt, J.L. Gland, Surf. Sci. 109 (1981) 367-380.

[30] G.P. Smith, D.M. Golden, M. Frenklach, N.W. Moriarty, B. Eiteneer, M. Goldenberg, C.T. Bowman, R.K. Hanson, S. Song, W.C. Gardiner, V.V. Lissianski, Z. Qin, GRI-Mech 3. 0. http://www.me.berkeley.edu/gri_mech/ (1999).

[31] C.R. Arumainayagam, G.R. Schoofs, M.C. McMaster, R.J. Madix, J. Phys. Chem. 95 (1991) 1041-1047, doi: 10.1021/j100156a005.

[32] J.M. Essen, J. Haubrich, C. Becker, K. Wandelt, Surf. Sci. 601 (2007) 3472-3480.

[33] A.K. Galwey, M.E. Brown, Thermochim. Acta. 300 (1997) 107-115.

[34] M.C. Costache, D. Wang, M.J. Heidecker, E. Manias, C.A. Wilkie, Polym. Adv. Technol. 17 (2006) 272-280.

[35] P. Ollero, A. Serrera, R. Arjona, S. Alcantarilla, Fuel. 81 (2002) 1989-2000.

Figures

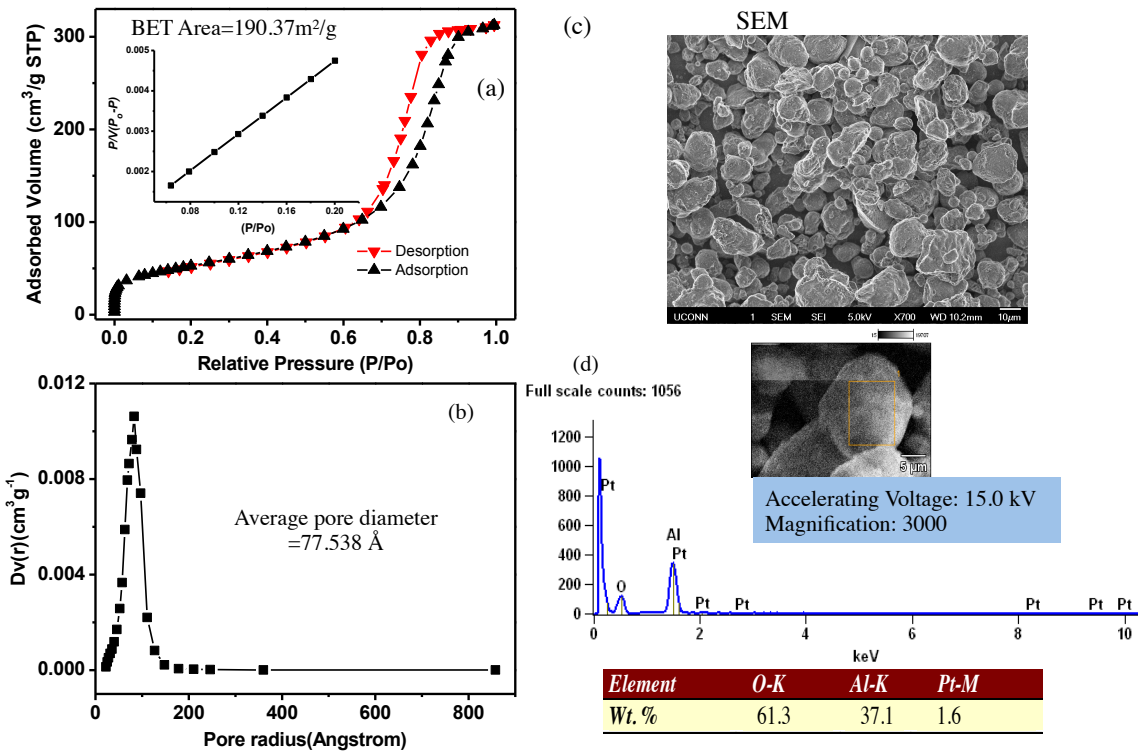

Figure 1: Surface characterization of Pt/Al_2O_3 powder catalysts: (a) N_2 adsorption/desorption analysis; (b) BJH desorption pore size distribution; (c) Elemental analysis acquired under SEM; (d) ICP analysis. The weight percentage of Pt is found to be 1%.

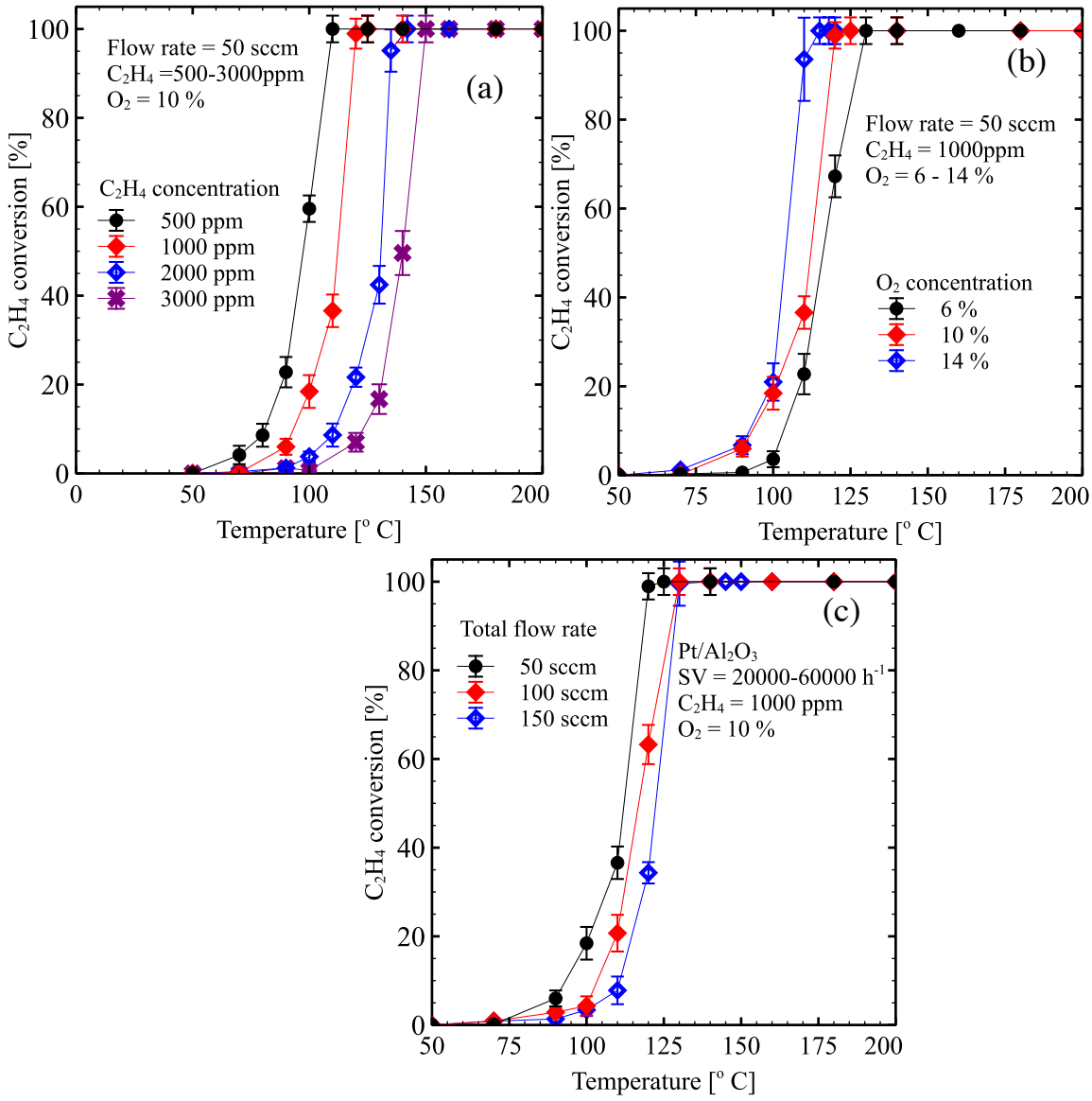

Figure 2 : Experimental conversion profiles of C_2H_4 oxidation on Pt/Al_2O_3 catalyst showing the effect of C2H4 concentration (in panel a), effect of oxygen concentration (in panel b), and the effect of total flow rate (in panel c) on the light off temperature.

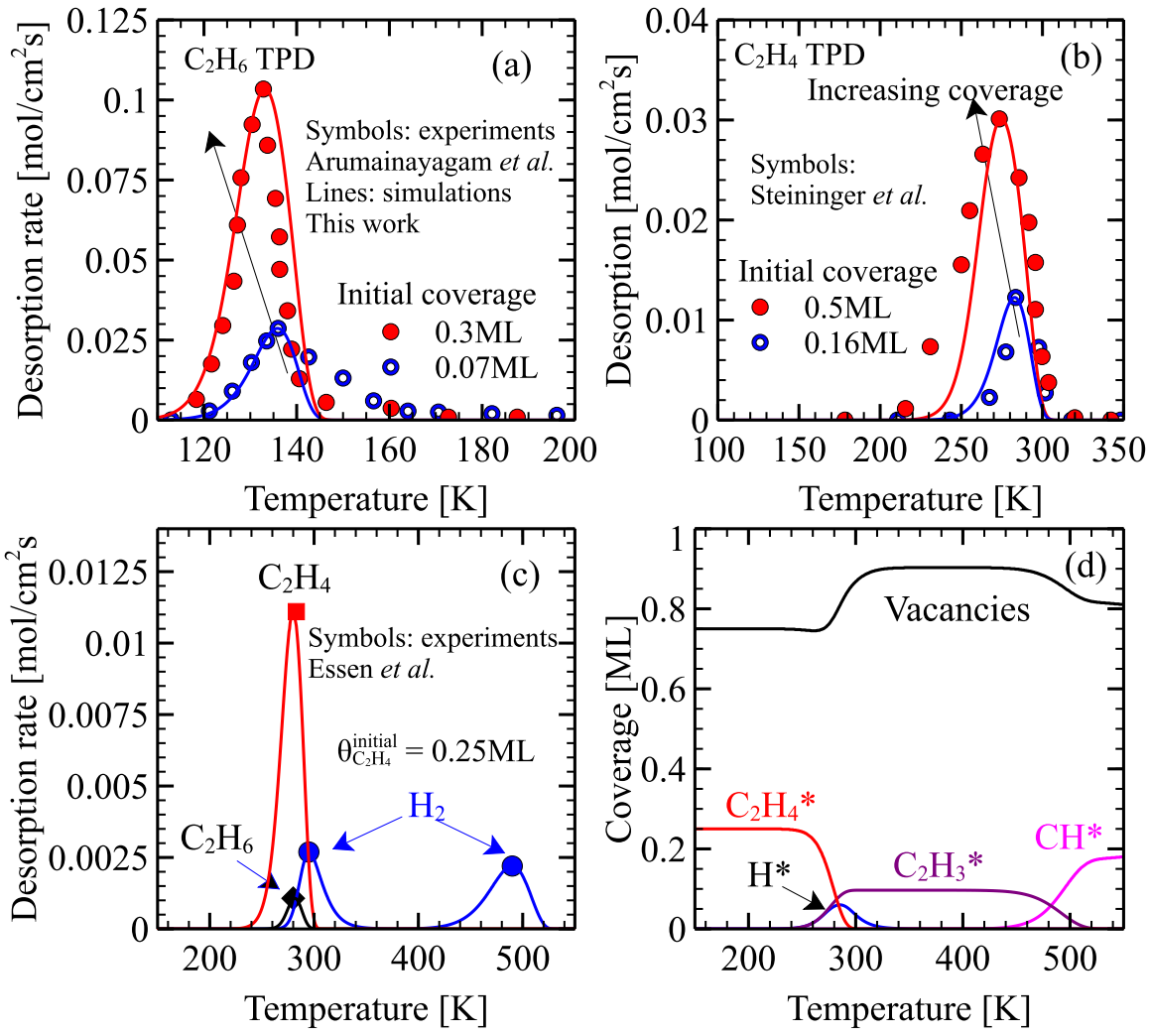

Figure 3: UHV-TPD analysis of (a) C_2H_6 desorption, (b) C_2H_4 desorption, (c) C_2H_4 decomposition, (d) C_2H_4 simulated coverage profiles, on Pt. Symbols represent the experimental data, whereas lines represent our simulations. Panel a: C_2H_6 TPD; [31] initial high and low C_2H_6* coverages are 0.3 ML and 0.07 ML, respectively; ramp rate =

5 K/s. Panel b: C_2H_4 TPD[16]; initial high and low C_2H_4* coverages are 0.5 ML and 0.16 ML, respectively; ramp rate = 2 K/s. Panel c: C_2H_4 decomposition TPD[32]; initial C_2H_4* coverage is 0.25ML; ramp rate = 2 K/s. Panel d: simulated surface coverage profile of C_2H_4* decomposition TPD; experimental conditions are same as Panel c. See Table 2 for the extracted kinetic parameters from these simulations.

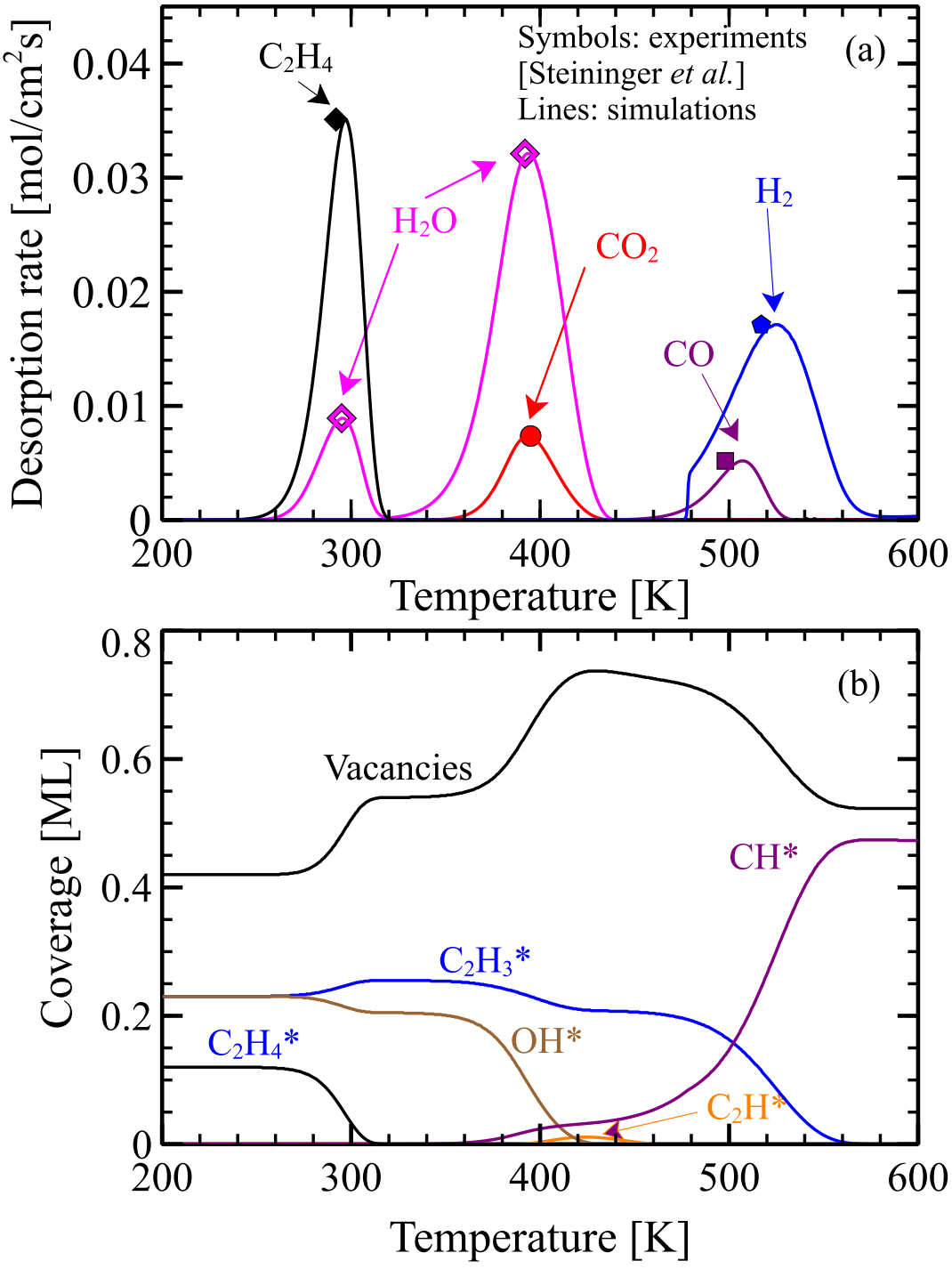

Figure 4: UHV-TPR analysis of C_2H_4 oxidation on Pt(111). Panel a shows the rate of desorption of species and panel b shows the model simulated coverage profiles of surface species over a range of temperature. Symbols represent the experimental data, [16]

whereas lines represent the simulations. Operating conditions: initial surface coverages of O^* and $C_2H_4^*$ are 0.23 ML and 0.35 ML, respectively; ramp rate=15.5 K/s. Simulations are in good agreement with the experimental data.

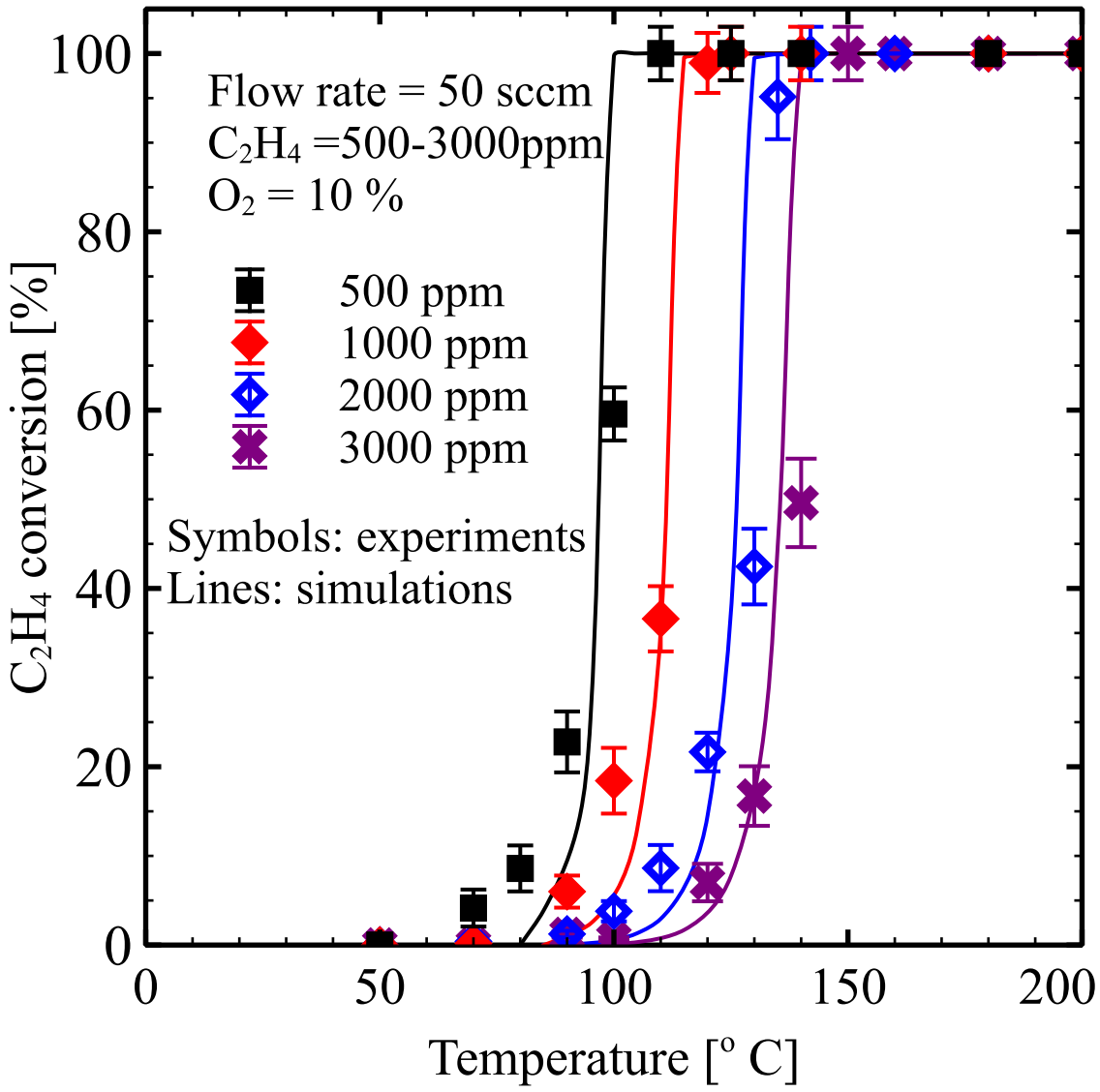

Figure 5: Model performance for prediction of C_2H_4 concentration imapcts on light off tempeature. Lines are the simulations and symbols are the experimental data points. Operating conditions are same as in Figure 2.

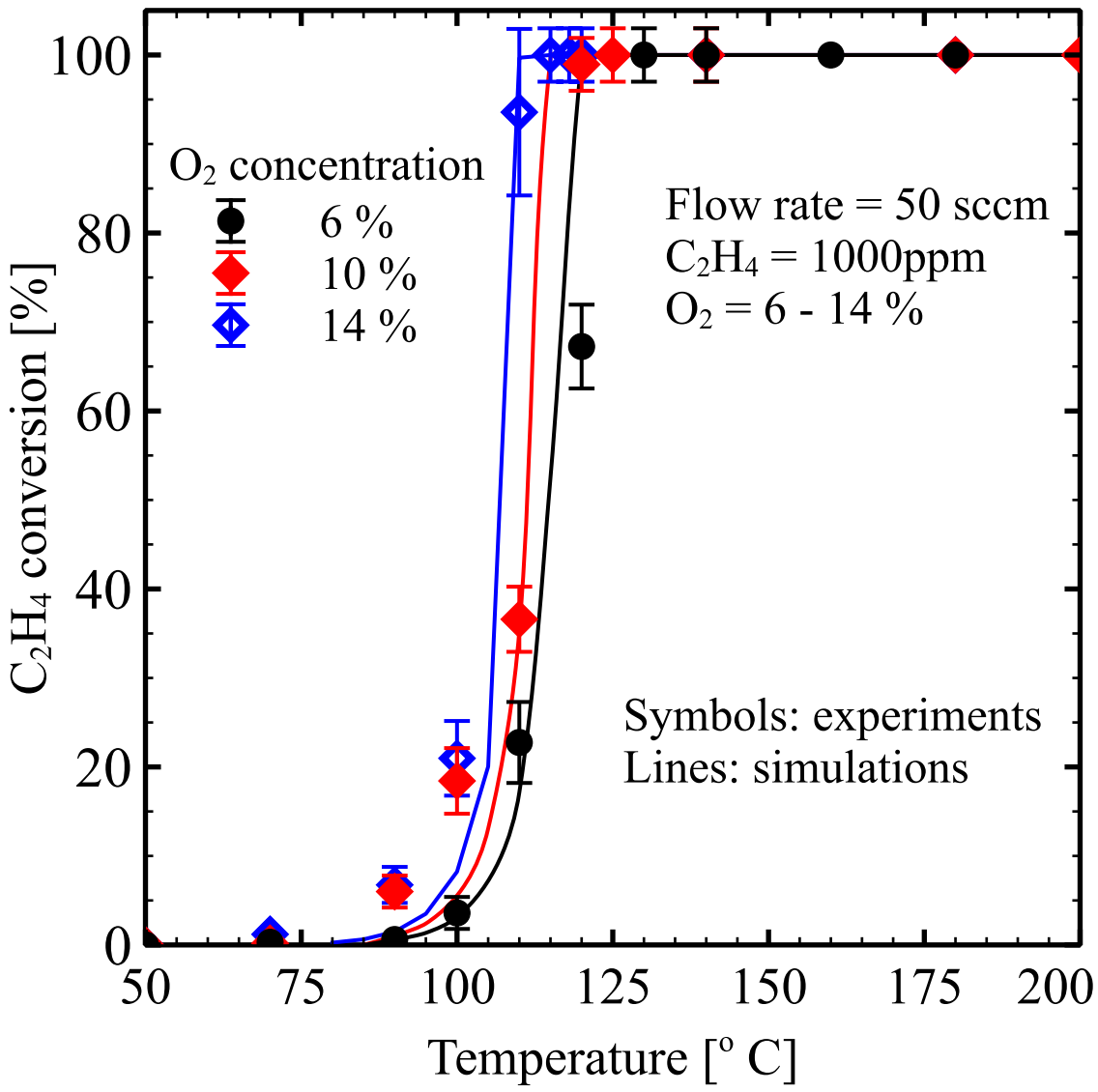

Figure 6: Model performance for prediction of O_2 concentration effects on light off tempeature. Lines are the simulations and symbols are the experimental data points. Operating conditions are same as in Figure 2.

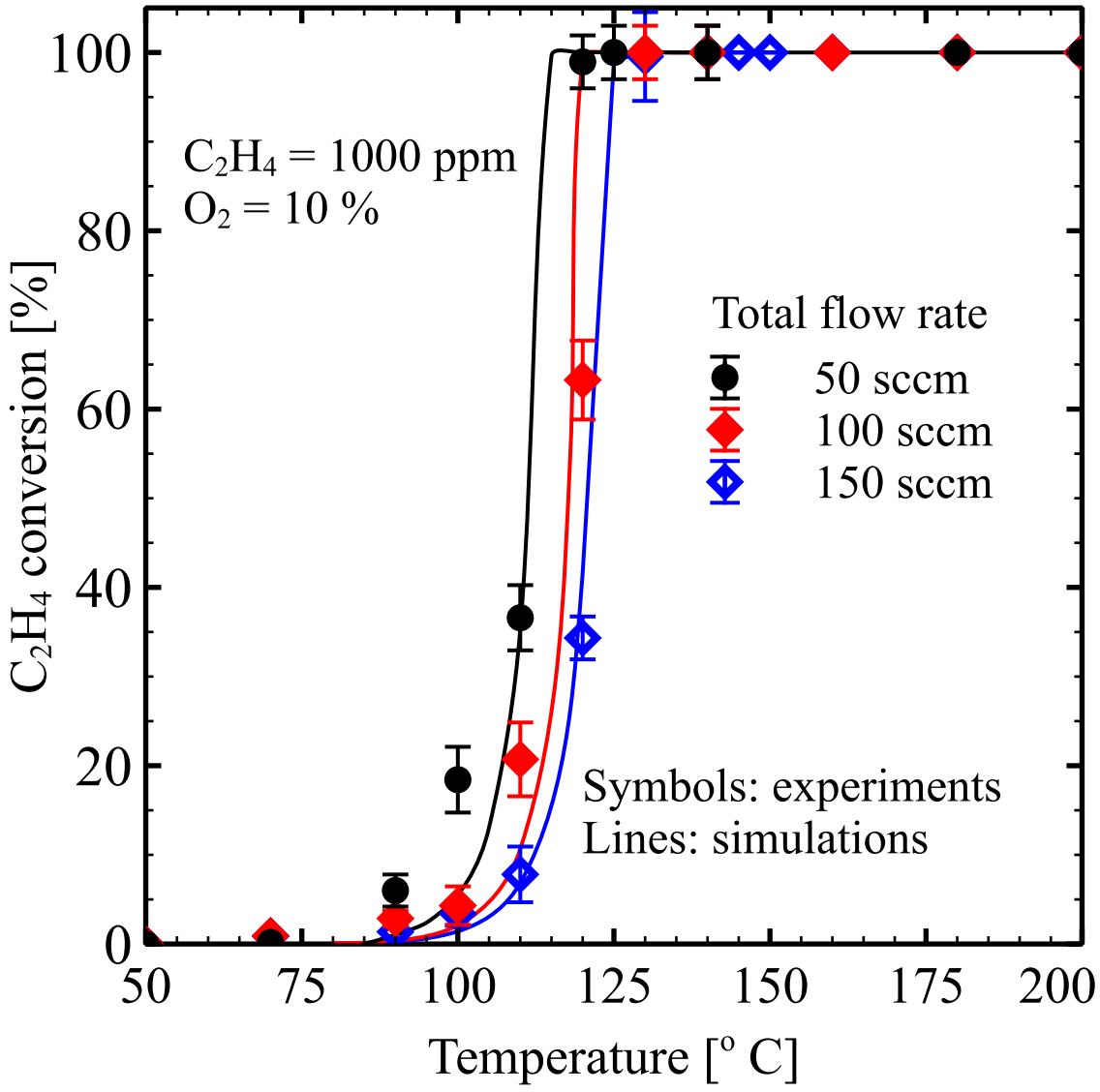

Figure 7: Model performance for prediction of flow rate effects on light off tempeature. Lines are the simulations and symbols are the experimental data points. Operating conditions are same as in Figure 2.

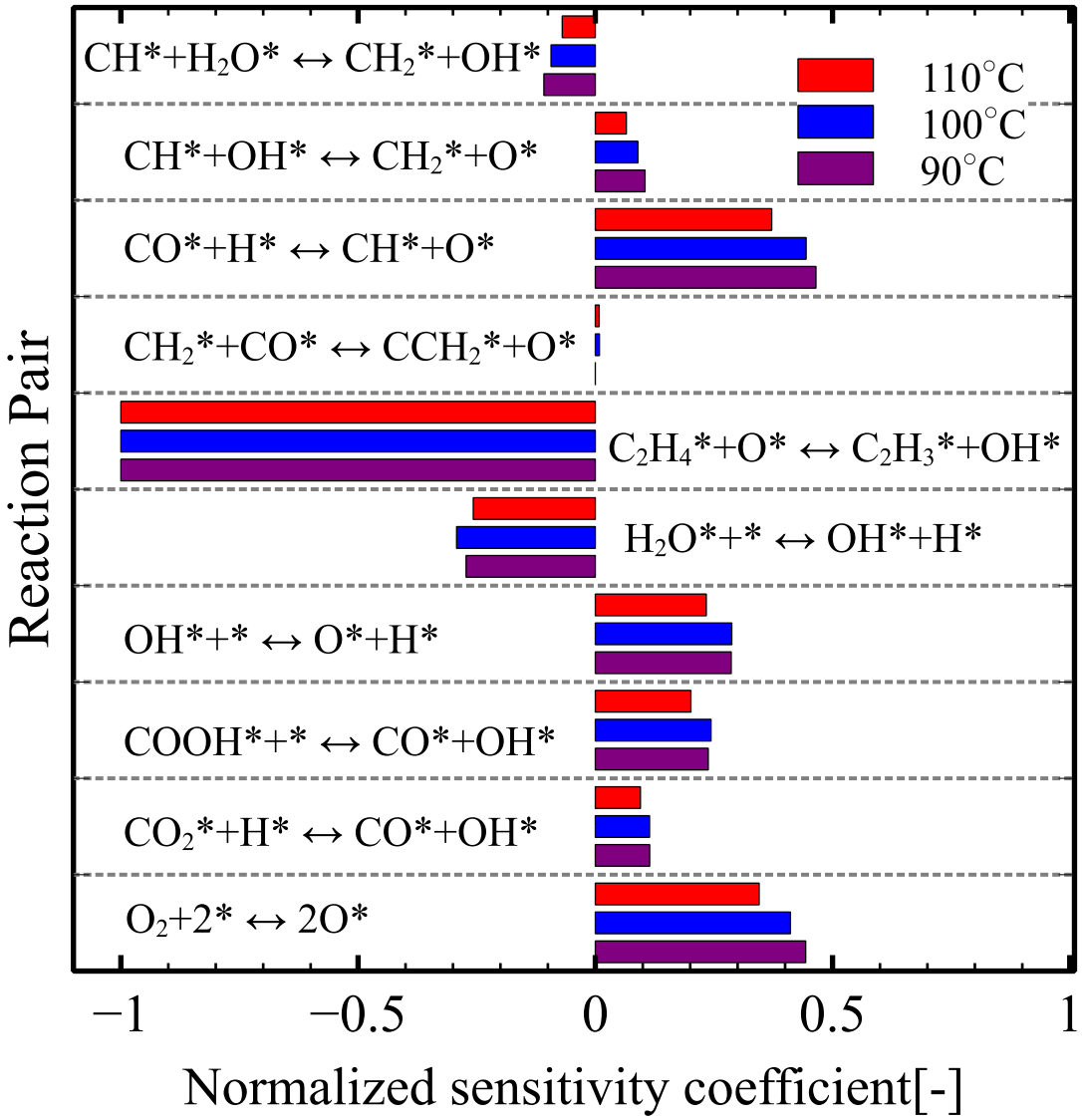

Figure 8: Sensitivity analysis for the microkinetic model responses with respect to the pre-exponential factor pairs in the surface reaction mechanism shown in Table 2. Pre-exponentials are modified pairwise without perturbing the equilibrium constant. Only those reaction pairs with the highest normalized sensitivity coefficients [dlnR/dlnP, i.e., (dR/dP)×(P/R)] are shown here. The sensitivity coefficients at three representative

temperatures (i.e. 90 °C, 100 °C, and 110 °C) are shown. Operating conditions are the same as in Figure 3.

Table 1: Species binding energies along with the coverage dependence.

SN	Surface species	Extracted/calculated binding energy Q (kcal/mol)	Coverage dependence α (kcal/mol)	Source /Reference
1	O*	86.01	$13.3\theta_O$	TPD[2]
2	H*	60.89	$1.9\theta_H$	TPD[2]
3	OH*	63.0	$33\theta_O$	DFT[2]
4	H_2O*	10.27	-	TPD[2]
5	CO*	40.0	$8.3\theta_{CO}$	TPD[2]
6	CO_2*	3.6	-	TPD[2]
7	C*	158.20	-	DFT[2]
8	CH*	157.73	-	DFT (this work)
9	CH_2*	93.62	-	DFT (this work)
10	C_2H_2*	50.0	-	DFT (this work)
11	C_2H_3*	67.5	-	DFT (this work)
12	C_2H_4*	17.9	$1.8\theta_{C2H4}$	TPD simulation (this work)
13	C_2H*	103.6	-	DFT (this work)
14	CCH_2*	107.1	-	DFT (this work)
15	COOH*	56.26	-	DFT[2]

Table 2: Activation energies in the last column are temperature and coverage dependent, but only representative values are shown at 300 K. Coverage dependence originates from the use of UBI-QEP for the estimation of activation energies, whereas the temperature dependence is derived from the statistical mechanics based calculations for degrees of freedom lost/gained upon adsorption. Further details on the functional form 'f' are given in Appendix B.

No.	Reactions	Bond index (BI) [unitless]	Sticking coefficient [unitless] or Pre exponential factor [s^{-1}]	Activation energy at 300 K [kcal/mol]
	Oxygen adsorption/desorption			
R_1	$O_2 + 2* \rightarrow 2O*$	0.5	0.05	0
R_2	$2O* \rightarrow O_2 + 2*$	0.5	1×10^{13}	$52.9 - 26.6\theta_o + f(T)$
	CO oxidation			
R_3	$CO + * \rightarrow CO^*$	0.5	0.5 [29]	0
R_4	$CO^* \rightarrow CO + *$	0.5	5.7×10^{16}	$40 - 8.3\theta_{CO} - 2R\Delta T$
R_5	$CO_2 + * \rightarrow CO_2^*$	0.5	1	0
R_6	$CO_2^* \rightarrow CO_2 + *$	0.5	1×10^{13}	$3.6 - 2R\Delta T$
R_7	$CO_2^* + * \rightarrow CO^* + O^*$	0.73	1×10^{11}	$23.4 + f(\theta_O, \theta_{CO}, T)$
R_8	$CO^* + O^* \rightarrow CO_2^* + *$	0.73	1×10^{10}	$18.6 + f(\theta_O, \theta_{CO}, T)$
	H_2 oxidation			
R_9	$H_2 + 2* \rightarrow 2H^*$	0.5	1	0
R_{10}	$2H^* \rightarrow H_2 + 2*$	0.5	1×10^{13}	$17.6 - 3.8\theta_H + f(T)$
R_{11}	$H_2O + * \rightarrow H_2O^*$	0.5	1	0
R_{12}	$H_2O^* \rightarrow H_2O + *$	0.5	1×10^{13}	$10.3 - 2.5R\Delta T$ [120, 121]
R_{13}	$OH^* + * \rightarrow H^* + O^*$	0.5	1×10^{11}	$27 + f(\theta_O, \theta_H, T)$
R_{14}	$H^* + O^* \rightarrow OH^* + *$	0.5	1×10^{11}	$8.6 + f(\theta_O, \theta_H, T)$
R_{15}	$H_2O^* + * \rightarrow OH^* + H^*$	0.5	1×10^{11}	$18.3 + f(\theta_O, \theta_H, T)$
R_{16}	$OH^* + H^* \rightarrow H_2O^* + *$	0.5	1×10^{11}	$12.6 + f(\theta_O, \theta_H, T)$
R_{17}	$H_2O^* + O^* \rightarrow 2OH^*$	0.5	1×10^{11}	$9.4 + f(\theta_O, T)$
R_{18}	$2OH^* \rightarrow H_2O^* + O^*$	0.5	1×10^{11}	$22.1 + f(\theta_O, T)$

	Water promoted CO oxidation			
R_{19}	$CO_2^* + H^* \rightarrow CO^* + OH^*$	0.5	1×10^{11}	$5.4 + f(\theta_O, \theta_{CO}, \theta_H, T)$
R_{20}	$CO^* + OH^* \rightarrow CO_2^* + H^*$	0.5	1×10^{11}	$19 + f(\theta_O, \theta_{CO}, \theta_H, T)$
R_{21}	$COOH^* + * \rightarrow CO^* + OH^*$	0.5	1×10^{11}	$5.8 + f(\theta_O, \theta_{CO}, T)$
R_{22}	$CO^* + OH^* \rightarrow COOH^* + *$	0.5	1×10^{11}	$18.7 + f(\theta_O, \theta_{CO}, T)$
R_{23}	$COOH^* + * \rightarrow CO_2^* + H^*$	0.5	1×10^{11}	$2.1 + f(\theta_H, T)$
R_{24}	$CO_2^* + H^* \rightarrow COOH^* + *$	0.5	1×10^{11}	$1.3 + f(\theta_H, T)$
	C_2H_4 oxidation			
R_{25}	$C_2H_4 + * \rightarrow C_2H_4^*$	0.5	1	0.0
R_{26}	$C_2H_4^* \rightarrow C_2H_4 + *$	0.5	1×10^{13}	$17.9 - 1.8\theta_{C2H4} - 3R\Delta T$
R_{27}	$C_2H_4^* + * \rightarrow C_2H_3^* + H^*$	0.5	1×10^{11}	$16.35 + f(\theta_H,\theta_{C2H4,}T)$
R_{28}	$C_2H_3^* + H^* \rightarrow C_2H_4^* + *$	0.5	1×10^{11}	$15.6 + f(\theta_H,\theta_{C2H4,}T)$
R_{29}	$C_2H_4^* + O^* \rightarrow C_2H_3^* + OH^*$	0.75	1×10^{11}	$11.2 + f(\theta_H,\theta_{OH,}T)$
R_{30}	$C_2H_3^* + OH^* \rightarrow C_2H_4^* + O^*$	0.75	1×10^{11}	$28.8 + f(\theta_H,\theta_{OH,}T)$
R_{31}	$C_2H_2^* + OH^* \rightarrow C_2H_3^* + O^*$	0.5	1×10^{11}	$32.27 + f(\theta_H,\theta_{OH,}T)$
R_{32}	$C_2H_3^* + O^* \rightarrow C_2H_2^* + OH^*$	0.5	1×10^{11}	$5.54 + f(\theta_H,\theta_{OH,}T)$
R_{33}	$CCH_2^* + OH^* \rightarrow C_2H_3^* + O^*$	0.5	1×10^{11}	$39.23 + f(\theta_H,\theta_{OH,}T)$
R_{34}	$C_2H_3^* + O^* \rightarrow CCH_2^* + OH^*$	0.5	1×10^{11}	$0.0 + f(\theta_H,\theta_{OH,}T)$
R_{35}	$C_2H_2^* + H_2O^* \rightarrow C_2H_3^* + OH^*$	0.5	1×10^{11}	$23.32 + f(\theta_{OH,}T)$
R_{36}	$C_2H_3^* + OH^* \rightarrow C_2H_2^* + H_2O^*$	0.5	1×10^{11}	$9.26 + f(\theta_{OH,}T)$
R_{37}	$CO^* + CH_2^* \rightarrow CCH_2^* + O^*$	0.5	1×10^{11}	$39.77 + f(\theta_O,\theta_{CO,}T)$
R_{38}	$CCH_2^* + O^* \rightarrow CO^* + CH_2^*$	0.5	1×10^{11}	$7.92 + f(\theta_O,\theta_{CO,}T)$
R_{39}	$C_2H_2^* + O^* \rightarrow C_2H^* + OH^*$	0.5	1×10^{11}	$19.61 + f(\theta_O,\theta_{OH,}T)$
R_{40}	$C_2H^* + OH^* \rightarrow C_2H_2^* + O^*$	0.5	1×10^{11}	$19.56 + f(\theta_O,\theta_{OH,}T)$
R_{41}	$C_2H_2^* + OH^* \rightarrow C_2H^* + H_2O^*$	0.5	1×10^{11}	$12.7 + f(\theta_{OH,}T)$
R_{42}	$C_2H^* + H_2O^* \rightarrow C_2H_2^* + OH^*$	0.5	1×10^{11}	$0.0 + f(\theta_{OH,}T)$
R_{43}	$CH^* + CO^* \rightarrow C_2H_2^* + O^*$	0.5	1×10^{11}	$86.64 + f(\theta_O,\theta_{CO,}T)$
R_{44}	$C_2H_2^* + O^* \rightarrow CH^* + CO^*$	0.5	1×10^{11}	$0.0 + f(\theta_O,\theta_{CO,}T)$
R_{45}	$CO^* + H^* \rightarrow CH^* + O^*$	0.5	1×10^{11}	$44.7 + f(\theta_O, \theta_H, \theta_{CO,}T)$
R_{46}	$CH^* + O^* \rightarrow H^* + CO^*$	0.5	1×10^{11}	$10.94 + f(\theta_O, \theta_H, \theta_{CO,}T)$
R_{47}	$CH^* + OH^* \rightarrow CH_2^* + O^*$	0.5	1×10^{11}	$43.5 + f(\theta_O,\theta_{OH,}T)$
R_{48}	$CH_2^* + O^* \rightarrow CH^* + OH^*$	0.5	1×10^{11}	$1.28 + f(\theta_O,\theta_{OH,}T)$
R_{49}	$CH^* + H_2O^* \rightarrow CH_2^* + OH^*$	0.5	1×10^{11}	$33.6 + f(\theta_{OH,}T)$
R_{50}	$CH_2^* + OH^* \rightarrow CH^* + H_2O^*$	0.5	1×10^{11}	$4.06 + f(\theta_{OH,}T)$
R_{51}	$C_2H_2 + * \rightarrow C_2H_2^*$	0.5	1	0.0
R_{52}	$C_2H_2^* \rightarrow C_2H_2 + *$	0.5	1×10^{13}	$50 - 3R\Delta T$